Ab initio description of electron transport through nanoscale systems

Zur Erlangung des akademischen Grades eines

DOKTORS DER NATURWISSENSCHAFTEN

der Fakultät für Physik des Karlsruhe Institute of Technology

genehmigte

DISSERTATION

von

Dipl.-Phys. Marius Bürkle

Tag der mündlichen Prüfung : 28.10.2011

Referent	Prof. Dr. Gerd Schön
	Institut für Theoretische Festkörperphysik Karlsruhe Institute of Technology
Korreferent	Prof. Dr. Juan Carlos Cuevas
	Departmento de Física Teórica de la Materia Condensada Universidad Autónoma de Madrid

Contents

Part I

Introduction

The development of functional nanostructures has become a very important and active research area over the last decades. On the one hand the miniaturization of existing technology moves more and more into the nanoscale regime. For example the distance between two nodes on today's commercially available microprocessors is just around 22 nm and will halve in size until 2015 [1]. On the other hand there is also strong interest in the development of new classes of devices for instance combining electrical and mechanical functionality in nanoelectromechanical systems [4] or nanogenerators which harvest energy by means of piezo- or thermoelectric effects [5, 6]. So far, most of these technologies are still based on silicon semiconductors and are fabricated in a top-down approach miniaturizing macroscopic technology. But as the dimensions of nanoscale devices slowly approach the molecular level it seems promising to work bottom-up, assembling small (molecular) building blocks to larger functional units. Based on these ideas molecular electronics aims to explorer and to provide functional molecular structures for nanoscale devices.

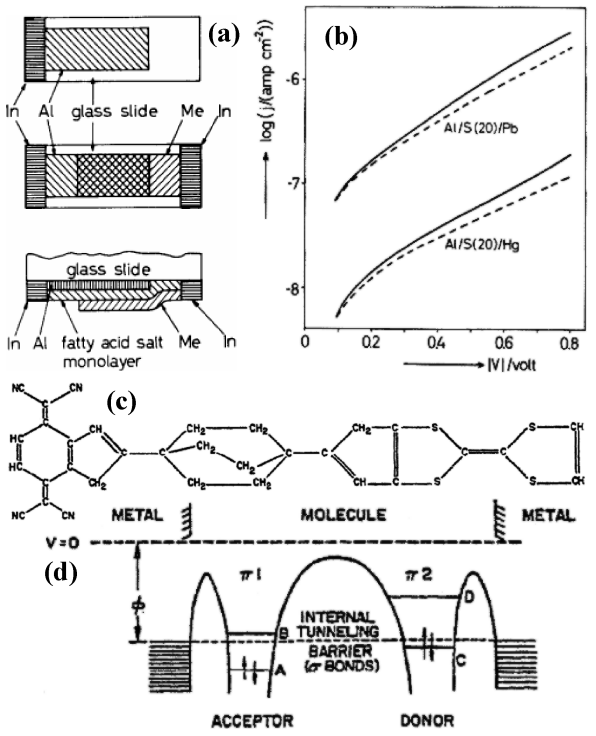

Fig. 1.1: (a) Arrangements for measuring the current through AI/S(n)/Me as used by Kuhn et al. [2]. S(n) symbolizes a monolayer of the Cd salt of $CH3(CH2)_{n-2}COOH$. (b) Sketch of the experimental setup with Me = Pb or AI. (c) Example of the rectifier molecule as proposed by Aviram and Ratner. (d) Sketch of the energy versus distance inside molecular junction based on the molecule in (c) [3].

The idea to design molecular structures with specific electronic properties was introduced already 40 years ago by Hans Kuhn [2]. Kuhn and coworkers proposed functional units on the basis of predefined molecular systems. They were able to form molecular junctions based on Langmuir-Blodgett films connected to metallic electrodes, to drive current through them and to measure their conductance [7, 8]. Their experimental setup and the originally measured current voltage characteristic are displayed in Fig. 1.1a and b. A few years later Avi-

ram and Ratner suggested theoretically the possibility of building a molecular rectifier which works like a traditional diode based on an acceptor-donor system formed by a single aromatic molecule [3]. The proposed molecule can be seen in Fig. 1.1c and d. Kuhn as well as Aviram and Ratner already pointed out that it is crucial to be able to manipulate and contact individual molecules in a controlled way. However, it took another 10 years until the invention of the scanning tunneling microscope (STM) which allowed for the first time the imaging, manipulation and contacting of individual molecules [9, 10]. Subsequently, by means of STM and mechanically controllable break junctions (MCBJs) (see Fig. 1.2), transport measurements on atomic wires [11, 12] were the first step towards the fabrication of single molecule junctions. The first measurement of the current through an individual molecule was performed by Reed and Tour in 1997 [13]. They succeeded in forming stable gold-benzene-1,4-dithiol junctions by means of the MCBJ technique. Even though a lot of improvement in the experimental techniques has been achieved since then it remains a challenging task to perform measurements at the single-molecule level. It is still an open question how to form reliable and reproducible molecular junctions because it has become clear that the electrode geometry and the properties of the electrode-molecule interfaces play a crucial role in the transport through single molecules. Therefore a lot of effort from the experimental side as well as from theory is put into gaining more control over the properties of organic-inorganic interfaces. A promising attempt in this direction are new kinds of anchoring groups, like amine or nitrile to link the molecules in a selective manner to the electrodes [14, 15]. Presently it is still necessary to take the statistical nature of the experiment into account and to determine conductance histograms by means of the statistical analysis of several hundreds or thousands of consecutive measurements on the same STM or MCBJ setup [16]. Despite of all the challenges which still remain when measuring the current through single molecules, also new concepts are introduced to the field of molecular electronics, like for example thermoelectric- and optical-effects. Reddy et al. showed recently that it is possible to determine thermoelectric properties of molecular junctions. They measured by means of STM techniques the junction Seebeck coefficients of benzenedithiol-based molecules connected to gold electrodes [17]. Optical active organic materials are already used for example in organic light emitting diods [18]. Marquardt et al. showed that it is also possible to fabricate optical active single molecule junctions. They were able to trigger electroluminescence from a single nanotube–molecule–nanotube system via the applied bias voltage [19].

Starting from the synthesis and design of specific molecules, over the charge transport measurements to the interpretation of the data and finally also development of applications, the field of molecular electronics requires a close collaboration between experiment and theory as well as between different disciplines of science like chemistry, physics and material science. As this thesis is dealing with the theoretical description of charge transport through molecular junctions, we will briefly set the role of the theory into the context of molecular electronics.

In the theoretical description of molecular junctions one has to deal with complex open

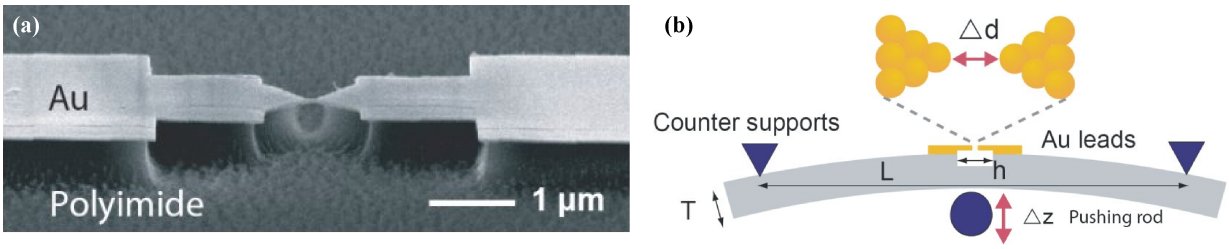

Fig. 1.2: (a) Scanning electron microscope picture of a free-standing Au constriction on top of a polyimide-coated stainless steel substrate. (b) Principle of a MCBJ. While bending the flexible substrate using a push-rod, a metallic constriction can be broken to form a pair of atomic sized contacts [20].

systems out of equilibrium. Even though it is possible to understand basic transport properties by simplified models, it is essential from the applications point of view to take the atomistic and chemical details into account. This can be achieved by combining ab initio electronic structure calculations with an appropriate transport formalism. A convenient way to include the open boundary conditions and the nonequilibrium properties of the system as well as the electronic structure is provided by the formulation of the transport problem by means of nonequilibrium Green's functions (NEGF) [21]. In addition the NEGF technique allows in a systematic way to take additional effects like electron-phonon [22] or electron-electron correlation [23] into account.

The three main tasks of the theory are on the one hand to interpret experimental data, to gain insight into the underlying transport mechanisms and to relate them to specific chemical and atomistic properties. On the other hand it is not possible to investigate the virtually infinite number of molecular systems in experiment. But with increasing insight into the transport mechanisms and systematic analysis, theory can provide proposals for specific molecules or molecular systems with desired properties [24, 25].

Outline of this thesis

This thesis is split into three part. In the first part we deal with the theoretical description of the molecular junctions with respect to their electronic structure, vibrational properties, and electric current. The aim is to extend the cluster-based density-functional approach to quantum transport developed by Fabian Pauly et al. [26]. Thereby, additionally to the elastic current, the focus is mainly on providing also an ab initio description of inelastic transport through atomic and molecular junctions due to vibrations in the framework of Kohn-Sham density functional theory (KS-DFT). The main task in the calculation of the electron-phonon coupling constants will be the derivation of analytical formulas for the first derivatives of the KS-Operator and the implemantation of the according matrix elements into the quantum chemistry package

Turbomole [27]. Beside the inelastic current we also deal with the calculation of transmission eigenchannel wave-functions within the NEGF formalism, which provide an intuitive picture to interpret the transport properties of nanoscale devices.

After we have introduced the theoretical concepts in the first part, we will apply them to specific atomic and molecular systems. Part II will thus mainly be concerned with mono-atomic Pb and Al contacts. However, in the beginning we will first examine a 4-atomic-long Au chain connected to Au electrodes. This system has been studied extensively in the litrature, here it serves primarily as a test system to validate the implementation of the inelastic tunneling spectra (IETS) calculations and of the procedure to obtain the transmission eigenchannel wave-functions. For Pb and Al we will study the evolution of the elastic current and of the IETS upon opening and closing of the atomic junctions. We will relate distinct features in the elastic as well as inelastic conductance during the opening and closing to atomic rearrangements inside the junctions. To conclude this part we will compare the specific properties of Pb and Al.

The third part will deal with organic molecules connected to Au electrodes. On the one hand we will explore the conductance properties of aromatic biphenyl-based molecules. The presented results were obtained in close cooperation with experiments conducted in the group of Thomas Wandlowski at the University of Bern. We show that the molecular conformation as well as the molecule-metal interface have a large influence on the electric conductance and on the thermoelectric properties, respectively. The importance of the degree of the π-electron conjugation for the conduction properties is illustrated by means of the transmission eigenchannels of the system. On the other hand we are investigating aliphatic octane-dithiol and octane-diamine molecules. This part is based on experiments performed in Elke Scheer's group at the University of Konstanz. The experimentally obtained signatures of electron-phonon interaction are assigned to specific molecular vibrations by comparing experimental and calculated IETS. Special attention will be paid to the comparison of the thiol and amine linkers with respect to the vibrations between the anchoring groups and the gold electrodes.

Every chapter of this thesis starts with a brief overview and concludes with a short summary of the results. In the end of this thesis we summarize all the results and give an outlook on possible extensions and further investigations.

Part II

Theoretical description of molecular junctions: electronic structure, vibrational properties and electric current

Introduction

In this part we present the theoretical framework required for this thesis. In Section 2 we derive the adiabatic approximation and the closely related Born-Oppenheimer approximation, the latter is the basis or at least the starting point for almost all solid state and molecular calculations dealing with electronic or vibronic properties. Then we show how the first order contribution to the electron-phonon interaction and the harmonic approximation for the lattice vibrations can be obtained from the adiabatic approximation. Even though we could have started directly from the electronic Hamiltonian using the harmonic approximation for the lattice vibrations the derivation is very instructive and provides important insights into the physical processes and the validity of the Born-Oppenheimer approximation. Most of this chapter is based on the excellent book from Max Born and Kun Huang on "Dynamical theory of lattice dynamics" [28] and the works by Chester and Houghton [29, 30].

In Section 3 we introduce the Kohn-Sham density functional theory (KS-DFT) approach to electronic structure and vibrational properties of molecular systems. For this introduction to KS-DFT we follow mainly Ref. [31], focusing thereby on the basic concepts and the relevant formulas rather than giving complete derivations and proofs. Then we introduce the linear combination of atomic orbitals (LCAO) Ansatz which is used to solve the KS-equation numerically. For the calculation of the vibrational modes the second derivative of the total energy is necessary. We shortly sketch how it can be obtained analytically within the LCAO Ansatz. A more detailed derivation is given for the analytic first-order derivative of the KS-Operator as this is the central quantity in the calculation of the electron-phonon coupling constants.

All the calculations of the electronic structure and vibrational properties presented in this work were performed with the quantum chemistry package TURBOMOLE [27]. To calculate electron-phonon coupling constants from first principles, we implemented them during this thesis into TURBOMOLE.

Section 4 deals with the quantum description of electron transport through molecular

junctions. First we derive the Meir-Wingreen formula for the current through an interacting region by means of NEGF techniques. For the case of noninteracting electrons the Meir-Wingreen formula reduces to the well known Landauer formula. On its basis we introduce the concept of transmission eigenchannel and present a procedure to calculate the eigenchannels wave-functions directly in the NEGF formalism. Then we show how thermoelectric properties can be described within the Landauer formalism. We will focus on the calculation and interpretation of the thermopower. After we have dealt with the elastic properties we take advantage of the general Meir-Wingreen formula to take into account inelastic correction to lowest non-vanishing order in the electron-phonon interaction.

2 Electronic and nuclear Hamiltonian

2.1 Adiabatic and Born-Oppenheimer approximation

The non-relativistic Hamiltonian for a system consisting of A atoms of masses M_I with atomic number (charge) Z_I, and $N = \sum_{I=1}^{N} Z_I$ electrons is given by

$$\hat{H} = \hat{T}_I + \hat{T}_e + \hat{V}_{ee}(\vec{r}) + \hat{V}_{II}(\vec{R}) + \hat{V}_{eI}(\vec{r}, \vec{R}) \tag{2.1}$$

with the kinetic energy of the nuclei

$$\hat{T}_I = \sum_{I=1}^{L} \frac{1}{2M_I} \hat{P}_I^2 \tag{2.2}$$

and electrons

$$\hat{T}_e = \sum_{\alpha=1}^{N} \frac{1}{2m_e} \hat{p}_\alpha^2, \tag{2.3}$$

the repulsive electron-electron interaction

$$\hat{V}_{ee}(r) = \frac{1}{2} \sum_{ij, i \neq j}^{N} \frac{e^2}{\left|\vec{r}_i - \vec{r}_j\right|}, \tag{2.4}$$

the repulsive nucleus-nucleus interaction

$$\hat{V}_{II}(r) = \frac{1}{2} \sum_{IJ, I \neq J}^{L} \frac{e^2 Z_I Z_J}{\left|\vec{R}_I - \vec{R}_J\right|}, \tag{2.5}$$

and the attractive electron-nucleus interaction

$$\hat{V}_{eI}(r) = \sum_i v(r_i) = -\sum_{iI} \frac{e^2 Z_I}{\left|\vec{r}_i - \vec{R}_I\right|}. \tag{2.6}$$

Here $\vec{R} = \{\vec{R}_I\}$ and $\vec{r} = \{\vec{r}_i\}$ denote all nuclear and electronic positions at once, $\hat{P}_I = -\mathrm{i}\vec{\nabla}_{\vec{R}_I}$ is the momentum operator of the I-th nucleus at position $\vec{R}_I$ and $\hat{p}_i = -\mathrm{i}\vec{\nabla}_{r_i}$ is the momentum operator of the i-th electron at position $\vec{r}_i$ respectively. For simplicity we omit the "hat" on the momentum and position operators in the following. The time-independent Schrödinger equation corresponding to the above Hamiltonian (Eq. (2.1)) is given by

$$\hat{H}(\vec{r},\vec{R})\left|\Psi(\vec{r},\vec{R})\right\rangle = E\left|\Psi(\vec{r},\vec{R})\right\rangle. \tag{2.7}$$

In the Hamiltonian given by Eq. (2.1) the scale of the kinetic energy of the nuclei is much smaller than all the other contributions and given by $m_e/M_I \approx 10^{-4} - 10^{-5} \ll 1$ [32]. Hence it seems plausible to neglect the kinetic energy of the nuclei in zeroth order. Therefore we split the full Hamiltonian (Eq. (2.1)) in the following way,

$$\hat{H} = \hat{H}^e + \hat{T}_I + \hat{V}_{II}(\vec{R}), \tag{2.8}$$

gathering all terms which depend on the electronic coordinates in

$$\hat{H}^e = \hat{T}_e + \hat{V}_{ee}(\vec{r}) + \hat{V}_{eI}(\vec{r},\vec{R}). \tag{2.9}$$

For a fixed set of nuclear coordinates $\vec{R}$ we can then define a "clamped-nuclei" Schrödinger equation for the electronic part which depends just parametrically on $\vec{R}$

$$\hat{H}^e\left|\phi_\alpha(\vec{r};\vec{R})\right\rangle = \epsilon_\alpha(\vec{R})\left|\phi_\alpha(\vec{r};\vec{R})\right\rangle. \tag{2.10}$$

As the solutions $\left|\phi_\alpha(\vec{r};\vec{R})\right\rangle$ to Eq. (2.10) form a complete set of basis states for all $\vec{R}$, we can choose as an Ansatz for the solution of the full Schrödinger equation (Eq. (2.7)) an expansion of the form [28]

$$\left|\Psi(\vec{r},\vec{R})\right\rangle = \sum_\alpha \chi_\alpha(\vec{R})\left|\phi_\alpha(\vec{r};\vec{R})\right\rangle. \tag{2.11}$$

Inserting this Ansatz into Eq. (2.7) and multiplying from the left with the electronic wave-function $\left\langle\phi_\beta(\vec{r};\vec{R})\right|$ yields

$$\left(\hat{T}_I + \hat{V}_{II}(\vec{R}) + \epsilon_\beta(\vec{R})\right)\chi_\beta(\vec{R}) + \sum_\alpha \hat{C}_{\beta\alpha}\chi_\alpha(\vec{R}) = E\chi_\beta(\vec{R}) \tag{2.12}$$

with

$$\hat{C}_{\beta\alpha} = \hat{A}_{\beta\alpha} + \hat{B}_{\beta\alpha}, \tag{2.13}$$

$$\hat{A}_{\beta\alpha} = -\sum_I \frac{1}{M_I} \left\langle \phi_\beta(\vec{r};\vec{R}) \middle| \vec{\nabla}_{\vec{R}_I} \phi_\alpha(\vec{r};\vec{R}) \right\rangle \vec{\nabla}_{\vec{R}_I} \tag{2.14}$$

and

$$\hat{B}_{\beta\alpha} = -\frac{1}{2}\sum_I \frac{1}{M_I} \left\langle \phi_\beta(\vec{r};\vec{R}) \middle| \vec{\nabla}^2_{\vec{R}_I} \middle| \phi_\alpha(\vec{r};\vec{R}) \right\rangle. \tag{2.15}$$

If we assume that the electronic wave functions $\langle r|\phi_\alpha(\vec{r};\vec{R})\rangle = \phi_\alpha(\vec{r};\vec{R})$ are purely real (no magnetic fields), we find for the diagonal terms $\hat{A}_{\alpha\alpha} = 0$. Splitting $\hat{C}_{\beta\alpha}$ into diagonal and off-diagonal contributions we can rewrite Eq. (2.12)

$$\left(\hat{T}_I + \hat{V}_{II}(\vec{R}) + \epsilon_\beta(\vec{R}) + \hat{C}_{\beta\beta}\right)\chi_\beta(\vec{R}) + \sum_{\alpha\neq\beta} \hat{C}_{\beta\alpha}\chi_\alpha(\vec{R}) = E\chi_\beta(\vec{R}). \tag{2.16}$$

The off-diagonal part $\hat{C}_{\beta\alpha}$ gives rise to non-adiabatic transitions between different electronic states. In contrast to this $\hat{B}_{\beta\beta}$ yields adiabatic corrections to a fixed electronic state. Neglecting the off-diagonal terms leads to the so called adiabatic approximation, where we have for each electronic state a Schrödinger equation for the nuclei moving in an effective potential due to the electrons

$$\left(\hat{T}_I + V_{II}(\vec{R}) + \epsilon_\beta(\vec{R}) + \hat{B}_{\beta\beta}\right)\chi_\beta(\vec{R}) = E\chi_\beta(\vec{R}). \tag{2.17}$$

This result can be further simplified by neglecting also the diagonal terms $\hat{B}_{\beta\beta}$. This is then the so called Born-Oppenheimer approximation. Both the adiabatic as well as the Born-Oppenheimer approximation lead to a decoupled system of equations with no coupling between different nuclear states$\chi_\beta(\vec{R})$. Before continuing we make short remark on the validity of the adiabatic approximation. The corrections due to $\hat{A}_{\beta\alpha}$ and $\hat{B}_{\beta\alpha}$ are of the order of $(m_e/M_I)^{3/4}$ and (m_e/M_I) respectively [33]. In this sense the separation of the electronic and nuclear motion seems plausible. However the gradient term in Eq. (2.14) can be brought into the following form [33]

$$\left\langle \phi_\beta(\vec{r};\vec{R}) \middle| \vec{\nabla}_{\vec{R}_I} \phi_\alpha(\vec{r};\vec{R}) \right\rangle = \frac{\left\langle \phi_\beta(\vec{r};\vec{R}) \middle| \vec{\nabla}_{\vec{R}_I} \hat{H}_{el} \middle| \phi_\alpha(\vec{r};\vec{R}) \right\rangle}{\epsilon_\alpha(\vec{R}) - \epsilon_\beta(\vec{R})}. \tag{2.18}$$

From this we find the condition that as long as the energy surfaces $\epsilon_\alpha(\vec{R})$ are well separated the coupling remains small. For $\epsilon_\alpha(\vec{R}) \approx \epsilon_\beta(\vec{R})$ however, the correction can become very large and the adiabatic approximation breaks down. In the following we assume that all the electronic states are well separated and that we can hence neglect the non-adiabatic coupling.

2.2 Electron-phonon coupling and harmonic approximation

Now we assume that we are in an equilibrium configuration $\vec{R}_I^{(0)}$ of the nuclei and that we can treat the displacements $\vec{Q}_I$ of the nuclei as small perturbations. Following

Refs. [29] and [30] we set $\vec{R}_I = \vec{R}_I^{(0)} + \vec{Q}_I = \vec{R}_I^{(0)} + \kappa\vec{u}_I$. The dimensionless expansion parameter is given by $\kappa = (m_e/M)^{1/4}$ (where $M = 1836 \times m_e$ is the proton mass) and chosen such that the leading (second) order term in the nuclear Schrödinger equation Eq. (2.17) gives rise to harmonic oscillations of the lattice. In the electronic Schrödinger equation (Eq. (2.10)) we expand $\hat{H}_{el}$ to leading order in κ

$$\hat{H}_{el} = \hat{H}_{el}\big|_{\vec{u}=0} + \kappa H_{el}^{(1)} = \hat{H}_{el}\big|_{\vec{R}=\vec{R}_0} + \sum_I \vec{Q}\cdot\vec{\nabla}_{\vec{R}_I}\hat{H}_{el}\Big|_{\vec{R}=\vec{R}_0} \tag{2.19}$$

where $\sum_I \vec{Q}\cdot\vec{\nabla}_{\vec{R}_I}\hat{H}_{el}$ describes the electron-phonon interaction.

To find a zeroth order approximation for the nuclear wave functions we expand both sites of the nuclear Schrödinger equation (Eq. (2.17)) and sort the resulting terms in powers of κ, where the kinetic energy term $\hat{T}_I$ is of the order of κ^2

$$\begin{aligned}
&\left[\left(\hat{V}_{II}^{(0)} + \epsilon_\beta^{(0)} - E^{(0)}\right)\chi_\beta^{(0)}\right] \\
&+\left[\left(\hat{V}_{II}^{(0)} + \epsilon_\beta^{(0)} - E^{(0)}\right)\chi_\beta^{(1)} + \left(\hat{V}_{II}^{(1)} + \epsilon_\beta^{(1)} - E^{(1)}\right)\chi_\beta^{(0)}\right]\kappa \qquad (2.20)\\
&+\left[\left(\hat{V}_{II}^{(0)} + \epsilon_\beta^{(0)} - E^{(0)}\right)\chi_\beta^{(2)} + \left(\hat{V}_{II}^{(1)} + \epsilon_\beta^{(1)} - E^{(1)}\right)\chi_\beta^{(1)}\right. \\
&\left.+\left(\hat{T}_I/\kappa^2 + \hat{V}_{II}^{(2)} + \epsilon_\beta^{(2)} - E^{(2)}\right)\chi_\beta^{(0)}\right]\kappa^2 = 0 \qquad (2.21)
\end{aligned}$$

From the zeroth order term follows $\hat{V}_{II}^{(0)} + \epsilon_\beta^{(0)} = E^{(0)}$. The first order term gives $\hat{V}_{II}^{(1)} + \epsilon_\beta^{(1)} = E^{(1)} = 0$ since $E^{(1)}$ vanishes for the equilibrium geometries (for a more rigorous treatment see Ref. [28]). Therefore $\chi_\beta^{(0)}$ is determined from the second order term κ^2

$$\left(\hat{T}_I/\kappa^2 + \hat{V}_{II}^{(2)} + \epsilon_\beta^{(2)}\right)\chi_\beta^{(0)} = E^{(2)}\chi_\beta^{(0)}. \tag{2.22}$$

Defining the Hessian-matrix $\mathcal{H}_{Ik,Jl} = \dfrac{\partial^2\left(\hat{V}_{II}(\vec{R}) + \epsilon_\beta(\vec{R})\right)}{\partial R_{Ik}\partial R_{Jl}}$ and with the help of $\vec{Q}_I = \kappa\vec{u}_I$ we can bring the nuclear Hamilton operator $\hat{H}_I = \kappa^2\left(\hat{T}_I/\kappa^2 + \hat{V}_{II}^{(2)} + \epsilon_\beta^{(2)}\right)$ into the following form

$$\hat{H}_I = \frac{1}{2}\left(\sum_{I=1}^{N_I}\sum_{k}^{\{x,y,z\}}\frac{1}{M_I}P_{Ik}^2 + \sum_{I,J=1}^{N_I}\sum_{k,l}^{\{x,y,z\}}Q_{Ik}\mathcal{H}_{Ik,Jl}Q_{Jl}\right). \tag{2.23}$$

By rescaling the coordinates according to $p_{Ik} = \sqrt{\dfrac{1}{M_I}}P_{Ik}$ and $q_{Ik} = \sqrt{\dfrac{1}{m_e}}Q_{Ik}$ we express the nuclear Hamilton operator as [32]

$$\hat{H}_I = \frac{1}{2}(\boldsymbol{p}^{\mathbf{t}}\cdot\boldsymbol{p} + \boldsymbol{q}^{\mathbf{t}}\cdot\boldsymbol{D}\cdot\boldsymbol{q}), \tag{2.24}$$

where we have introduced the impulse $\boldsymbol{p}^{\mathsf{t}} = (p_1, ..., p_{3N})$ and position $\boldsymbol{q}^{\mathsf{t}} = (q_1, ..., q_{3N})$ vectors , and the dynamical matrix

$$\boldsymbol{D}_{Ikjl} = \frac{1}{\sqrt{M_{Ik} M_{Jl}}} \mathcal{H}_{Ik,Jl}. \tag{2.25}$$

The dynamical matrix $\boldsymbol{D}$ can be diagonalized by a unitary transformation to normal coordinates $\tilde{\boldsymbol{p}} = (\tilde{p}_1, ..., \tilde{p}_{3N})^{\mathsf{t}} = \boldsymbol{C} \cdot \boldsymbol{p}$ and $\tilde{\boldsymbol{q}} = (\tilde{q}_1, ..., \tilde{q}_{3N})^{\mathsf{t}} = \boldsymbol{C} \cdot \boldsymbol{q}$

$$\boldsymbol{C}^{\dagger} \cdot \boldsymbol{D} \cdot \boldsymbol{C} = \boldsymbol{\Omega} = \begin{pmatrix} \omega_1^2 & \dots & 0 \\ \vdots & \ddots & \vdots \\ 0 & \cdots & \omega_{3N}^2 \end{pmatrix}, \tag{2.26}$$

where $\boldsymbol{C}$ is normalized according to $\boldsymbol{C}^{\dagger}\boldsymbol{C} = \mathbf{1}$. Expressed in normal coordinates

$$\hat{H}_I = \frac{1}{2} \sum_{i=1}^{3N} \left(\tilde{p}_i^2 + \omega_i^2 \tilde{q}_i^2 \right) \tag{2.27}$$

becomes a Hamilton operator of $3N$ independent harmonic oscillators. For this we need the second derivatives of the nucleus-nucleus potential $\hat{V}_{II}(\vec{R})$ and the second derivatives of the total electronic energy $\epsilon_\beta(\vec{R})$. The contribution arsing from bare nuclei-nuclei interaction can directly be obtained by taken the second derivative of $\hat{V}_{II}(\vec{R})$ at $\vec{R}_0$. For the electronic part we show in Section 3.2 how the second derivatives of the total electronic energy can be calculated within DFT.

3 Approximate electronic and vibrational structure

3.1 Kohn-Sham Density Functional Theory

In this section we describe the basics of KS-DFT which is used to find a solution to the ground state of the electronic part $\hat{H}_{el}$ (Eq. (2.9)) of the many-body Hamiltonian introduced in Section 2.1. This Hamiltonian describes N electrons moving in the "external" potential of the nuclei $V_{ext} = V_{eI}(r) = \sum_i v(r_i)$. The external potential V_{ext} in DFT is not restricted to the choice we made, as a matter of fact it can be any kind one-particle potential [31]. However if we are referring to the external potential V_{ext} in the following, we always have in mind the coulomb interaction V_{eI} between the electrons and the nuclei.

The usual way to obtain the ground state properties of some specified system would be to choose $v(\vec{r})$, which means to specify the atomic coordinates of the desired system, setup up the according Schrödinger equation and solve for the ground state wave-

functionΨ, from which the expectation values of the desired observables can be calculated. This scheme can be summarized as

$$v(\vec{r}) \overset{SE}{\Longrightarrow} \Psi(\vec{r}_1, ..., \vec{r}_N, \vec{R}_1, ..., \vec{R}_M) \overset{\langle\Psi|...|\Psi\rangle}{\Longrightarrow} \text{expectation values.} \tag{3.1}$$

However it is complicated is to find the ground state wave-function or a good approximation to it. A variety of different methods exist to tackle this problem; perturbative approaches like Møller–Plesset perturbation theory [34], or expansion of the wave-functions in terms of Slater determinants like configuration interaction [35] and many others. All of these approaches have a common drawback. They can not be applied to larger molecular system or even solids and hybrid systems, because they are all computationally very demanding.

An conceptually different approach is taken by DFT. It replaces the wave-function as principle variable, by the ground state electron density $n_0(\vec{r})$ and maps the full many body problem onto an effective single particle problem. Expressed in the same sense as above, in DFT the ground state electron density, fixes the ground state wave-function which in turn determines the potential and all other observables. This can be depicted by the following scheme [31]

$$n_0(\vec{r}) \Longrightarrow \Psi(\vec{r}_1, ..., \vec{r}_N, \vec{R}_1, ..., \vec{R}_M) \Longrightarrow v(\vec{r}) \ . \tag{3.2}$$

The basis for the statement above is provided by the Hohenberg-Kohn theorem. Here we state the theorem without proof. They can be found in the original work by Hohenberg and Kohn [36] or any textbook on DFT e.g. [37, 38, 39]. For simplicity we consider in Eq. (3.2) and below only the non degenerate ground state for a closed-shell system. The generalization to degenerate ground states and spin polarized systems is possible without any conceptional problems, e.g. [37, 38, 39].

The Hohenberg-Kohn theorem for a non degenerate ground state of a $N-$electron system can be summarized in the following three statements [40] :

1. There exists a one-to-one correspondence between the ground state electron density $n_0(\vec{r})$ and the external potential $V_{ext}(\vec{r})$ experienced by electrons. Thus the external potential and hence the Hamiltonian is uniquely determined by the ground state density alone.

2. The ground-state energy E_0 of a system with some external potential $V_{ext}(\vec{r})$ can be obtained from $n_0(\vec{r})$, which means that the ground state energy is a functional of the density, $E[n]$ which gives the ground state energy if and only if n is the true ground state density n_0. That the following variational principle holds for any electron density n

   $$E_0 = E[n_0] \leq E[n]. \tag{3.3}$$

   The ground state energy can be expressed in terms of some universal functional $F[n] = T[n] + V_{ee}[n]$ which does not depend on $V_{ext}(\vec{r})$ and one determined from

the external potential $V[n] = \int \mathrm{d}r^3 V_{ext}(\vec{r})n(\vec{r})$,

$$E[n] = F[n] + V[n] = F[n] + \int \mathrm{d}r^3 V_{ext}(\vec{r})n(\vec{r}). \tag{3.4}$$

The Hohenberg-Kohn theorem presented above is the basis of DFT, but almost all pratical applications of DFT are based on the scheme introduced by Kohn and Sham [41], leading to Kohn-Sham Density-Functional-Theory (KS-DFT). The idea of KS-DFT is to construct a reference system of N non-interacting electrons moving in some effective external potential with the same ground state density as the full interacting many body problem. The associated Hamilton operator is

$$\hat{H}_s = -\frac{1}{2}\sum_{i=1}^{N} \nabla_i^2 + V_s(\vec{r}) \tag{3.5}$$

since V_{ee} vanishes by assumption and the ground state density in terms of the auxiliary orbitals $\psi_i(\vec{r})$ is given by

$$n_s(\vec{r}) = \sum_{i=1}^{N} |\psi_i(\vec{r})|\,. \tag{3.6}$$

To proceed further we rewrite the energy functional (Eq. (3.4)) of the interaction system (Eq. (2.9)) as

$$E[n] = T_s[n] + J[n] + E_{xc}[n] + \int \mathrm{d}r^3 V_{ext}(\vec{r})n(\vec{r}) \tag{3.7}$$

where the exchange-correlation energy

$$E_{xc}[n] = T[n] - T_s[n] + V_{ee}[n] - J[n] \tag{3.8}$$

is the difference between the kinetic energy T of the interacting system and the kinetic energy T_s of the non-interacting reference system plus the difference of the full electron electron interaction V_{ee} and the Hartree energy $J[n] = \frac{1}{2}\int \mathrm{d}r^3 \int \mathrm{d}r'^3 \frac{n(\vec{r})n(\vec{r}')}{|r-r'|}$.

From the variational principle (Eq. (3.3)) it follows that the functional derivative of $E[n]$ with respect to n has to vanish for $n = n_0$, which means n_0 is determined from an Euler equation

$$\left.\frac{\delta E[n]}{\delta n}\right|_{n=n_0} = \left.\frac{\delta F[n]}{\delta n}\right|_{n=n_0} + V_{ext}(\vec{r})|_{n=n_0} = 0. \tag{3.9}$$

This holds on the one hand for the non interacting reference system (Eq. (3.5))

$$\frac{\delta E_s[n]}{\delta n} = \frac{\delta T_s[n]}{\delta n} + V_s(\vec{r}) \tag{3.10}$$

and on the other hand also for the interacting system (Eq. (2.9))

$$\frac{\delta E[n]}{\delta n} = \frac{\delta T_s[n]}{\delta n} + V_{ext}(\vec{r}) + J(\vec{r}) + V_{xc}(\vec{r}), \tag{3.11}$$

where $J(\vec{r}) = \int \mathrm{d}r^3 \frac{n(\vec{r})}{|r-r'|}$ is the Hartree potential and the exchange-correlation potential $V_{xc}(\vec{r}) = \frac{\delta E_{xc}[n]}{\delta n}$ is formally given as the functional derivative of E_{xc} with respect to the density. Comparing Eq. (3.10) and Eq. (3.11) one finds that for $V_s(\vec{r}) = V_{ext}(\vec{r}) + J(\vec{r}) + V_{xc}(\vec{r})$ both Euler equations deliver the same ground state density $n_s(\vec{r}) = n_0(\vec{r})$. Therefore one can solve instead of the interacting system (Eq. (2.9)) the effective single particle Schrödinger-like Kohn-Sham (KS) equations

$$\left(-\frac{1}{2} \sum_{i=1}^{N} \nabla_i^2 + V_{ext}(\vec{r}) + J(\vec{r}) + V_{xc}(\vec{r}) \right) \psi_i(\vec{r}) = \epsilon_i \psi_i(\vec{r}). \tag{3.12}$$

In practical applications one needs to use some approximation for $V_{xc}(\vec{r})$ because the actual functional expression of $E_{xc}[n]$ is unknown. The most widely used approximations are the local density approximation (LDA) [42, 43, 44, 45] and the generalized gradient approximations (GGA) [46, 47, 48, 49] but there exist more families of exchange-correlation functionals. Discussion of the different functionals is not the scope of this thesis but can be found in any standard textbook on DFT e.g. [37, 38, 39].

3.1.1 Linear combination of atomic orbitals Ansatz

To solve the KS equations (Eq. (3.12)) one needs to employ some Ansatz for the the KS orbitals $\{\psi_i(\vec{r})\}$ which can be handled computationally. Here we will consider the so called linear combination of atomic orbitals (LCAO) Ansatz.. Therefor the KS orbitals are conveniently expanded in a (not necessarily orthogonal) finite basis-set $\left\{\phi_\mu(\vec{r})\right\}$

$$\psi_i(\vec{r}) = \sum_{\mu=1}^{L} c_{\mu i} \phi_\mu(\vec{r}) \tag{3.13}$$

where the expansion coefficients $c_{\mu i}$ and the basis functions $\phi_\mu(\vec{r})$ are assumed to be real in the following. Inserting this expansion into the KS equation (Eq. (3.12)) yields the algebraic equations

$$\sum_{\nu=1}^{L} \left(F_{\mu\nu} - \epsilon_i S_{\mu\nu} \right) c_{\nu i} = 0, \tag{3.14}$$

with the overlap matrix

$$S_{\mu\nu} = \langle \mu | \nu \rangle = \int \mathrm{d}r^3 \phi_\mu^\star(\vec{r}) \phi_\nu(\vec{r}) \tag{3.15}$$

and the Kohn-Sham-Fock (KSF) matrix which is defined as the matrix elements of the KSF operator

$$\hat{F} = \hat{h} + \hat{J} + \hat{V}^{xc} \tag{3.16}$$

and given by

$$F_{\mu\nu} = \langle \mu | \hat{F} | \nu \rangle = \int \mathrm{d}r^3 \phi_\mu^\star(\vec{r}) \hat{F} \phi_\nu(\vec{r}) = h_{\mu\nu} + J_{\mu\nu} + V_{\mu\nu}^{xc}. \tag{3.17}$$

Where

$$\hat{h} = -\frac{\hbar^2}{2m_e}\nabla^2 - \sum_I V_I(\vec{r}) \tag{3.18}$$

is the one electron operator with $V_I(\vec{r}) = \dfrac{e^2 Z_A}{\left|\vec{r} - \vec{R}_I\right|}$,

$$\hat{J} = \sum_{\sigma\lambda} P_{\sigma\lambda} \int \mathrm{d}r'^3 \phi_\sigma^\star(\vec{r}') \frac{e^2}{\left|\vec{r} - \vec{r}'\right|} \phi_\lambda(\vec{r}') \tag{3.19}$$

is the Coulomb operator with the density matrix (with a factor two for the spin degree of freedom)

$$D_{\sigma\lambda} = 2 \sum_{i=1}^{N/2} c_{\sigma i} c_{\lambda i} \tag{3.20}$$

from which the ground state electron density can be obtained as

$$n(\vec{r}) = \sum_{\mu\nu} \phi_\mu(\vec{r}) D_{\mu\nu} \phi_\nu(\vec{r}). \tag{3.21}$$

The last part in the KSF operator is the exchange-correlation operator

$$\hat{V}^{xc} = V^{xc}(\vec{r}), \tag{3.22}$$

the matrix elements $V_{\mu\nu}^{xc}$ are related to the exchange-correlation energy via

$$V_{\mu\nu}^{xc} = \frac{\partial E_{xc}}{\partial D_{\mu\nu}}. \tag{3.23}$$

The exchange-correlation energy is either defined via the exchange-correlation energy functional $f(n(\vec{r}))$ as

$$E_{xc} = \int \mathrm{d}^3\vec{r} f(n(\vec{r})) \tag{3.24}$$

or by the exchange-correlation energy density $\epsilon_{xc}(n(\vec{r}))$ as [37]

$$E_{xc} = \int \mathrm{d}^3\vec{r} n(\vec{r}) \epsilon_{xc}(n(\vec{r})). \tag{3.25}$$

With in LCAO Ansatz the total ground-state energy can be expressed as

$$E = \sum_{\mu\nu} P_{\mu\nu} h_{\mu\nu} + \frac{1}{2} \sum_{\mu\nu\kappa\lambda} D_{\mu\nu} D_{\kappa\lambda} \left(\mu\nu \middle| \kappa\lambda\right) + E_{xc}, \tag{3.26}$$

and is directly related to the KSF matrix

$$F_{\mu\nu} = \frac{\partial E}{\partial D_{\mu\nu}}, \tag{3.27}$$

where we have introduced the standard notation for the Coulomb type integrals in quantum chemistry [35]

$$\left(\mu\nu\middle|\kappa\lambda\right) = \int \mathrm{d}r \int \mathrm{d}r'^3 \phi^\star_\mu(\vec{r})\phi_\nu(\vec{r})\frac{e^2}{\left|\vec{r}-\vec{r}'\right|}\phi^\star_\kappa(\vec{r}')\phi_\lambda(\vec{r}') \tag{3.28}$$

The above equations yield a set of coupled integral equations which have to be solved self-consistently because the KS-matrix itself depends on the expansion coefficients which are obtained by diagonalizing the eigenvalue problem given by Eq. (3.14). Since the so obtained KS-orbitals are eigenfunctions of the hermitian KSF operator, they are orthogonal and are chosen to fulfill the following orthonormality relation

$$\left\langle \psi_i(\vec{r})\middle|\psi_j(\vec{r})\right\rangle = \sum_{\mu=1}^{L}\sum_{\nu=1}^{L} c_{\mu i} S_{\mu\nu} c_{\nu j} = \delta_{ij}. \tag{3.29}$$

So far we have just considered the closed-shell case. Hence the spin degree of freedom just appears as a factor of 2 in the density matrix (Eq. (3.20)). The extension to the unrestricted case is straightforward. The total number of electrons is than given by the sum of the electrons in $\alpha-$orbitals and $\beta-$orbitals respectively, $N = N_\alpha + N_\beta$. The one-electron and coulomb part do not depend explicitly on the spin degree of freedom but via the exchange-correlation part the KS-matrix depends explicitly on the spin. Therefore we have to solve two coupled KS-equations yielding separate KS-orbitals for spin α and β, respectively.

One possibility for the choice of the actual basis-set would be Slater-type orbitals which are known as the analytical solution of hydrogen like atoms, they exhibit an exponential decay at long range and have the correct analytical behavior at short distances, i.e. they fullfil the cusp condition at the nuclear position [50]. But on the other hand the calculation of overlap and Coulomb integrals is computationally very expansive. Therefore one takes advantage of the fact that the Slater orbitals can be approximated by Gaussian type orbitals [51] for which the overlap and Coulomb integrals can be calculated semi-analytically and efficiently [52, 53, 54].

3.2 Phonons within DFT

As shown in Section 2.2 we need to diagonalize the dynamical matrix (Eq. (2.25)) to obtain the phonon modes in the harmonic approximation. For this we need the Hessian

matrix of the total electronic energy and of the nuclear repulsion energy V_{II}. Hence we have to calculate the second derivative of both quantities with respect to the Cartesian components of the atomic coordinates $\vec{R}_I$ evaluated at their equilibrium positions $\vec{R}_I^{(0)}$. For the classical nuclear repulsion energy V_{II} this is a trivial task as we can take the second derivative directly. For the total electronic energy, however, we have to take the second derivative of the DFT ground state energy (Eq. (3.26)). In the following we will use the abbreviation $\partial/\partial a$ for the derivative with respect to one of the Cartesian components of the atomic coordinate $\vec{R}_A$. Differentiating the total energy (Eq. (3.26)) with respect to a gives

$$\frac{\partial E}{\partial a} = \sum_{\mu\nu} D_{\mu\nu} \frac{\partial h_{\mu\nu}}{\partial a} + \frac{1}{2} \sum_{\mu\nu\kappa\lambda} D_{\mu\nu} D_{\kappa\lambda} \frac{\partial (\mu\nu|\kappa\lambda)}{\partial a} + \sum_{\mu\nu} D_{\mu\nu} \left(\langle \frac{\partial \mu}{\partial a} | V^{xc} | \nu \rangle + \langle \mu | V^{xc} | \frac{\partial \nu}{\partial a} \rangle \right) + \sum_{\mu\nu} \frac{\partial D_{\mu\nu}}{\partial a} h_{\mu\nu} + \sum_{\mu\nu\kappa\lambda} \frac{\partial D_{\mu\nu}}{\partial a} D_{\kappa\lambda} (\mu\nu|\kappa\lambda) + \sum_{\mu\nu} \frac{\partial D_{\mu\nu}}{\partial a} V^{xc}_{\mu\nu}. \tag{3.30}$$

The derivative of the density matrix can be eliminated from the above equation. Taking the derivatives of the orthonormality relation (Eq. (3.29)) for $i = j$ and multiplying by $\sum_i \epsilon_i$ yields with the help of the KS-equation (Eq. (3.14)) [55]

$$\sum_{\mu\nu} \frac{\partial D_{\mu\nu}}{\partial a} F_{\mu\nu} = -\sum_{\mu\nu} W_{\mu\nu} \frac{\partial S_{\mu\nu}}{\partial a} \tag{3.31}$$

where we have defined the energy-weighted density matrix $W_{\mu\nu} = \sum_i \epsilon_i c_{\mu i} c_{\nu i}$. This expression equals the second line of Eq. (Eq. (3.30)) and hence we get

$$\frac{\partial E}{\partial a} = \sum_{\mu\nu} D_{\mu\nu} \frac{\partial h_{\mu\nu}}{\partial a} + \frac{1}{2} \sum_{\mu\nu\kappa\lambda} D_{\mu\nu} D_{\kappa\lambda} \frac{\partial (\mu\nu|\kappa\lambda)}{\partial a} + \sum_{\mu\nu} D_{\mu\nu} \left(\langle \frac{\partial \mu}{\partial a} | V^{xc} | \nu \rangle + \langle \mu | V^{xc} | \frac{\partial \nu}{\partial a} \rangle \right) - \sum_{\mu\nu} W_{\mu\nu} \frac{\partial S_{\mu\nu}}{\partial a}. \tag{3.32}$$

Deriving $\partial E/\partial a$ now we respect to b yield the second derivative of the energy

$$\frac{\partial^2 E}{\partial a \partial b} = \sum_{\mu\nu} D_{\mu\nu} \frac{\partial^2 h_{\mu\nu}}{\partial a \partial b} + \frac{1}{2} \sum_{\mu\nu\kappa\lambda} D_{\mu\nu} D_{\kappa\lambda} \frac{\partial^2 (\mu\nu|\kappa\lambda)}{\partial a \partial b} \tag{3.33}$$

$$+ \sum_{\mu\nu} D_{\mu\nu} \frac{\partial}{\partial b} \left(\langle \frac{\partial \mu}{\partial a} | V^{xc} | \nu \rangle + \langle \mu | V^{xc} | \frac{\partial \nu}{\partial a} \rangle \right) - \sum_{\mu\nu} W_{\mu\nu} \frac{\partial^2 S_{\mu\nu}}{\partial a \partial b} \tag{3.34}$$

$$+ \sum_{\mu\nu} \frac{\partial D_{\mu\nu}}{\partial b} \left(\frac{\partial h_{\mu\nu}}{\partial a} + \sum_{\kappa\lambda} D_{\kappa\lambda} \frac{\partial (\mu\nu|\kappa\lambda)}{\partial a} + \langle \frac{\partial \mu}{\partial a} | V^{xc} | \nu \rangle + \langle \mu | V^{xc} | \frac{\partial \nu}{\partial a} \rangle \right) \tag{3.35}$$

$$- \sum_{\mu\nu} \frac{\partial W_{\mu\nu}}{\partial b} \frac{\partial S_{\mu\nu}}{\partial a}. \tag{3.36}$$

The expression for the the second derivative of E cannot simply be evaluated because in $D_{\mu\nu}$ and $W_{\mu\nu}$ the derivatives of the expansion coefficients $\partial c_{\mu i}/\partial a$ appear. This derivatives can be obtained from the coupled perturbed Kohn-Sham theory (CPKS) which applies first order perturbation theory within KS-DFT to calculate $\partial c_{\mu i}/\partial a$ [55, 56]. On the one hand CPKS provides highly accurate analytical second derivatives for E which avoids numerical problems when calculating vibrational frequencies, but on the other hand it is computationally very expansive and therefor the most time consuming step in the calculation of the vibrational modes and electron-phonon coupling constants.

3.3 Analytic derivative of the Kohn-Sham-Fock-Operator

For the electron-phonon coupling matrix elements (Eq. (4.47)), which will be introduced in the next chapter, we need the matrix elements of the first derivative of the electronic Hamilton operator $\hat{H}_{el}$ with respect to the Cartesian components of the nuclear coordinates. In the framework of KS-DFT we thus need derivatives of the KSF operator $\hat{F}$. One possibility to obtain the derivatives of $\hat{F}$ is by means of numerical differentiation, for which one needs to deflect all N atoms in the 3 Cartesian components and hence needs to calculate at least $3N$ structures to obtain the needed finite differences. This is computationally very expansive and suffers from the limitations of the accuracy of numerical differentiation. To overcome this we determine an analytic expression for the derivative of $\hat{F}$. This is possible since we employ Gaussian basis sets.

In this chapter we will contrary to the preceding ones consider explicitly the spin dependency. This will be mainly important for the derivative of the exchange-correlation Operator apart from that it will just effect the definition of the density matrix $D_{\mu\nu} = D^{\alpha}_{\mu\nu} + D^{\beta}_{\mu\nu}$ appearing in the Coulomb operator.

The KSF operator within the LCAO Ansatz was introduced in Section 3.1.1 and is formally given by

$$\hat{F} = \hat{h} + \hat{J} + \hat{V}^{xc}. \tag{3.37}$$

In the following we want to derives explicit formulas for the matrix elements of the first derivative of the KS-operator

$$F^{A}_{\mu\nu} = \left\langle \mu \middle| \frac{\partial \hat{F}}{\partial a} \middle| \nu \right\rangle. \tag{3.38}$$

First we deal with the one-electron operator where we take into account the possibility that some of electrons are described by means of effective core potentials $U^{\hat{E}CP}_{A}(\vec{r})$ [57, 58]

$$\hat{h} = -\frac{\hbar^2}{2m_e}\nabla^2 - \sum_{A}\left(V_A(\vec{r}) + U^{ECP}_{A}(\vec{r})\right). \tag{3.39}$$

Taking the derivative of $\hat{h}$ with respect to a gives

$$\frac{\partial \hat{h}}{\partial a} = \frac{\partial}{\partial a}\left(V_A + U_A^{ECP}\right). \tag{3.40}$$

In principle it would be possible to derive V_a and U_a^{ECP}explicitly but we can take advantage of the translation invariance of the integrals [59, 60] due to that fact the potentials and the basis functions just depend on $\left|\vec{r} - \vec{R}_A\right|$. For two basis functions ϕ_μ centered at nucleus B and ϕ_ν centered at nucleus C respectively, we can obtain the matrix-element of $\partial\hat{h}/\partial a$ from

$$\left\langle \mu \middle| \frac{\partial}{\partial a}\left(\hat{V}_A + U_A^{ECP}\right) \middle| \nu \right\rangle = -\left\langle \frac{\partial \mu}{\partial b} \middle| \left(\hat{V}_A + U_A^{ECP}\right) \middle| \nu \right\rangle - \left\langle \mu \middle| \left(\hat{V}_A + U_A^{ECP}\right) \middle| \frac{\partial \nu}{\partial c} \right\rangle, \tag{3.41}$$

where a, b and c act on the same Cartesian component. As the derivative of a Gaussian basis functions are again Gaussians [35] we can evaluated the matrix elements in the same way as the matrix elements of $\hat{h}$ [52].

Taking the derivative of the Coulomb-Operator

$$\hat{J} = \sum_\sigma \sum_\lambda D_{\sigma\lambda} \int d^3 r_2 \phi_\sigma(\vec{r}_2) \frac{e^2}{r_{12}} \phi_\lambda(\vec{r}_2) \tag{3.42}$$

yields with the help of the product rule

$$\frac{\partial \hat{J}}{\partial a} = \sum_\sigma \sum_\lambda \left(\frac{\partial D_{\sigma\lambda}}{\partial a}\right) \int d^3 r_2 \phi_\sigma(\vec{r}_2) \frac{e^2}{r_{12}} \phi_\lambda(\vec{r}_2) + \sum_\sigma \sum_\lambda D_{\sigma\lambda} \frac{\partial}{\partial a}\left(\int d^3 r_2 \phi_\sigma(\vec{r}_2) \frac{e^2}{r_{12}} \phi_\lambda(\vec{r}_2)\right). \tag{3.43}$$

The according matrix-elements are given by

$$\left\langle \mu \middle| \frac{\partial \hat{J}}{\partial a} \middle| \nu \right\rangle = \sum_\sigma \sum_\lambda \left(\frac{\partial D_{\sigma\lambda}}{\partial a}\right) \left(\mu\nu \middle| \sigma\lambda\right) + \sum_\sigma \sum_\lambda D_{\sigma\lambda} \left[\left(\mu\nu \middle| \frac{\partial \sigma}{\partial a}\lambda\right) + \left(\mu\nu \middle| \sigma \frac{\partial \lambda}{\partial a}\right)\right]. \tag{3.44}$$

The second term can be calculated in the same way as the usual Coulomb integrals but the first term involves the derivative of the density matrix $D_{\mu\nu}$. The derivatives of $D_{\mu\nu}$ already appeared in Section 3.2 in the equations for the Hessian matrix, and as mentioned, they can be obtained within CPKS theory. Since the calculation of the Hessian matrix usually precedes the calculation of $\partial\hat{J}/\partial A$ we can reuse $\partial D_{\sigma\lambda}/\partial A$ and have in this step just to perform the contraction with $\left(\mu\nu\middle|\sigma\lambda\right)$.

The last part of Eq. (3.37) is the exchange-correlation operator which is the functional derivative of the exchange-correlation energy with respect to the electron density

$$\hat{V}^{xc} = \frac{\delta E^{xc}}{\delta n}. \tag{3.45}$$

First we consider the LDA case, for which E^{xc} just depends on the density via the exchange-correlation functional $f(n(\vec{r}))$ (Eq. (3.24)). In the spin-unrestricted case the exchange-correlation energy is given by

$$E^{xc}_{LDA}[n_\alpha(r), n_\beta(r)] = \int \mathrm{d}^3\vec{r} f_{LDA}(n_\alpha(\vec{r}), n_\beta(\vec{r})). \tag{3.46}$$

Taking for example the functional derivative with respect to n_α gives the exchange-correlation potential for the spin component α [37]

$$\hat{V}^{xc,\alpha}_{LDA} = \frac{\delta E^{xc}_{LDA}}{\delta n_\alpha} = \frac{\partial f_{LDA}(n_\alpha(r), n_\beta(r)).}{\partial n_\alpha} \tag{3.47}$$

Now we can differentiate with respect to a and get with the help of the chain rule

$$\frac{\partial \hat{V}^{xc,\alpha}_{\alpha}}{\partial a} = \frac{\partial^2 f(n_\alpha, n_\beta)}{\partial^2 n_\alpha}\frac{\partial n_\alpha}{\partial a} + \frac{\partial^2 f(n_\alpha, n_\beta)}{\partial n_\alpha \partial n_\beta}\frac{\partial n_\beta}{\partial a}. \tag{3.48}$$

Because the explicit formula for the exchange-correlation functional $f_{LDA}(n_\alpha, n_\beta)$ is known in LDA one can evaluate the derivatives with respect to the density. The derivative of the electron density

$$\begin{aligned}\frac{\partial n_{\alpha,\beta}(r)}{\partial a} &= \sum_{\mu\nu}\frac{\partial}{\partial a}\left(\phi_\mu(r)\phi_\nu(r)\right) D^{\alpha,\beta}_{\mu\nu} + \sum_{\mu\nu}\phi_\mu(r)\phi_\nu(r)\frac{\partial D^{\alpha,\beta}_{\mu\nu}}{\partial a} \\ &= 2\sum_{\mu\nu}\phi_\mu(r)\frac{\partial \phi_\nu(r)}{\partial a} D^{\alpha,\beta}_{\mu\nu} + \sum_{\mu\nu}\phi_\mu(r)\phi_\nu(r)\frac{\partial D^{\alpha,\beta}_{\mu\nu}}{\partial a}\end{aligned} \tag{3.49}$$

involves, beside the first derivatives of the basis functions, also derivatives of the electron density matrix $D^{\alpha,\beta}_{\mu\nu}$. The matrix elements of $\left\langle \mu \middle| \partial \hat{V}^{xc}_{\alpha}/\partial a \middle| \nu \right\rangle$ can be evaluated by standard quadrature techniques similar to the evaluation of $\left\langle \mu \middle| \hat{V}^{xc}_{\alpha} \middle| \nu \right\rangle$ [27].

In the case of GGA functionals the exchange-correlation energy depends not only on the electron density but also on its gradient

$$E^{xc}_{GGA}[n_\alpha(r), n_\beta(r)] = \int \mathrm{d}^3 r f_{GGA}(n_\alpha(r), n_\beta(r), \vec{\nabla} n_\alpha(r), \vec{\nabla} n_\beta(r)). \tag{3.50}$$

Due to symmetry reasons the actual dependence on $\vec{\nabla} n_\alpha(r)$ and $\vec{\nabla} n_\beta(r)$ is given by [61]

$$f(n_\alpha, n_\beta, \vec{\nabla} n_\alpha, \vec{\nabla} n_\beta) = f(n_\alpha, n_\beta, \left|\vec{\nabla} n_\alpha\right|^2, \left|\vec{\nabla} n_\beta\right|^2, \vec{\nabla} n_\alpha \vec{\nabla} n_\beta), \tag{3.51}$$

by noting this and taking the functional derivative of E^{xc} with respect to n_α, we get the

exchange-correlation potential for the spin component α [37]

$$\begin{aligned}
\hat{V}^{xc,\alpha}_{GGA} &= \frac{\delta E^{xc}_{GGA}}{\delta n_\alpha} \\
&= \frac{\partial f_{GGA}}{\partial n_\alpha} - \vec{\nabla} \cdot \frac{\partial f_{GGA}}{\partial \vec{\nabla} n_\alpha} \\
&= \frac{\partial f_{GGA}}{\partial n_\alpha} - \vec{\nabla} \cdot \left(2 \frac{\partial f_{GGA}}{\partial (\left| \vec{\nabla} n_\alpha \right|^2)} \vec{\nabla} n_\alpha + \frac{\partial f_{GGA}}{\partial (\vec{\nabla} n_\alpha \cdot \vec{\nabla} n_\beta)} \vec{\nabla} n_\beta \right). \qquad (3.52)
\end{aligned}$$

For the derivative of $V^{xc,\alpha}_{GGA}$ with respect to a we find after some lengthy calculations

$$\begin{aligned}
\frac{\partial V^{xc,\alpha}_{GGA}}{\partial a} &= \frac{\partial^2 f_{GGA}}{\partial n_\alpha^2} \frac{\partial n_\alpha}{\partial a} + \frac{\partial^2 f_{GGA}}{\partial n_\alpha \partial n_\beta} \frac{\partial n_\beta}{\partial a} \\
&+ \left(2 \frac{\partial^2 f_{GGA}}{\partial n_\alpha \partial (\vec{\nabla} |n_\alpha|^2)} \vec{\nabla} n_\alpha + \frac{\partial^2 f_{GGA}}{\partial n_\alpha \partial (\vec{\nabla} n_\alpha \cdot \vec{\nabla} n_\beta)} \vec{\nabla} n_\beta \right) \cdot \frac{\partial \vec{\nabla} n_\alpha}{\partial a} \\
&+ \left(2 \frac{\partial^2 f_{GGA}}{\partial n_\alpha \partial (\vec{\nabla} |n_\beta|^2)} \vec{\nabla} n_\beta + \frac{\partial^2 f_{GGA}}{\partial n_\alpha \partial (\vec{\nabla} n_\alpha \cdot \vec{\nabla} n_\beta)} \vec{\nabla} n_\alpha \right) \cdot \frac{\partial \vec{\nabla} n_\beta}{\partial a} \\
&- \vec{\nabla} \cdot \left[2 \frac{\partial f_{GGA}}{\partial (\left| \vec{\nabla} n_\alpha \right|^2)} \frac{\partial \vec{\nabla} n_\alpha}{\partial a} + \frac{\partial f_{GGA}}{\partial (\vec{\nabla} n_\alpha \cdot \vec{\nabla} n_\beta)} \frac{\partial \vec{\nabla} n_\beta}{\partial a} \right. \\
&+ \left(2 \frac{\partial^2}{\partial (\left| \vec{\nabla} n_\alpha \right|^2) \partial n_\alpha} \vec{\nabla} n_\alpha + \frac{\partial^2 f_{GGA}}{\partial (\vec{\nabla} n_\alpha \cdot \vec{\nabla} n_\beta) \partial n_\alpha} \vec{\nabla} n_\beta \right) \frac{\partial n_\alpha}{\partial a} \\
&+ \left(2 \frac{\partial^2}{\partial (\left| \vec{\nabla} n_\alpha \right|^2) \partial n_\beta} \vec{\nabla} n_\alpha + \frac{\partial^2 f_{GGA}}{\partial (\vec{\nabla} n_\alpha \cdot \vec{\nabla} n_\beta) \partial n_\beta} \vec{\nabla} n_\beta \right) \frac{\partial n_\beta}{\partial a} \\
&+ \left(4 \frac{\partial^2}{\partial (\left| \vec{\nabla} n_\alpha \right|^2)^2} \vec{\nabla} n_\alpha + 2 \frac{\partial^2 f}{\partial (\vec{\nabla} n_\alpha \cdot \vec{\nabla} n_\beta) \partial (\left| \vec{\nabla} n_\alpha \right|^2)} \vec{\nabla} n_\beta \right) \left(\vec{\nabla} n_\alpha \cdot \frac{\partial \vec{\nabla} n_\alpha}{\partial a} \right) \\
&+ \left(4 \frac{\partial^2}{\partial (\left| \vec{\nabla} n_\alpha \right|^2) \partial (\left| \vec{\nabla} n_\beta \right|^2)} \vec{\nabla} n_\alpha + 2 \frac{\partial^2 f}{\partial (\vec{\nabla} n_\alpha \cdot \vec{\nabla} n_\beta) \partial (\left| \vec{\nabla} n_\beta \right|^2)} \vec{\nabla} n_\beta \right) \left(\vec{\nabla} n_\beta \cdot \frac{\partial \vec{\nabla} n_\beta}{\partial a} \right) \\
&+ \left(2 \frac{\partial^2}{\partial (\left| \vec{\nabla} n_\alpha \right|^2) \partial (\vec{\nabla} n_\alpha \cdot \vec{\nabla} n_\beta)} \vec{\nabla} n_\alpha + 2 \frac{\partial^2 f_{GGA}}{\partial (\vec{\nabla} n_\alpha \cdot \vec{\nabla} n_\beta)^2} \vec{\nabla} n_\beta \right) \left(\vec{\nabla} n_\beta \cdot \frac{\partial \vec{\nabla} n_\alpha}{\partial a} \right) \\
&+ \left. \left(2 \frac{\partial^2}{\partial (\left| \vec{\nabla} n_\alpha \right|^2) \partial (\vec{\nabla} n_\alpha \cdot \vec{\nabla} n_\beta)} \vec{\nabla} n_\alpha + 2 \frac{\partial^2 f_{GGA}}{\partial (\vec{\nabla} n_\alpha \cdot \vec{\nabla} n_\beta)^2} \vec{\nabla} n_\beta \right) \left(\vec{\nabla} n_\alpha \cdot \frac{\partial \vec{\nabla} n_\beta}{\partial a} \right) \right] \qquad (3.53)
\end{aligned}$$

Where the derivatives of the gradient terms are given by

$$\frac{\partial \vec{\nabla} n_{\alpha,\beta}(r)}{\partial a} = \sum_{\mu\nu} \left[\frac{\partial}{\partial a} \vec{\nabla} \left(\phi_\mu(r) \phi_\nu(r) \right) D_{\mu\nu}^{\alpha,\beta} \right] + \sum_{\mu\nu} \vec{\nabla} \left(\phi_\mu(r) \phi_\nu(r) \right) \frac{\partial D_{\mu\nu}^{\alpha,\beta}}{\partial a}. \quad (3.54)$$

To avoid the calculation of the Laplacian $\vec{\nabla}^2$ in the second part of Eq. (3.51) the gradient term is transferred to the basis functions by partial integration, when calculating the matrix elements $\langle \mu | \frac{\partial V^{xc}}{\partial a} | \nu \rangle$.

4 Quantum transport

4.1 Current formula

In this paragraph we derive a formula for the current through an interacting region connected to two non-interacting leads. The system we have in mind is shown in Fig. 4.1. This formula was first derived by Meir and Wingreen [62] using the Keldysh nonequilibrium Green's function formalism in an orthogonal basis. However, the nonorthogonal basis introduces additional intricacy due to the ambiguity of the definition of the charge within a specific region. Thygessen derived a Meir-Wingreen like formula for the current through an interacting region in the nonorthogonal case by orthogonalizing the central region with respect to leads by introducing the dual basis set in the central region [63].

By defining the charges in L, C and R by sets of localized orbitals we can introduce partial charges according to the Mullikan population analysis scheme [64], Viljas et al. derived in that way a formula similarly to Thygessen's result [22].

Since we are mainly interested in the electron-phonon interaction which is given by a single-particle potential acting on the electrons, we will restrict our self to a single particle Hamiltonian of the form

$$\hat{H} = \sum_{ij} \hat{d}_i^{\dagger} H_{ij} \hat{d}_i \tag{4.1}$$

with

$$\boldsymbol{H} = \begin{pmatrix} \boldsymbol{H}_{LL} & \boldsymbol{H}_{LC} & 0 \\ \boldsymbol{H}_{CL} & \boldsymbol{H}_{CC} & \boldsymbol{H}_{CR} \\ 0 & \boldsymbol{H}_{RC} & \boldsymbol{H}_{RR} \end{pmatrix}. \tag{4.2}$$

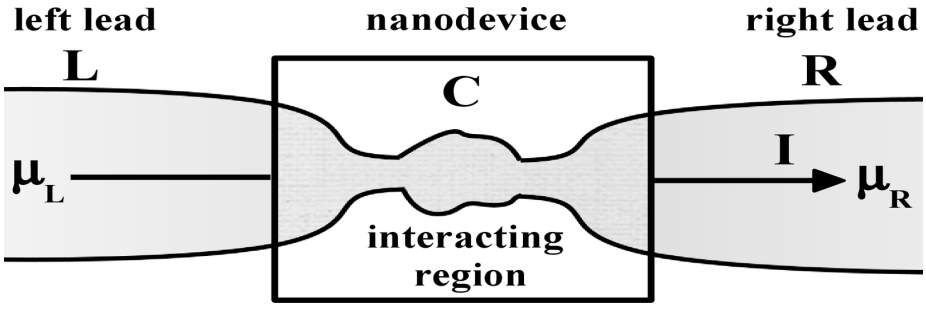

Fig. 4.1: Transport through nano-systems. The actual device region in which interactions can occur, is connected to two leads modeled by reservoirs of non-interacting electrons which connect the system to infinitely large reservoirs at chemical potentials μ_L and μ_R, respectively.

Here $\boldsymbol{H}_{CC} = \boldsymbol{H}^0 + \boldsymbol{V}_{int}$, where $\boldsymbol{V}_{int}$ can be considered as a perturbation to the free (mean-field) Hamiltonian H^0. For $\boldsymbol{H}_{LL} = \boldsymbol{H}_{RR}$ we assume an non-interacting electron gas, $\boldsymbol{H}_{CL}$, $\boldsymbol{H}_{LC}$, $\boldsymbol{H}_{CR}$ and $\boldsymbol{H}_{RC}$ describe the coupling between the leads and the central region and we assume that the left and right leads are completely decoupled hence $\boldsymbol{H}_{LR} = \boldsymbol{H}_{RL} = 0$ and $\boldsymbol{S}_{LR} = \boldsymbol{S}_{RL} = 0$, where $S_{ij} = \langle i|j\rangle$ is the overlap matrix element between the orbitals i and j (Eq. (3.15)).

We will follow the approach by Viljas et al. and divide the total charge or number of electrons, according to

$$N = N_L + N_C + N_R = \sum_{j\in L,k} D_{jk}S_{kj} + \sum_{j\in C,k} D_{jk}S_{kj} + \sum_{j\in R,k} D_{jk}S_{kj} \tag{4.3}$$

where D_{ij} is the density matrix (Eq. (3.20)). Normally one considers a local continuity equation and calculates the current between the boundary of L and C or R and C [65], but here we will consider a continuity equation for the total number of electrons in the central region and then identify the individual contributions from the particle flow between C, L and C, R respectively. The total number of electrons in the central region is given by

$$N_C(t) \;=\; \mathrm{tr}\left\{\boldsymbol{D}\boldsymbol{S}\right\}_{CC} = -\mathrm{i}\hbar\mathrm{tr}\left\{\boldsymbol{G}^<(t,t)\boldsymbol{S}\right\}_{CC} \tag{4.4}$$

where we have expressed the density matrix by the lesser Green's function for $t = t^{'}$ [66] and the trace runs over all orbitals in the central region.

Taking the time derivative of N_C yields

$$\frac{\partial}{\partial t}N_C(t) \;=\; -\mathrm{i}\lim_{t\to t'}\left(\frac{\partial}{\partial t}+\frac{\partial}{\partial t'}\right)\mathrm{tr}\left\{\boldsymbol{G}^<(t,t')\boldsymbol{S}\right\}_{CC} = \tag{4.5}$$

$$= -\mathrm{i}\lim_{t\to t'}\left(\mathrm{tr}\left\{\frac{\partial}{\partial t}\left(\boldsymbol{S}_{CC}\boldsymbol{G}^<_{CC}(t,t') + \boldsymbol{S}_{LC}\boldsymbol{G}^<_{CL}(t,t') + \boldsymbol{S}_{RC}\boldsymbol{G}^<_{CR}(t,t')\right)\right\}\right. \tag{4.6}$$

$$\left. + \mathrm{tr}\left\{\frac{\partial}{\partial t'}\left(\boldsymbol{G}^<_{CC}(t,t')\boldsymbol{S}_{CC} + \boldsymbol{G}^<_{CL}(t,t')\boldsymbol{S}_{LC} + \boldsymbol{G}^<_{CR}(t,t')\boldsymbol{S}_{RC}\right)\right\}\right), \tag{4.7}$$

where we have used the cyclic invariance of the trace in the second line for the term with $\partial/\partial t$ and have explicitly written the terms contributing to the trace over C. The equations of motions for $\frac{\partial}{\partial t}\boldsymbol{S}\boldsymbol{G}^<(t,t')$ and $\frac{\partial}{\partial t'}\boldsymbol{G}^<(t,t')\boldsymbol{S}$ are given by Eq. (B.34) and Eq. (B.35). We replace the derivatives in the third line and $\frac{\partial}{\partial t}S_{CC}G^<_{CC}(t,t')$ in the second line

$$\begin{aligned}\frac{\partial}{\partial t}N_C(t) \;=\; &\frac{1}{\hbar}\lim_{t\to t'}\mathrm{tr}\left\{\boldsymbol{H}_{CC}\boldsymbol{G}^<_{CC}(t,t') + \boldsymbol{H}_{CL}\boldsymbol{G}^<_{LC}(t,t') + \boldsymbol{H}_{CR}\boldsymbol{G}^<_{RC}(t,t')\right.\\
&+\mathrm{i}\hbar\frac{\partial}{\partial t}\left(\boldsymbol{S}_{LC}\boldsymbol{G}^<_{CL}(t,t') + \boldsymbol{S}_{RC}\boldsymbol{G}^<_{CR}(t,t') - \boldsymbol{S}_{CL}\boldsymbol{G}^<_{LC}(t,t') - \boldsymbol{S}_{CR}\boldsymbol{G}^<_{RC}(t,t')\right)\\
&\left.-\boldsymbol{G}^<_{CC}(t,t')\boldsymbol{H}_{CC} - \boldsymbol{G}^<_{CL}(t,t')\boldsymbol{H}_{LC} - \boldsymbol{G}^<_{CR}(t,t')\boldsymbol{H}_{RC}\right\}\end{aligned} \tag{4.8}$$

In the steady state we have $\frac{\partial}{\partial t} N_C(t) = 0$ and the Green's functions just depend on $t - t'$. Fourier transforming the above equation and taking the limit $t \to t'$ yields

$$0 = \frac{1}{h}\mathrm{tr}\left\{(\boldsymbol{H}_{CL} - \boldsymbol{S}_{CL}E)\,\boldsymbol{G}^{<}_{LC}(E) - (\boldsymbol{H}_{LC} - \boldsymbol{S}_{LC}E)\,\boldsymbol{G}^{<}_{CL}(E)\right. \tag{4.9}$$

$$\left. + (\boldsymbol{H}_{CR} - \boldsymbol{S}_{CR}E)\,\boldsymbol{G}^{<}_{RC}(E) - (\boldsymbol{H}_{RC} - \boldsymbol{S}_{RC}\boldsymbol{E})\,\boldsymbol{G}^{<}_{CR}(E)\right\} \tag{4.10}$$

Now we can identify the current associated with the electron flow between the left lead and the central region

$$I_L = \frac{e}{h}\mathrm{tr}\left\{\boldsymbol{G}^{<}_{CL}(E)\,(\boldsymbol{H}_{LC} - \boldsymbol{S}_{LC}E) - (\boldsymbol{H}_{CL} - \boldsymbol{S}_{CL}E)\,\boldsymbol{G}^{<}_{LC}(E)\right\} \tag{4.11}$$

and between the right lead and the central region,

$$I_R = \frac{e}{h}\mathrm{tr}\left\{\boldsymbol{G}^{<}_{CR}(E)\,(\boldsymbol{H}_{RC} - \boldsymbol{S}_{RC}E) - (\boldsymbol{H}_{CR} - \boldsymbol{S}_{CR}E)\,\boldsymbol{G}^{<}_{RC}(E)\right\} \tag{4.12}$$

and we see that $I_L = -I_R$. We choose the current to be $I = I_L$ hence we obtain

$$I = \frac{e}{h}\mathrm{tr}\left\{\boldsymbol{G}^{<}_{CL}(E)t_{LC}(E) - t_{CL}(E)\boldsymbol{G}^{<}_{LC}(E)\right\} \tag{4.13}$$

where we use the definition $t_{XY}(E) = (\boldsymbol{H}_{XY} - \boldsymbol{S}_{XY}E)$ (Eq. (B.42)). With the help of the Keldysh equations we arrive after some algebra at[1]

$$I = \frac{2\mathrm{e}}{h}\int \mathrm{d}E\mathrm{Tr}\left\{(f_L(E)\boldsymbol{\Gamma}_L(E) - f_R(E)\boldsymbol{\Gamma}_R(E))\,(\boldsymbol{G}^r(E) - \boldsymbol{G}^a(E))\right\} \tag{4.14}$$

$$+\mathrm{Tr}\left\{(\boldsymbol{\Gamma}_L(E) - \boldsymbol{\Gamma}_R(E))\,\boldsymbol{G}^{<}(E)\right\}. \tag{4.15}$$

4.2 Elastic current

4.2.1 Landauer formula

If we assume non-interacting electrons in the central region the current formula for the interacting case (Eq. (4.14)) reduces to the well-known two-probe Landauer formula [67, 68]. For the non-interacting case we have a closed solution for the Dyson equation in the central part [69, 66] which enables us to write

$$I = \frac{2\mathrm{e}}{h}\int \mathrm{d}E\mathrm{Tr}\left\{\boldsymbol{\Gamma}_L\boldsymbol{G}^r_{CC}\boldsymbol{\Gamma}_R\boldsymbol{G}^a_{CC}\right\}(f_L(E) - f_R(E)) = \frac{2\mathrm{e}}{h}\int \mathrm{d}E\tau(E)\,(f_L(E) - f_R(E)) \tag{4.16}$$

[1] Here we have included a factor of 2 for the spin.

where we have defined the transmission probability

$$\tau(E) = \mathrm{Tr}\left\{\boldsymbol{G}^r_{CC}(E)\boldsymbol{\Gamma}_L(E)\boldsymbol{G}^a_{CC}(E)\boldsymbol{\Gamma}_R(E)\right\} = \mathrm{Tr}\left\{\boldsymbol{t}^\dagger(E)\boldsymbol{t}(E)\right\} \tag{4.17}$$

and have introduced transmission the transmission amplitude matrix [26]

$$\boldsymbol{t}(E) = \sqrt{\boldsymbol{\Gamma}_L(E)}\boldsymbol{G}^a_{CC}(E)\sqrt{\boldsymbol{\Gamma}_R(E)}. \tag{4.18}$$

In the linear response regime, i.e. for low temperature and low bias we find that the conductance G is given by the transmission at the Fermi energy E_F times the conductance quantum $G_0 = 2\mathrm{e}^2/h$. In this limit we can write

$$G = \lim_{V\to 0}\lim_{T\to 0}\frac{dI}{dV} = G_0 \lim_{V\to 0}\int \mathrm{d}E \frac{1}{2}\left(\delta(E - E_F + \mathrm{e}V/2) + \delta(E - E_F - \mathrm{e}V/2)\right) T(E) \tag{4.19}$$

$$G = G_0\tau(E_F), \tag{4.20}$$

where we have assumed $\mu_{L,R} = E_F \mp eV/2$ for the chemical potentials of the left and right lead.

If we evaluate the trace in the expression for the transmission (Eq. (4.20)) in the eigenbasis of $\boldsymbol{t}^\dagger(E)\boldsymbol{t}(E)$, we can write the trace as a sum over the transmission eigenchannels τ_n at E_F

$$G = G_0\tau(E_F) = G_0\sum_n \tau_n(E_F). \tag{4.21}$$

The properties of the transmission eigenchannels will be discussed in more detail in the next paragraph. In the following discussion we omit the energy dependence of all the quantities, and they will always be evaluated at E_F.

4.2.2 Transmission eigenchannels

The transport through the system depicted in Fig. 4.1 and described byEq. (4.16) is in the Landaur Büttiker picture a scattering problem where the incoming wave functions $\left|\Psi_{n\mathrm{L}}\right\rangle$ of channel n in lead L will be scattered in the central region C. With a certain probability either back reflected in a channel n' in lead L or transmitted into one of the channels m in lead R. In this sense the channel wave-functions are eigenfunctions of the semi-infinite leads but not of the entire device, hence Eq. (4.17) will not be diagonal in this basis, usually called the natural basis. Here the conductance reads instead [70]

$$G = G_0 \sum_{n\in\alpha, m\in\beta} \tau_{nm}. \tag{4.22}$$

Alternatively we can diagonalize Eq. (4.17) by means of a unitary transformation U of the channel wave functions into a new set of orthogonal modes $|\tilde{\phi}_{l,L}\rangle = \sum_n |\Psi_{n,L}\rangle\, U_{nl}$

which are simultaneously eigenstates of the semi-infinite leads and of the scattering region. In the basis of the eigenchannels $|\tilde{\phi}_{l,\alpha}\rangle$ the conductance becomes [70]

$$G = G_0 \sum_n \tau_n, \tag{4.23}$$

which means that a charge traveling in an eigenchannel $|\tilde{\phi}_{l,\alpha}\rangle$ will remain in this channel an not mix with any other channels, regardless of whether it is reflected or transmitted at the scattering region.

Paulsson et al. show in Ref. [71] that the projection of the eigenchannels onto the central region $|\phi_{l,\alpha}\rangle = \hat{P}_C |\tilde{\phi}_{l,\alpha}\rangle$ can be obtained without solving for the scattering states in the leads by means of quantities already at hand in the Greens function formalism. The so obtained eigenchannels $|\phi_{l,\alpha}\rangle$ posses well defined, energy normalized amplitudes [71] hence they allow for the comparison between different eigenchannels at the same energy.
Our procedure to construct the eigenchannels follows Ref. [71]. However, our procedure avoids the Löwdin orthogonalization and is formulated consistently within the nonequilibrium Greens function formalism presented in the previous chapter in terms of a nonorthogonal local basis (Appendix A). As shown in Ref. [71] we can write the transmission function (Eq. (4.17)) as

$$\tau = \mathrm{Tr}\left\{\boldsymbol{A}_L \boldsymbol{\Gamma}_R\right\} \tag{4.24}$$

where we define the spectral density matrix

$$\boldsymbol{A}_L = \boldsymbol{G}^r_{CC} \boldsymbol{\Gamma}_L \boldsymbol{G}^a_{CC}. \tag{4.25}$$

as the projection of the full spectral density matrix originating from scattering states in lead L onto C [71]. Motivated by the above equation we define the transmission probability operator

$$\hat{\tau} = \hat{A}_L \hat{\Gamma}_R \tag{4.26}$$

and the corresponding eigenvalue equation

$$\hat{\tau} |\phi_n\rangle = \tau_n |\phi_n\rangle \tag{4.27}$$

where $|\phi_n\rangle$ are the device-projected transmission eigenchannels and τ_n the eigenchannel transmission probabilities, respectively.
We now show how the eigenchannel wave-function for waves coming from the left lead are conveniently obtained from the right eigenvectors of $\hat{\tau}$. From the hermitian, positive-semidefinite eigenvalue equation

$$\hat{A}_L |\chi_k\rangle = \lambda_k |\chi_k\rangle \tag{4.28}$$

we can define a new set of basis states as $|\tilde{\chi}_k\rangle = \sqrt{\lambda_k/2\pi}\,|\chi_k\rangle$ and the corresponding dual basis states as $|\tilde{\chi}^k\rangle = \sqrt{2\pi/\lambda_k}\,|\chi_k\rangle$ (for all $\lambda_k \neq 0$) . As shown in Ref. [71] the $|\tilde{\chi}_k\rangle$

are the device part of orthogonal linear combinations of energy-normalized, left moving scatterings states. The transmission eigenchannels defined in Eq. (4.27) are expanded as

$$|\phi_n\rangle = \sum_k |\tilde{\chi}_k\rangle\, c_{kn}, \tag{4.29}$$

with $c_{kn} = \langle\tilde{\chi}^k|\phi_n\rangle$. By multiplying Eq. (4.27) from the right with $\langle\tilde{\chi}^k|$ and using Eq. (4.28) and Eq. (4.29) we obtain the expansion coefficients c_{kn} from the eigenvalue equation

$$2\pi \sum_r \langle\tilde{\chi}_k|\hat{\Gamma}_R|\tilde{\chi}_r\rangle c_{rn} = \tau_n c_{kn}. \tag{4.30}$$

Normalizing the expansion coefficients according to $\sum_r c^*_{rn} c_{rm} = \delta_{rm}$ preserves the energy normalization of the left-incoming states used in the expansion of Eq. (4.29). The matrix elements of the operators are usually calculated in the nonorthogonal atomic basis set $|e_i\rangle$ (with $i \in C$) employed in the quantum chemistry calculations (see Section 4.1 and Section 3.1.1) . Using the completeness relation (Eq. (A.2)) we transform Eq. (4.30) into the atomic basis $\langle\tilde{\chi}_k|\hat{\Gamma}_R|\tilde{\chi}_r\rangle = \sum_{ij} \tilde{d}^*_{ik}(\Gamma_R)_{ij}\tilde{d}_{rj}$, where $(\Gamma_R)_{ij} = \langle e_i|\hat{\Gamma}_R|e_j\rangle$ are the matrix elements in the atomic basis and $\tilde{d}_{ik} = \langle e^i|\tilde{\chi}_k\rangle = \sqrt{\lambda_k/2\pi}d_{ik}$ are determined from $\hat{A}_L$ by multiplying Eq. (Eq. (4.28)) with $\langle e_i|$ from the left and inserting the completeness relation. This leads to the generalized eigenvalue problem

$$\sum_{ijl} S_{ki}(A_L)^{ij}S_{jl}d_{lk} = \lambda_k \sum_i S_{ik}d_{ik}, \tag{4.31}$$

with $d_{ik} = \langle e^i|\chi_k\rangle$ and $\sum_{ij} d^*_{ik}S_{ij}d_{jr} = \delta_{kr}$. Putting these results together, the explicit form of the eigenchannel wave-function for region C in position space express in terms of the atomic basis functions is obtained from

$$\phi_n(\vec{r}) = \langle\vec{r}|\phi_n\rangle = \sum_{ik}\langle\vec{r}|e_i\rangle\tilde{d}_{ik}c_{kn}. \tag{4.32}$$

With the procedure presented above we can calculate the transmission eigenchannels directly in the nonorthogonal basis.

To conclude this paragraph we make a remark on the visualization of the wave-functions. The transmission eigenchannels $\phi(\vec{r}) = |A(\vec{r})|e^{i\varphi(\vec{r})}$ will in general be complex valued functions with spatially varying amplitude $|A(\vec{r})|$ and phase $\varphi(\vec{r})$. The wave-functions will be plotted by means of color-coded isosurfaces. For a certain value $c > 0$ the isosurface is the hyper-surface defined by $|A(\vec{r})| = c$ and the phase $\varphi(\vec{r})$ will be represented by the color coding of the hyper-surface.

4.2.3 Thermopower

So far we have dealt with the electric current through nano-devices as a response to an applied bias voltage. However, the Landauer formalism is not limited to electric current

alone. It can be used to study to other transport properties related to thermal transport and thermoelectric effects arising from the electronic degrees of freedom [72].

Besides the conductance G also the Peltier coefficient Π, the thermopower Q and the electronic contribution to the thermal conductance κ can be expressed in terms of the transmission function (Eq. (4.17)) [72, 73]. In the following we focus on the thermopower Q.

Applying a temperature difference $\Delta T = T_L - T_R$ on the ends of a sample induces a current flow along the temperature gradient, in turn a voltage difference $\Delta V = V_L - V_R$ builds up. We define the thermoelectric voltage ΔV as the voltage compensating the thermally induced current in the steady state, $I = 0$. The thermopower is the ratio of the applied temperature difference and the thermoelectric voltage

$$Q = -\left.\frac{\Delta V}{\Delta T}\right|_{I=0}. \tag{4.33}$$

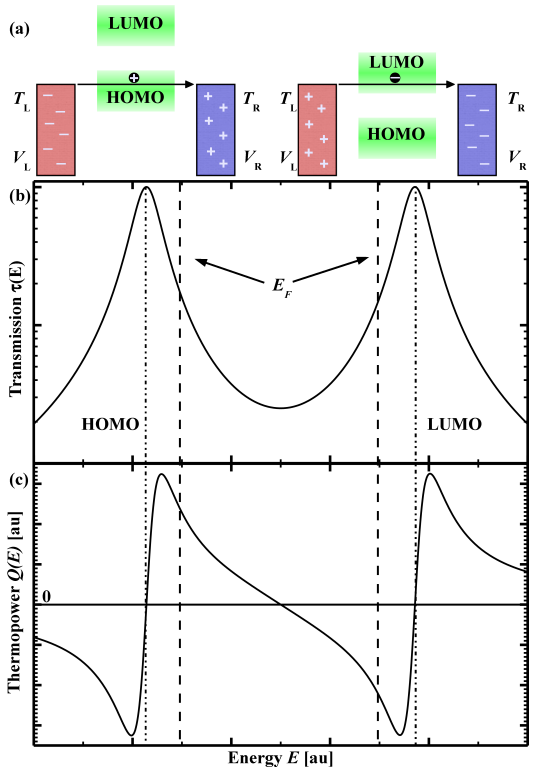

Fig. 4.2: (a) For hole transport through the HOMO $\Delta V > 0$, for electron transport through the LUMO $\Delta V < 0$. (b) Idealized $\tau(E)$ curve. E_F lies in the HOMO-LUMO gap, indicated for two different positions (dashed lines) one close to the HOMO and one close the LUMO resonance (dotted lines). (c) Resulting $Q(E)$. For E_F as indicated in (b) we have either $Q > 0$ or $Q < 0$.

An important observation from the definition above is that the sign of the majority charge carriers is related to the sign of the thermopower. In semiconductor physics it is well known, that hole-conducting p-type semiconductors show $Q > 0$ and electron-conducting n-type semiconductors show $Q < 0$ respectively [74]. Assuming that $T_L > T_R$ ($\Delta T > 0$) then the charge carriers are transported along the temperature gradient from the left to right side of the sample. In molecular junctions can we now discriminate between the two situations shown in Fig. 4.2a and b. In Fig. 4.2a holes (positive charge) are transported through the highest occupied molecular orbital (HOMO) resulting in a negative thermovoltage $\Delta V < 0$. From Eq. (4.33) follows that the thermopower becomes positive, $Q > 0$. Contrary for electron (negative charge) transported through the lowest unoccupied orbital (LUMO) as shown in Fig. 4.2b, the thermovoltage becomes negative $\Delta V > 0$. Respectively the thermopower becomes positive $Q < 0$.

If there is no external bias voltage applied, the difference between the chemical poten-

tials μ_L and μ_R of the left and right leads will be given by the temperature-induced voltage difference $\Delta\mu = \mu_L - \mu_R = \mathrm{e}\Delta V$. Assuming that we are in the linear response regime, i.e. $\Delta\mu$ and ΔT are small, we can expand the Fermi functions in Eq. (4.16)

$$f_L(E) - f_R(E) \approx -\frac{\partial f(E, E_F, T)}{\partial E}\left(e\Delta V + \frac{\Delta T}{T}(E - E_F)\right). \tag{4.34}$$

Inserting the expansion (Eq. (4.34)) into the Landauer formula yields

$$I = G_0 \int \mathrm{d}E\tau(E)\left(-\frac{\partial f(E, E_F, T)}{\partial E}\right)\left(e\Delta V + \frac{\Delta T}{T}(E - E_F)\right). \tag{4.35}$$

In the steady state, $I = 0$, we can directly obtain the thermopower from the above expression as

$$Q = -\frac{K_1(T)}{eTK_0(T)}, \tag{4.36}$$

where we have defined the following integrals

$$K_n = \int \mathrm{d}E\tau(E)\left(-\frac{\partial f(E, E_F, T)}{\partial E}\right)(E - E_F)^n. \tag{4.37}$$

This result can be further simplified if expand also the transmission function around E_F. In the low temperature limit the thermopower can then be expressed by the logarithmic derivative of $\tau(E)$ [75]

$$Q = -\frac{\pi^2 k_B^2}{3e} T \frac{\tau'(E_F)}{\tau(E_F)}. \tag{4.38}$$

From Eq. (4.38) it follows that the sign as well as the absolute value of Q depends on the slope of the transmission function at the Fermi energy. In single molecule junctions the Fermi energy is determined by the metal electrodes and lies normally somewhere in the HOMO-LUMO gap (Fig. 4.2b). If E_F is closer to the HOMO resonance the slope of $\tau(E)$ will be negative hence Q becomes positive, in contrast to this if E_F is closer to the LUMO resonance, the slope of $\tau(E)$ will be positive and hence Q becomes negative. In off-resonant transport Q will increase, if E_F moves closer to the resonance. However, on resonance Q will be strongly suppressed due to the vanishing slope of $\tau(E)$. In Fig. 4.2b and Fig. 4.2c these findings are illustrated, and we can clearly see the dependence of Q on the position of E_F with respect to the HOMO and LUMO resonances.

4.3 Inelastic corrections to the elastic current

4.3.1 Formula for the inelastic current

Before considering explicitly to the electron-phonon interaction we split, the current formula (Eq. (4.13)) into its elastic and inelastic contributions. Since we restrict the in-

teractions to C we write the Keldysh equation (Appendix B.1) for this part as

$$\tilde{\boldsymbol{G}}^{<}_{CC} = \boldsymbol{g}^{<}_{CC} + \tilde{\boldsymbol{G}}^{r}_{CC}\boldsymbol{t}_{CL}\boldsymbol{g}^{<}_{LL}\boldsymbol{t}_{LC}\tilde{\boldsymbol{G}}^{a}_{CC} + \tilde{\boldsymbol{G}}^{r}_{CR}\boldsymbol{t}_{CR}\boldsymbol{g}^{<}_{RR}\boldsymbol{t}_{RC}\tilde{\boldsymbol{G}}^{a}_{CC} - \tilde{\boldsymbol{G}}^{r}_{CC}\boldsymbol{\Sigma}^{<}_{CC}\tilde{\boldsymbol{G}}^{a}_{CC}. \tag{4.39}$$

Inserting the above expression into Eq. (4.13) enables us to split the current as [22]

$$I = I_{el} + I_{inel} \tag{4.40}$$

with the elastic contribution

$$I_{el} = \frac{2e}{h}\int \mathrm{d}E \mathrm{Tr}\left\{\tilde{\boldsymbol{G}}^{r}_{CC}\boldsymbol{\Gamma}_R\tilde{\boldsymbol{G}}^{a}_{CC}\boldsymbol{\Gamma}_L\right\}(f_L - f_R) \tag{4.41}$$

and the inelastic contribution

$$I_{inel} = -\mathrm{i}\frac{2e}{h}\int \mathrm{d}E \mathrm{Tr}\left\{\tilde{\boldsymbol{G}}^{r}_{CC}\boldsymbol{\Gamma}_R\tilde{G}^{a}_{CC}\left[(f_L - 1)\,\boldsymbol{\Sigma}^{<}_{CC} - f_L\boldsymbol{\Sigma}^{>}_{CC}\right]\right\}. \tag{4.42}$$

The elastic contribution looks formally similar to the Landauer formula (Eq. (4.16)). However, compared to $\boldsymbol{G}^{r,a}_{CC}$, appearing in Eq. (4.16), $\tilde{\boldsymbol{G}}^{r,a}_{CC}$ includes in addition the self-energy $\boldsymbol{\Sigma}^{r,a}_{CC}$ due to the interactions in C.

4.3.2 First-order electron-phonon interaction

The Hamilton operator of the coupled electron-phonon system we are considering is given by [22]

$$\hat{H} = \hat{H}^{e} + \hat{H}^{vib} + \hat{H}^{e-vib}, \tag{4.43}$$

where written in second quantization

$$\hat{H}^{e} = \sum_{\mu\nu} d^{\dagger}_{\mu} H^{e}_{\mu\nu} d_{\nu} \tag{4.44}$$

describes the uncoupled electronic system (Eq. (2.9)) on a single-particle level and will be identified with the KS-Operator (Eq. (3.14)). Here $H_{\mu\nu}$ are the matrix elements of a single particle Hamiltonian. In the framework of KS-DFT they are given by the KS-matrix (Eq. (3.17)) and $d^{\dagger}_{\mu}$ (d_{μ}) are the electron creation (annihilation) operators in a non-orthogonal basis (Appendix A) satisfying $\{d_{\alpha}, d^{\dagger}_{\beta}\} = (S^{-1})_{\alpha\beta}$.

$$\hat{H}^{vib} = \sum_{\alpha} \omega_{\alpha} b^{\dagger}_{\alpha} b_{\alpha} \tag{4.45}$$

is the second-quantized form of the uncoupled vibrational Hamiltonian in the harmonic approximation (Eq. (2.27)), and the last term

$$\hat{H}^{e-vib} = \sum_{\mu\nu}\sum_{\alpha} d^{\dagger}_{\mu}\lambda^{\alpha}_{\mu\nu} d_{\nu}(b^{\dagger}_{\alpha} + b_{\alpha}) \tag{4.46}$$

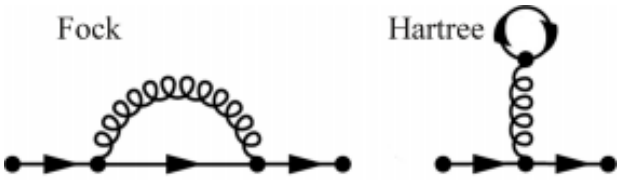

Fig. 4.3: The first order corrections to the electronic system due to the electron-phonon coupling.

is the second quantized form of the first-order electron-phonon interaction (Eq. (2.19)). Here ω_α are the vibrational frequencies and $b_\alpha^\dagger$ (b_α) are the creation (annihilation) operators of the phonon modes, satisfying $[b_\alpha, b_\beta^\dagger] = \delta_{\alpha\beta}$. The electron-phonon coupling constant is given by [22]

$$\lambda_{\mu\nu}^{\alpha} = \left(\frac{\hbar}{2\omega_\alpha}\right)^{1/2} \sum_{B,k} \langle \mu | \frac{\partial \hat{H}^e}{\partial R_B^k} | \nu \rangle A_{B\alpha} \tag{4.47}$$

where $\sum_{B,k}$ runs over all Cartesian components $k = \{x, y, z\}$ of all the nuclear coordinates $\vec{R}_B$ and $A_{B\alpha} = \frac{1}{\sqrt{M_B}} C_{B\alpha}$ are the mass-normalized eigenvectors of the dynamical matrix (Eq. (2.25)), where M_B is the mass of the nuclei at position $\vec{R}_B$.

The lowest-order corrections to the electronic system arsing from the Hamiltonian (Eq. (4.46)) are described by the diagrams shown in Fig. 4.3. They give rise to the following electron-phonon self-energies [22]

$$\Sigma_{e-vib}^{<}(E) = -\frac{\mathrm{i}}{2\pi} \sum_\alpha \int \mathrm{d}\omega D_\alpha^<(\omega) \left[\boldsymbol{\lambda}^\alpha \boldsymbol{G}^<(E-\omega)\boldsymbol{\lambda}^\alpha\right] \tag{4.48}$$

and

$$\Sigma_{e-vib}^{r} = \frac{\mathrm{i}}{2\pi} \sum_\alpha \int \mathrm{d}\omega \big(D_\alpha^<(\omega) \left[\boldsymbol{\lambda}^\alpha \tilde{\boldsymbol{G}}^r(E-\omega)\boldsymbol{\lambda}^\alpha\right] + D_\alpha^<(\omega) \left[\boldsymbol{\lambda}^\alpha \tilde{\boldsymbol{G}}^>(E-\omega)\boldsymbol{\lambda}^\alpha\right] \tag{4.49}$$

$$- \boldsymbol{\lambda}^\alpha \mathrm{Tr}\left\{\tilde{\boldsymbol{G}}^<(\omega)\boldsymbol{\lambda}^\alpha D_\alpha^r(0)\right\}\big). \tag{4.50}$$

For the Green's functions $\tilde{\boldsymbol{G}}^r$ appearing in the current formulas Eq. (4.41) and Eq. (4.42) we use the perturbative expansion

$$\tilde{\boldsymbol{G}}^r = \boldsymbol{G}^r + \boldsymbol{G}^r \boldsymbol{\Sigma}_{e-ph}^r \boldsymbol{G}^r + ..., \tag{4.51}$$

where $\boldsymbol{G}^r$ does just include the self-energies due to the coupling to the leads but not the electron-phonon self-energy. Inserting the above expansion into the current formulas we get for the lowest order contribution in $\boldsymbol{\lambda}^\alpha$ [22]

$$I_{el}^0 = \frac{2e}{h} \int \mathrm{d}E \mathrm{Tr}\left\{\boldsymbol{G}^r \boldsymbol{\Gamma}_R \boldsymbol{G}^a \boldsymbol{\Gamma}_L\right\} (f_L - f_R), \tag{4.52}$$

$$\delta I_{el}^{0} = \frac{4e}{h} \int \mathrm{d}E \mathrm{ReTr} \left\{ \mathbf{\Gamma}_L \boldsymbol{G}^r \mathbf{\Sigma}_{e-vib}^r \boldsymbol{G}^r \mathbf{\Gamma}_R \boldsymbol{G}^a \right\} (f_L - f_R) \tag{4.53}$$

and

$$I_{inel} = -\mathrm{i}\frac{2e}{h} \int \mathrm{d}E \mathrm{Tr} \left\{ \boldsymbol{G}^a \mathbf{\Gamma}_L \boldsymbol{G}^r \left[(f_L - 1) \mathbf{\Sigma}_{e-vib}^{<} - f_L \mathbf{\Sigma}_{e-vib}^{>} \right] \right\}. \tag{4.54}$$

In practice we resort to the wide-band limit (WBL) when evaluating the above equations, assuming that all Green's functions and self-energies can be evaluated at the Fermi energy. The explicit formulas in the WBL are given in Appendix C.2.

Part III

Transport through mono atomic metallic contacts

5 Mono-atomic gold junction

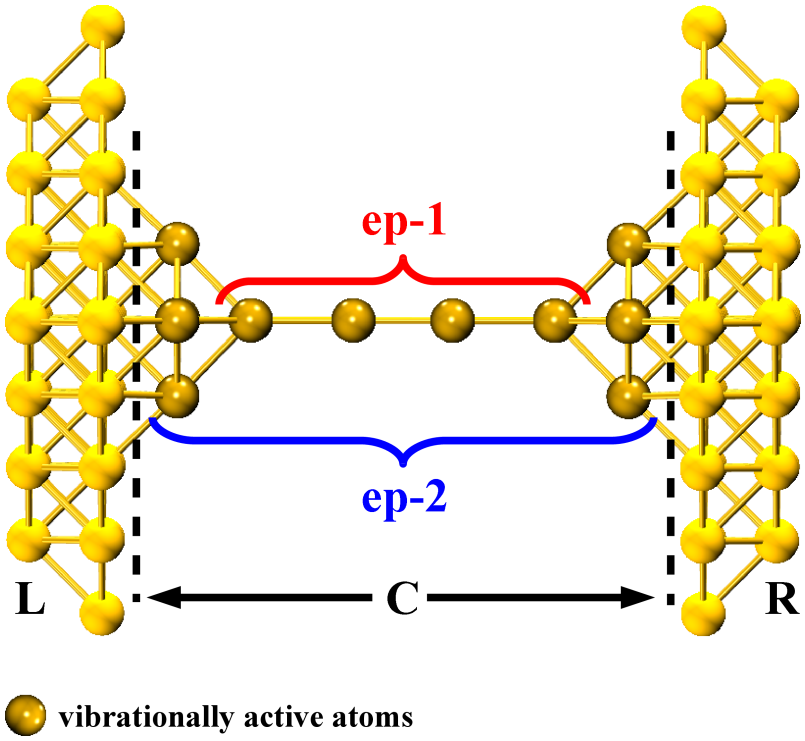

Fig. 5.1: ECC of the investigated 4-atom Au chain connected to Au electrodes. All the atoms in C have been relaxed. The vibrationally active regions are marked with ep-1 and ep-2, respectively.

In this section we examine a 4 atom Au-chain connected to two Au $\langle 100 \rangle$ electrodes, each consisting of 45 atoms (Fig. 5.1). We started from an ideal geometry with an equilibrium lattice constant of $a = 0.408\,\text{nm}$ [76], where the electrodes are oriented in the fcc $\langle 100 \rangle$ direction. Then the C region, which consists of the 4 chain atoms and the first 4 atoms of each electrode, is fully relaxed. The other atoms have been kept fixed at their ideal fcc Bravais lattice positions.

This system has already been studied with respect to its elastic conductance [77, 78, 79, 26], inelastic signatures in the IV-characteristic due to the electron phonon coupling [80,

81, 22], and also the transmission eigenchannel wave-functions have been calculated recently [71]. Therefore it serves here as a test system for the methods developed in the course of this thesis. First we will show that we obtain a elastic conductance close to $1\,G_0$ for this system and that it arises from one completely transparent transmission channel for which we will present the wave function. Second we will deal with the inelastic correction to the current showing that mainly longitudinal phonon modes give rise to signals in the IV curves and we will show how the choice of the vibrationally active atoms influences the phonon frequencies as well as the IETS characteristics.

5.1 Elastic current

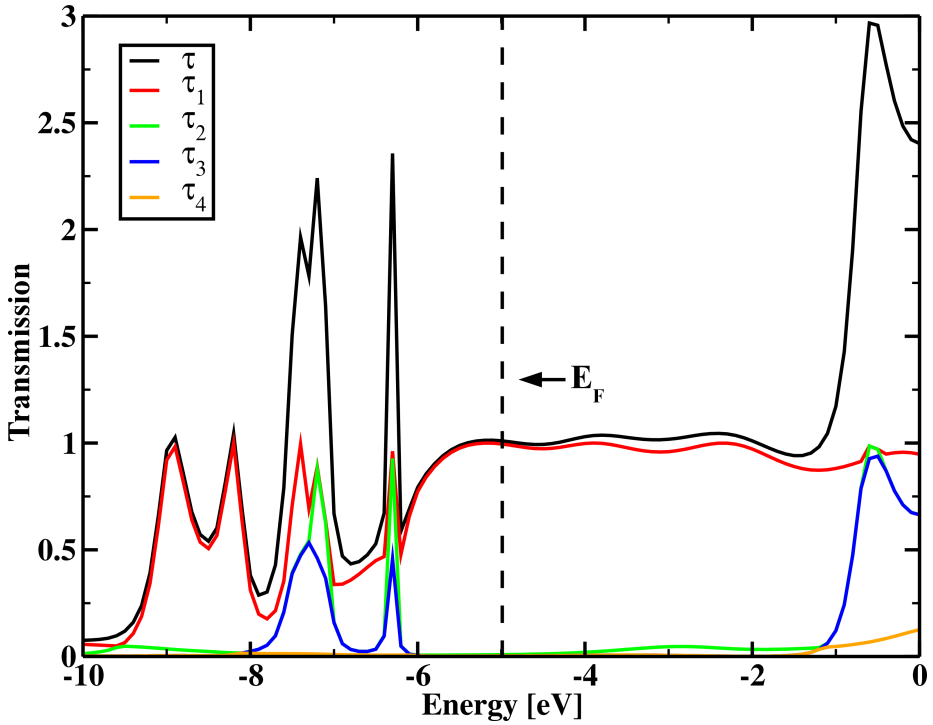

Fig. 5.2: Transmission $\tau(E)$ and the four largest transmission channels $\tau_1(E)$ to $\tau_4(E)$ calculated for the 4-atom Au chain.

In Fig. 5.2 the transmission $\tau(E)$ and the four transmission channels, τ_1-τ_4, with the largest contribution to the transmission are displayed. We find in agreement with previous studies [77, 78, 79, 26] that the transmission is roughly constant around the Fermi-energy $E_F = -5\,\text{eV}$ and close to 1 from $-6\,\text{eV}$ up to -2 eV. The peaks occurring below E_F between $-8\,\text{eV}$ and $-6\,\text{eV}$ are due to the Au d-states [26]. We obtain a total conductance $G = 1.01\,G_0$, which is in agreement with experimental measurements [12, 82, 83].
If we now consider the channel decomposition displayed in Fig. 5.2, we see that at E_F

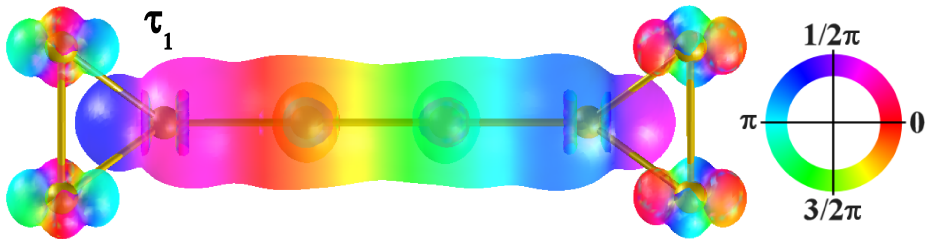

Fig. 5.3: Wave-function (left-incoming) of the dominant transmission channel τ_1, plotted for a isosurface value of $c = 0.03\,\text{a.u.}^{-3/2}$. On the right the color code for the phase is displayed.

the transport is dominantd by one almost completely transparent transmission channel $\tau_1 = 0.996$. Its corresponding left-incoming wave-function is shown in Fig. 5.3. The wave-function posses rotational symmetry in the transport direction along the chain and is mainly formed from the s-valence orbitals of the Au atoms. The phase-factor of the wave-function changes continuously, along the transport direction.

The transmission channels $\tau_2 = 0.009$, $\tau_3 = 0.003$, and $\tau_4 = 0.003$ are contributions from the tails of transmission resonances of the d-states which are around 1.5 eV below E_F (see Fig. 5.2). These eigenchannels are evanescent waves decaying in the transport direction along the chain. Therefore we choose them to be purely real. From Fig. 5.4 we can see that they are of d character on the Au chain. The transport direction defines a distinguished direction, which we will choose to be z-axis. Then wave-functions of τ_2 can be mainly attributed to Au d_{z^2}-states which are rotationally symmetric along the transport direction. Channel τ_3 and τ_4 are degenerate at E_F and their wave-functions are formed from the Au d_{xz}-states and Au d_{yz}-states respectively. The channels corresponding to the other two d-states have a much smaller transmission and are not shown here.

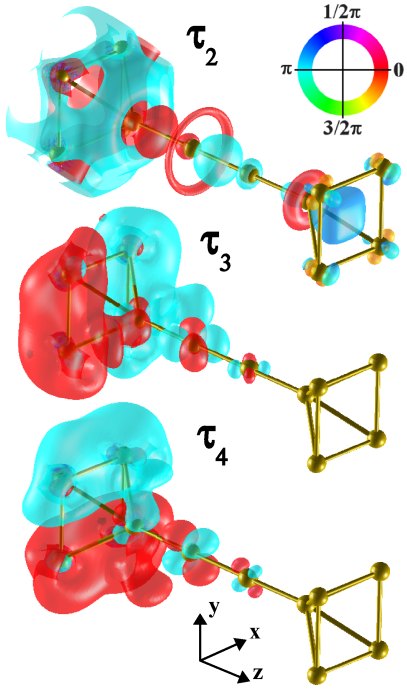

Fig. 5.4: The wave-function (isosurface value, $c = 0.01\,\text{a.u.}^{-3/2}$) of the channel corresponding to τ_2,τ_3, and τ_4.

5.2 Inelastic current

We have considered two different vibrationally active regions in which we take the electron-phonon coupling into account (Fig. 5.1). For region ep-1 we include the electron-phonon coupling just for the 4 chain atoms, keeping the 8 Au atoms in C fixed which belong to the electrodes. For region ep-2 we consider electron-phonon coupling for all the Au atoms in C. First we notice that the number of phonon modes depends on the number of atoms included in the vibrationally active region. For ep-1 we have 4 atoms resulting in 12 phonon modes and for ep-2 we have 12 atoms in the active region, yielding 36 phonon modes. In Fig. 5.5a we have summarized the phonon modes for ep-1 and for ep-2. For ep-2 we have selected only those modes which resemble the vibrational modes of the 4-atom chain for ep-1. Even though we have relaxed the atoms in C the symmetry of the ideal contact is only weakly disturbed. Hence the transverse modes (v4-v7) remain basically two-fold degenerate. Enlarging the vibrationally active region from ep-1 to ep-2 leads for the 4 modes with the highest energy (v1-v4) to a blue shift of the frequencies. For the other 4 modes (v5-v8) the frequencies are red shifted respectively. Overall the changes in the frequencies remain small, however.
The calculated differential conductance is given in Fig. 5.5b. We can see that mainly the three longitudinal modes (v1-v3) lead to signals in the $\mathrm{d}I/\mathrm{d}V$ and $\mathrm{d}^2I/\mathrm{d}V^2$. As the longitudinal modes, due to symmetry, mainly couple to the first transmission channel τ_1, they tend to decrease the conductance according to the so called "1/2 rule" which states that at $V = \hbar\omega/e$, the differential conductance increases ($\mathrm{d}^2I/\mathrm{d}V^2 > 0$) for channels with $(\mathrm{d}I/\mathrm{d}V)/G_0 < 1/2$ and decreases ($\mathrm{d}^2I/\mathrm{d}V^2 < 0$) for channels with $(\mathrm{d}I/\mathrm{d}V)/G_0 > 1/2$, respectively [84, 85]. Here mode v1 gives rise to the largest decrease of the conductance followed by v2 and v3. Comparing the results for ep-1 and ep-2 we find that the curves remain qualitatively the same but that the signals for v1-v3 are shifted to higher bias voltages for ep-2, as expected from the phonon frequencies in Fig. 5.5a. Most of those additional modes of ep-2, which are mainly localized in the electrodes, do not give rise to signals in the $\mathrm{d}I/\mathrm{d}V$.
At a bias voltage which corresponds to the transversal mode v4, 7.89 meV for ep-1 and 8.11 meV for ep-2 respectively, we can see a small increase in the conductance. It follows from the symmetry of the channel wave-functions (Fig. 5.4) that just τ_3 and τ_4 can couple to mode v4 and according to the "1/2 rule" the conductance increases because both channels have a transmission smaller than 1/2.
Increasing the temperature from $T = 0.01\,\mathrm{K}$ to $T = 1.00\,\mathrm{K}$ tends to smear out the sharp steps in the $\mathrm{d}I/\mathrm{d}V$. This can clearly be seen in the $\mathrm{d}^2I/\mathrm{d}V^2$ (Fig. 5.5c), where increasing the temperature leads to much broader peaks at the phonon frequencies. All the presented results for ep-1 are in good agreement with previous tight-binding and ab initio [22, 80, 81] studies. For larger vibrationally active regions (ep-2) there exist to our knowledge no other calculations.

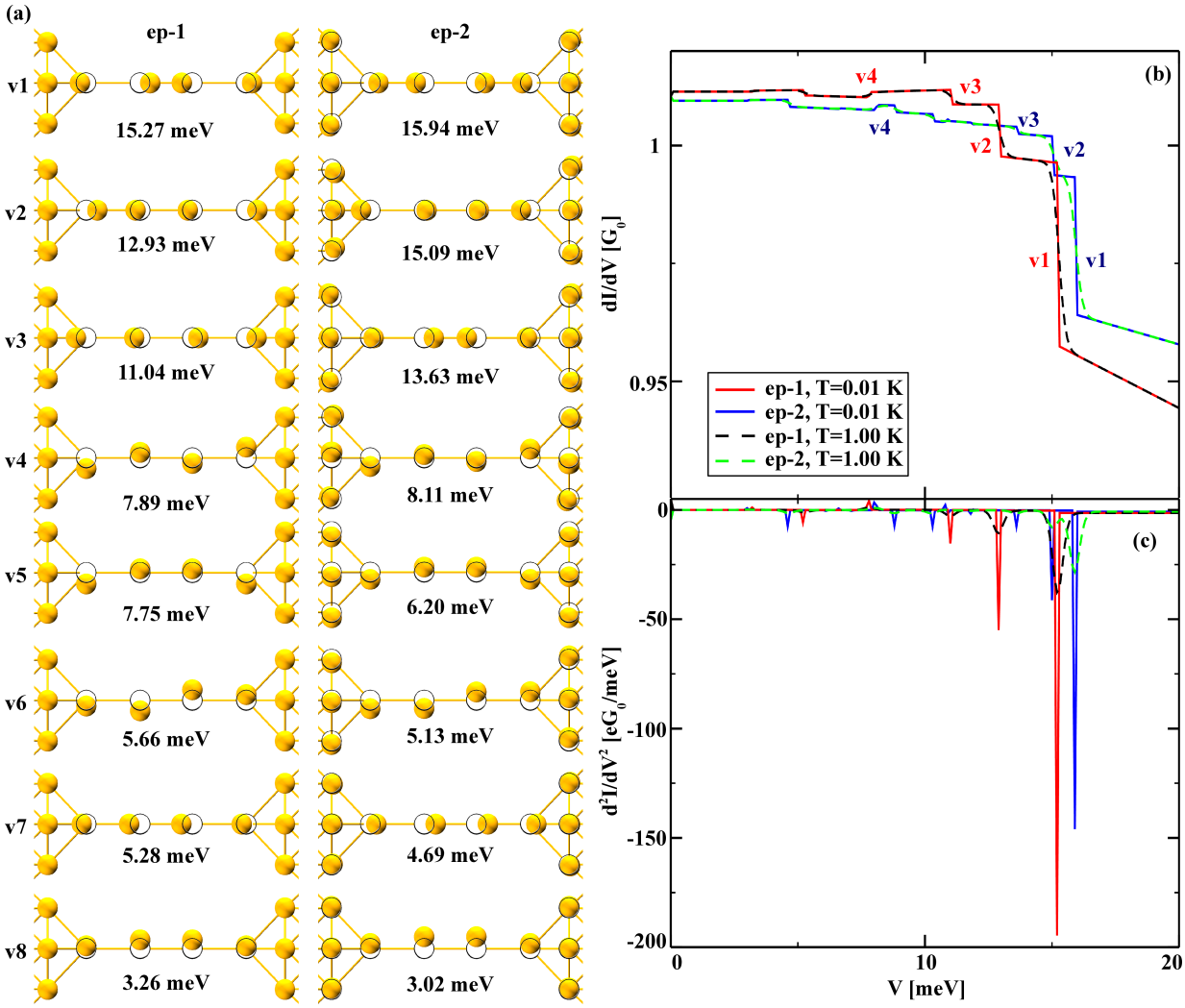

Fig. 5.5: (a) Vibrational modes for ep-1 and ep-2. For ep-2 those modes are listed which are mainly localized on the chain and resemble the modes of ep-1. (b) Differential conductance $\mathrm{d}I/\mathrm{d}V$ for the two active regions ep-1 and ep-2 each for two different temperatures $T = 0.01\,\mathrm{K}$ and $T = 1.00\,\mathrm{K}$. (c) First derivative of the differential conductance $\mathrm{d}^2I/\mathrm{d}V^2$ displayed in (b).

6 Multivalent metals

6.1 Introduction

In this section we deal with mono-atomic point contacts of multivalent metals, namely lead (Pb) and aluminum (Al). It is known that the conduction properties of metallic point contacts depend on the valence structure of the metal [86, 87]. Pb and Al are s-p like metals with 4 and 3 valence electrons, respectively. For s-p like metals the current is usually carried by three channels, one σ-channel and two π-channels. For Pb all three channels are widely open [88, 86, 87], while for to Al, the two π-channels are partially closed and just the σ- channels is completely transparent [88, 86, 87].

The following study aims to analyze and to compare the conduction properties of Pb and Al point contacts. We start with an analysis of the transmission channels. We characterize the channels by means of the symmetry of their wave-functions. Our findings are consistent with the expected channel structure for s-p like metals. In Section 6.2.2 and Section 6.3.2 we discuss the opening and closing process of Pb and Al contacts. We attribute jumps in the conductance during the elongation to atomic rearrangements inside the junction. We find that the opening and closing curves of Pb and Al differ qualitatively. The study is completed by an analysis, of the vibrational properties of the junctions and their IETS at the different elongation stages. For Al we compare the calculated IETS with experimental results from the group of E. Scheer [89]. The chapter concludes with a comparison between the specific properties of the Pb and Al junctions.

6.2 Lead atomic-contacts

6.2.1 Transmission channels

In this section we are considering Pb atomic-contacts. The ECC is modeled by two Pb $\langle 111 \rangle$ electrodes (61 atoms) connected via a single Pb atom (Fig. 6.1b). The contacts are described as closed-shell systems and are treated within a restricted Hartree-Fock ansatz [35]. Starting from the ideal fcc Bravais lattice positions with a lattice constant of $a = 4.95$ Å, the central (C) part is relaxed, the left (L) and right (R) parts are kept fixed.

The conduction properties of metallic atomic contacts depend strongly on the number of valence electrons. Basically the number of valence electrons gives an upper bound for the number of the transmitting channels [66]. From the electron configuration $[\mathrm{Xe}]4f^{14}5d^{10}6s^26p^2$ of Pb follows that Pb has 4 valence electrons, namely two 6s and two 6p electrons. However, for Pb point-contacts we expect just 3 channels, due to the $s-p$ hybridization of the valence orbitals of the central Pb atom [90, 86, 87]. In Fig. 6.1b the energy-dependent transmission $\tau(E)$ and the four largest transmission channels τ_1-τ_4 are shown. The main contribution to the transmission $\tau = 2.93$ at the Fermi-energy $E_F = -3.77$, arises indeed from three channels. The first two channels, $\tau_1 = \tau_2 = 1$, are perfectly transmitting and they are degenerate. Channel $\tau_3 = 0.91$ shows a slightly lower transmittance. The conductance $G = 2.93G_0$ of the system is within the range of typical experimental values for Pb atomic contacts [88]. The left-incoming wave-functions of the three dominant channels are shown in Fig. 6.2. The wave-functions of the two degenerate channels τ_1 and τ_2 correspond to a combination of the p_x and p_y

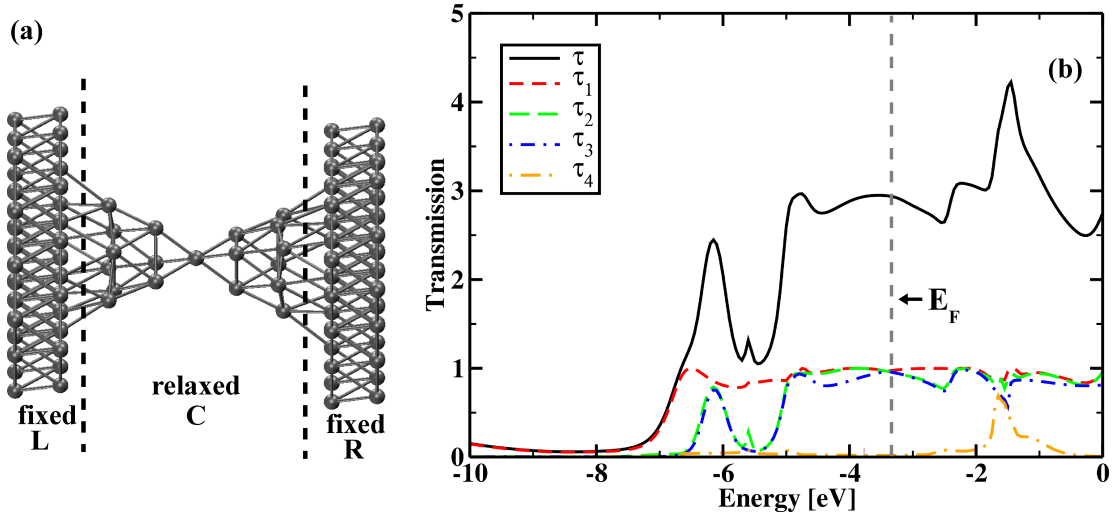

Fig. 6.1: (a) Division of the ECC into L, C and R. (b) Energy-dependent transmission τ and the four largest transmission channels τ_1-τ_4. The Fermi-energy E_F is indicated by the dashed, vertical line.

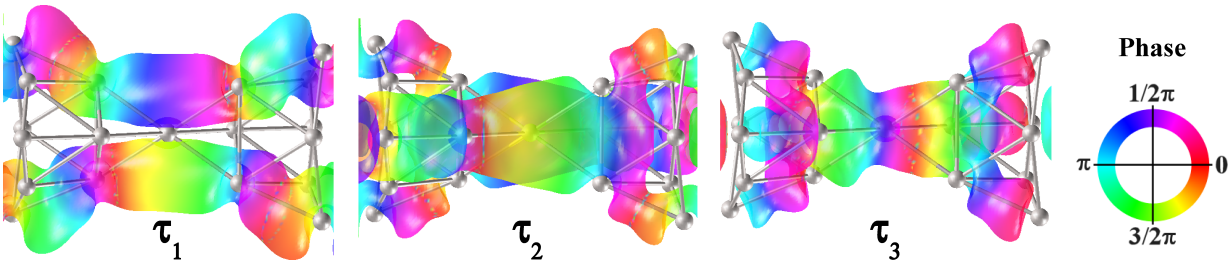

Fig. 6.2: Left-incoming wave-functions of the three dominant transmission channels τ_1-τ_3 (isosurface value $c = 0.2\,\text{a.u.}^{-3/2}$).

orbitals (z-axes along the transport direction) [90, 86, 87]. These two wave-functions show π-symmetry. The wave-function of τ_1 has a nodal plane parallel to the x-z plane, and the nodal plane of τ_2 is defined by the y-z plane (Fig. 6.2). In Section 6.2.2 we show that the plastic deformation during the closing of the junction lifts the degeneracy of the two π-channels. The wave-function of channel τ_3 has rotational symmetry with respect to the z-axes and is formed from the combination of the symmetric s and p_z orbitals [90, 86, 87].

6.2.2 Opening and closing curves

In this section we are concerned with the evolution of the conductance during the opening and closing of the atomic junction. We start from the structure displayed in Fig. 6.1a and Fig. 6.4 ($d = 0.0\,\text{a.u.}$). As indicated in Fig. 6.4 we increase (decrease) in each elongation step the distance between the left and right electrode symmetrically by $2\Delta d = 0.8\,\text{a.u.}$. In each step the two outermost Pb layers are fixed, while the complete inner part of the junction is relaxed (Fig. 6.1a). In this way, we simulate an adiabatic opening (closing) trajectory with equilibrium junction geometries for all the elongation stages. The junction configurations at selected stages are given in Fig. 6.4.
From Fig. 6.3 we see that during the opening of the contact the transmission decreases just weakly with increasing electrode distance. At $d = 4.00\,\text{a.u.}$ the contact breaks, resulting in an abrupt drop of the transmission by one order of magnitude. The decrease of τ between $d = 0.0$ .a.u. and $d = 3.2$ .a.u. can be attributed to a decrease of the transmission in the σ-channel τ_3. The transmission through the two π-channels remains basically constant. Furthermore, the degeneracy between τ_1 and τ_2 is not lifted until the rupture of the contact.
If we close the contact by decreasing the electrode separation, we see that in the beginning τ increases slightly due to an increase of τ_3. τ_1 and τ_2 remain constant and degenerate. At $d = -2.4\,\text{a.u.}$ the contact is plastically deformed as shown in Fig. 6.4. The rearrangement of the atoms in C leads to a partial opening and closing of transmission channels. The degeneracy between τ_1 and τ_2 is lifted and their transmission decreases to $\tau_1 = 0.96$ and $\tau_2 = 0.87$. The transmission of the third channel halves to $\tau_3 = 0.48$.

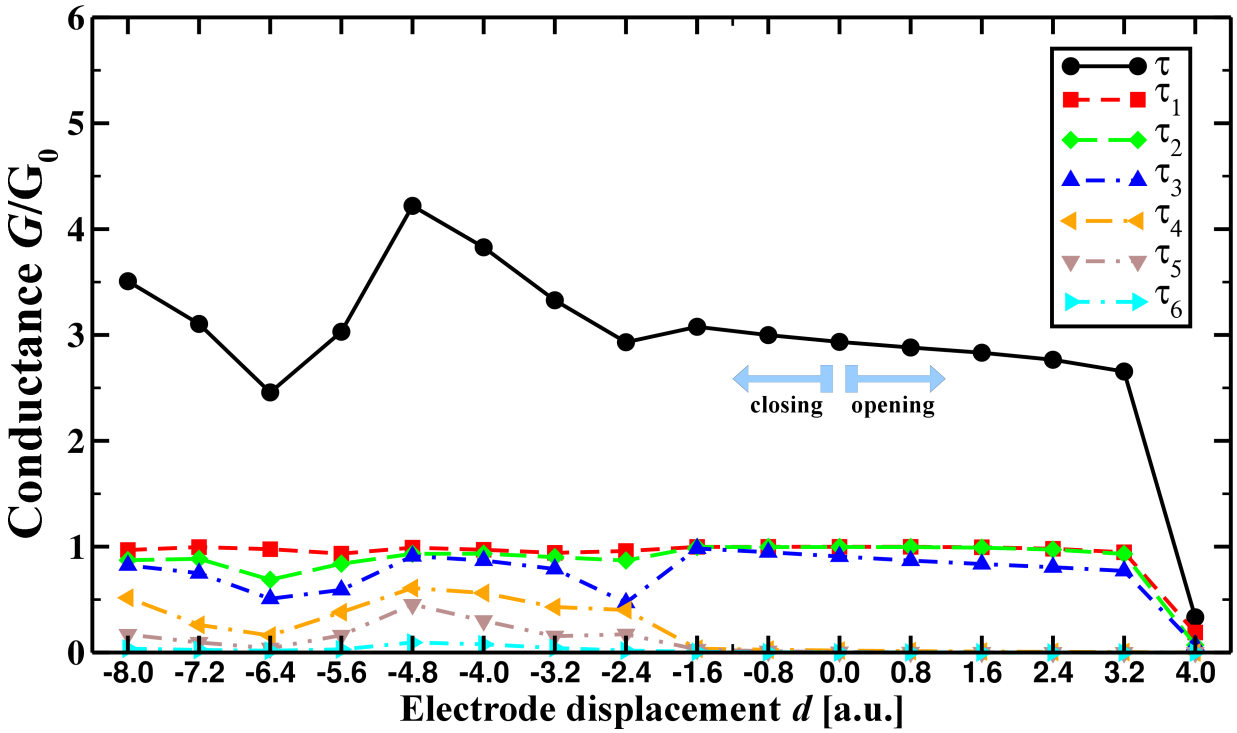

Fig. 6.3: Evolution of the transmission τ and of the six largest transmission channels $\tau_1 - \tau_6$ calculated at the E_F during the opening and closing of the contact. We open and close the contact starting at $d = 0.0$ a.u.. Positive electrode displacements $d > 0$ correspond to opening steps and negative electrode displacements $d < 0$ to closing steps, respectively.

Besides the partial closing of the first three channels, two new channels $\tau_4 = 0.40$ and $\tau_5 = 0.17$ are partially opened. Until $d = -4.8$ a.u. the contact is again elastically deformed, and the transmission increases monotonically up to $\tau = 4.22$. This increase can be observed for all channels considered in Fig. 6.3. The atomic rearrangement at $d = -5.6$ a.u. leads to a large drop in the transmission $\tau = 3.01$ due to a decrease of the transmission in the channels τ_2-τ_5. τ_1 on the other hand remains roughly constant. The subsequently plastic deformation at $d = -7.2$ a.u. leads to a revival of the transmission. Summarizing the above observations, we find that during the elastic stage of the contact closing the transmission increases. However, plastic deformations of the contact can lead to an increase, or to a decrease of the transmission, depending on the actual atomic rearrangement.

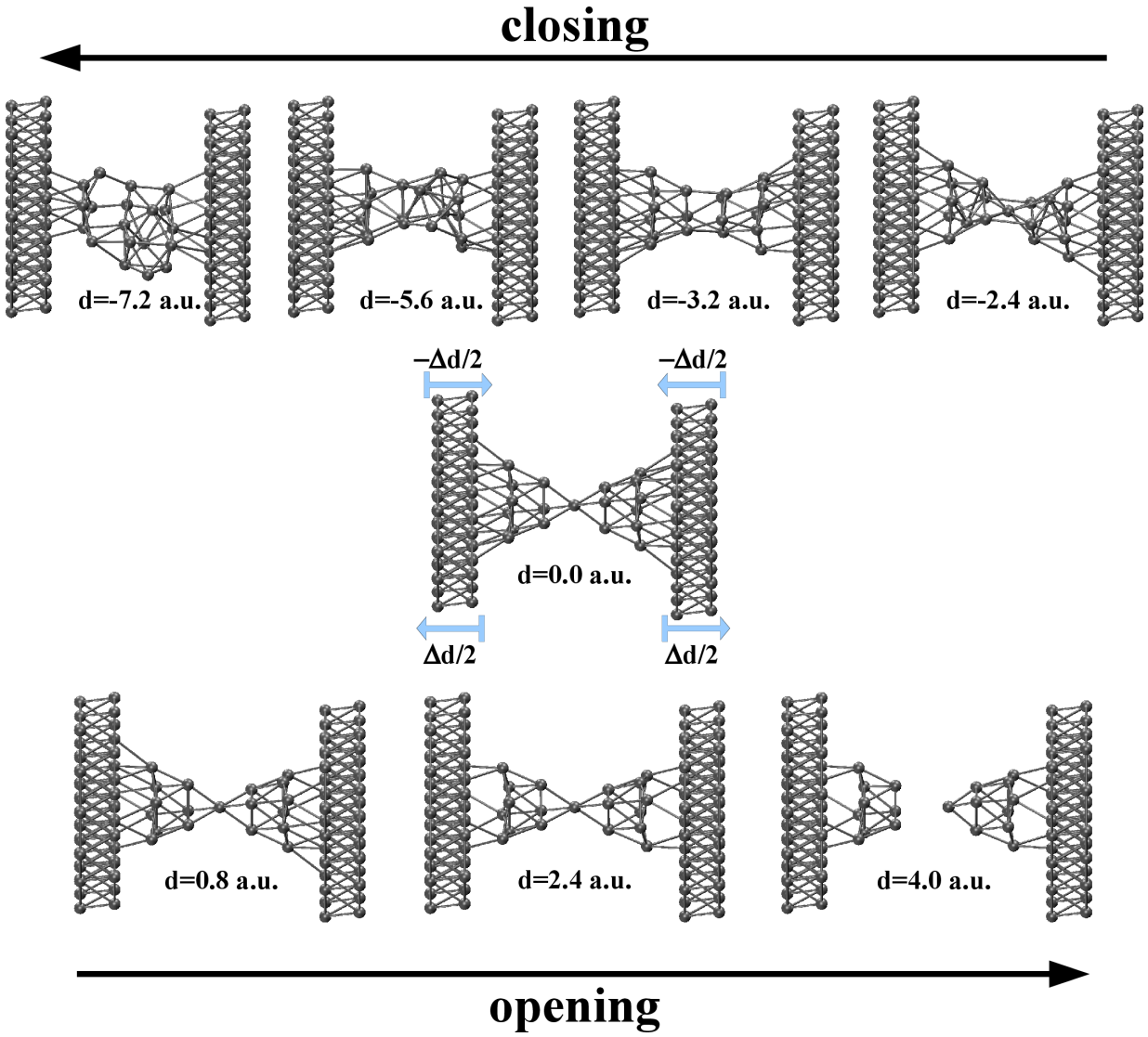

Fig. 6.4: Evolution of the contact geometries during the opening and closing of the contact.

6.2.3 Inelastic current

The partitioning of the ECC for the Pb contacts is displayed in Fig. 6.5. The atoms in L and R are kept fixed at their fcc Bravais lattice positions. The inner part C is relaxed. However, we do not take the electron-phonon (e-p) interaction into account for all atoms in C. The dynamical region is restricted to the tip atom, and to the inner most layers of the electrodes (Fig. 6.5).
First we consider the elongation steps between $d = -1.6$ a.u. and $d = 3.2$ a.u., where the initial single atom contact is just elastically deformed and no atomic rearrangements have occurred yet. During the elastic stages of the junction opening (closing) process the character of the vibrational modes remains basically unchanged. In Fig. 6.6 the vibrational modes for $d = 0.0$ a.u. are displayed, where those modes have been selected which give rise to signals in the IETS. The atoms belonging to L and R have been omitted. The energy of the vibration modes ranges between 3.8 meV and 13.1 meV. The three modes with the lowest energy, v1-v3, correspond to transversal vibrations with respect to the transport direction. Mode v4 is mostly a longitudinal vibration of the central atom. Mode v5 is mainly localized at the outer layers and the vibration is transversal to the Pb-Pb bonds. Mode v6 is a combination of a transversal Pb-Pb vibration of the outer atoms and a longitudinal vibration of the central atom. The amplitude of the longitudinal component of v6 increases with increasing electrode displacement, and decreases with decreasing electrode displacement, respectively. Mode v7 is a longitudinal Pb-Pb mode of the outer atoms. V8 is a mixed longitudinal and transversal vibration of the outer atoms. Mode v9 has a large longitudinal Pb-Pb component of the outer atoms and a large transversal vibration of the tip atom.Mode v10 has the largest energy and is mainly a longitudinal vibration of the tip atom. In Fig. 6.7 the IETS for the initial

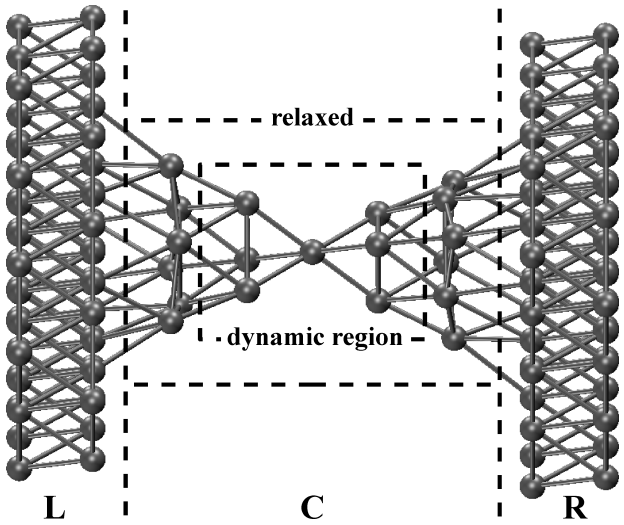

Fig. 6.5: Partitioning of the ECC in to L, C, R and into the dynamical region, in which vibrations are taken into account.

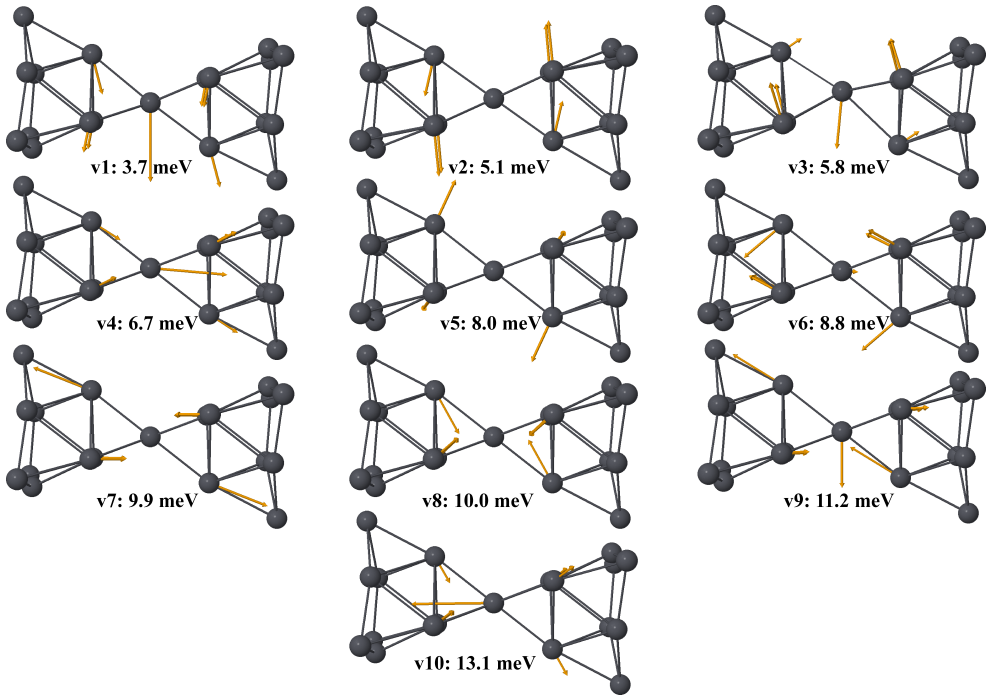

Fig. 6.6: Vibrational modes of the initial geometry ($d = 0.0$ a.u.) which give rise to signals in the IETS. The character of the modes remains unchanged during the elastic stage between $d = -1.6$ a.u. and $d = -3.2$ a.u.. The atoms in L and R have been omitted.

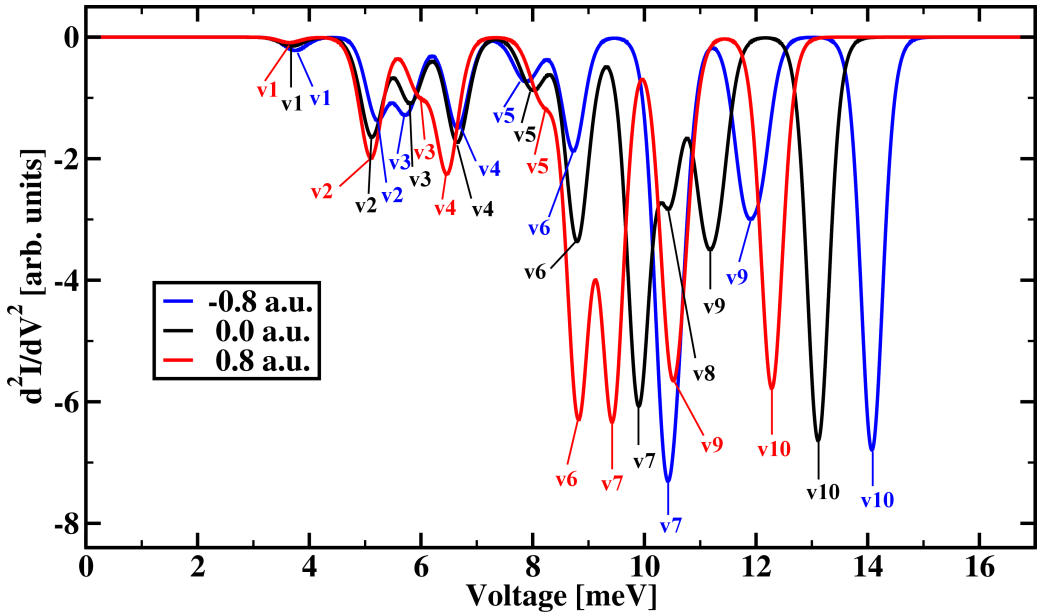

Fig. 6.7: IETS calculated at $T = 1$ K for $d = -0.8$ a.u., $d = 0.0$ a.u., and $d = 0.8$ a.u.. The assigned modes are shown in Fig. 6.6.

geometry ($d = 0.0$ a.u.), the first opening step ($d = 0.8$ a.u.) and the first closing step ($d = -0.8$ a.u.) are shown. Here we have assumed a temperature of $T = 1.0$ K. First we note that we have three dominant transmission channels with $\tau_i \approx 1$ (Fig. 6.3), hence the e-p interaction tends to decreases the conductance ($d^2I/dV^2 < 0$) according to the "1/2 rule" (Section 5.2) [84, 85]. The transversal modes, v1-v3, in the low energy range of the spectrum give just rise to small signals in the IETS. Their position remains roughly constant during the contact elongation. The signal of the low-energy longitudinal mode v4 is somewhat larger and the energy is red shifted for increasing d. The amplitude of the IETS signal of v6 increases strongly with increasing electrode separation due to an increase of the longitudinal component of the vibration. The vibration energy, however, remains roughly constant. Modes v7 and v9 experience a substantial red shift with increasing d. This is due to the decrease of the Pb-Pb "spring constant" between the outer atoms with increasing Pb-Pb bond length (increasing electrode separation). The largest red shift, occurs for the longitudinal mode v10. This can be attributed to the large change in the Pb-Pb bond lengths between the central atom, and the atoms in the first electrode layer during the opening process.

At $T = 1$ K the different modes in the IETS remain mostly well separated and can be distinguished. However, increasing the temperature will smear out the individual resonance, making it difficult or even impossible to identify individual peaks. In **??**a a comparison between the IETS at $T = 1$ K and $T = 4$ K is shown. We can see that most of the features are smeared out at $T = 4$ K. The broad peak between 3.5 meV and 8.5 meV

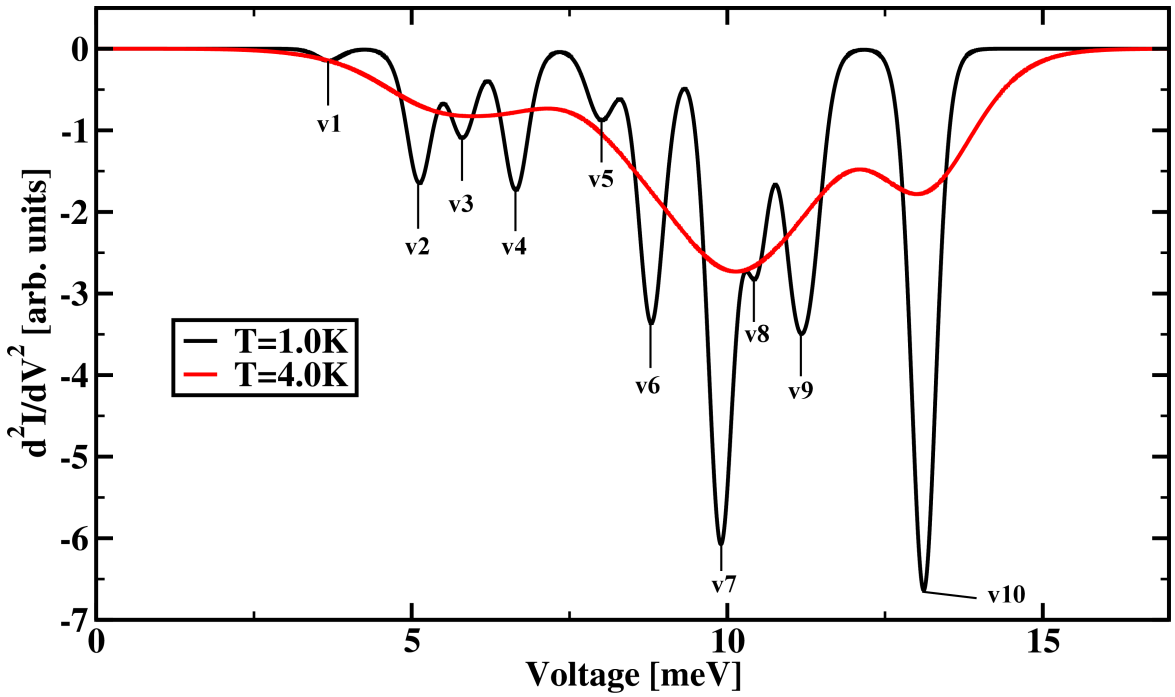

Fig. 6.8: Comparison of the IETS at $d = 0.0$ a.u. for $T = 1$ K 4 K.

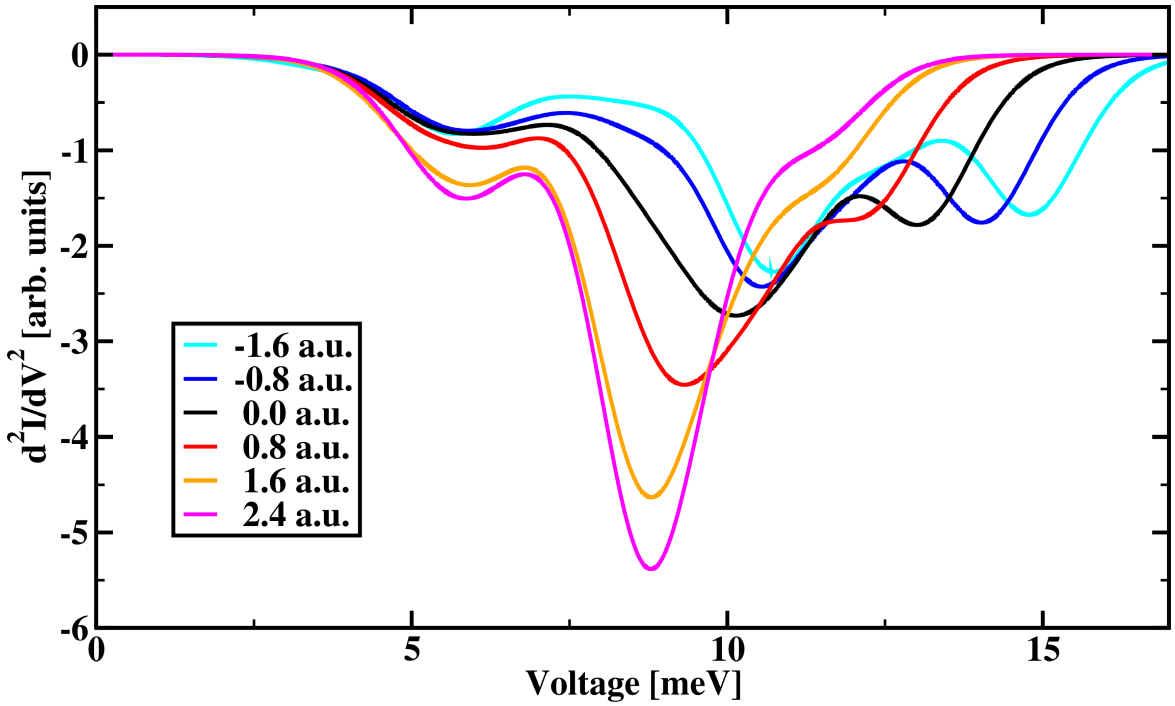

Fig. 6.9: IETS calculated at $T = 4\,\mathrm{K}$ for the different electrode separations in the elastic stage at the beginning of the junction elongation.

can be mainly attributed to the transversal modes v1-v3. The peak centered at 8 meV is formed from v6-v9. The only peak which can be assigned to an individual vibration is the signal of the high energy longitudinal mode v10 (13 meV.). Even if we cannot resolve the individual vibrational modes in the IETS for $T = 4\,\mathrm{K}$, it is possible to identify the general features. As shown in **??**b, we observe the red shift of the vibrational energies, as well as, the increase of the absolute value of the amplitude, with increasing electrode distance.So far we have just considered the elastic stage in the beginning of the elongation process, but it is also possible to observe signatures of the atomic rearrangements in the IETS. Basically a plastic deformation of the contact leads to a large qualitative change of the observed IETS. In Fig. 6.10 we see the changes of the IETS between steps in which the contact is plastically deformed. If we go form $d = -1.6\,\mathrm{a.u.}$ to $d = -2.4\,\mathrm{a.u.}$ we observe an increase of the conductance ($d^2I/dV^2 > 0$) at low voltages. This corresponds to the partial opening of transmission channels with $\tau_i < 1/2$ (Fig. 6.3). According to the "1/2 rule", the transmission probability for these channels is increased by the e-p coupling (Section 5.2) [84, 85]. On the other hand, the high energy modes mainly disappear from the spectra. The plastic deformation at $d = -3.2\,\mathrm{a.u.}$ increases the cross section of the contact to two atoms and lifts thereby most of the symmetries of the contact. We observe just one very broad peak, for d^2I/dV^2, centered at 8.3 meV. However, this peak cannot be attributed anymore to specific vibration modes, due to the large deformation of the central part (Fig. 6.4).

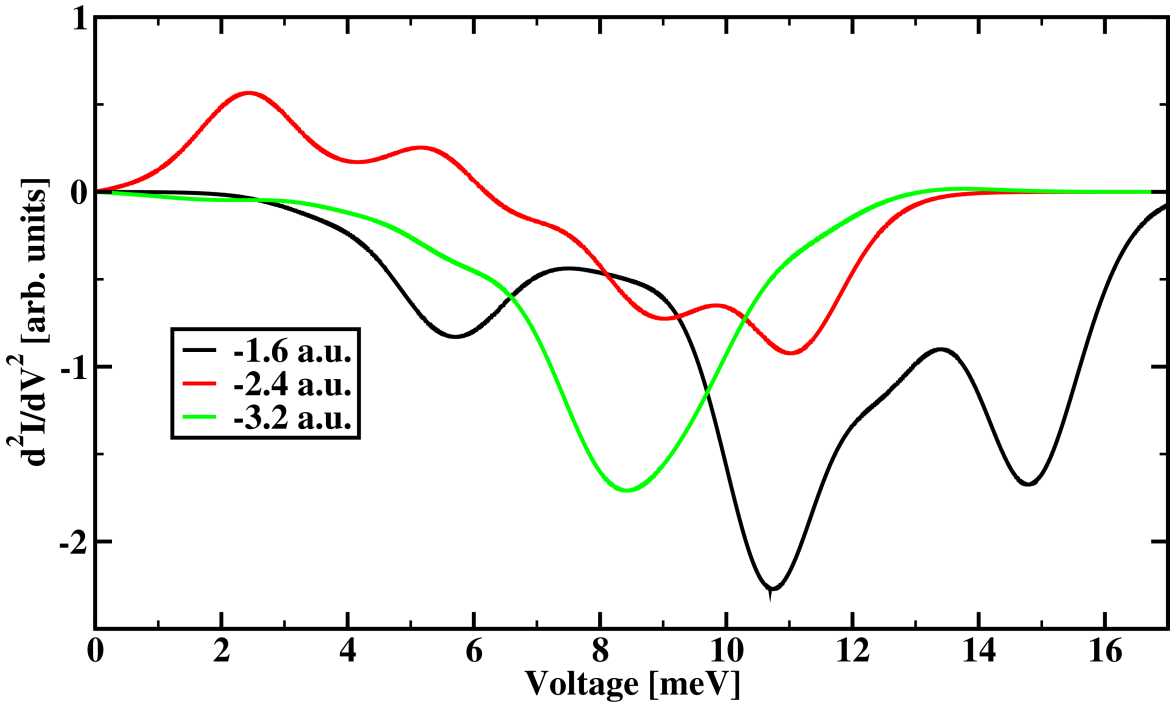

Fig. 6.10: Change of the IETS ($T = 4\,\mathrm{K}$) at stages of plastic deformation of the contact during the closing of the junction.

6.3 Aluminum atomic-contacts

6.3.1 Transmission channels

The Al atomic-contacts are modeled by the ECC shown in Fig. 6.11a. The ECC consists of two Al ⟨111⟩ electrodes (61 atoms) connected via a single Al atom. The contacts are described as open-shell systems with one unpaired electron. Starting from the ideal fcc Bravais lattice positions (lattice constant $a = 4.05$ Å) the central (C) part is relaxed, while the left (L) and right (R) parts of the electrodes are kept fixed.
The conductance of the contact is given by $G = 1.52\,G_0$. Comparing the transmission in the α and β spin-channel in the inset of Fig. 6.11b, we see that both channels yield the same transmission $\tau(E)$ in the whole considered energy range, from -10 eV to 0 eV. Therefore, we do not explicitly take the spin degree of freedom into account in the following discussion.
From the electron configuration, [Ne] $3s^2 3p^1$, of Al, we would expect 3 non vanishing transmission channels from the 3 valence electrons. However, from the channel decomposition of $\tau(E)$ we find, at the Fermi energy $E_F = -4.25$ eV, one completely open channel $\tau_1 = 1$ (Fig. 6.11b) and two degenerate channels, $\tau_2 = \tau_3 = 0.26$, with much smaller transmission probability. As argued in Refs. [86] and [87] the open channel τ_1 is given by a σ-channel formed from the combination of the s-p_z valence orbitals. The wave-function of the first channel shows indeed σ-character, with rotational symmetry along the transport direction (z-axis), as we can see from Fig. 6.12. The wave-functions belonging to the channels 2 and 3 are of π-character and formed from the combinations of the p_x and p_y orbitals. Where the wave-function belonging to τ_2 has a a nodal plane

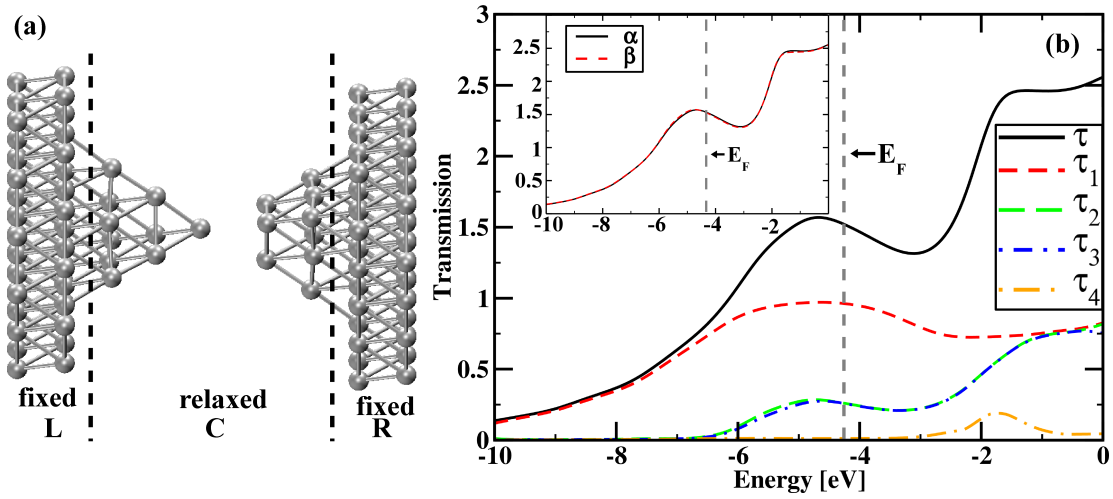

Fig. 6.11: (a) Division of the ECC into L, C and R. (b) Energy-dependent transmission τ and the four largest channel transmission probabilities τ_1-τ_4. The Fermi-energy E_F is indicated by the dashed, vertical line.

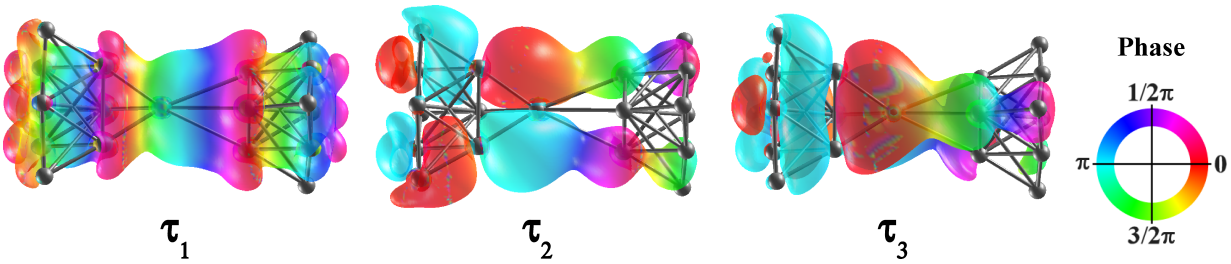

Fig. 6.12: Left-incoming wave-functions of the three dominant transmission channels τ_1-τ_3 (isosurface value $c = 0.2\,\text{a.u.}^{-3/2}$).

in the x-z plane and the nodal plane of the wave-function belonging to τ_3 is the y-z plane. Due to the suppression of the transmission probability of channel 2 and 3, the left-incoming wave-function is first purely real and decaying along the transport direction, before coupling into a Bloch-wave on the right-hand side of the contact (Fig. 6.12).

6.3.2 Opening and closing curves

To simulate the opening and closing process of the Al junction, we start from the ideal structure displayed in Fig. 6.11a, and follow the procedure described in Section 6.2.2 for Pb. The junction configurations at selected stages of the elongation are given in Fig. 6.13.

The evolution of the conductance during the elongation process, shown in Fig. 6.14, can basically be divided in three stages. From $d = 0.0\,\text{a.u.}$ to $d = 4.0\,\text{a.u.}$ the conductance decreases monotonically. From $d = -0.8\,\text{a.u.}$ to $d = -3.2\,\text{a.u.}$ the conductance is roughly constant and the contact is mainly elastically deformed. At $d = -4.0\,\text{a.u.}$ a plastic deformation occurs which leads to a large increase of the transmission.
Already at $d = 0.0\,\text{a.u.}$ a asymmetric contact is formed in the geometry optimization process. The tip atom is pulled towards the left electrode. The bond length between the tip Al atom and the atoms in the first electrode layer is given by $(\text{Al-Al})_{left} = 5.23\,\text{a.u.}$. However, the distance between the tip Al atom and the right electrode $(\text{Al-Al})_{right} =$

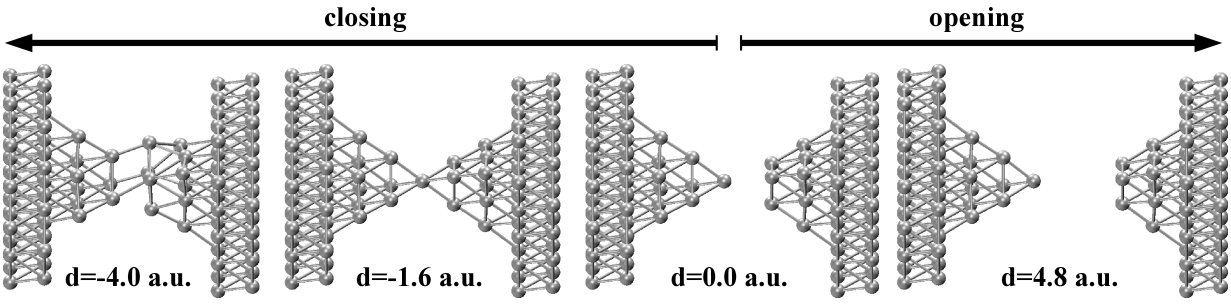

Fig. 6.13: Evolution of the contact during the opening and closing process.

6.96 a.u. is much larger. Increasing the distance between the fixed electrode layers by $\Delta d = 0.8$ a.u. increases the distance between the tip atom and the right electrode by roughly $0.8\,\text{a.u.}/\sqrt{2} = 0.57$ a.u. in each elongation step. We can see from Fig. 6.14 that the transmission decreases monotonically during the contact opening. The decay of the transmission, between $d = 0.8$ a.u. and $d = 4.8$ a.u. can be well fitted to $G = A\exp(-\beta d)$ (inset of Fig. 6.14), where the prefactor is found to be $A = 2.03$ and the attenuation factor is given by $\beta = 0.721/\text{a.u.}$. The exponential decay of the transmission indicates that we are in the tunneling regime for these d.

During the closing of the contact an elastic plateau, with a roughly constant constant, can be observed between $d = -0.8$ a.u. and $d = -3.2$ a.u.. The transmission $G \approx 2.5\,G_0$, and the plateau length of 2.4 a.u. corresponds well to the experimental results of Ref. [88]. From Fig. 6.11 we can see that the atomic rearrangement at $d = -4.0$ a.u. increases the cross section of the contact from one to four atoms. The larger cross section of the contact allows for further open transmission channels. The resulting transmission of $G \approx 5.0\,G_0$ is factor of 2 larger than before the plastic deformation at $d = -3.2$ a.u..

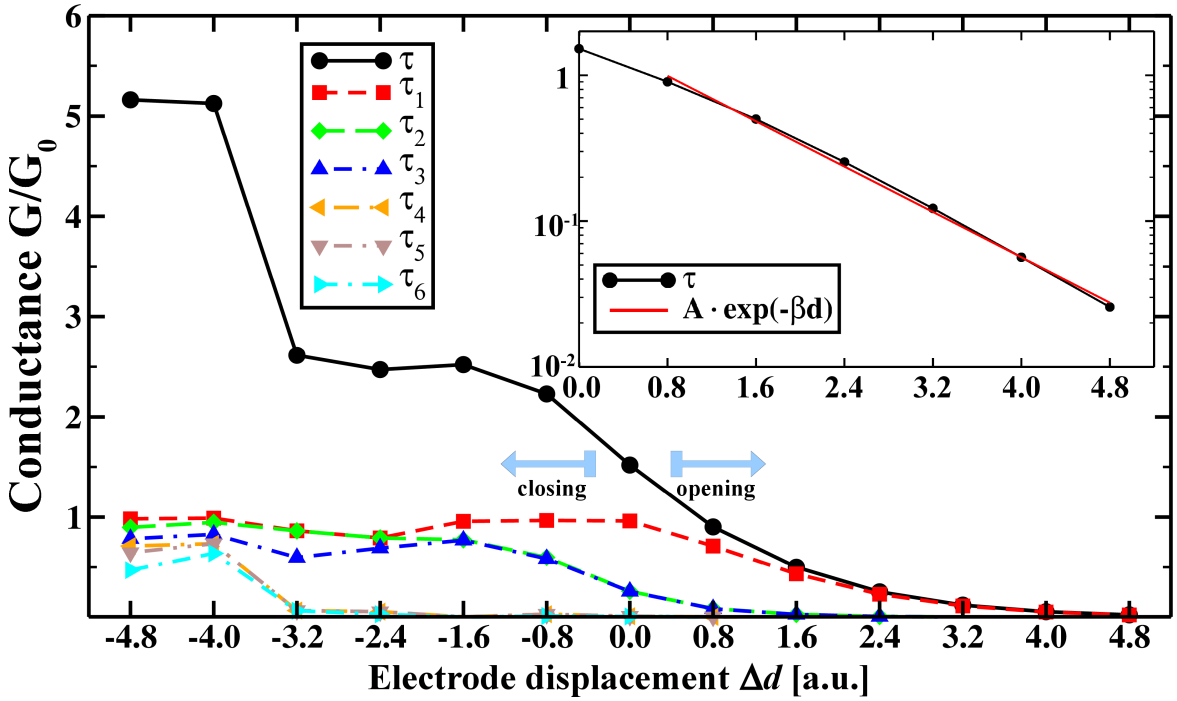

Fig. 6.14: Evolution of the transmission τ and of the six largest transmission channels $\tau_1 - \tau_6$ during the opening (closing) of the contact. We start to open (close) the contact at $d = 0.0$ a.u.. Positive electrode displacements $d > 0$ correspond to opening steps, negative electrode displacements $d < 0$ to closing steps, respectively.

6.3.3 Inelastic current

For the Al junctions we consider the same partitioning of the ECC as for the Pb contacts iSection 6.2.3. We do relax all the atoms in C, but restrict the dynamic region to the 7 central atoms (Fig. 6.5). As discussed in Section 6.3.2, the elongation process of the Al contact can basically be divided into three stages, namely two plateau-like and the tunneling regime.
First we will consider the crossover from the tunneling regime to the plateau with constant transmission. In Fig. 6.15 the IETS calculated for the geometries at $d = 0.0$ a.u. and at $d = -0.8$ a.u. are shown. Here we have assumed a temperature of $T = 1$ K, to resolve all the signatures of the individual vibrational modes in the IETS. The form of the vibrational modes contributing to the IETS are sketched in Fig. 6.16a for $d = 0.0$ a.u., and in Fig. 6.16b for $d = -0.8$ a.u. First we note that for $d = 0.0$ a.u. the vibration modes are mainly localized either on the left, or on the right electrode (Fig. 6.16a). This is in contrast to $d = -0.8$ a.u., where the vibrations are mostly localized on both electrodes simultaneously (Fig. 6.16b).
For $d = 0.0$ a.u., the IETS signals in the low energy range between 6.5 meV and 13.5 meV are due to the transversal modes v1-v4. They couple mainly to the π-symmetric transmission channels 2 and 3 (Fig. 6.12). The coupling of the transversal vibrations to the channels τ_2 and τ_3 leads to an increases of the transmission ($\mathrm{d}^2I/\mathrm{d}V^2 > 0$). The negative IETS signals between 16.50 meV and 20.60 meV correspond to the longitudinal vibrational modes v5-v8. They couple mainly to the σ-channel τ_1. The modes with higher energy yield just small signals in the IETS. For $d = -0.8$ a.u. we can observe a

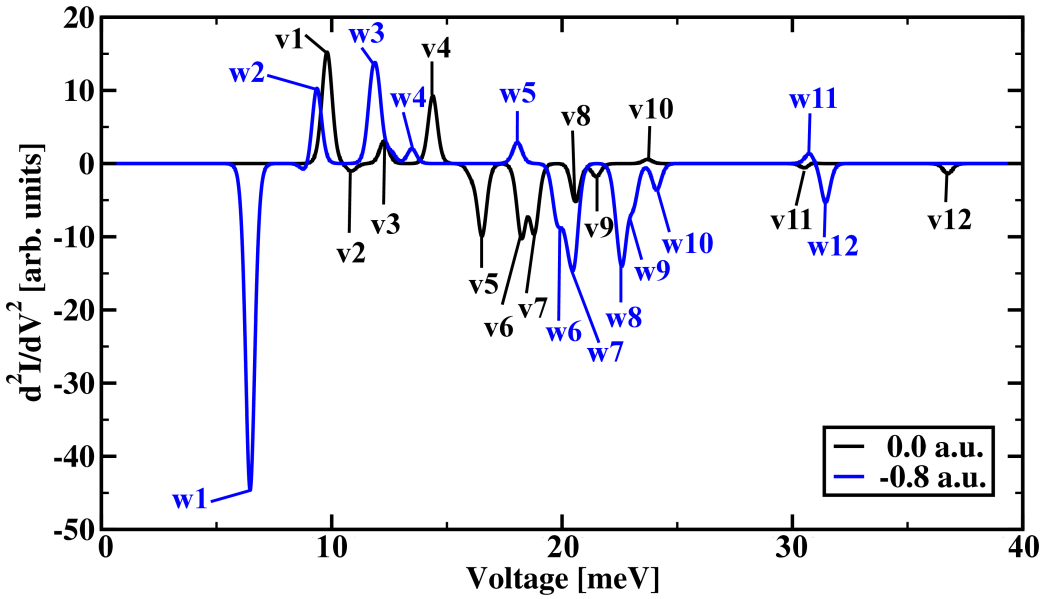

Fig. 6.15: IETS, calculated at $T = 1$ K, for $d = 0.0$ a.u. and for $d = -0.8$ a.u.. The assigned modes are shown inFig. 6.16.

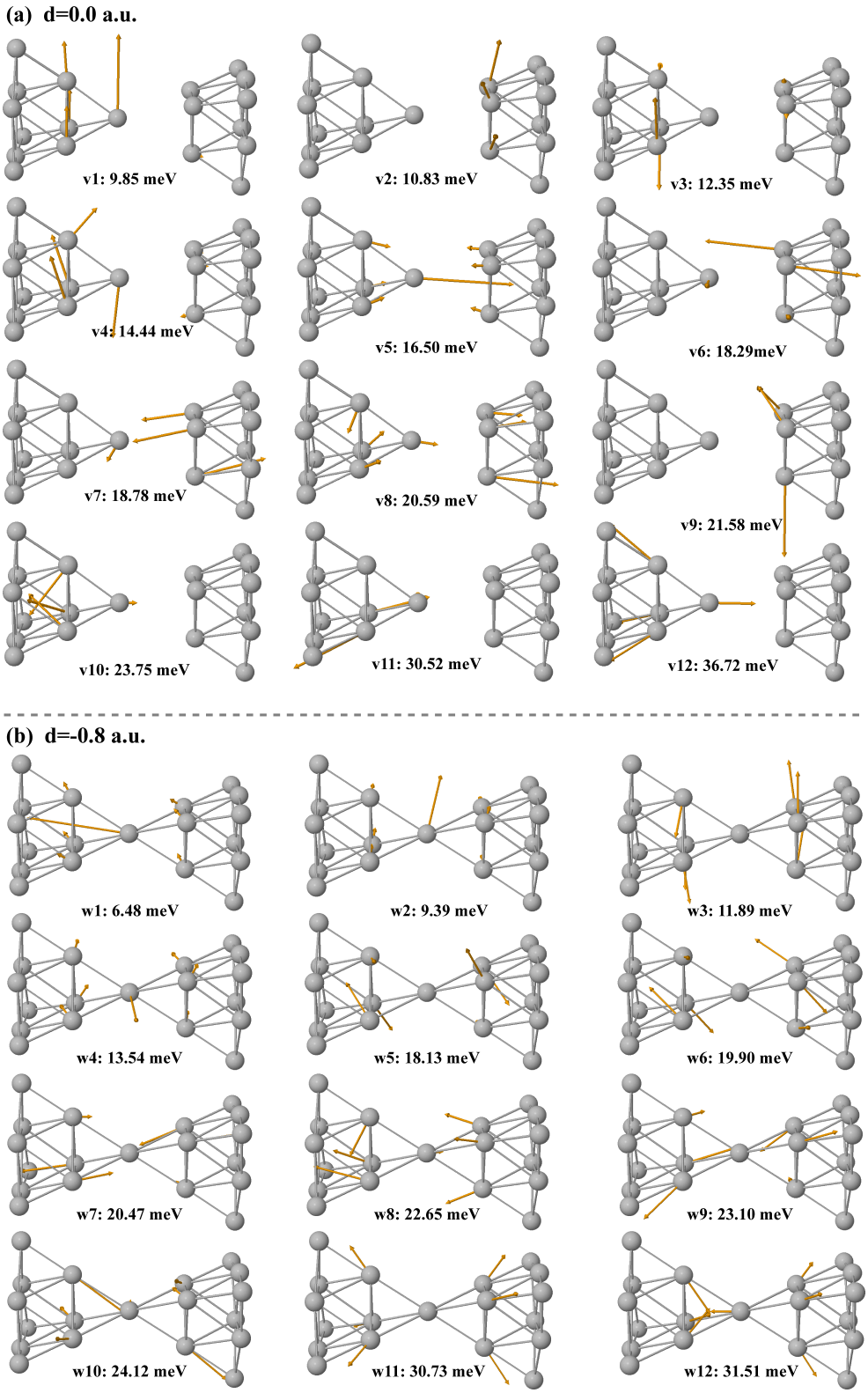

Fig. 6.16: Vibrational modes, which give rise to signals in the IETS. The displayed modes are for the geometry at (a) $d = 0.0$ a.u. and (b) $d = -0.8$ a.u.. The atoms belonging to L and R have been omitted.

prominent peak with $\mathrm{d}^2I/\mathrm{d}V^2 < 0$ at 6.48 meV. For $d = 0.0$ a.u. this peak is absent. These signal corresponds to a strong longitudinal vibration of the tip atom (w1), which couples strongly to the σ-channel τ_1 (Fig. 6.12). The transversal vibrational modes, w2-w4, have comparable energies as the transversal modes v1, v3 and v4 and they yield similar signals in the IETS. The remaining modes are blue shifted as compared to $d = 0.0$ a.u.. However, it is not possible to unambiguously characterize these modes, because they are often a combination of longitudinal and transversal vibrations.
In order to compare to the experimental results of Ref. [89], we assume in the following a temperature of $T = 10$ K. A comparison between the IETS calculated at $T = 1$ K and $T = 10$ K is shown in the insets of Fig. 6.17a ($d = 0.0$ a.u.) and Fig. 6.17b ($d = -0.8$ a.u.). We can see that the individual features are largely smeared out at $T = 10$ K. However, it is still possible to attribute the broad peaks to transversal or longitudinal modes, because they are well separated in energy.
Next we consider electrode separations between $d = 0.0$ a.u. and $d = 4.0$ a.u.. As indicated in Fig. 6.17a, the peak centered at 11 meV, corresponds to the transversal vibrations v1-v4. The peak position remains constant during the opening of the contact. The amplitude of the peak decreases with increasing d. The peak position, at the constant energy of 11 meV and the decrease of the peak amplitude upon opening of the contact correspond well to the experimental findings of Ref. [89]. The negative IETS signal of the longitudinal modes experiences a blue shift of around 4 meV during the opening of the contact, shifting from 18 meV ($d = 0.0$ a.u.) to 22 meV ($d = 4.0$ a.u.). These vibrations could not be observed in the experiments of Ref. [89]. However, as argued there, it was not possible to determine the exact structure of the IETS for these energies due to additional signals of bulk phonons. Furthermore, it seems that the "1/2 rule" is not valid here. Irrespective of the transmission probability of the individual channels, we observe for transversal modes always an increase and for longitudinal modes always a decrease of the conductance. However, in Refs. [91] and [92] it was shown that the "1/2 rule" is strictly valid just for a very narrow parameter regime. For example, the "1/2 rule" assumes a symmetric coupling of the central part to the left and right electrodes. This does presumably not hold for the asymmetric junctions analyzed here.
In the IETS of the contact with $d = -0.8$ a.u. we observe a prominent peak at 6.48 meV corresponding to the longitudinal vibration w1 (Fig. 6.17b). Low energy longitudinal modes in the range of 6 – 11 meV have also been observed in the experiments of Ref. [89]. If the contact is closed further, the longitudinal vibration w1 disappears again (Fig. 6.17b). Moreover, the structure of the IETS below 20 meV changes in every elongation step. For energies above 20 meV we always observe the signatures of the longitudinal modes. As indicated in Fig. 6.17b, they experience a substantial blue shift of around 15 meV with the closing of the contact. The amplitude of the peak, corresponding to the modes w7-w10, decreases with decreasing d. The peak corresponding to the longitudinal vibration of the tip atom (w12), increases during the closing of the junction.

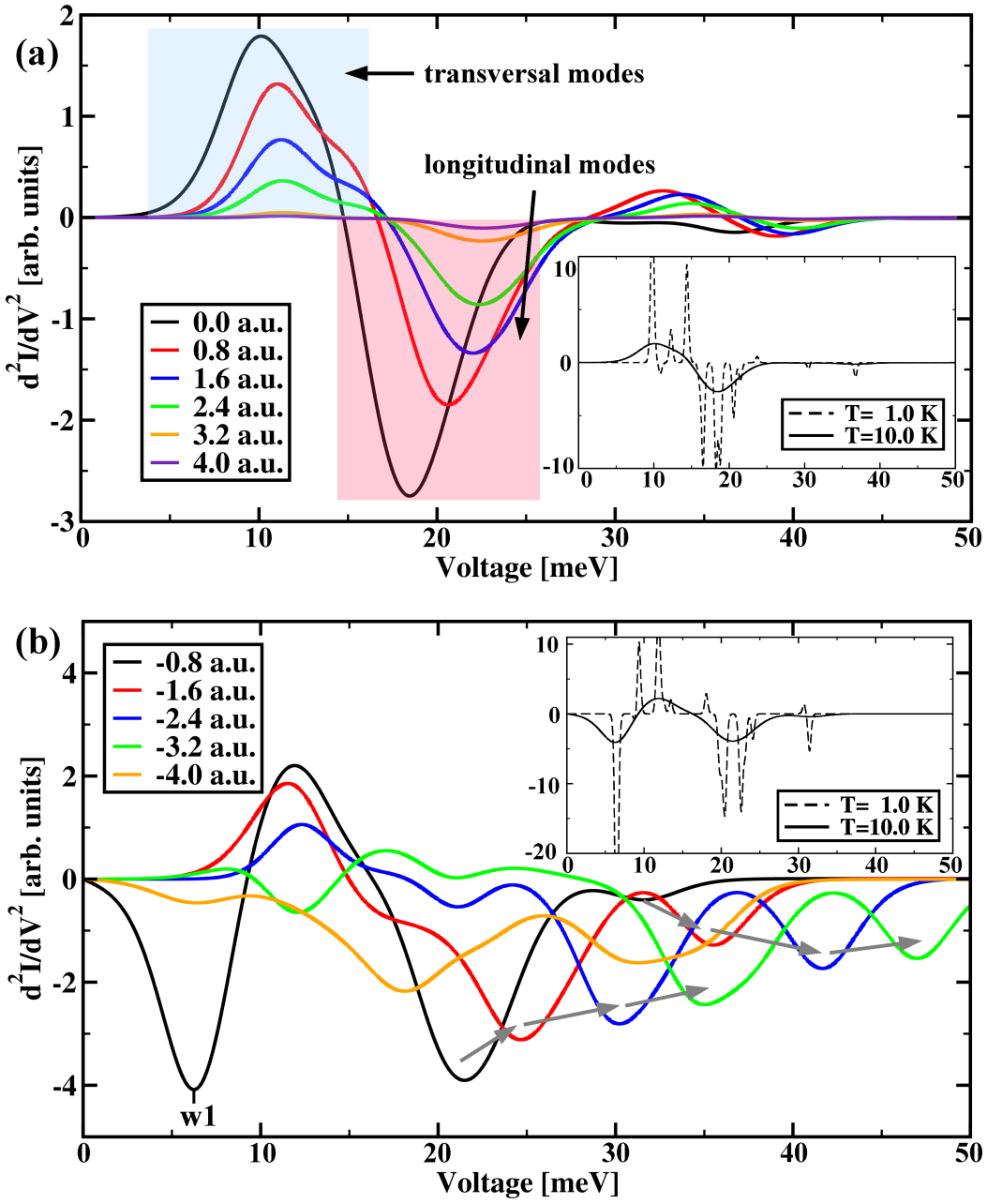

Fig. 6.17: (a) IETS, calculated at $T = 10\,\mathrm{K}$ for the elongation stages $d \geq 0.0\,\mathrm{a.u.}$. The blue shaded area indicates signals corresponding to transversal modes, while the red shaded area indicates signals originating from longitudinal modes. The inset shows the IETS for $d = 0.0\,\mathrm{a.u.}$, calculated for $T = 1\,\mathrm{K}$ and for $T = 10\,\mathrm{K}$. (b) IETS, calculated at $T = 10.0\,\mathrm{K}$ for the elongation stages $d \leq -0.8\,\mathrm{a.u.}$. The arrows indicate the shift of the longitudinal peaks with decreasing d. The inset shows the IETS for $d = -0.8\,\mathrm{a.u.}$, calculated for $T = 1\,\mathrm{K}$ and $T = 10\,\mathrm{K}$.

6.4 Comparison between Pb and Al junctions

For Pb as well as for Al, we could connect their valence structure to the transmission channels of the single-atom junctions. We found for both metals three dominant transmission channels.One channel is of σ-character and is formed from the hybridized s-p_z orbitals. The two other channels are degenerate combinations of the p_x and p_y orbitals, hence they are of π-character. For Pb all three channels are almost completely transparent. In contrast to Al, where just the σ-channel is perfectly transmitting. The two degenerate π-channels are only partially open. Their transmission probability is around0.25.

The opening curve differs qualitatively between Pb and Al. For Pb we find that the conductance remains almost constant until the contact breaks. This is opposed to the Al junction, for which the conductance decays exponentially with increasing electrode separation. Jumps in the conductance during the closing of the contact could be attributed to the (partially) opening or closing of transmission channels, due to atomic rearrangements when the contact is plastically deformed.

The vibrational energies are for both systems of the order of several meV. For Al the vibrational energies range between 6.5 meV and 32 meV. Compared to 3.7 meV and 13 meV for Pb, they are on average around factor of two larger. During the initial elastic elongation stage of the Pb junction the energy of the transversal modes remains constant. The longitudinal modes, on the other hand, are red shifted with increasing electrode separation. However, the qualitative character of the modes is preserved until the contact rupture. For Al we observe a similar behavior in the region where the conductance decays exponentially. However, during the closing of the contact, the IETS changes qualitatively, even though, the contact is not plastically deformed.

Part IV

Transport through organic molecules

7 Introduction

In this part we are concerned with the charge transport properties of metal-molecule hybrid systems. As mentioned in the very beginning of this thesis the precise atomistic details inside the molecular junction and especially the properties of the metal-molecule interface have a strong influence on the transport properties. Achieving a larger degree of control over these details is an important topic in the current research in molecular electronics.

Therefore we explore the influence of different anchoring groups on the transport properties for two distinct classes of molecules. The first class are aliphatic octane-based systems (Section 8), namely octance-dithiol (ODT), where sulfur (S) linkers are used and octance-diamine (ODA), where amino (NH_2) groups serve as linkers to the Au electrodes. In these rather linear molecules the electron transport proceeds through the σ-bonds between the carbon atoms. Accompanying experiments conducted in the group of Elke Scheer et al., we are simulating IETS for ODT and ODA. These simulations support the experimental findings that ODT is much stronger bonded to the Au electrodes than ODA and that during the opening process thiol-anchored octanes cause deformations of the Au-contacts.

The second class are aromatic biphenyl-based molecules. In these molecules the charge transport is in most cases dominated by the π-electron system and depends strongly on the degree of π-conjugation. For these systems we are also concerned with the influence of the molecule-metal interface on conduction properties. We analyze different anchoring groups but take also different coordinations of the molecular anchors with respect to the Au-surface into account. On the other hand we study the influence of "internal" molecular properties on the conductance, namely the torsion angle φ between the two phenyl rings. The reduction of the π-π coupling between the two phenyl rings with increasing φ leads to a decrease of the π-conjugation.
In Section 9.2 we show for biphenyl-dithiol (BPDT) molecules that variation of the S-Au coordination can lead to large changes of the conductance. This is explained by the different degree of hybridization between molecular orbitals and states in the electrodes and by the difference in the charge transfer onto the molecule for the different binding sites. However, independent of the S-Au coordination we find that the conductance decreases as $\cos^2 \varphi$ with increasing torsion angle φ. The findings are illustrated by means of transmission eigenchannels.
In Section 9.3 we are considering nitrile (CN) anchored biphenyls. In collaboration with

the experimental group of Thomas Wandlowski from the University of Bern we showed that CN, in contrast to S, binds selectively to the Au-electrodes and gives therefore rise to well-defined peaks in the conductance histograms. The bond between the CN anchor and the Au surface is formed via the nitrogen lone-pair and we find that only bonds to At atoms with a low coordination are stable. Furthermore the electron-donating nature of CN leads to electron transport through the lowest unoccupied molecular orbital (LUMO).
In Section 9.4 the focus lies on the thermoelectric properties of the biphenyl-based molecular junctions. We are calculating the junction thermopower (Q) for thiol, amine, and nitrile linked biphenyl-gold-junctions. The anchoring groups play here a crucial role for the sign and well as for the absolute value of Q. We also explore the influence of the π-conjugation on Q. We show that Q decreases as $\cos^2 \varphi$ with increasing φ. The observed variations are within experimental resolution. Hence we are providing a proposal for future experiments concerned with thermoelectric effects in aromatic molecules.

8 Elastic and inelastic transport through octane molecules

8.1 Experimental motivation

Comparing the experimental results ofElke Scheer et al. with our theoretical calculations we analyze the charge transport through single-molecule junctions with respect to the influence of molecular end groups. For both amine-ended and thiol-ended octanes contacted to gold electrodes, we study signatures of chain formation by analyzing kinks in conductance traces, the junction length, and inelastic electron tunneling spectroscopy (IETS). We try to gain further insight into the underlying processes during the opening of the contact, by simulating the junction stretching. The results show that for amine-ended molecular junctions no atomic chains are pulled under stretching, whereas the Au electrodes strongly deform for thiol-ended molecular junctions. This provides evidence that the amine anchors bind only weakly to Au. The relevant vibrational modes for transport are characterized by comparing experimental and calculated IETS. Thereby we focus on the signatures of the S-Au and NH_2-Au vibrations to gain further insight into the properties of the molecule-metal interface. The S-Au vibration frequency remains roughly constant during the junction stretching, due to the deformation of the contact, contrary to the N-Au mode which experiences a red shift until the rupture of the N-Au bond. This can be attributed to the different strengths of the S-Au and N-Au bonds and further supports that amine anchors bind much weaker to Au than S linkers.

8.2 Linear conductance and opening curves

To gain insight into the processes occurring during the opening of the molecular junctions, we performed simulations of the stretching of ODT and ODA single-molecule junctions using a DFT-based scheme. We model the ECC of the ODT and ODA junctions by two Au clusters of 20 atoms on the left and the right bridged by the respective molecule. The clusters resemble ideal Au $\langle 111 \rangle$ pyramids and represent the tips of the semi-infinite Au electrodes. The molecules are connected to the tip atoms of the pyramids via their anchoring groups. Starting from the geometries headed "0.00 Å", we separate the electrodes to the left and right symmetrically by a distance of 0.105 Å in each step as shown in Fig. 8.1a,b. While we keep the two outermost Au layers fixed in this process, we relax the complete inner part of the junction, as indicated in Fig. 8.1a,b. In this way, we simulate an adiabatic stretching trajectory with equilibrium junction geometries for all the elongation stages. As displayed in Fig. 8.1a, we observe strong deformations of the Au electrodes upon stretching for ODT junctions. In particular, atomic Au chains are being pulled. For the ODA junctions shown in Fig. 8.1b, we do not find the formation of Au atomic chains. Indeed the Au electrodes remain intact in

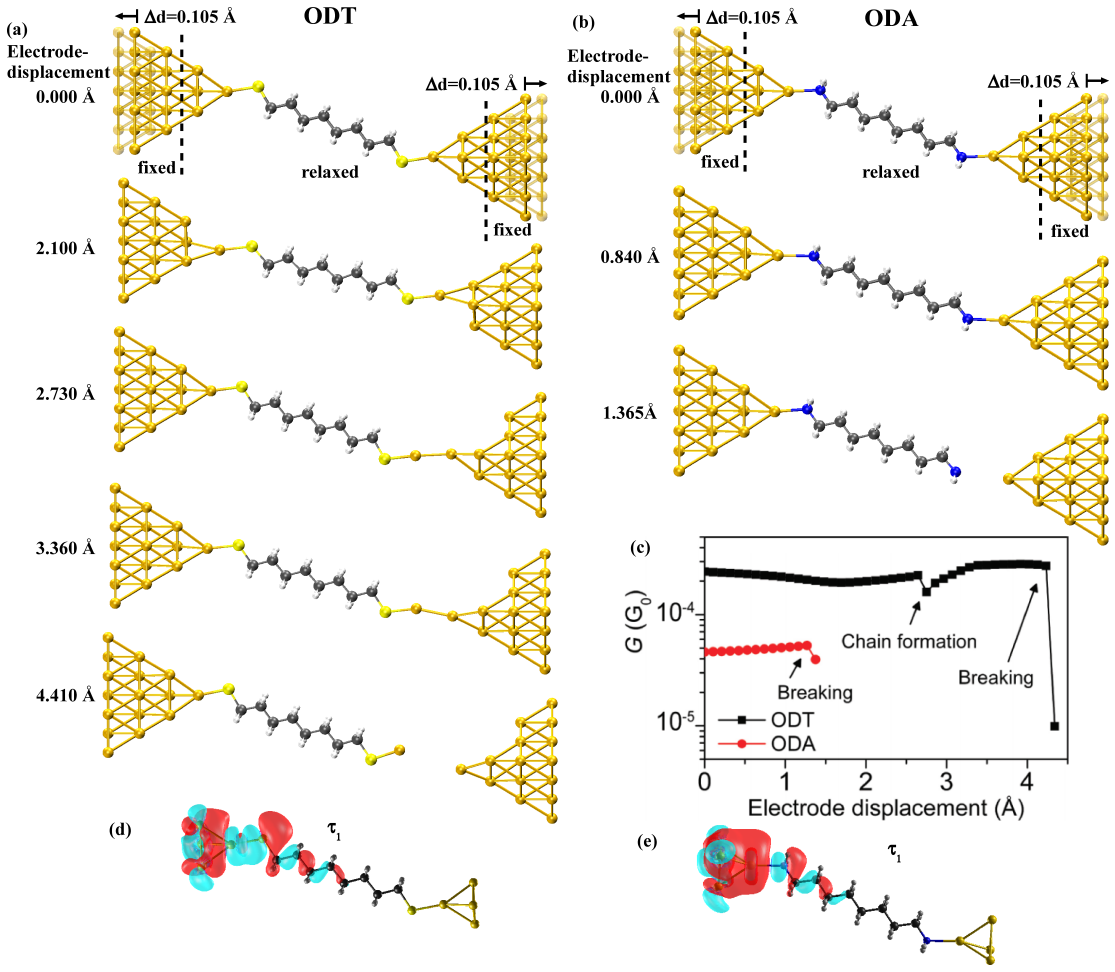

Fig. 8.1: Junction geometries for both anchoring groups, ODT (a) and ODA (b) at different electrode displacements. (c) Evolution of the elastic conductance. The dominationg transmission channel is of σ-character for both anchoring groups, displayed for ODT in (d) and for ODA in (e).

their initial geometries during the stretching process. This is a result of the lower binding energy of the Au-N bond (0.92 eV) as compared to the Au-S (1.76 eV) and the Au-Au bonds. Besides the equilibrium structures at the different elongation stages, we determined the conductance and find it to range between $1 \times 10^{-4} G_0$ and $3 \times 10^{-4} G_0$ for ODT contacts. As indicated in Fig. 8.1c it is possible to observe signatures of the chain formation in the conductance. The chain formation, starting at a electrode displacement of 2.730 Å, leads to a abrupt decrease of the conductance. With further stretching the conductance increases again until it saturates at around $3 \times 10^{-4}\, G_0$ and drops suddenly at the contact rupture. For ODA the conductance is between $4 \times 10^{-4} G_0$ and $6 \times 10^{-5} G_0$, as shown in Fig. 8.1c. Compared to the experiment, the conductance is overestimated in both cases by a factor of around 3. This may be related to uncertainties in the de-

scription of the alignment of the molecular states and the metal Fermi energy, as well as the band gap problem of DFT [38, 39, 66]. However, the deviations appear acceptable considering the lack of knowledge with respect to the precise contact geometry. The reduced conductance, by a factor of around 5, for similar junction geometries of ODA as compared to ODT is in qualitative agreement with the experimental observations and previous reports in the literature [93, 94]. We find that the transport for both ODT and ODA is dominated by one transmission channel formed from the σ-bonds between the carbon atoms Fig. 8.1d,e.

8.3 Inelastic Electron Tunneling Spectroscopy

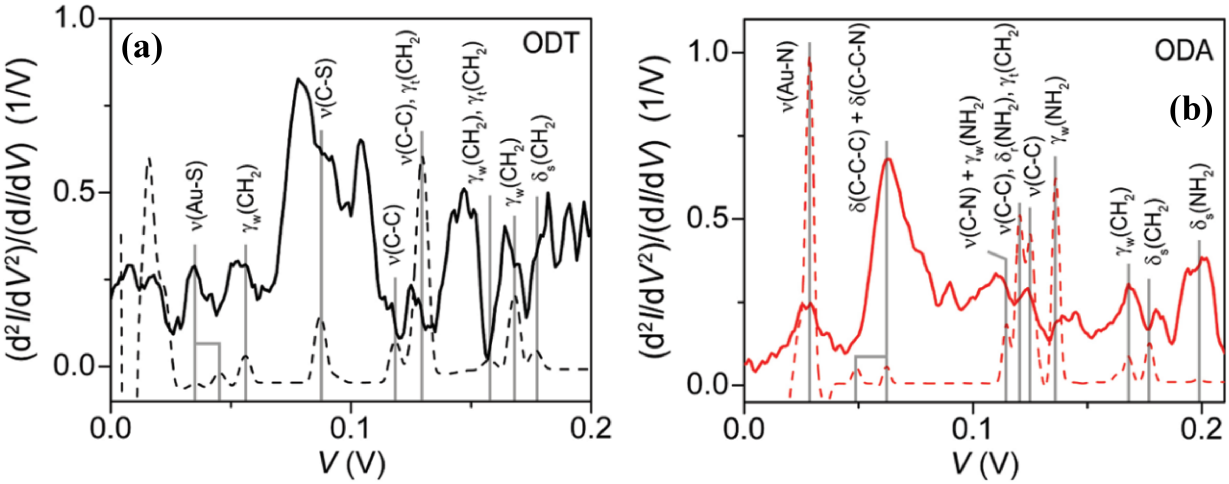

Fig. 8.2: Comparison of experimental (solid lines) and theoretical (dashed lines) IETS spectra of (a) ODT and (b) ODA single-molecule junctions. The character of the modes is specified by the symbols explained in the text. The separation by a comma means that the peak is due to several modes, while "+" is used to indicate the mixed character of a mode.

Following the experiments, we calculated the IETS at $T = 4.2\,\mathrm{K}$ and we broaden it by an ac voltage of 6 mV (root-mean-square) [95, 96]. We normalize the second derivative of the IV curves ($\mathrm{d}^2I/\mathrm{d}V^2$) with the dfferential conductance ($\mathrm{d}I/\mathrm{d}V$) in order to compensate for the conductance change due to distance changes of the electrodes. Hence, the IETS amplitude is defined as $(\mathrm{d}^2I/\mathrm{d}V^2)/(\mathrm{d}I/\mathrm{d}V)$ [97, 98]. With changing electrode distance the measured IETS spectra vary; that is, peaks vary in height and positions. The positions may shift by some 10mV due to the changes in the junction geometry. Fig. 8.2a and b shows measured IETS spectra of Au-ODT-Au and Au-ODA-Au junctions, respectively. In the low-energy regime of the IETS spectra, i.e., below 200 mV (which is regarded as the "fingerprint regime" of a molecular junction because the fundamental vibrational modes typically fall in this energy range), prominent molecular

vibrational peaks are observed for both ODT and ODA molecular junctions. Due to the many modes below 25 mV, these energies are excluded from the discussion. We characterize the vibrational modes both by performing DFT calculations of the eigenmodes of the molecular junctions and by computing IETS spectra by means of a lowest order expansion in the electron-vibration coupling (see Section 4.3). In this way, we determine peak positions, peak heights, and the evolution of vibrational energies during the stretching of the molecular contacts. We show them as the dashed lines beside the experimental spectra in Fig. 8.2. The main character of those modes is indicated, which are responsible for the peaks in the calculated spectra. Since the theoretical IETS spectra have been calculated close to our starting geometries (see the geometries with an elongation of 0.00 Å in Fig. 8.1), we compare them to experimental spectra taken from the middle part of stretching experiments, because in this situation a straight, but not strongly elongated molecular junction can be assumed. Those modes identified by the comparison between theory and experiment are summarized in Table 1. According to our analysis, the peak at around 35mV in Fig. 8.2a results from the ν(Au-S) stretching mode and those at 29 mV in Fig. 8.2b from the ν(Au-N) stretching mode. They signal that both amine and thiol end groups are robustly bonded to the Au atomic electrodes. Further main peaks in the experimental IETS at around 53, 78, 125, 164, and 182 mV for the Au-ODT-Au junction are attributed to $\gamma_w(CH_2)$ wagging, ν(C-S) stretching, ν(C-C) stretching and $\gamma_t(CH_2)$ twisting, $\gamma_w(CH_2)$ wagging, and $\delta_s(CH_2)$ scissoring, respectively, in accordance with previous studies [99, 100, 97, 101, 102, 103]. For the Au-ODA-Au junction we assign the main peaks at 63, 110, 124, 139, 168, 180, and 200mV to combined δ(C-C-C) and δ(C-C-N) bending, combined ν(C-N) stretching and $\gamma_w(NH_2)$ wagging, ν(C-C) stretching, $\gamma_w(NH_2)$ wagging, $\gamma_w(CH_2)$ wagging, $\delta_s(CH_2)$ scissoring, and $\delta_s(NH_2)$ scissoring, respectively. As expected, the higher energy modes above 100 meV, affecting mainly the C and H atoms of the molecule, appear at similar energies for ODA and ODT, however with different amplitudes. Modes including motions of the NH_2 groups appear in a broad energy range. We observe that some modes appearing in the experimental spectra are absent in the theoretical ones and vice versa. This discrepancy is due to the fact that only single spectra are compared, likely corresponding to different contact configurations. Choosing the peak at 104 mV in the spectrum of ODT as an example, it has been shown [104] that the $\delta_r(CH_2)$ rocking modes, to which we ascribe the peak, may be excited only in certain configurations, which lift particular symmetries. Other prominent features, not explained by our calculations, could be due to combined $\gamma_w(CH_2)$ wagging and $\gamma_t(CH_2)$ twisting modes at 147 meV for ODT and $\delta_r(CH_2)$ rocking modes at 90 meV for ODA. In summary, the detailed comparison of theoretical and experimental IETS reveals the complex interplay of molecular coordination and inelastic transport. Changing the anchoring group has an important influence on the vibrational spectrum and the possibility to excite modes electrically. In the following we shall concentrate on metal anchor group vibrations, and also the low-energy Au vibrational modes are discussed in this context below.

ODT modes[2]	description[2]	peak position[1] (mV) experiment	theory
ν(Au-S)	Au-S stretching	35	35, 45
$\gamma_w(CH_2)$	CH_2 wagging	53	56
ν(C-S)	C-S stretching	78	86
ν(C-C)	C-C stretching		118
ν(C-C), $\gamma_t(CH_2)$	C-C stretching, CH_2 twisting	125	130
$\gamma_w(CH_2)$, $\gamma_t(CH_2)$	CH_2 wagging, CH_2 twisting		157
$\gamma_w(CH_2)$	CH_2 wagging	164	168
$\delta_s(CH_2)$	CH_2 scissoring	182	178
ODA			
ν(Au-N)	Au-N stretching	29	29
δ(C-C-C)+δ(C-C-N)	C-C-C bending, C-C-N bending	63	50, 64
ν(C-N)+$\gamma_w(NH_2)$	C-N stretching, NH_2 wagging	110	115
ν(C-C), $\delta_r(CH_2)$, $\gamma_t(CH_2)$	C-C stretching, CH_2 rocking, CH_2 twisting		121
ν(C-C)	C-C stretching	124	126
$\gamma_w(NH_2)$	NH_2 wagging	139	137
$\gamma_w(CH_2)$	CH_2 wagging	168	169

Tab. 1: Summary of the Vibrational Mode Assignment in the IETS Spectra for ODT and ODA Molecular Junctions, Shown in Fig. 8.2.

8.4 Gold-Molecule Interface

According to our theoretical investigations, the binding energy of the Au-N bond (0.92 eV) is significantly weaker than those of the Au-S bond (1.76 eV) for the binding in top position [105, 106]. Indeed, in our simulations we find that this difference results in the pulling of Au chains for ODT (Fig. 8.1a) [107, 100], while they are absent for ODA (Fig. 8.1b). Fig. 8.1c shows an example of a calculated opening trace revealing a kink between two rather flat plateau regions at the moment when the Au chain starts to be formed. In the experiments, however, the conductance plateaus usually exhibit a negative slope throughout the whole stretching process. Therefore, we identify a kink by a change of the conductance distance slope from negative to positive, as shown by the arrow in Figure 1b. We use their appearance in the opening conductance as a signature of chain formation or, more generally, a mechanical deformation of the Au electrodes. In the experiments the signatures of chain formation during the stretching process occur mainly for thiol-linked molecules, whereas they are mostly absent for amine-linked molecules [108]. Moreover, the average plateau lengths upon stretching of Au-ODT-Au junctions (30 ± 11 Å) are significantly larger than those of Au-ODA-Au junctions (11 ± 3 Å) [108]. In the experiment, however, the apparent plateau lengths are much

[1]Peak positions in the spectra are identfied by our IETS calculations and previous IETS experiments and calculations for ODT [99, 100, 97, 101, 102, 103].

[2]When we separate modes by a comma, there are several contributing to the same peak. When we use "+" or "with", a single mode has a mixed character.

larger than those in the simulations. We observe from Fig. 8.1c that the electrode displacement of the ODT junction can be changed by ∼4.4 Å before rupture, while this displacement for ODA of ∼ 1.4 Å is clearly smaller. Although this agrees qualitatively with the differences in average single-molecule plateau lengths [108], the discrepancy between experiment and theory amounts to a factor of ∼ 10. We attribute this to the fact that we start in our calculations with rather straight molecules bonded to the ends of Au tips (see Fig. 8.1a and b). In the experiments, the molecules can be twisted and stretched upon elongation, or their anchoring group may "slide" along the metallic electrodes on both sides toward the tip ends. For ODT deformations of the metal electrode can arise in addition, which we cannot account for entirely in the calculations due to the limited amount of flexible atoms in the Au electrodes. Nevertheless, the experimental and theoretical results consistently suggest that strong mechanical deformations of the Au electrodes are involved for ODT, possibly including the formation of Au chains, while such deformations are essentially absent for ODA.

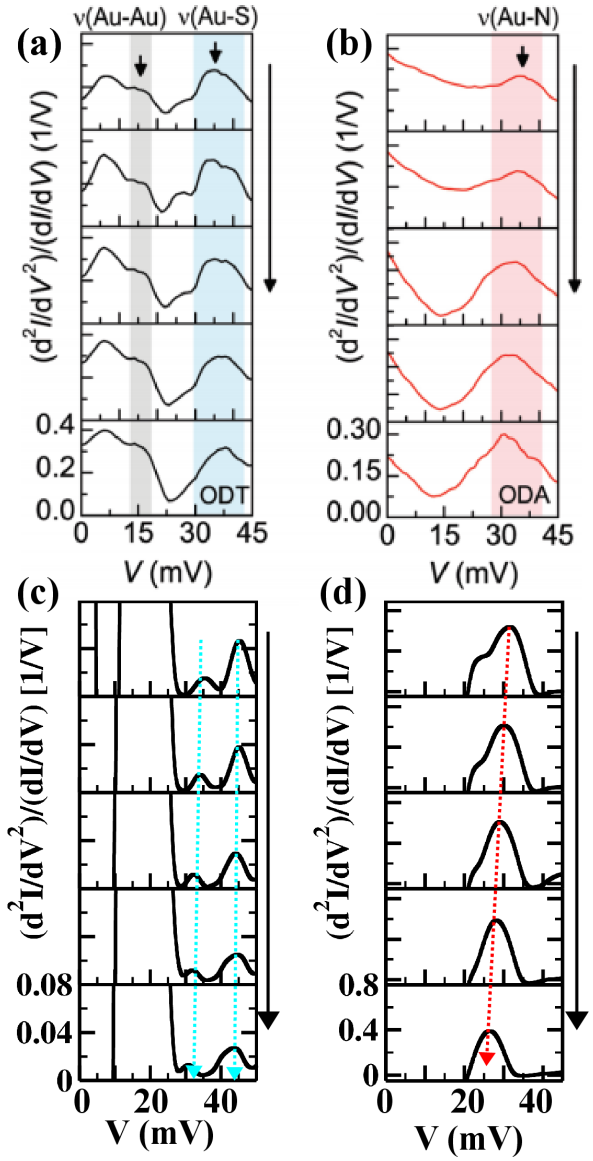

Fig. 8.3: (a,b) Experimental (c,d) theoretical evolution of the IETS spectra, for the stretching (in the order of the arrow) of a molecular junction containing ODT and ODA.

The different behavior of thiol ended and amine ended molecular junctions is further elucidated, when we compare the ν(Au-S) and ν(Au-N) vibrational modes in the IETS for increasing electrode separation in the lowest conductance regime. In Fig. 8.3a,b the experimental and in Fig. 8.3c,d the calculated IETS spectra below 45mV are presented for increasing stretching distance in the order from top to bottom. In Fig. 8.3a and c the ν(Au-S) mode is very stable, and no significant change of vibrational energy during the stretching of the junction can be noticed. Hence experiment and theory are consistent. In contrast, in the Au-ODA-Au junction

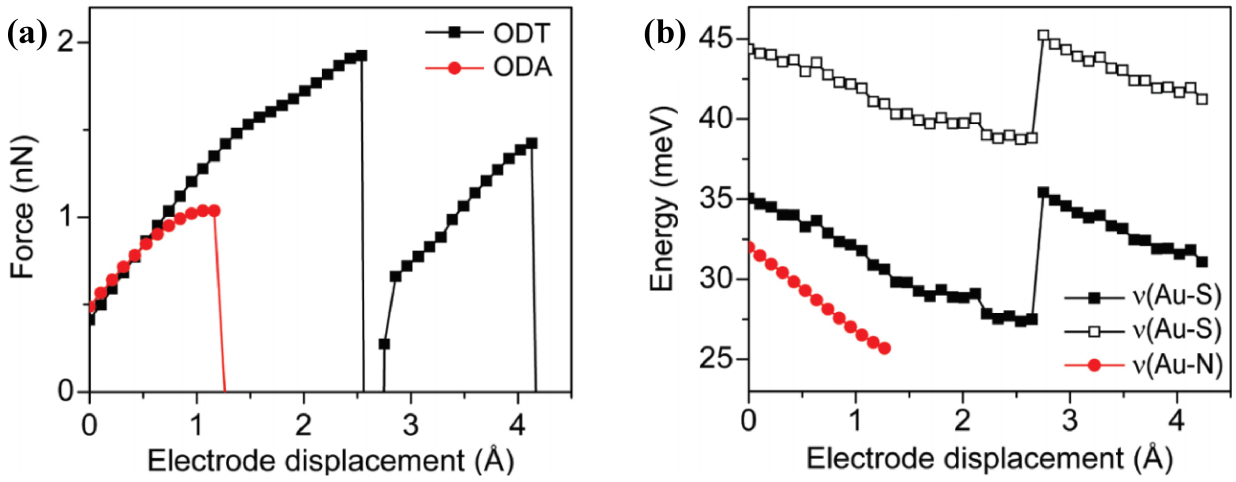

Fig. 8.4: (a) The tension force and (b) the vibrational energies of gold anchor group stretching modes as a function of the electrode displacement for ODT and ODA molecular contacts. The ν(Au-S) and ν(Au-N) modes shown are those causing the peaks in the calculated IETS spectra in Fig. 8.2.

of Fig. 8.3b and d, the energy of the ν(Au-N) mode is red-shifted by more than 5 mV with increasing electrode separation. This behavior is consistent with an increase of the Au-N bond length due to its weak bond strength, going along with the reduction of force constants.

In Fig. 8.4a we show the calculated evolution of the tension force during the stretching process, obtained as the derivative of the total energy with respect to the displacement distance. Elastic and plastic stages can be distinguished, where forces increase roughly linearly during the elastic stages. Finally, the stress is released abruptly in plastic stages by mechanical deformation of the gold electrodes or bond rupture. We note that for the ODT contact that breaks at an Au-Au bond, we obtain a breaking force of 1.5 nN, which is in good agreement with breaking forces measured for atomic chain geometries of Au atomic contacts [109]. In contrast, the breaking force for ODA contacts of 1 nN is lower. In Fig. 8.4b we plot the evolution of the energy of the ν(Au-S) and ν(Au-N) vibrations for ODT and ODA junctions, which lead to the peaks in the computed IETS in Fig. 8.2. We find a substantial red shift of the ν(Au-S) and ν(Au-N) vibrational energies upon stretching for both kinds of junctions (see Fig. 8.3b and Fig. 8.4b). The ν(Au-N) mode shows a behavior in good agreement with the experiment. In contrast, the decreasing frequency of the ν(Au-S) modes during the elastic stages does not comply with the experimental observations. However, we expect that the calculations underestimate the deformability of the Au electrodes due to the limited reservoir of mobile Au atoms assumed for practical reasons. Indeed, when stress is released by pulling gold atoms out of the electrodes in the plastic stages, we observe a "revival", i.e., an increase of the ν(Au-S) vibrational frequencies. Our theoretical findings hence support the experimental suggestion that the force constants of the Au-S stretching modes stay

effectively constant on the experimental time scales due to the mechanical deformations of the metal electrodes [108]. Overall, this comparison of ν(Au-S) and ν(Au-N) modes with the help of the experimental IETS measurements and theoretical calculations of IETS and vibration and binding energies clearly demonstrates that the Au-N bond is significantly weaker than the Au-S bond.

8.5 Conclusion

We performed calculations of IETS spectra, comparing to the measurements of the group of E. Scheer, for both Au-ODT-Au and Au-ODA-Au single-molecule junctions at 4.2 K using the MCBJ technique. We determined stable contact geometries under stretching, elastic transport properties, and inelastic electron tunneling spectra by considering the electron-vibration coupling perturbatively to lowest order. We presented for the first time inelastic transport data and the corresponding theoretical information for Au-ODA-Au junctions and found good agreement. Our results demonstrate that the amine-ended molecules bind only weakly to Au, in contrast to the thiol-ended ones. In particular, the strong Au-thiol bond causes major mechanical deformations of the Au electrodes including the pulling of Au chains, while such deformations are largely absent for the quickly breaking Au-amine bonds. These findings can play an important role for the controlled design of future molecular electronic devices.

9 Biphenyl-based single molecule junctions

9.1 Introduction

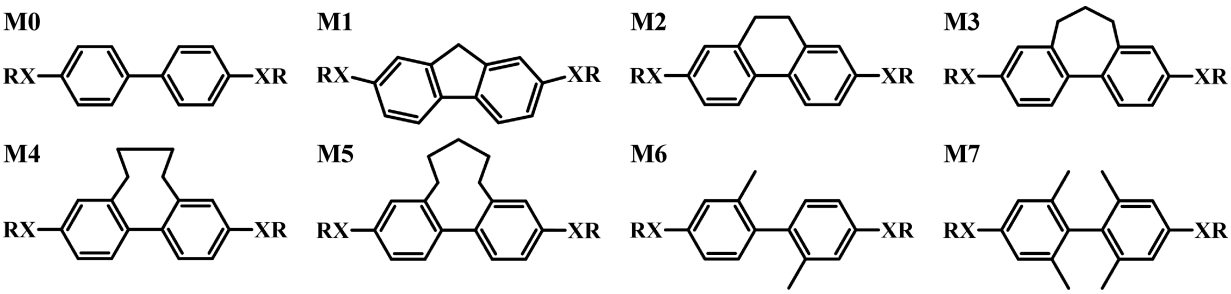

Figure 9.1: Chemical structure of the investigated molecules. Here RX = {S, NH_2, CN} stands for one of the anchoring groups used throughout this part and R represents the acetyl group for the synthesized form of the molecules, a hydrogen atom after the in-situ deprotection, or the Au electrode for the transport measurements.

In this section we present a systematic study of the transport properties of biphenyl-based molecules connected to gold electrodes. In this class of molecules the transport properties are mainly dominated by the π-electron system and depend strongly on the degree of the π-conjugation between the two phenyl rings. It was demonstrated recently [14, 110] that the degree of π-conjugation and hence the conductance can be controlled by the molecular conformation, namely the torsion angle φ between the two phenyl rings. Venkataraman et al. [14] showed for diamine terminated biphenyl molecules that φ can be changed by means of different chemical substituents and found that the conductance decreases as $\cos^2 \varphi$ with increasing φ. In this work we will consider the set of molecules displayed in Fig. 9.1 named here M0-M7. The molecular conformation is in difference to the work by Venkataraman et al., varied by the use of alkyl chains and methyl side groups. Using alkyl chains avoids largely substituent-related shifts of the molecular levels which are known to have a non-negligible influence on the conduction properties [111, 112, 113]. This will be especally important when we deal with the thermoelectric properties of the molecular junctions in Section 9.4.
The studies which we present in the following we give a comprehensive overview of the transport properties of biphenyl-based molecular junctions. The first two sections are concerned with the electric conductance through bipheny molecules and originate from the collaboration with the experimental group of Thomas Wandloski of University Bern.
In Section 9.2 we explored the conduction properties of biphenyl-dithiol (BPDT) molecules. We study a systematic set of contact geometries and place special emphasis on transport for perpendicular ring orientations. The conduction mechanisms are revealed by means of a tight-binding model (TBM), the more frequently used Lorentz

model (LM), and the eigenchannel decomposition of the conductance. Our calculations suggest that the coordination site ("top", "bridge", or "hollow") of the anchoring sulfur (S) atom at the Au surface plays a decisive role in conduction through the molecular junction.
In Section 9.3 discuss nitrile-terminated biphenyl molecules. In experiment they give rise to well-defined peaks in the conductance histograms as a result of the high selectivity of the N-Au binding. We study two stable binding sites of nitrile (CN) with respect to the Au surface. Our calculations show that the transport takes place through the tail of the LUMO which is in contrast to thiolated biphenyls were the conductance is HOMO dominated.
Besides the electric conductance which is explored in the first two sections, we will be concerned with thermoelectric properties of single-molecules in Section 9.4. We will determine the junction thermopower of sulfur, amine and cyano-terminated biphenyl molecules connected to Au electrodes. We find that the absolute value of the thermopower Q exhibits a weak $\cos^2\varphi$ dependence with a variation that is within experimental resolution. We show that the observed $\cos^2\varphi$ dependence is robust with respect to different anchoring groups and binding positions. The anchoring group determines the sign of the thermopower. Sulfur and amine give rise to $Q > 0$ and cyano to $Q < 0$, respectively. Different binding positions, on the contrary, lead to variations of the absolute values of the thermopower. The observed ab initio results are found to be described well by means of the TBM model introduced in Section 9.2. With the TBM we can explain the variation of the thermopower with respect to anchoring group and binding position by the different Fermi level alignment of molecular states and their broadening due to the electrodes.

9.2 Conductance properties of thiolated biphenyl-based molecules

9.2.1 Contact geometries

The statistical nature of the single-molecule conductance experiments [110] does not provide an a priori assignment of representative junction geometries. Therefore, we have decided to study three contact structures with different coordinations of the terminal sulfur atoms. The procedure adopted to determine the structure of the ECC is summarized in Fig. 9.2.

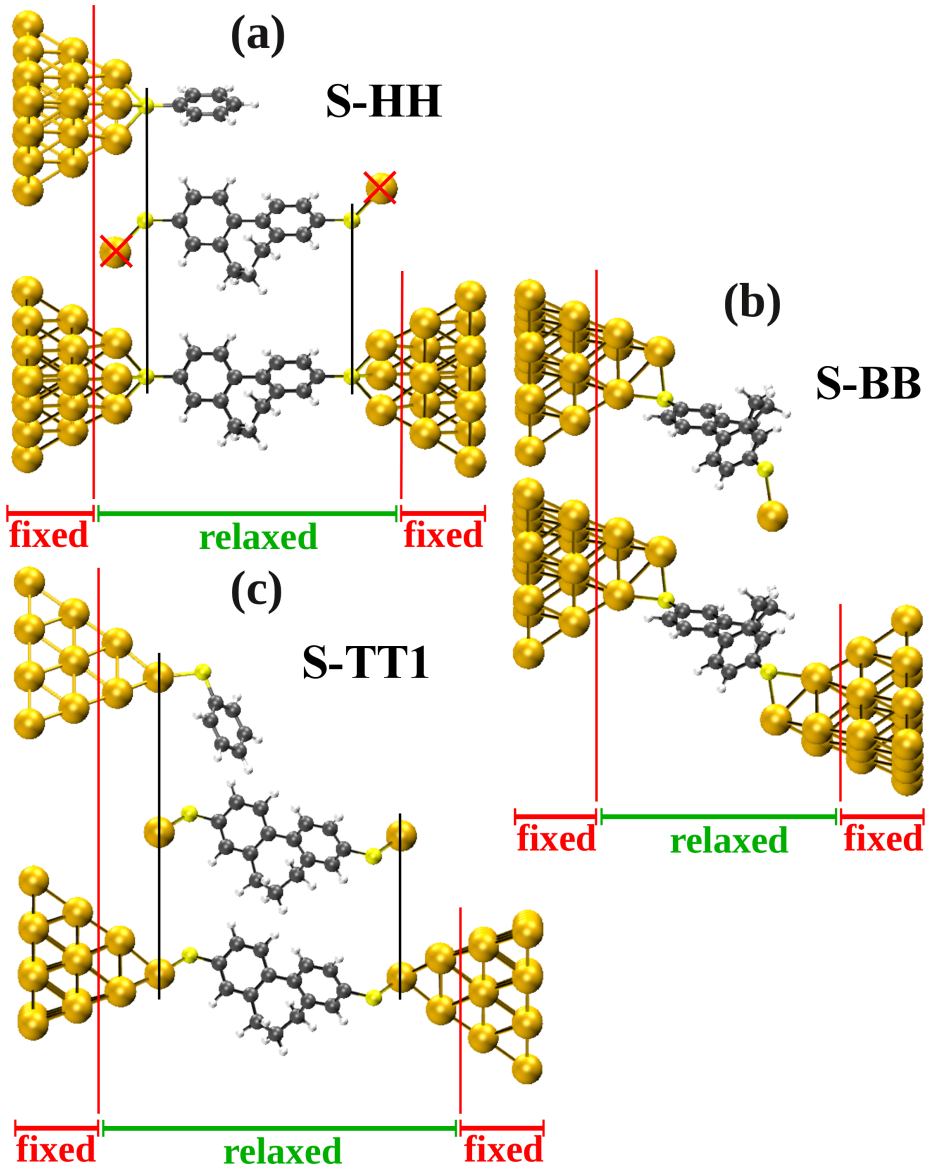

Fig. 9.2: Procedure used to set up the contact geometries for (a) S-HH, (b) S-BB, and (c) S-TT1 binding, respectively.

In order to model the molecular junctions, we connect the molecule to two Au ⟨111⟩ pyramids, both stemming from the same ideal fcc Bravais lattice. We consider the following three types: For hollow-hollow (S-HH) (Fig. 9.2a) the S atoms of the molecule are bound at each side to three Au atoms, for bridge-bridge (S-BB) (Fig. 9.2b) to two Au atoms, and for top-top (S-TT1) (Fig. 9.2c) to only a single Au atom. Junctions of the form HB, HT etc. should also occur in the experiments, but they are not considered here.
For the determination of the S-HH and S-TT1 geometries, we start from the gas-phase structure of each molecule (with SR=H in Fig. 9.1), replace the terminal H atoms by

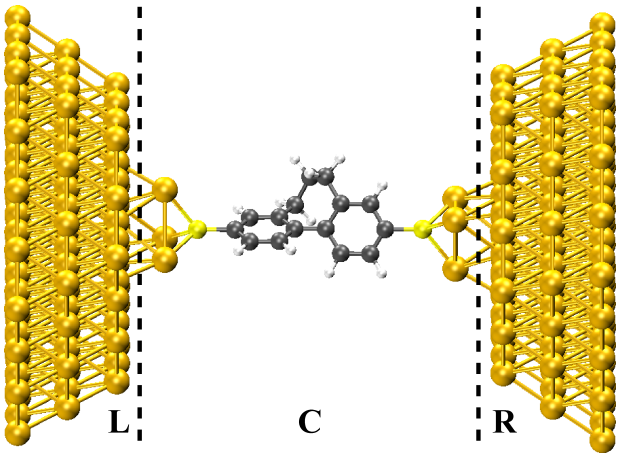

Fig. 9.3: Division of the ECC into the L, C, and R regions. A large number of gold atoms (around 120 in L and R, respectively) is used to represent the electrodes in the DFT calculations.

an S-Au_1 group (R=Au_1 in Fig. 9.1), and compute ground-state geometries. For S-HH contacts, the Au_1 atoms are removed. An Au_{19} cluster, resembling a Au $\langle 111 \rangle$ pyramid with a thiolated benzene attached, is computed separately. The cluster is positioned at each side of the BPDT such that the S atoms on top of the pyramids coincide with the S atoms of the molecule (Fig. 9.2a). To obtain the S-TT1 geometries, the molecule is oriented such that each Au_1 atom coincides with a tip atom of the Au_{20} pyramids (Fig. 9.2c). To determine the equilibrium structure for both S-HH and S-TT1, the inner part is relaxed and only the two outermost gold layers, consisting of 6 and 10 atoms, are kept fixed in the ideal Au fcc structure.

For the S-BB geometries we follow slightly different steps. First the terminal H atoms of the gas-phase molecules (with SR=H in Fig. 9.1) are replaced with S, one side is connected to a Au_{20} pyramid in bridge position, while the other one is terminated with Au_1. The outermost gold layers of the pyramid are kept fixed, while the rest is optimized. A second Au_{20} pyramid is finally added to the Au_1-terminated side, where the relative distances of the binding S atom with respect to the new Au_{20} cluster are chosen to be the same as for the S atom in bridge position at the Au_{20}-terminated side (Fig. 9.2b). Fixing again only the two outermost Au layers, the structure is optimized to determine the ground-state geometry.

We note that the contact geometries do not only differ with respect to the coordination of the sulfur atoms to the gold electrodes, but also in the stress exerted on the molecules. As visible in Fig. 9.2a, the $\langle 111 \rangle$ direction is located in the ring plane of a mono-thiolated benzene molecule on top of a Au pyramid. Since the S-S axis is along the same direction, the BPDT molecule is expected to adopt a minimum-energy configuration inside the S-HH junction with φ close to its gas-phase angle. In contrast, in the S-TT1 geometries the biphenyl derivative bridges the gold tip atoms, which are opposite to each other. In this case the sulfur atoms are deflected from their equilibrium positions, which would

be located along the $\langle 111 \rangle$ direction on top of the pyramids (Fig. 9.2c). In the geometry optimizations we find that the phenyl ring planes of the biphenyl molecules tend to align parallel to the surfaces of the pyramids. Since this may not be possible on both sides of the junction, some torque is exerted. Beside effects related to charge transfer, which may also be present for the S-HH contacts, geometric constraints thus yield an additional contribution to the change of the torsion angle. Similar effects as for S-TT1 are also present for the S-BB contacts, since the orientations of the phenyl rings with respect to the gold pyramids on both sides are generally different according to our construction.
We have determined binding energies by subtracting the total energy of the contact geometries from those of the frozen separate parts, namely the left and right Au clusters and the S-terminated biphenyl (without hydrogen on the sulfur atoms). With this procedure, we find the following averaged binding energies for the set of molecules: 5.9 ± 0.3 eV (S-HH), 2.9 ± 0.2 eV (S-BB), and 2.2 ± 0.2 eV (S-TT1). Hence, we find a trend of decreasing binding energies with decreasing coordination of the sulfur atoms to Au.
For reasons of computational feasibility, the structural optimizations (and calculations of binding energies) are carried out with Au pyramids consisting of 19 atoms for S-HH, and 20 atoms for S-TT1 and S-BB, respectively. To ensure a proper description of the Fermi-level alignment in the transport calculations, the gold pyramids are extended to 115 (S-HH) and 116 atoms (S-BB, S-TT1), as displayed in Fig. 9.3. All added atoms are positioned on the ideal fcc lattice with a lattice constant $a = 0.408$ nm, matching those of the fixed layers for the smaller pyramids. No further geometry optimization is carried out for contacts with extended Au pyramids, and transport properties are computed after a self-consistent, single-point DFT calculation.

9.2.2 Molecular Conformation

Fig. 9.4 shows the torsion angle between the two phenyl rings for the molecules as determined by X-ray measurements and by DFT calculations in the gas-phase as well as in the junction geometries.
We notice that gas-phase angles (with SR=H in Fig. 9.1) generally coincide well with the angles from the X-ray measurements [114, 115, 116]. The discrepancy for M6 by roughly 10° has been observed previously [110]. It is likely due to differences between gas-phase and crystal structures caused by the limited stabilization of the conformation, when there is just a single methyl group on each phenyl ring. Note that no X-ray structure measurement exists for M0.
For the contacted molecules deviations of φ from the gas-phase conformation are small for S-HH, but can be larger for the S-BB and S-TT1 geometries. This is expected from the discussion in Section 9.2.1. The conformation of the alkyl-bridged BPDTs M1 to M5 is very stable. A slight trend of increasing φ variations for the molecules with the longer, configurationally more flexible alkyl chains can be recognized, however. The torsion angles of M0 and M6 result from the balance between conjugation and modest steric

repulsion effects due to H atoms or single CH_3 groups in the ortho position with respect to the ring-connecting carbons [117]. Therefore, their φ should be rather sensitive to the geometric constraints in the contacts or the charge transfer between the molecule and the electrodes. As a result, deflections of φ from the gas phase values of up to 40° occur in the calculations. In contrast, the additional methyl side groups in M7 efficiently stabilize φ [117].

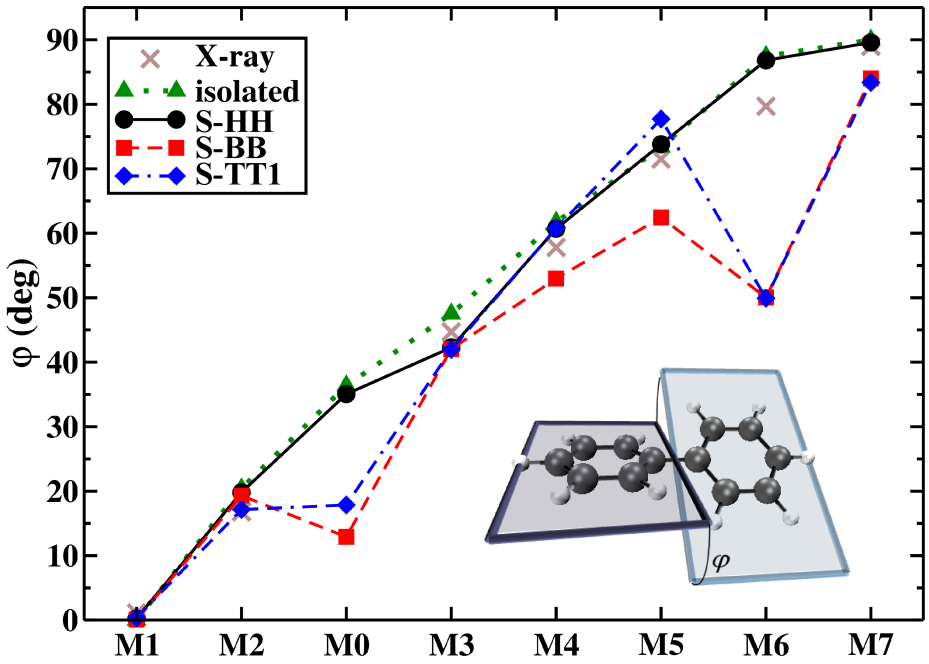

Fig. 9.4: Comparison of the torsion angle φ as determined from X-ray measurements and from DFT calculations in the gas phase (isolated; XR=H in Fig. 9.1) as well as in the molecular junctions (S-HH, S-BB, S-TT1; see Fig. 9.2).

9.2.3 Conductance

In Fig. 9.5 we present the computed conductance values as a function of the torsion angle φ, which the biphenyl molecules adopt in the optimized junction geometries.
On the linear conductance scale we find a reasonable $G = a\cos^2\varphi$ dependence for all binding situations with best fit coefficients[2] $a_{\mathrm{HH}} = 2.3 \cdot 10^{-2} G_0$, $a_{\mathrm{BB}} = 1.2 \cdot 10^{-1} G_0$, $a_{\mathrm{TT}} = 1.1 \cdot 10^{-1} G_0$. This behavior is characteristic for off-resonant charge transport dominated by π-π coupling and is consistent with the experimental observations. Fig. 9.6 shows, for the sample molecule M2, that irrespective of the coordination site, the transport is indeed off-resonant and dominated by the highest occupied molecular orbital

[2]We note that small differences in the slope values a as compared to Ref. arise from the study of a different junction geometry for S-TT1 and a slightly modified ECC for S-BB.

(HOMO) level.
The results suggest large variations in the conduction properties for the different coordination sites of sulfur to gold. The conductance of junctions with S-HH geometry is roughly one order of magnitude lower as compared to S-BB and S-TT1, with the sequence of slopes $a_{\mathrm{HH}} \ll a_{\mathrm{TT}} \approx a_{\mathrm{BB}}$. Similar behavior of the conductance of dithiolated aromatic molecules on binding site has been reported before by other authors [118, 119, 106].
For aliphatic alkane molecules, the conductance in the bridge-bonded configuration was reported to be higher than in the top-bonded one [120]. While these findings are compatible with our results in Fig. 9.5, transport through alkanes is σ-like [120, 102, 108] and hence differs substantially from the typical π-dominated transport through aromatic molecules. Beside the coordination of the anchoring group the molecular tilt, which determines the overlap of the delocalized π electrons with the electrode, hence plays a crucial role for the conductance of aromatic molecules [121, 122, 123]. We discuss these aspects further below. However, we note that our contact geometries do not allow us to clearly separate the effects of coordination site and tilt, since both are changed simultaneously.
With regard to absolute values, we observe that the calculated conductances are three (S-BB and S-TT1 geometries) and two (S-HH geometry) orders of magnitude higher than the experimental ones [115, 110]. We attribute this overestimation mostly to the interpretation of Kohn-Sham orbitals as approximate quasi-particle energies [124, 125]. However, also the experimentally measured conductances are subject to uncertainties. Indeed, we compare our results to the "typical" experimental values, as given by the peak position in a conductance histogram, and these peaks are rather broad. Further variations of molecular conductance, for example due to interactions of the molecules with the solvent and other close-by biphenyl molecules or the influence of vibrations, have not been accounted for in our calculations of static junctions in vacuum. The differences on a quantitative level remain as a major challenge for future work.
Finally, we note that our calculations do not reproduce the experimental deviation observed for M1 [110]. Since φ is unchanged upon contacting (see Fig. 9.4), we can exclude an explanation based on conformational changes, which would decrease the degree of conjugation and lead to reduced conductances. In spite of the slightly bent structure due to the short CH_2 bridge (see Fig. 9.1), the intact M1 shows the highest calculated conductances for all coordination geometries (see Fig. 9.5).

9.2.4 Analysis of transmission resonances

In order to understand better the charge transport through the BPDT single-molecule junctions, we analyze the transmission in terms of a TBM and a LM. We use the TBM of Ref. [126], which is sketched in Fig. 9.6a. It describes the delocalized π-electron system, relevant for transport away from the perpendicular orientation of the phenyl

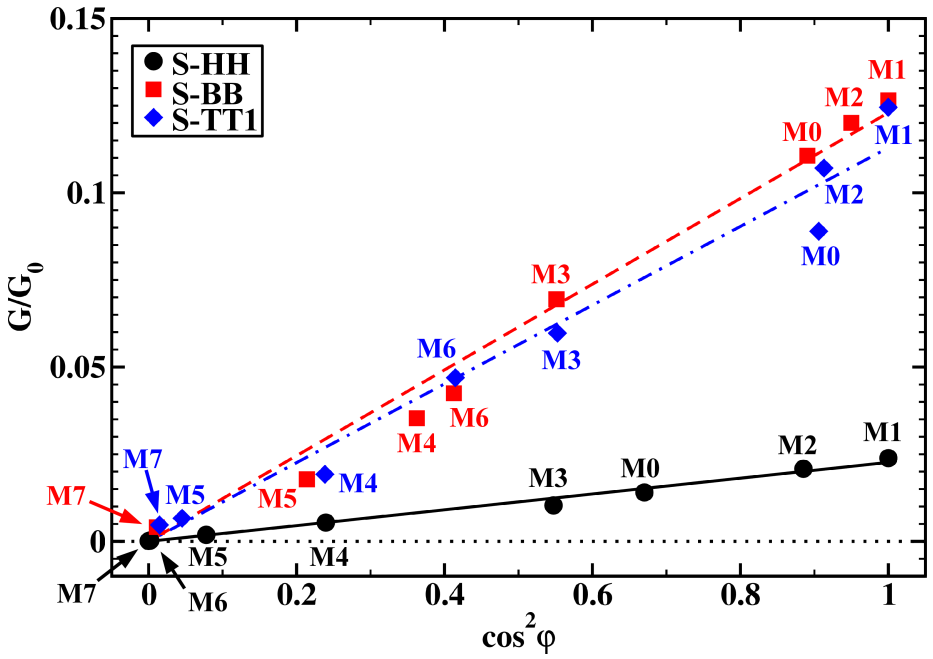

Fig. 9.5: Calculated conductance as a function of $\cos^2\varphi$ for the three types of contact geometries S-HH, S-BB, and S-TT1. The angles φ are those of the computed junction geometries. In all cases, lines show best fits for $G = a\cos^2\varphi$ with $a_{\mathrm{HH}} = 2.3\cdot 10^{-2} G_0$ (solid), $a_{\mathrm{BB}} = 1.2\cdot 10^{-1} G_0$ (dashed), $a_{\mathrm{TT}} = 1.1\cdot 10^{-1} G_0$ (dash-dotted).

rings. The Hückel-like, molecular Hamiltonian contains three parameters, namely the onsite energy ϵ_0 of each carbon atom, the hopping t between nearest-neighbor atoms on each ring, and the torsion angle φ, specific to the considered junction geometry. Together, t and φ determine the matrix element between the ring-connecting carbon atoms $t' = t\cos\varphi$. For the description of transport we make use of the wide-band approximation, according to which the retarded self energy Σ^r_X due to the coupling to the electrode $X = L, R$ is determined by the line-broadening matrix Γ_X as $\Sigma^r_X = -i\Gamma_X/2$. We assume a symmetric junction $\Gamma = (\Gamma_L)_{\alpha\alpha} = (\Gamma_R)_{\omega\omega}$ and, in line with the nearest-neighbor coupling in the molecule, consider the self energy to be nonvanishing only on the terminal carbon atoms α and ω of the biphenyl backbone (see Fig. 9.6a). The TBM is hence characterized by the four parameters φ, ϵ_0, t, Γ, where φ is fixed by the considered junction geometry.

The parameters of the LM are derived from those of the TBM. For that purpose we solve the non-Hermitian eigenvalue problem $\sum_k (H + \Sigma^r)_{jk} v^\mu_k = \lambda_\mu v^\mu_k$ and select the complex eigenvalues corresponding to the HOMO and the lowest unoccupied molecular orbital (LUMO). In the eigenvalue equation H_{jk} and $(\Sigma^r)_{jk} = (\Sigma^r_L + \Sigma^r_R)_{jk}$ are the Hamiltonian matrix and the self-energy matrix of the TBM, respectively, and $\lambda_\mu = \epsilon_\mu + i\gamma_\mu$. We measure the real part of the complex eigenvalues with respect to the Fermi energy, introducing $\tilde{\epsilon}_H = \epsilon_{HOMO} - E_F$ and $\tilde{\epsilon}_L = \epsilon_{LUMO} - E_F$. Due to the symmetries of the

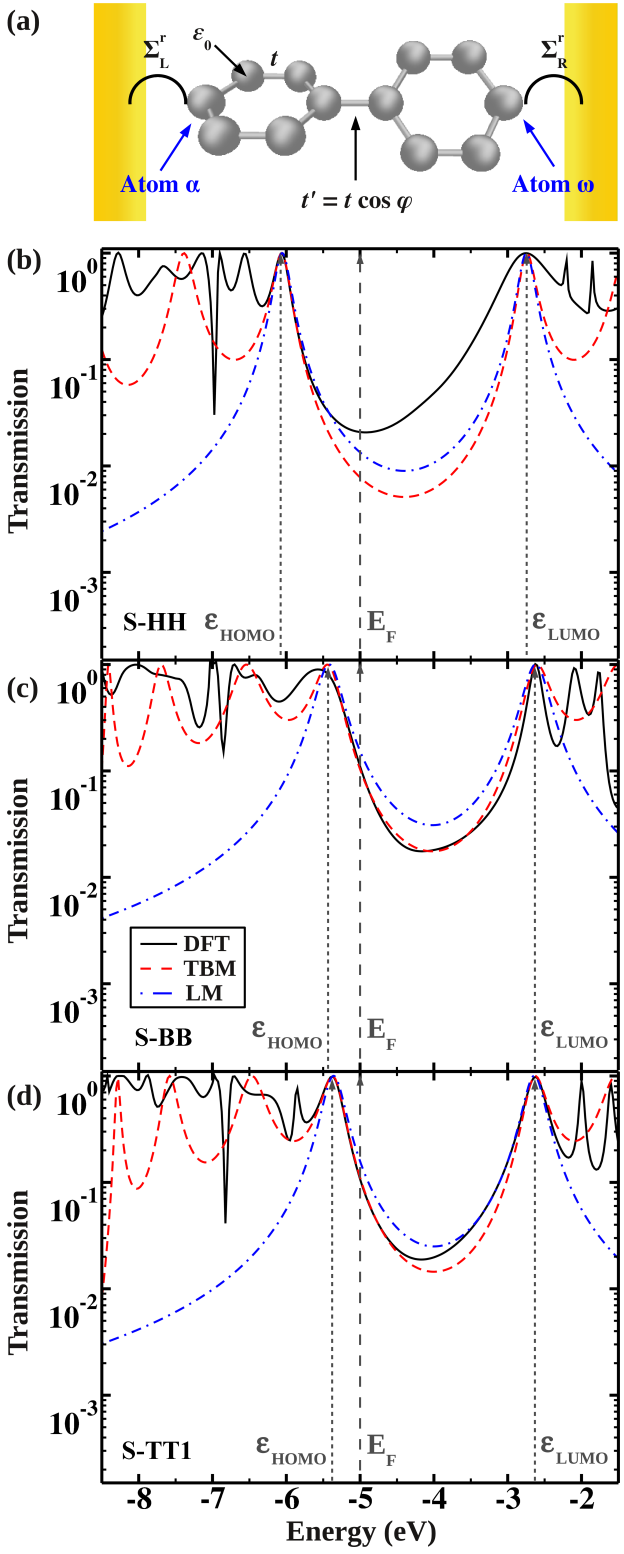

Fig. 9.6: (a) Sketch of the π-orbital TBM used to describe the transport through BPDT molecules. ϵ_0 is the onsite energy, identical for all carbon atoms, t the coupling between nearest-neighbor atoms on each phenyl ring, $t' = t \cos \varphi$ the inter-ring coupling, and φ the torsion angle realized in the particular junction geometry. The terminal atoms of the biphenyl backbone to the left and right are indexed α and ω, respectively, and their couplings to the L, R electrodes are described by the self energies Σ_L^r, Σ_R^r. (b-d) Transmission as a function of energy for M2 in the different junction geometries S-HH, S-BB, and S-TT1. The solid line is the DFT result, the dashed line the fit with the TBM, and the dash-dotted line corresponds to the LM. Vertical dashed lines indicate, in the order of increasing energy, the position of the HOMO, the Fermi energy, and the LUMO.

	ϵ_0	t	Γ	$\tilde{\epsilon}_H^{M2}$	$\tilde{\epsilon}_L^{M2}$	$\tilde{\Gamma}^{M2}$
S-HH	-4.40	-2.30	0.70	-1.05	2.25	0.11
S-BB	-4.02	-1.95	1.10	-0.42	2.38	0.18
S-TT1	-4.00	-1.90	0.96	-0.36	2.36	0.15

Tab. 2: Parameters of the TBM ϵ_0, t, Γ obtained by fitting the DFT-based $\tau(E)$ curves for M1-M4. The parameters $\tilde{\epsilon}_H^{M2}$, $\tilde{\epsilon}_L^{M2}$, $\tilde{\Gamma}^{M2}$ of the LM are those derived from the TBM for M2. All values are given in units of eV.

TBM we find for the imaginary parts $\gamma_{HOMO} = \gamma_{LUMO}$, and set $\tilde{\Gamma} = |\gamma_{HOMO}|$. From the relation between the TBM and the LM discussed in Appendix D (see Eq. (D.2)) we can identify $\tilde{\Gamma}$ with the width of the Lorentzian transmission resonances related to the HOMO and the LUMO. Finally, we determine the transmission for the LM via Eq. (D.2) as a sum over these two frontier orbitals only. The LM is thus characterized by $\tilde{\epsilon}_H$, $\tilde{\epsilon}_L$, $\tilde{\Gamma}$ and is specific to a certain molecule and junction geometry, as described by φ, ϵ_0, t, Γ in the TBM.

Using the physically motivated TBM, we have fitted the transmission $\tau(E)$ of the well-conjugated molecules M1-M4, as determined by the DFT calculations. Setting φ to the value of the torsion angle realized in the particular junction geometry, we place special emphasis on a good fit in the region of the HOMO-LUMO gap. When such a fit is too ambitious due to the simplicity of the TBM, we describe well at least the region between the HOMO and E_F, to determine effective parameters for the dominant transmission resonance, as well as the position of the LUMO peak. In this way, we obtain the values for ϵ_0, t, Γ given in Table 2.

Specific LM parameters for M2 are provided in the same table, and DFT, TBM, and LM transmission curves for M2 are shown in Fig. 9.6b-d.

The differences between the curves of the TBM and the LM in Fig. 9.6b-d in the region of the HOMO-LUMO gap illustrate approximations related to the neglect of interference effects in the LM. Indeed, we find that the transmission is slightly overestimated when it is regarded as the superposition of incoherent transmission resonances. In the following we restrict our discussion to the parameters of the LM for M2, since they are easy to interpret and those of the generic TBM contain similar information.

The data in Table 2 shows very similar values of $\tilde{\Gamma}^{M2}$ for the different junction geometries. While the increasing linewidth $\tilde{\Gamma}^{M2}$ when going from S-TT1 to S-BB is consistent with the expectation of a better electronic coupling for a higher coordination of the sulfur atom, also the molecular tilt plays a role. The perpendicular orientation of the BPDTs for geometry S-HH thus leads to a reduced $\tilde{\Gamma}^{M2}$. As an important conclusion, the values of $\tilde{\epsilon}_H^{M2}$ and $\tilde{\epsilon}_L^{M2}$ show that the HOMO is closer to E_F than the LUMO by more than 1 eV. In addition, the reduced conductance for S-HH in Fig. 9.5 is explained by the HOMO level being around 0.5 eV further away from E_F than for S-BB and S-TT1.

We attribute the shift of the HOMO level towards lower energies for increasing coordination number of the sulfur atoms to the different amounts of transferred charge

at the molecule-Au interface. Indeed, both Löwdin and electrostatic-potential-derived charges yield a leakage of electrons from the molecule, including the S atoms, to the Au electrodes, when going from S-TT1 over S-BB to the S-HH geometry. Variations of the conductance therefore mostly arise from changes in the alignment of the HOMO level with respect to the Fermi energy of the Au electrodes, and originate from charge redistributions, which are sensitive to the coordination site of the sulfur atom at the molecule-electrode interface.

9.2.5 Transmission eigenchannels

To explore further the electron transport through BPDT molecules, especially for the situation $\varphi \simeq 90°$ where the TBM looses its validity, we consider the eigenchannel decomposition of the conductance and the corresponding wavefunctions. The results are displayed in Fig. 9.7 and Fig. 9.8. We observe one dominant eigenchannel, whose transmission probability is decreasing gradually with increasing torsion angle for geometries with $\varphi \lesssim 80°$ (Fig. 9.8). The wavefunction of this channel is formed from those p orbitals of the C atoms, which are perpendicular to the phenyl-ring planes (see the results for M1 and M2 in Fig. 9.7). The resulting π orbitals, which comprise the terminal thiol groups, hence exhibit nodes in the ring planes. The findings agree with the expectation that for the small torsion angles, resulting in a high degree of conjugation, electric transport should occur via the delocalized π-electron system of the BPDTs.

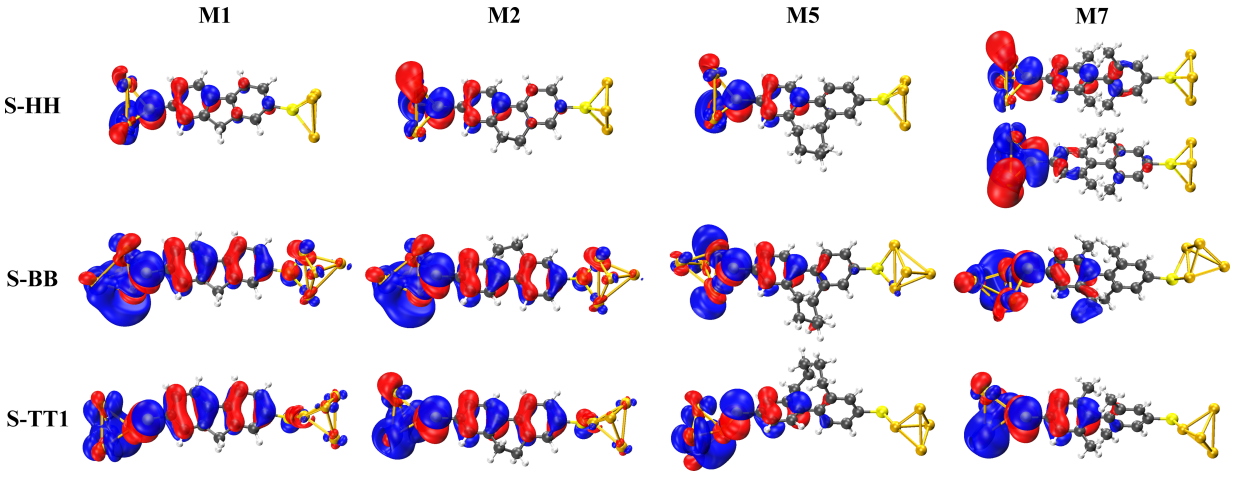

Fig. 9.7: Wavefunction of the dominant, left-incoming transmission eigenchannel for selected BPDT molecules in the S-HH, S-BB, and S-TT1 geometries. The same isosurface value of the wavefunctions is used in all the plots to allow for their comparison. However, the isosurface value has been reduced by a factor of 4 on the right phenyl ring of M7 for S-HH to visualize the π-σ and σ-π character of the two eigenchannel wavefunctions, which yield the same contribution to the conductance.

The π-π coupling between the rings is suppressed for $\varphi \approx 90°$, since it varies as $\cos\varphi$ [119, 117, 127]. In this case the molecular states become more localized on the individual rings. The incoming Bloch waves from the leads can still couple through the sulfur linker atom into the π-electron system of one of the rings, but they are back-reflected at the ring-connecting carbon atom. This results in a large suppression of the transmission (Fig. 9.8), and becomes manifest in a low amplitude of the wavefunction on the second ring (see the results for M5 and M7 in Fig. 9.7). In this regime, the π-σ coupling, proportional to $\sin\varphi$, dominates [119, 127]. The σ character of the wavefunctions is apparent from the absence of nodal planes in the phenyl ring planes and the high amplitude of the eigenchannel wavefunction on the axis which connects the neighboring carbon atoms. The isolated biphenyl molecules M0 and M7 (XR=H in Fig. 9.1) with φ set to 90° possess D_{2d} symmetry. Then, σ-π and π-σ orbitals are degenerate, which should lead to two dominant transmission eigenchannels with the same contribution to the conductance [119, 127]. However, the presence of the electrodes generally leads to a low symmetry of the junction as a whole and may also modify the molecular geometry.

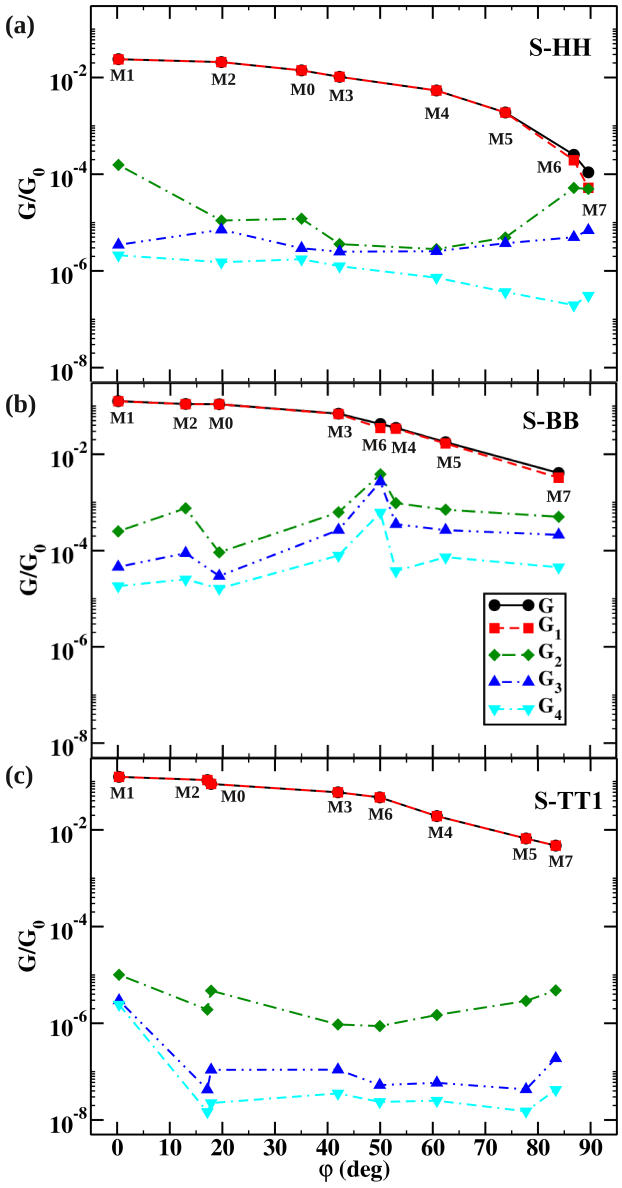

Fig. 9.8: Calculated conductance G and the conductance $G_n = G_0\tau_n(E_F)$ with $n = 1,\ldots,4$ of the four transmission eigenchannels with the highest contribution to G for the set of BPDTs in (a) S-HH, (b) S-BB, and (c) S-TT1 configurations.

Hence, it is interesting to analyze the degeneracy of eigenchannels in the different coordination geometries for M7 with the nearly perpendicular gas phase torsion angle. Using the ratio of the channel conductances G_2/G_1 with $G_n = G_0\tau_n(E_F)$ as a measure for the degeneracy, we find the values given in Table 3.

The data in Table 3 demonstrates the general absence of the channel degeneracy and a

high sensitivity of G_2/G_1 to the junction geometry. Only for the S-HH contact geometry we find a nearly perfect degeneracy of the two dominant transmission eigenchannels. Consistent with this, Fig. 9.7 demonstrates that their wavefunctions are indeed of π-σ and σ-π type. The degeneracy can be explained by the fact that M7 in the S-HH geometry stands perpendicular to the electrodes. The torsion angle of the contacted molecule is hence close to those in the gas phase (see Fig. 9.4), and the overlap of the molecular π orbitals with the electrode states is such that the degeneracy of molecular orbitals is not strongly lifted. Therefore, the transmission reflects symmetry properties of the molecule. For the S-BB and S-TT1 junctions, deviations from the channel degeneracy result from the geometric constraints set by the electrodes, which cause φ in the junctions to deviate from 90°, and from the asymmetric overlap of the molecular π states with the electrode states to the left and right. Thus, our results clearly show that the reduced symmetry of the complete junction has to be considered for transport and not just the symmetry of the isolated molecule alone [128].
These findings suggest that measurements of the transmission eigenchannel degeneracy may serve as a sensitive probe to determine the coordination geometry in biphenyl-type single-molecule junctions. However, there are several factors not included in our idealized treatment. Thus, it would be interesting to study, how strongly a finite bias voltage will lift an existing π-σ and σ-π channel degeneracy by breaking of the left-right symmetry. Furthermore, also dynamic effects due to vibrational modes and Jahn-Teller distortions should lead to an effective splitting of the two dominant eigenchannels. Beside these issues, it remains an experimental challenge to determine the conduction eigenchannel transparencies for contacts with a low transmission, since the existing techniques, employing superconducting electrodes [88] or shot noise [129], yield very low signals in such situations.
Our calculations illustrate that the alkyl chains do not participate significantly in transport, as expected from the large gaps between HOMO and LUMO levels of alkanes [120]. Considering the dominant transmission eigenchannels in Fig. 9.7, we see that there is indeed practically no weight of the wavefunction on the alkyl chain, even for the short chains present in M1 and M2.

	S-HH	S-BB	S-TT1
M7	0.95	0.15	$1.0 \cdot 10^{-3}$

Tab. 3: Ratio G_2/G_1 of the highest eigenchannel contributions to the conductance for M7 in the three junction geometries studied.

9.2.6 Conclusions

Motivated by recent experiments [115, 110], we have presented a detailed theoretical analysis of the charge transport properties of Au-BPDT-Au single-molecule junctions. The three different types of contact geometries in our DFT-based study differed in es-

sential aspects at the molecule-metal interface. They were mainly the coordination site of the anchoring sulfur atoms and the tilt of the molecule with respect to the electrodes. Given the extensive statistical analysis in the experiments, this set of geometries is clearly very limited. Furthermore, without an analysis of the junction formation process, it is difficult to make a statement on the probability of their occurrence. However, we hope that they can be used to describe general trends, such as the influence of molecular conformation on conductance and the variability of transport properties with contact geometry.

We have investigated electrode-induced changes of the molecular conformation due to charge transfer and geometric constraints and find that they are rather small for most molecules and types of junctions considered here. Compared to the somewhat larger variations for M0 and M6, whose φ is not fixed by an alkyl strap or strong steric effects, our calculations show that the appropriate design of the side groups can help to stabilize the torsion angle.

The transport calculations confirm a $\cos^2 \varphi$ dependence of the conductance for the well-conjugated molecules in each type of junction geometry. This is in accordance with the experimental observations and is characteristic for off-resonant transport through the π-electron system [117]. For biphenyl molecules with torsion angles close to the perpendicular orientation, however, we observe systematic deviations in our experimental data from the $\cos^2 \varphi$ law predicted by a simplified π-orbital TBM. In that regime of a broken conjugation, our analysis of DFT-based transmission eigenchannel wavefunctions reveals residual conductance contributions from a pair of π-σ-type conduction channels.

Finally, our calculations suggest that molecular junctions with sulfur atoms bound to the "hollow" site of gold electrodes could exhibit an order of magnitude smaller conductance as compared to junctions with sulfur atoms bound via "top" or "bridge" sites. Our analysis shows that the transport is dominated by the molecular HOMO level in all cases, and variations of the conductance arise from changes in the alignment of that level with respect to the Fermi energy of the Au electrodes. These changes in turn originate from the charge transfer between the molecule and the electrode, which is sensitive to the coordination site of the sulfur atom.

9.3 Nitrile-Terminated Biphenyls

9.3.1 Experimental motivation

In this chapter we are dealing with transport through a family of CN-terminated biphenyl molecules (BPDN) connected to Au electrodes. In contrast to the previous chapter we do not consider all molecules displayed in Fig. 9.1, but restrict our self to the ones relevant for the corresponding experiments, namely M0-M4 and M7. For these six molecules Mishchenko et al. found in experiments that nitrile-terminated molecules give rise to well-defined peaks in the conductance histograms resulting from the high selectivity of the N-Au binding. As an example a conductance histogram for M3, measured by means of the scanning tunneling microscope based break junction technique, is shown Fig. 9.9. The main panel in Fig. 9.9 displays the corresponding one-dimensional histogram on a logarithmic conductance scale constructed from ∼20000 individual stretching traces of M3. The sharp peaks in the histogram around integer multiples of G_0 represent the conductance of gold atomic point contacts [130]. The prominent peak with a maximum at $G_{max} = 4 \cdot 10^{-5}\, G_0$ is attributed to the most probable conductance of a single M3 molecule bound to two Au electrodes.

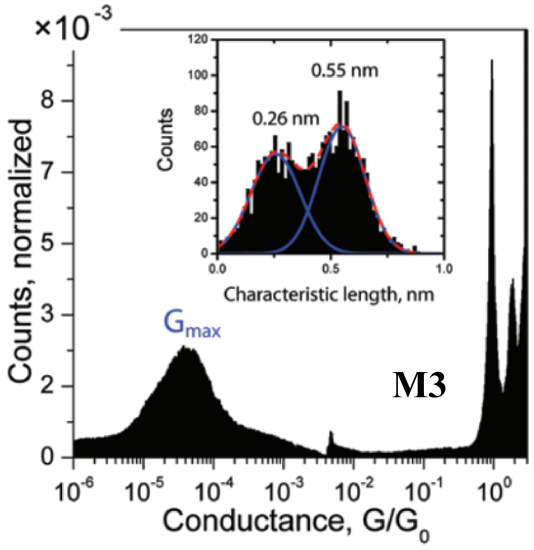

Fig. 9.9: 1D logarithmic conductance histogram and (inset) characteristic length histogram.

To gain further insights into the actual properties of the molecule-metal interface and the conduction mechanisms, we will analyze the set of molecules studied in the experiment by means of ab inito calculations.

9.3.2 Contact geometries

As mentioned above, the well-defined peaks in the conductance histograms which were found in experiment suggest that the CN-Au binding is highly selective. To find possible stable binding sites we therefore explored, similar to the BPDT junctions in Section 9.2 various binding geometries (specifically top, hollow, and bridge).

To construct the molecular junctions, each molecule was firstly relaxed on top of a single Au_{20} (Au_{19}) cluster for CN-TT1 (CN-TT2) grown along the $\langle 111 \rangle$ direction. Then, a second cluster stemming from the same ideal fcc Bravais lattice, was attached to the

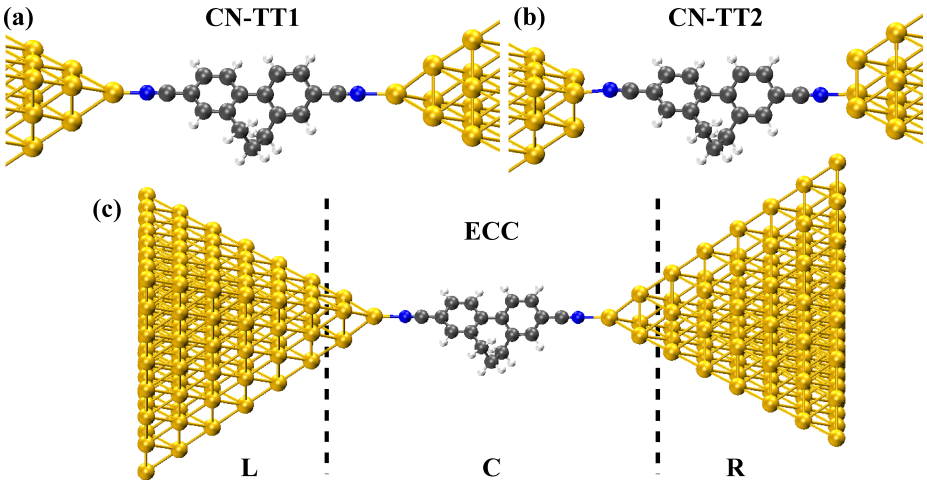

Fig. 9.10: The two contact geometries considered for the CN-anchored molecules. For CN-TT1 (a) the N atom is bind to a low coordinated Au atom in top position and for CN-TT2 (b) to a higher coordinated Au atom. (c) Division of the ECC into left (L), central (C) and right (R) regions.

other end and the whole structure was optimized again. In all optimizations, the two outermost layers in each cluster were kept fixed. For the transport calculations the Au cluster was extended to 120 (119) atoms to ensure a proper Fermi-level alignment of the molecular orbitals. Note that the shape of the Au electrode clusters in this section is different from those used in Section 9.2 and Section 9.4 (compare Fig. 9.10c and Fig. 9.3). We found that only atop binding geometries of the CN-Au contact are stable where N binds only to a single Au atom. This result is due to the coordinative nature of the covalent N-Au bond, which is established by the nitrogen lone pair. In the following we will focus on two representative top structures. In the first one (denoted as CN-TT1 in Fig. 9.10), the molecule is bound to a low-coordination-number gold adatom through a linear CN-Au bond. In the second one (denoted as CN-TT2 in Fig. 9.10), the molecule attaches to a "terrace-type" gold atom with a higher coordination number, and the CN-Au angle assumes a value of ∼160°. The binding energies for

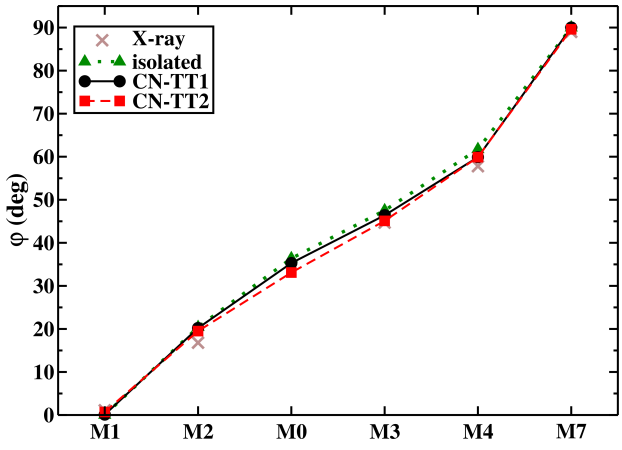

Fig. 9.11: Comparison of the torsion angle φ as determined from X-ray measurements and from DFT calculations in the gas phase (isolated; XR=H in Fig. 9.1) as well as in the molecular junctions (CN-TT1, CN-TT2; see Fig. 9.10).

all the molecules in the two geometries are very similar and around 1 eV. We have determined the binding energies as described in Section 9.2.1 by subtracting the total energy of the contact geometry from those of the the left and right Au clusters and the CN-terminated biphenyl.
For the CN-linked molecules we do, in contrast to the thiolated biphenyls (Fig. 9.4), not observe larger variations of the torsion angle φ with respect to the different junction geometries. Inside the molecular junction φ is for both contact geometries basically identical to the torsion angle of the isolated molecules in the gas-phase (Fig. 9.11).

9.3.3 Transport properties

From the calculated transmission curves we find that, for all contact geometries, the transport takes place through the tail of the LUMO (off-resonant tunneling). This is consistent with the results of previous calculations [131, 132] and thermopower measurements [133] in nitrile-terminated molecular junctions. The transmission curves for the CN-TT2 geometry show an approximately 20 meV broader transmission resonance at a slightly lower energy (by ∼20 meV) than for the CN-TT1 geometry (see the comparison for molecule M3 in the inset of Fig. 9.12a) for all of the molecules. The energy difference between the first two transmission resonances above the Fermi energy was found to decrease with increasing torsion angle, which is in agreement with results reported for biphenyl dithiols in Ref. [110].
The computed values of the junction conductances are plotted in Fig. 9.12b as a function of the square of the cosine of

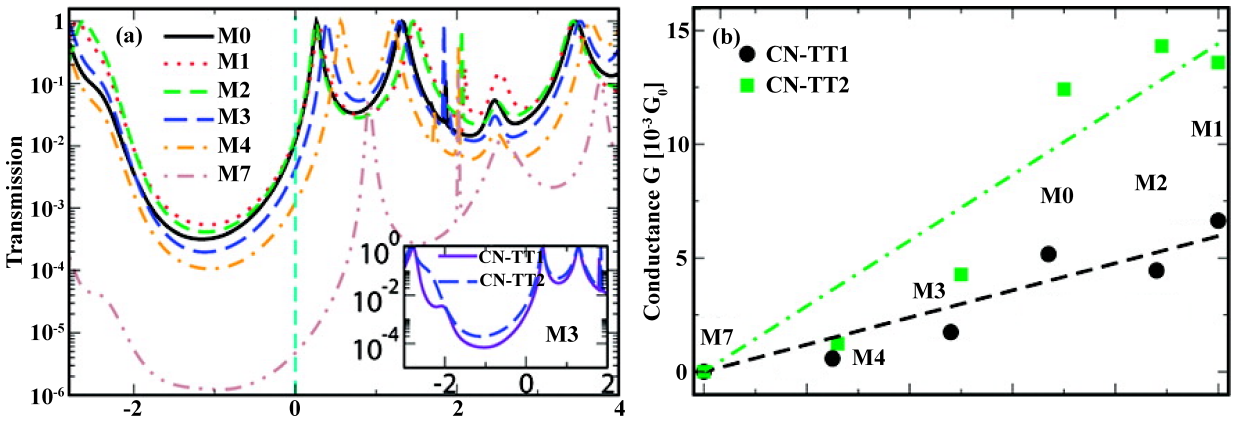

Fig. 9.12: (a) Transmission as a function of energy (measured with respect to the Fermi energy, E_F) for all of the molecules in the CN-TT2 geometry. The inset shows a comparison of the transmission curves for M3 bound in the CN-TT1 (solid curve) and CN-TT2 (dashed curve) geometries. (b) Computed conductances of M0-M4 and M7 as functions of $\cos^2 \varphi$ for the two contact geometries

the calculated torsion angle. The dashed lines represent the linear fit $G = a\cos^2\varphi$. The slope for the CN-TT2 geometry ($a = 1.44 \cdot 10^{-2} G_0$) is higher than that obtained for the CN-TT1 geometry ($a = 5.9 \cdot 10^{-3} G_0$) because a better coupling between the molecular π-system and the metal states yields a broader resonance in the former case. The computed conductance values are 2 orders of magnitude higher than the experimental ones, which is mostly due to the underestimation of the HOMO-LUMO gap by DFT [134, 66]. We note that both the experimental and theoretical conductances obtained for the BPDN family are lower than the values reported for biphenyl dithiols [110]. We find that this is due to a lower coupling (by a factor of $\sim$3) in the case of the BPDN derivatives relative to the biphenyl dithiols, and we attribute this to the presence of one more atom in nitrile than in thiol, which acts as a spacer.

9.3.4 Transmission channels

To gain further insight into the nature of the transport through these molecules, we also analyzed the contributions of the individual conduction channels to the total conductance. In Fig. 9.10a,b we show as example the channel decomposition for M3 in both

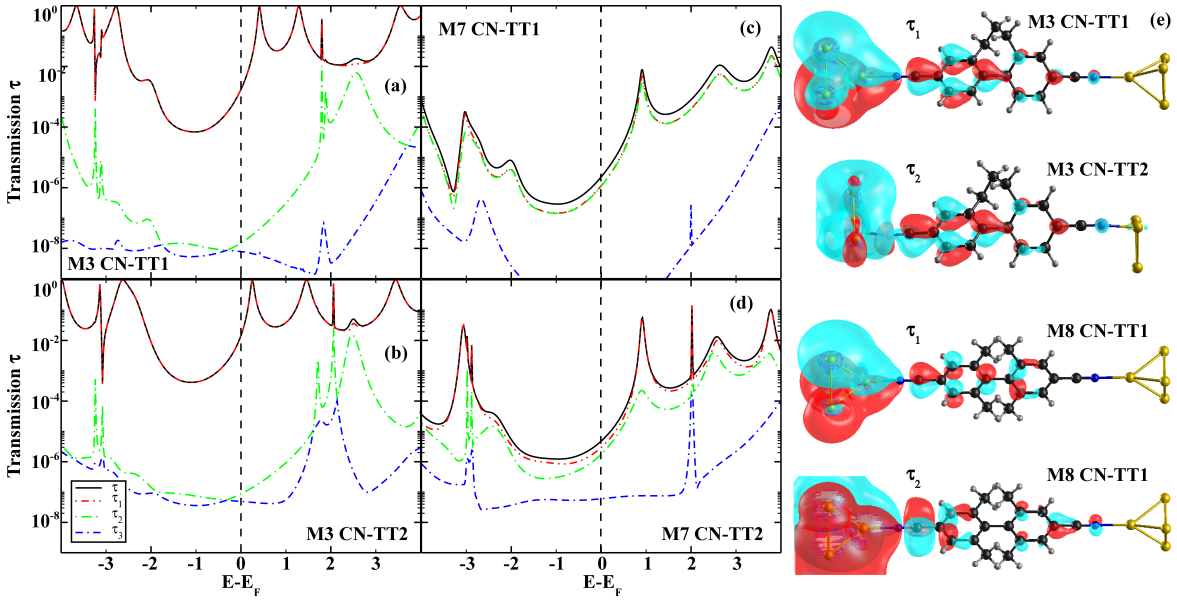

Fig. 9.13: (a-d) Energy dependence of the total transmission τ and of the three individual channels, τ_1-τ_3, with the largest contribution to τ. (e) The wave-function (isosurface $c = 0.02\,\mathrm{au}^{-3/2}$) of the dominant channel for M3 in CN-TT1 and CN-TT2 is clearly of π-orbital character. This also holds for the other well-conjugated molecules (M0-M4) which are not shown here. For M7 in CN-TT1 τ_1 and τ_2 are twofold degenerate and the wave-functions are of π-σ and σ-π character (where the isosurface on the second ring has been scaled by a factor of 4).

contact geometries. We found that for the well-conjugated molecules, M0-M4, the conductance is dominated by a single channel τ_1. This channel is of π-orbital character as we can see from the wave-function plotted in Fig. 9.13e. There the π- conjugation of the two phenyl rings proceeds through the anchoring group and couples directly to the gold electrodes.
For M7 however the π-electron coupling between the two rings is strongly suppressed because of the almost perpendicular ring orientation. We would expect from the symmetry of the isolated molecule that the conductance should be dominated by degenerate π-σ, σ-π channels. However as already discussed in Section 9.2.4 this degeneracy depends strongly on the symmetry of the whole junction and the coupling strength of the molecules to the electrodes. From the channel decomposition (Fig. 9.13c) we can see that for the more symmetric CN-TT1 geometry a twofold degeneracy of τ_1 and τ_2 can be observed and that the two channel wave-functions are indeed of π-$\sigma$and σ-π character (Fig. 9.13e). For the less symmetric CN-TT2 contact however, the degeneracy is lifted as visible in Fig. 9.13d.

9.3.5 Conclusion

To conclude, we have studied the conductance of a family of biphenyl derivatives wired to gold electrodes via nitrile anchoring groups. The well-defined features in the conductance histograms can be attribute to a site-selective N-Au bond. We observed a decrease in the single-molecule conductance with increasing torsion angle due to the π-electron dominated transport, where the transport proceeds through the tail of the LUMO. The high probability of spontaneously forming gold nitrile bonds, as demonstrated by the experiments and supported by our theoretical calculations, constitutes another important advantage of the nitrile-terminated molecules. These findings indicate that nitrile-based metal-molecule-metal junctions represent a unique platform for the reliable construction of nanoscale molecular assemblies with very uniform electric properties.

9.4 Seebeck effect

In this section we will deal with the thermopower Q of sulfur (S), amine (NH_2) and cyano (CN) terminated biphenyl-based molecules connected to Au electrodes. Here we will consider the molecules M0-M4 and M7 displayed in Fig. 9.1. For each molecule we studied seven different contact geometries (Fig. 9.14). For S we have chosen the same three representative binding sites as in Section 9.2, where S is bond covalently [135] either to three Au-atoms in hollow position (S-HH), to two Au atoms in bridge position (S-BB) or to one Au atom in top position (S-TT1). NH_2 and CN bind selectively to a single Au via the nitrogen lone pair, compare Section 9.3 and Refs. [124, 15]. Here we consider two different top sites for NH_2 (NH_2-TT1, NH_2-TT2) and CN (CN-TT1, CN-TT2) respectively. The ECC is similar to those studied in Section 9.2 and its construction follows the procedures given in Section 9.2.1.
In the following Q will be calculated for $T = 10\,\mathrm{K}$ by means of Eq. (4.36), i.e. by taking into account the thermal broadening due to the finite temperature. The differences compared to the values obtained with Eq. (4.38) turn out to be small even at room temperature ($T = 300\,\mathrm{K}$). Hence room temperature values can be obtained from the values at 10 K as $Q_{300\mathrm{K}} \approx T \times Q_{10\mathrm{K}}/10\mathrm{K}$.

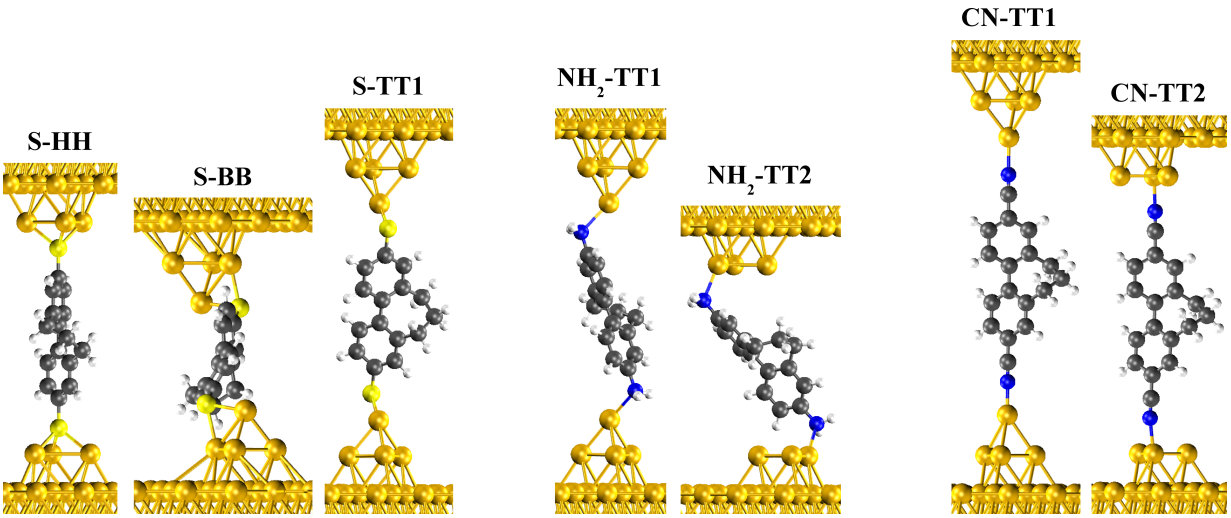

Fig. 9.14: For S we consider hollow (S-HH), bridge (S-BB) and top (S-TT1) binding sites, for NH_2 and CN we consider binding to a single Au atom in two different top positions NH_2-TT1, CN-TT1 and NH_2-TT2, CN-TT2 respectively.

9.4.1 Dependence of the thermopower on the metal-molecule interface

In Table 4 we have summarized the torsion angle φ, which is defined as the dihedral angle between the two phenyl rings (Fig. 9.15c), and the thermopower for each molecule

in the various contact geometries. We notice that the sign of the thermopower is determined by the anchoring group. For the electron-donating S- and NH_2-linker groups [136] the energy of the π-electron system of the molecule is increased and the HOMO energy is close to E_F as we can see in the transmission curves plotted in Fig. 9.17. This results in hole conduction through the HOMO and $Q > 0$ [137, 75, 138], in agreement with previous experimental [17, 139] and theoretical results [26, 140, 141]. In contrast to this for the electron-withdrawing CN linker group[136] we have electron transport through the LOMO [132] and $Q < 0$. Up to now there exist, to our knowledge, no experimental or theoretical data on the thermopower of cyano terminated biphenyls.
Comparing the absolute value of the thermopower we see in Fig. 9.15 that Q varies strongly between the contact geometries. For the thiolated molecules we find that the thermopower for S-BB and S-TT1 is comparable but both are significantly larger than the values obtained for S-HH. The thermopower shows the same behavior as the conductance of the thiolated molecules, where top and bridge geometries yield much larger conductance values than those for hollow sites [142, 143, 120]. For the amins NH_2-TT1 gives a larger thermopower than NH_2-TT2. This is a result of the larger charge transfer onto the molecule when bound in NH_2-TT1 position, which moves the HOMO closer to E_F as compared to NH_2-TT2 [144]. The level broadening for NH_2 is roughly independent of the binding position, as we will see later. Comparing with the thiols we see that both NH_2-linked geometries give rise to a thermopower well below those of S-BB and S-TT1 but still larger than for S-HH. The CN-linked molecules show the largest absolute values for the thermopower, whereby molecules in CN-TT1 position are charged more positive and hence show a smaller Q than the molecules in CN-TT2 position.
Regarding M0 we can compare against previous experimental results. For biphenyldiamines a thermopower of $Q^{\text{NH}_2\text{-EXP}} = 4.9\,\mu\text{V/K}$ (at $T = 300\,\text{K}$) was found [139], which compares reasonable well to our calculated values of $Q^{\text{NH}_2\text{-TT1}} = 10.52\,\mu\text{V/K}$ and $Q^{\text{NH}_2\text{-TT2}} = 4.6\,\mu\text{V/K}$ (at $T = 300\,\text{K}$). Furthermore recent calculations within a DFT approach with an approximate self-interaction correction for comparable geometries showed results comparable to ours [145].
For biphenyldithiols the comparison is more difficult as our calculated values vary by one order of magnitude for the different geometries, from $Q^{\text{S-HH}} = 0.11\,\mu\text{V/K}$ to

	S-HH		S-BB		S-TT1		NH_2-TT1		NH_2-TT2		CN-TT1		CN-TT2	
	φ	Q	φ	Q	φ	Q	φ	Q	φ	Q	φ	Q	φ	Q
M0	35.1	0.002	12.9	1.230	17.9	0.907	32.9	0.343	33.2	0.150	33.1	-2.389	35.3	-1.566
M1	0.3	0.064	0.1	1.313	0.4	1.280	0.2	0.436	0.7	0.201	0.7	-2.281	0.1	-1.423
M2	19.8	0.048	19.3	1.208	17.2	1.266	20.4	0.429	19.1	0.191	19.5	-2.252	20.2	-1.404
M3	42.3	0.032	42.1	1.127	42.0	1.200	46.3	0.382	46.3	0.189	45.1	-1.878	46.4	-1.158
M4	60.7	0.034	53.0	1.006	60.8	0.981	61.6	0.400	58.4	0.158	59.2	-1.657	59.9	-0.938
M7	89.6	0.019	84.0	0.298	83.4	1.378	87.4	0.191	87.3	0.150	89.6	-1.173	89.9	-0.632

Tab. 4: Torsion angles φ in units of degrees and the thermopower Q at $T = 10\,\text{K}$ in units of $\mu\text{V/K}$ for all the various geometries.

$Q^{\text{S-BB}} = 40.06\,\mu\text{V/K}$ and $Q^{\text{S-TT}} = 28.08\,\mu\text{V/K}$ (at $T = 300\,\text{K}$). They scatter indeed around the experimental result of $Q^{\text{EXP}} = 13\,\mu\text{V/K}$ [17, 139].

9.4.2 Torsion angle dependence of the thermopower

For M0-M4 the main contribution to the conductance arises from one channel of π-orbital character see Section 9.2.5 and Refs. [14, 117, 110, 15]. Hence increasing the torsion angle between the two rings decreases the degree of π-conjugation. If one neglects the doping effects of the side-groups we would expect that the well conjugated molecules M0-M4 follow [26]

$$Q \approx a + b \cdot \cos^2\varphi. \tag{9.1}$$

For M7 Eq. (9.1) is not valid however, because at $\varphi \simeq 90^\circ$ the transport proceeds not through the π-channel but through two degenerate π-σ and σ-π channels as explained in Section 9.2. Despite the variations of Q with different anchoring groups and binding positions we observed in the previous section, we see from Fig. 9.15 that we find a weak but clear $\cos^2\varphi$ like decrease for M1-M4 in all geometries. M0 is an exception, however. Although the electron donating effect of the alkyl chains is expected to be small, it causes a shift to higher Q for M1-M4. To clarify this we calculated for the isolated gas phase molecules, by means of electrostatic potential fitting and Löwdin population analysis, the charge transferred from the alkyl side chains to the two phenyl rings. Both methods yield an overall negative charge on the phenyl rings which is practically independent of the chain length. Therefore the aligment of the HOMO level with respect to E_F is similar for M1-M4. This gives rise to just a constant shift towards larger Q for M1-M4, which explains that we can still observe the $\cos^2\varphi$ dependence for this series of molecules but M0 must be excluded. Considering now just the thermopower of molecules with alkyl chains attached (M1-

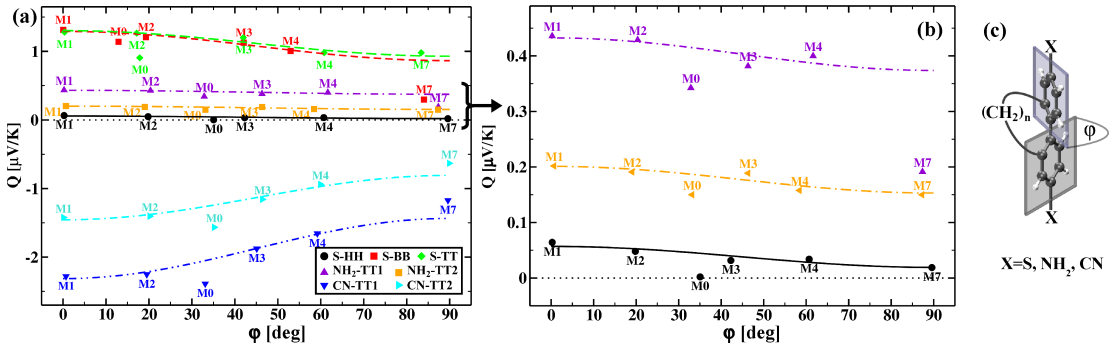

Fig. 9.15: (a) Evolution of Q with increasing torsion angle φ for all contact geometries The symbols are the calculated Q values and the lines are the curves obtained from fitting Eq. (9.1) for M1-M4. (b) Zoom to the Q values of S-HH, NH_2-TT1 and NH_2-TT2 respectively. (c) Definition of the torsion angle φ.

M4), we can fit Eq. (9.1), and define for this series the maximal decrease of Q as the ratio $r = (Q_{M1} - Q_{M4})/(Q_{M1} + Q_{M4})$. The results are summarized in Table 5. We find the largest decrease for S-HH followed by CN-TT2, which has a slightly larger r than CN-TT1, S-BB, S-TT1 and NH_2-TT2, the latter four junctions show roughly the same r and the smallest r is found for NH_2-TT1. M7 on the one hand has the largest charge transfer onto the phenyl rings due to the electron donating nature of the methyl side-groups, [136, 146], which increases Q. On the other hand the transport is dominated by rather badly conducting σ-π and π-σ channels. Hence M7 is not expected to follow the $\cos^2\varphi$ dependence, and we find that its absolute values are generally lower than predicted by the fit with Eq. (9.1). Only for S-TT1 and NH_2-TT2 it seems to fit the $\cos^2\varphi$ dependence but this is likely rather coincidentally.

	a [μV/K]	b [μV/K]	r [%]
S-HH	0.02	0.04	31
S-BB	0.86	0.43	13
S-TT1	0.93	0.37	13
NH_2-TT1	0.37	0.06	4
NH_2-TT2	0.15	0.05	12
CN-TT1	-1.44	-0.89	16
CN-TT2	-0.81	-0.65	20

Tab. 5: Parameters obtained from fitting the calculated results in Fig. 9.15 to Eq. (9.1). r describes the variation of Q between M1 and M4.

9.4.3 Thermopower within the tight-binding model and the Lorentz model

The sign as well as the absolute value of Q are determined by the alignment $\tilde{\epsilon}^{H,L} = \epsilon^{H,L} - E_F$ of the HOMO (ϵ^H) and LUMO (ϵ^L) level with respect to the Fermi energy E_F and the linewidth broadening due to the coupling to the electrodes. To analyze this further we consider for M1-M4 the TBM introduced in Section 2 to describe the π-orbital system of the molecules. An example of the fit for each linker group is shown in Fig. 9.17. We can see that the TBM reproduces the transmission in the energy range of the HOMO-LUMO gap very well. We find that the parameters for M1-M4 in the same binding geometry are basically identical, because Γ is independent of the specific molecule and t and ϵ_0 are molecule internal properties mainly affected by the charge transfer to the phenyl-rings, which is constant for the different alkyl chains and therefore just varies for different linker groups and binding positions, respectively. The obtained fitting parameters are summarized in Table 6. From the TBM the position of the HOMO and LUMO and hence their alignment $\tilde{\epsilon}^{H,L}$

	ϵ_0	t	Γ	$\tilde{\epsilon}^H$	$\tilde{\epsilon}^L$	$\Gamma^{H,L}$
S-HH	-4.40	-2.30	0.70	-1.05	2.25	0.11
S-BB	-4.00	-1.90	1.10	-0.36	2.36	0.18
S-TT1	-4.02	-1.95	0.96	-0.42	2.38	0.15
NH_2-TT1	-4.30	-2.29	0.60	-0.95	2.35	0.10
NH_2-TT2	-4.40	-2.32	0.66	-1.07	2.27	0.10
CN-TT1	-6.10	-2.00	0.14	-2.54	0.34	0.02
CN-TT2	-6.05	-1.99	0.15	-2.48	0.38	0.02

Tab. 6: Position $\tilde{\epsilon}^{H,L}$ of the HOMO and LUMO resonance with respect to E_F and the level broadening obtained from fitting the TBM to the DFT results in units of eV.

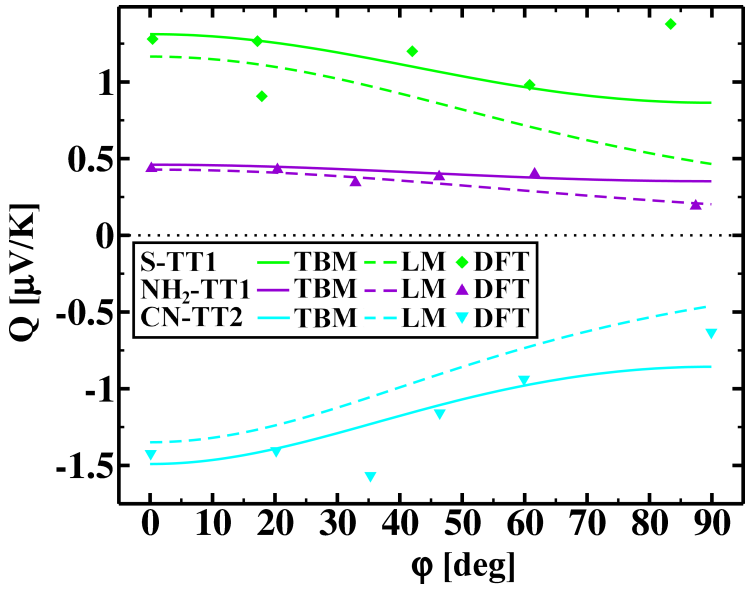

Fig. 9.16: Q as a continuous function of φ as obtained from the TBM and LM, compared with the DFT results.

with respect to the Fermi energy can be extracted. In addition, we obtain, as described in Appendix D, the individual broadening of the different resonances arsing from the molecular levels described within the TBM. As argued above, the position of the HOMO and the LUMO resonance with respect to E_F is mainly responsible for the differences of thermopower for the different linkers and binding positions. From Table 6 and Fig. 9.17 we see that we have clearly HOMO-dominated transport for S- and NH_2-linked molecules and LUMO-dominated transport for CN linkers. Considering $\tilde{\epsilon}^H$ in Table 6 we find that the HOMO resonance is around 0.6 to 0.7 eV closer to the E_F for S-BB and S-TT1 as compared to S-HH, NH_2-TT1 and NH_2-TT2 resulting in the much larger Q for the former two junction geometries. Furthermore, for both NH_2 and CN, the broadening is largely independent of the binding position and the difference in Q between TT1 and TT2 stems mainly from the different alignment of the HOMO and LUMO levels. Using the TBM we can calculate Q as a continuous function of φ. We find that this agrees with the fit of the DFT results to Eq. (9.1) for all the considered junctions, thus justifying the functional dependence assumed in Eq. (9.1).
The TBM can be related to the often used two-peak Lorentz model (LM) (see Appendix D) The transmission is then given by Eq. (D.2). The LM describes the transmission in the vicinity of the resonances quite well, but for the off-resonant transport situation present in this type of molecular junctions, it tends to slightly overestimate the transmission and to slightly under estimate its slope at the Fermi energy. As shown in Fig. 9.16, Q obtained from the LM is therefore somewhat smaller compared to the TBM and DFT results respectively, but still shows the same qualitative behavior which further supports that a decrease of π-conjugation decreases the absolute value of Q.

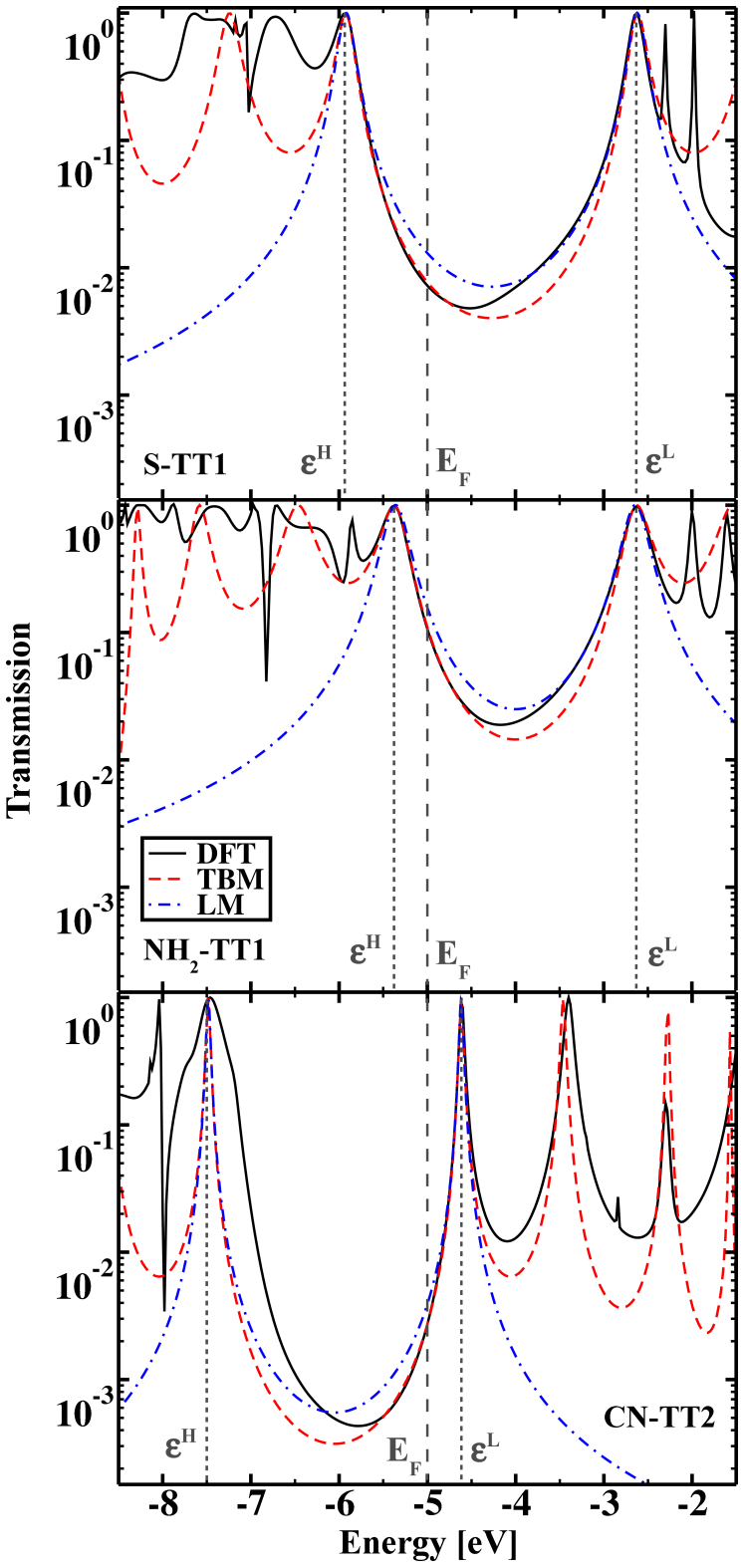

Fig. 9.17: Transmission for M2 obtained from DFT and the fits for the TBM and the LM.

9.4.4 Conclusions

We have studied the thermopower of biphenyl-based single-molecule junctions by means of ab-initio charge transport calculations. Our analysis showed that one can have either a positive or negative thermopower for the same molecule by replacing the anchoring group. A positive thermopower, which indicates hole transport through the HOMO, was found for molecules which are connected via S or NH_2 groups to the Au electrodes. In contrast to this we predict for CN-linked molecules a negative thermopower characteristic for electron transport through the LUMO. Different binding sites, on the contrary, do not affect the sign of Q but lead to variations of absolute value. For thiolated molecules in a bridge and top binding site Q is about one order of magnitude larger than Q for molecules bond in hollow position for S linkers. For NH_2 and CN the variations of Q between the two considered top sites is around a factor of 2. Despite these variations of the thermopower with respect to the properties of the molecule-metal interface, we observed for all investigated junction configurations a decrease of Q with increasing φ following a characteristic $\cos^2 \varphi$ law. We propose to measure the $\cos^2 \varphi$ dependence of the thermopower by means of biphenyl molecules where φ is adjusted by alkyl chains of different lengths. In this way substituent related shifts of Q, superimposing the weak $\cos^2 \varphi$ dependence, can be avoided to a large extent and are roughly independent of the chain length. Depending on the used anchoring group, the obtainable variation of Q for the series of biphenyls studied is expected to be between 10% and 30%. We are convinced that these variations are experimentally detectable.

9.5 Summary

In this part we showed that the properties of the metal-molecule interface as well as the molecular conformation have a large influence on the charge transport properties and that it is possible to relate to relate features of the experimentally measured conductance to specific atomistic and chemical properties of the molecular junction.

In Section 8 we showed by means of simulated junction stretching processes that thiol-linked octane molecules are much more strongly bond to Au electrodes than amine anchored octanes. We could relate experimentally observed "kinks" in the opening traces of ODT to plastic deformation of the electrodes. We observed the formation of an atomic Au chain upon stretching of the contact. For ODA chain formations are basically absent. This is also reflected in the binding energy for the S-Au bond (1.76 eV) which is around twice as large as the binding energy of the N-Au bond (0.92 eV). Furthermore we characterized the vibrational modes observed in the experiment by comparing experimentally measured to calculated IETS spectra. Thereby we paid special attention to the vibration between the anchoring group and the Au-electrodes. We found that the vibrational energy of ν(Au-S) ($\sim$35 meV) remains roughly constant during the opening of the contact, because the change in S-Au bond length is small. Instead atomic gold chains are pulled out of the contact during stretching. This behavior is in contrast to the vibrational energy of the ν(Au-N) mode (29 meV), which experiences a substantial red shift. These findings further support that the S-Au bond is much stronger than the N-Au bond.

In Section 9.2 biphenyl-dithiol-based molecular gold junctions were studied. The conductance shows large fluctuations for different coordination of the S atom with respect to the Au-surface. The conductance is one order of magnitude smaller for molecules bind in hollow position compared to bridge and top sites respectively. We explained the variation by the smaller overlap and hence the smaller degree of the hybridization between molecular orbitals with states in the Au-electrodes. The transport takes place through the tails of the HOMO resonance. For bridge and top bonded molecules the HOMO resonance is around 0.3-0.4 eV closer to the Fermi energy than for molecules bond in the hollow position. Besides the coordination of the anchoring groups to the Au-electrodes also the molecular conformation has a large influence on the conductance. We showed that the transport is dominated for well conjugated molecules with $\varphi < 80^\circ$ by one channel formed from the delocalized π-electrons. This was visualized by means of the transmission channel wave-function. We found that the conductance decreases as $\cos^2 \varphi$ with increasing φ. For perpendicular ring orientation the π-channel is completely blocked, suppressing the transport strongly. For the weakly bond hollow geometries we could observe in this case a degeneracy of the dominant $\pi - \sigma$ and $\sigma - \pi$ channels for molecules with D_{2d} symmetry. However for the less symmetric and more strongly hybridized bridge and top geometries this degeneracy is lifted.
Nitrile as an alternative linker between the molecule and the electrodes was investigated in Section 9.3. We confirmed that the experimentally observed well-defined peaks

in the conductance histograms result from the highly selective coordination of the nitrogen atom with respect to the Au-surface. We found that only top geometries are stable where the nitrogen binds to a single Au atom. We showed for two representative junctions that the variation of the conductance for the nitriles is much smaller than for thiolated molecules. Furthermore the conductance proceeds, contrary to the thiols, through the tails of the LUMO resonance. However the transport is also dominated by the π-electron system and hence we could observe the characteristic $\cos^2 \varphi$ dependence for the well conjugated molecules.
Besides the electric conductance we studied also thermoelectric properties of molecular junctions. Section 9.4 dealt with the thermopower of biphenyl-based molecular junctions. The absolute value of Q is sensitive with respect to different anchoring groups but also to the variation of the binding site and the orientation of the linker group with respect to the Au-surface. For the sign of Q the type of anchoring group plays the decisive role, we showed that S and NH_2 linkers give rise to $Q > 0$, characteristic for hole transport through the HOMO contrary to, CN where $Q < 0$ characteristic for electron transport through the LUMO. By taking into account the doping effects of the side-groups we showed that Q decreases as $\cos^2 \varphi$ with increasing torsion angle φ. This variation is rather weak but should be still within experimental resolution

Part V

Summary

The aim of this thesis was to provide a comprehensive study of the transport mechanisms in atomic and molecular junctions. We tried to cover a broad range of different systems, and to analyze them from various perspectives on the same theoretical footing. We focused on the systematical trends across the different classes of systems and on the underlying physical mechanisms of the charge transport at the nanoscale. This enabled us to address two of the fundamental question of molecular electronic, the relation of the atomistic and chemical structure inside the atomic or molecular junctions to the transport properties and the closely related problem of fabricating single-molecule circuits with well-defined molecular conductance.

In order to give a consistent description of the charge transport through nano-scale systems, it was necessary to describe, beside the elastic current, also its inelastic corrections due to electron-phonon interactions within the frame-work of density functional theory (DFT). The first part of this thesis was therefore concerned with the theoretical description of the inelastic current. To describe the inelastic current, it was necessary to calculated accurate electron-phonon coupling constants. We derived analytical formulas for the electron-phonon coupling constants to compute them within DFT. Based on these formulas we implemented their calculation into the quantum chemistry package Turbomole.

To provide an intuitive picture to interpret the charge transport properties of atomic and molecular junctions we used the concept of the transmission eigenchannels. Based on the work by Paulson et al., we generalized their procedure to calculate efficiently the eigenchannel wave-functions to the case of non-orthogonal basis sets avoiding any Löwdin transformations..

With the tools developed in the first part of this thesis, we studied the charge transport through various atomic and molecular junctions. In Part III we dealt with mono-atomic contacts. We started with the analysis of a 4-atom gold (Au) chain connected to two Au $\langle 100 \rangle$ electrodes. It served as a test system for the methods developed in the course of this thesis. In agreement with experiential measurements we found an an elastic conductance of 1 G_0 arising from one transmission channel. We could show that the according wave-function of σ-character. The IETS spectra showed that mainly longitudinal phonon modes of the Au-chain give rise to corrections to the elastic current. However, the main focus of Part III was the study of atomic contacts based on the multivalent metals lead (Pb) and aluminum (Al). We related the valence orbital structure to their conducting properties. In both metals the current is carried by three dominant transmission channels. By visualizing the eigenchannel wave-function, we showed that the s-p_z orbitals hybridize to a σ-channel, and the p_x and p_y orbitals hybridize to two

degenerate π- channels, respectively. For Pb all three channels are widely open, contrary to Al, where the two π-channels are partially closed for similar $\langle 111 \rangle$ single atom contacts.
We calculated for both metals the evolution of the conductance upon elongation of the contact. Jumps in the conductance during the junction closing could be attributed to the (partial) opening and closing of transmission channels due to atomic rearrangement. The opening curves for Pb and Al differ qualitatively in the elastic stage before the contact breaks. For Pb the conductance remains constant with increasing electrode separation until the rupture of the contact. For Al a monotonic decay of the conductance with increasing electrode separation was observed.

Furthermore, we simulated the inelastic tunneling spectra (IETS) to analyze the electron-phonon coupling in multivalent metals. We showed that the vibrational energy of transversal modes remains constant during the elastic deformation of the contact. Longitudinal modes, on the other hand, are red shifted with increasing electrode separation due to an increase of the bond length between Pb and Al atomis, respectively.

Metal-molecule-metal hybrid systems were the second class of molecular junctions we considered. Linking the molecule in a controlled and reproducible way to the metal electrodes is presently one of the most important issues in molecular electronics. Therefore we focused on analyzing the properties of the metal-molecule interface and its influence on the conductance of aliphatic and aromatic molecules.
Accompanying experiments in the group of Elke Scheer, we explored in Section 8 aliphatic octane-diamine and octane-dithiol molecules connected to gold electrodes. By comparing the experimental and simulated IETS we could characterize the molecular vibrations. Special attention was paid to the vibration between the linker groups and the electrodes. We could provide strong experimental and theoretical evidence that thiol binds much stronger to gold surfaces than amine.
The influence of the anchoring group on the conduction properties of aromatic biphenyl molecules was studied in Section 9. For thiol anchoring groups we observed a large influence of the sulfur binding site on the conductance. The conductance is by one order of magnitude larger for bridge and top binding positions as compared to hollow sites. We could explain the variation by the different alignment of molecular levels with respect to the metal Fermi energy due to different amount of charge transfer at the molecule-electrode interface. To provide an alternative linker group, which binds more selectively to the gold electrodes, we explored biphenyl-dinitrile based molecular junctions. We could explain the experimentally observed, well-defined peaks in the conductance histograms by the highly selective binding of the CN group to single atoms in the gold electrodes

To summarize we found that the properties of the metal-molecule interface are crucial for the transport through organic molecule. Thiol-anchored molecules allow to form stable molecular junctions via their strong covalent bond. On the other hand, their binding to the gold surface can take place in various coordination sites, making it diffi-

cult to obtain a well-defined molecular conductance. A promising alternative are nitrile anchors, which bind highly selectively to single Au atoms in the electrodes, providing a much better-defined molecular junction conductance.

In addition to the influence of the anchoring groups we also considered the influence of molecular internal properties on the conductance. In collaboration with the experimental group of Thomas Wandlowski we explored the conductance properties of biphenyl-based single molecule junctions. For these aromatic molecules the conductance depends strongly on the degree of π-conjugation. By means of the channel wave-functions, we could show that in the well conjugated molecules the current is indeed carried by the $\pi-$electron system. However, at perpendicular ring orientation the π-π channel is closed, and the transport is dominated by the π-σ coupling between the two rings. For molecules just weakly coupled to the electrodes, we could relate the molecular symmetry to the transmission channels. For M7 we observed that transport proceeds through two degenerate π-σ and σ-π channels.
Besides the electric conductance we studied the thermopower Q of biphenyl-based gold junctions. We considered three different linker groups, namely sulfur, amine, and nitrile in different bonding positions. The linker group determines the sign of Q. For thiol and amine we found $Q > 0$ and for nitrile $Q < 0$, respectively. Different binding positions on the other hand, lead to variations of the absolute value of Q. Irrespective of the observed variations we found that the absolute value of Q decreases weakly as $\cos^2 \varphi$ with increasing biphenyl torsion angle φ.

Despite the tremendous progress which has been achieved in molecular electronics in the recent years, the main goal of providing functional units based on molecular building blocks for nanoscale devices still faces some fundamental problems. However, many efforts are being made to overcome these problems. It is important that the involved different disciplines of science like chemistry, physics and material science apply complementary approaches to tackle the problem. In that sense, this work contributed to solve these problems from the theoretical side of physics.

A Nonorthogonal basis sets

A.1 Direct and dual basis

In this chapter we discuss the properties of nonorthogonal bases which are used for example in the LCAO expansion of the KS-orbitals (Eq. (3.13)) in Section 3.1.1 and in the formulation of the NEGF in Appendix B. As the basis functions used in quantum chemistry calculations are normally real, we will consider here just the real domain. However, as discussed in Ref. [147] the generalization to complex basis set is possible.

Let $\mathcal{H}$ be a real Hilbert space spanned by the basis $\{|e_i\rangle\}$ which we call the direct basis then there exists a dual basis set $\{|e^i\rangle\}$ uniquely defined by [147]

$$\langle e^i|e_i\rangle = \langle e_i|e^i\rangle = \delta^i_j. \tag{A.1}$$

The closure relation in $\mathbb{R}^n$ reads

$$\sum_i |e_i\rangle\langle e^i| = \sum_i |e^i\rangle\langle e_i| = 1. \tag{A.2}$$

Assuming now that we have the following metric for the direct basis $\{|e_i\rangle\}$

$$S_{ij} = \langle e_i|e_j\rangle, \tag{A.3}$$

which defines the overlap matrix $(S)_{ij} = S_{ij}$, permits us to express the closure relation (Eq. (A.2)) as

$$\sum_{ij} |e_i\rangle (S^{-1})_{ij} \langle e_j| = 1 \tag{A.4}$$

and

$$\sum_{ij} |e^i\rangle (S)_{ij} \langle e^j| = 1. \tag{A.5}$$

From this it follows for the metric of the dual basis that $\langle e^i|e^j\rangle = (S^{-1})_{ij}$.

For abstract vectors $|\psi\rangle$ in $\mathcal{H}$ the scalar products are given by tensors of rank one either in contravariant representation

$$\psi_i = \langle e_i|\psi\rangle \tag{A.6}$$

or covariant representation

$$\psi^i = \langle e^i | \psi \rangle. \tag{A.7}$$

For operators $\hat{H}$ in $\mathcal{H}$ the scalar products are given, respectively, by tensors of rank two either in the contravariant representation

$$H^{ij} = \langle e^i | \hat{H} | e^j \rangle, \tag{A.8}$$

in the covariant representation

$$H_{ij} = \langle e_i | \hat{H} | e_j \rangle \tag{A.9}$$

or in the mixed representations

$$H^i_j = \langle e^i | \hat{H} | e_j \rangle \tag{A.10}$$

and

$$H^j_i = \langle e_i | \hat{H} | e^j \rangle. \tag{A.11}$$

If we now introduce the two metric tensors $g_{ij} = (S)_{ij}$ and $g^{ij} = (S^{-1})_{ij}$ and contract over repeated indices (Einstein summation convention) we can write the transformation between the different representation in a compact form, e.g.

$$H^j_i = H_{ik} g^{kj} = g_{ik} H^{kj} = g_{ik} H^k_l g^{lj}. \tag{A.12}$$

Respectively, we can express the three closure relations as

$$1 = |e_i\rangle \delta^i_j \langle e^j| = |e_i\rangle g^{ij} \langle e_j| = |e^i\rangle g_{ij} \langle e^j|. \tag{A.13}$$

The representation of $|\psi\rangle$ in Dirac space in the basis $\{|e_i\rangle\}$ yields

$$|\psi\rangle = \sum_i c_{i\psi} |e_i\rangle = \sum_i \langle e^i | \psi \rangle |e_i\rangle \tag{A.14}$$

and its components are given by $\psi_j = \langle e_j | \psi \rangle = g_{ji} c^i_\psi$.

Now we consider the transformation between two nonorthogonal bases $\{|e_i\rangle\}$ and $\{|\tilde{e}_i\rangle\}$ spanning the same Hilbert space $\mathcal{H}$. Let $g_{ij} = \langle e_i | e_j \rangle$ be the metric of $\{|e_i\rangle\}$

and $\tilde{g}_{ij} = \langle \tilde{e}_i | \tilde{e}_j \rangle$ the metric of $\{|\tilde{e}_i\rangle\}$ respectively. The transformation laws between the basis functions can simply be obtained by means of the closure relation (Eq. (A.2))

$$|\tilde{e}_i\rangle = |e_j\rangle a_i^j = |e_j\rangle\langle e^j|\tilde{e}_i\rangle, \quad |\tilde{e}^i\rangle = |e^j\rangle b_j^i = |e^j\rangle\langle e_j|\tilde{e}^i\rangle \tag{A.15}$$

and

$$|e_i\rangle = |\tilde{e}_j\rangle \tilde{a}_i^j = |\tilde{e}_j\rangle\langle \tilde{e}^j|e_i\rangle, \quad |e^i\rangle = |\tilde{e}^j\rangle \tilde{b}_j^i = |\tilde{e}^j\rangle\langle \tilde{e}_j|e^i\rangle. \tag{A.16}$$

Be comparing the expansion coefficients we find the following relations between them $a_i^j = \tilde{b}_j^i$ and $\tilde{a}_i^j = b_j^i$ and by means of the definition of the dual basis we get $\tilde{a}_i^k \tilde{b}_k^j = \delta_i^j$ and $a_i^k b_k^j = \delta_i^j$.
In the same way the transformation laws between the matrix elements of an operator $\hat{H}$ are obtained as

$$\tilde{H}^{ij} = \tilde{a}_k^i H^{kl} \tilde{a}_l^j, \quad \tilde{H}_{ij} = a_i^k H_{kl} a_j^l \tag{A.17}$$

and

$$H^{ij} = a_k^i \tilde{H}^{kl} a_l^j, \quad H_{ij} = \tilde{a}_k^i \tilde{H}_{kl} \tilde{a}_j^l. \tag{A.18}$$

The transformations presented above are usually carried out by simple matrix multiplications, e.g. the transformation from $(\tilde{\boldsymbol{H}})_{ij} = \tilde{H}^{ij}$ to $(\boldsymbol{H})_{ij} = H_{ij}$ with the coefficient matrix $(\boldsymbol{A})_{ij} = a_j^i$ is given by

$$\tilde{\boldsymbol{H}} = \boldsymbol{A}^\dagger \boldsymbol{H} \boldsymbol{A}. \tag{A.19}$$

A.2 Fock space

Following Ref. [147] we now deal with the Fock space $\mathcal{F}$ of a fermionic system. Let $\{|e_i\rangle\}$ be a basis of the one-particle Hilbert space $\mathcal{H}_1$ of a fermionic system and $\{|e^i\rangle\}$ be its associated dual basis. A complete basis $\{D_N^i\}$ of a N-particle Hilbert space $\mathcal{H}_N$ can be build from all possible tensorial products of antisymmetrized N one-particle basis states. Furthermore we define $\mathcal{H}_0$ as the one-dimensional Hilbert space spanned by the vacuum state $|0\rangle$, where $|0\rangle$ is chosen to be the direct and the dual basis. Then $\mathcal{F}$ can be constructed from the direct sum of all possible N-particle Hilbert spaces

$$\mathcal{F} = \bigoplus_{N \geq 0} \mathcal{H}_N \tag{A.20}$$

and a basis of $\mathcal{F}$ will be given by the union $\bigcup_{N\geq 0} \{D_N^i\}$.

There vectors with the same number of particles will be nonorthogonal and orthogonal for different particle numbers. The creation and annihilation operators in $\mathcal{F}$ are defined by

$$\hat{c}_i|n_i\rangle = (-1)^{\sum_i}(1-n_i)|n_i+1\rangle \tag{A.21}$$

$$\hat{c}^i|n_i\rangle = (-1)^{\sum_i} n_i|n_i-1\rangle. \tag{A.22}$$

Here $\sum_i$ stands for all occupied one-particle states with indexes smaller than i. For $\hat{c}_i$ and $\hat{c}^i$ the following anticommutation relations hold

$$\{\hat{c}_i, \hat{c}_j\} = \left\{\hat{c}^i, \hat{c}^j\right\} = 0 \tag{A.23}$$

$$\left\{\hat{c}^i, \hat{c}_j\right\} = \delta^i_j. \tag{A.24}$$

From the definitions of $\hat{c}_i$ and $\hat{c}^i$ (Eq. (A.21) and Eq. (A.22)), it follows that they are not Hermitian conjugates to each other. Instead the Hermitian conjugation of the creation (annihilation) operator in the covariant basis is the annihilation (creation) operator in the dual basis

$$(\hat{c}_i)^\dagger|n^i\rangle = (-1)^{\sum_i} n_i|n^i-1\rangle \tag{A.25}$$

$$(\hat{c}^i)^\dagger|n^i\rangle = (-1)^{\sum_i}(1-n_i)|n^i+1\rangle. \tag{A.26}$$

The contravariant and covariant operators are related through the metric tensors of the one-particle basis [147]

$$\hat{c}_i = g_{ij}(\hat{c}^j)^\dagger, \quad \hat{c}^i = g^{ij}(\hat{c}_j)^\dagger. \tag{A.27}$$

A one-particle operator in second quantization takes the following form in, e.g., the covariant representation

$$\hat{H} = (\hat{c}^i)^\dagger H_{ij}\hat{c}^j \tag{A.28}$$

by defining $\hat{d}^\dagger_i = (\hat{c}^i)^\dagger$ and $\hat{d}_i = \hat{c}^i$ we write

$$\hat{H} = \hat{d}^\dagger_i H_{ij}\hat{d}_j. \tag{A.29}$$

This looks like the familiar representation known for orthogonal basis sets, but with different anti-commutation rules

$$\left\{\hat{d}_i, \hat{d}_j\right\} = \left\{\hat{d}_i^\dagger, \hat{d}_j^\dagger\right\} = 0 \tag{A.30}$$

$$\left\{\hat{d}_i, \hat{d}_j^\dagger\right\} = g^{ij} = (S^{-1})_{ij}. \tag{A.31}$$

However we recover indeed the orthogonal case for $(S^{-1})_{ij} = \delta_{ij}$.

To make the connection to the Green's function formalism (Appendix B), we expand the field operators in nonorthogonal basis. The field operators $\hat{\psi}^\dagger(\vec{r})$ and $\hat{\psi}(\vec{r})$ are creation and annihilation operators corresponding to position eigenstates $|\vec{r}\rangle$, $\hat{\psi}^\dagger(\vec{r})\,|0\rangle = |\vec{r}\rangle$ and $\hat{\psi}(\vec{r})\,|\vec{r}\rangle = |0\rangle$. They obey the following commutator relations

$$\left\{\hat{\psi}(\vec{r}_1), \hat{\psi}(\vec{r}_2)\right\} = \left\{\hat{\psi}^\dagger(\vec{r}_1), \hat{\psi}^\dagger(\vec{r}_2)\right\} = 0 \tag{A.32}$$

$$\left\{\hat{\psi}(\vec{r}_1), \hat{\psi}^\dagger(\vec{r}_2)\right\} = \delta(\vec{r}_1 - \vec{r}_2) \tag{A.33}$$

Expanding $|\vec{r}\rangle$ in the $\{|n_i\rangle\}$ basis yields

$$|\vec{r}\rangle = \sum_i \left|n^i\right\rangle \langle n_i|\vec{r}\rangle \tag{A.34}$$

$$= \sum_i \left|n^i\right\rangle \phi_i(\vec{r}), \tag{A.35}$$

where $\phi_i(\vec{r})$ is the representation of $\{|n_i\rangle\}$ in position space. By means of $(\hat{c}^i)^\dagger|0\rangle = \left|n^i\right\rangle$ we find

$$\hat{\psi}^\dagger(\vec{r}) = \sum_i (\hat{c}^i)^\dagger \phi_i(\vec{r}) \tag{A.36}$$

$$= \sum_i d_i^\dagger \phi_i(\vec{r}) \tag{A.37}$$

and

$$\hat{\psi}(\vec{r}) = \sum_i d_i \phi_i(\vec{r}). \tag{A.38}$$

B Nonequilibrium Green's functions

In this chapter we will introduce the nonequilibrium Green's function (NEGF) technique. We consider here just the the nonequilibrium situation. In that sense we show how we can describe the time evolution of a system out of equilibrium by means of the Keldysh formalism. The Keldysh formalism allows us to deal with time-dependent perturbations in a systematic way quite similar to equilibrium perturbation theory. This general formalism to calculate expectation values of nonequilibrium systems will then be applied to Green's functions. We will give the basic definitions of the Green's functions, and we introduce the relations important for the calculation of nonequilibrium transport properties through nanosystems. We will, however, not go into detail of the mathematical background of the Green's function technique, nor will we present detailed proofs of the introduced relations. Therefore we relate to the literature which exist on this topic. We find particularly useful Ref. [148] by R. van L. and N. E. Dahlen. and Ref. [149] by A.P Jouho which give a detailed introduction into the field of NEGF and the Keldysh formulation. A very instructive introduction to the NEGF technique in terms of applications to transport through molecular system can be found in the book on molecular electronics by J.C. Cuevas and E. Scheer [66].

B.1 Time-ordered Green's functions and perturbation theory

The system under consideration is divided into two parts, a time-independent Hamiltonian $\hat{H}_1 = \hat{H}_0 + \hat{H}_i$ where $\hat{H}_0$ is the Hamiltonian of free particles and $\hat{H}_i$ describes the interaction between them and a time-dependent perturbation $\hat{V}(t)$

$$\hat{H} = \hat{H}_0 + \hat{H}_i + \hat{V}(t). \tag{B.1}$$

We assume that $\hat{V}(t)$ can be switched on adiabatically at time $t = t_0$ and that for $t < t_0$ the system is in thermodynamic equilibrium, described by the following density matrix

$$\rho = \frac{e^{-\beta \hat{H}_1}}{\mathrm{Tr}(e^{-\beta \hat{H}_1})}, \tag{B.2}$$

with the inverse temperature $\beta = 1/k_B T$. The expectation value of an operator $\hat{A}$ at a certain time $t > t_0$ can be expressed as

$$\left\langle \hat{A} \right\rangle = \mathrm{Tr}\left\{ \hat{\rho} \hat{A}_H(t) \right\}, \tag{B.3}$$

where $\hat{A}_H(t)$ is given in the Heisenberg picture. To perform a perturbative expansion with respect to $\hat{H}_i$ and $\hat{V}(t)$ requires to express the above equation in terms of the density matrix of the non-interacting system $\hat{H}_0$ and to denote the operators in terms of creation and annihilation operators of the non-interaction system as well. For equilibrium

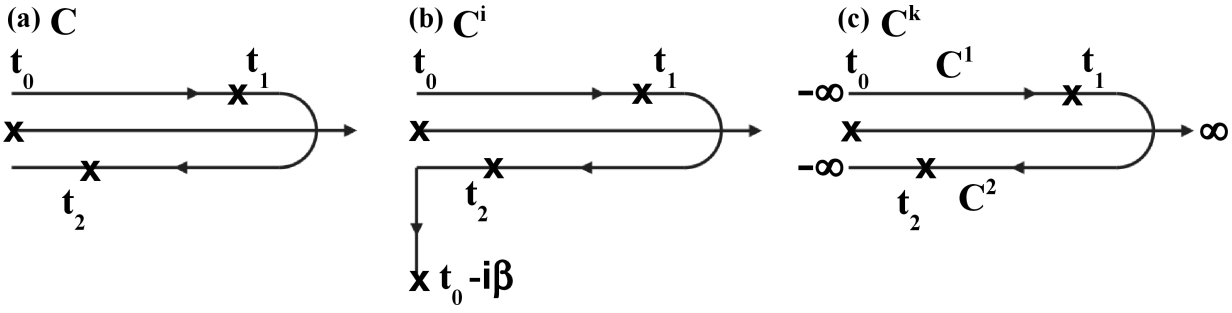

Fig. B.1: (a) Transformation contour C. (b) Interaction contour C^i. (c) Keldysh contour with upper C^1 and lower C^2 branch.

systems this can be achieved by means of the Gell-Mann and Low theorem which ensures that if the interaction is switched on adiabatically the initial non-interacting state is adiabatically coupled to the "interacting state" and when the interaction is adiabatically switched off it returns again to the initial non-interacting state [150, 149, 151, 69]. For non-equilibrium systems, however, the requirement that the systems returns to its initial state once the interaction is switched off does not hold, because the time-dependent interaction can induce transitions to excited states which do not necessarily relax to the initial ground state. To overcome this problem one introduces a "closed time path", which avoids the unknown final state by returning to the initial state at $t = t_0$. Therefore we define the contour ordered Green's function

$$G(1,2) = -\mathrm{i}\left\langle T_C\left[\psi_H(1)\psi_H^\dagger(2)\right]\right\rangle. \tag{B.4}$$

The contour C is defined in Fig. (Fig. B.1a), starts and ends at t_0 and passes every point on the contour just once, the fermionic field operators ψ_H and $\psi_H^\dagger$ (Appendix A.2) are in the Heisenberg picture and $(1) = (x_1, t_1)$ is shorthand for the set of the spatial coordinate x_1 and a time point t_1 on the contour C. The brackets $\langle ... \rangle$ donate a statistical average in the sense of Eq. (B.3). In order to apply Wicks theorem, one transforms the operators to the interaction picture using the non-interacting Hamiltonian $\hat{H}_0$. In the first step one transforms to an interaction picture such that the time-dependent perturbation is separated and $G(1,2)$ is related to an interacting equilibrium state with respect to H_1. To apply the statistical Wick theorem one performs a second transformation to an interaction picture with respect to the non-interacting and time-independent Hamiltonian H_0. The final results reads [149, 69]

$$G(1,2) = -\mathrm{i}\left\langle T_C\left[S_{C^i} S_C \psi_{H_0}(1)\psi_{H_0}^\dagger(2)\right]\right\rangle_0. \tag{B.5}$$

Here the integrals in

$$S_C = \exp\left[-\mathrm{i}\int_C \mathrm{d}\tau H'_{H_0}(\tau)\right] \tag{B.6}$$

$$S_{C^i} = \exp\left[-\mathrm{i}\int_{C^i} \mathrm{d}\tau H'_{H_0}(\tau)\right] \tag{B.7}$$

are defined along the contour C (Fig. B.1a) and C^i (Fig. B.1b), where $H'_{H_0}(\tau)$ and the field-operators ψ_{H_0} and $\hat{\psi}^\dagger_{H_0}$ are in the interaction picture with respect to $\hat{H}_0$, and the statistical average $\langle ... \rangle_0$ is performed with respect to the equilibrium density matrix $\rho_0 = \exp(-\beta\hat{H}_0)/\mathrm{Tr}\left\{\exp(-\beta\hat{H}_0)\right\}$ of the non-interaction system. In Eq. (B.4) we can now apply the statistical Wick theorem to perform a perturbative expansion [152, 153]. We can extend the two contours to minus and plus infinity, where $t_0 \to -\infty$ corresponds to neglecting the initial correlations [154] which are not import to us because we do not consider the transient regime. Extending beyond the largest time up to infinity is possible due to the unitarity of the time-evolution operator [154]. In this limit C and C^i are identical. The obtained contour is shown in Fig. B.1c and is called the Keldysh contour C^K, consisting of the upper branch C^1 which runs forward in time from $-\infty$ to ∞ and of a lower branch C^2 which runs backward in time from ∞ to $-\infty$ [155].

B.2 Keldysh formalism

The definition of the contour-ordered Green's function (Eq. (B.4)) allows to distinct between four possible locations of the two time arguments t_1 and t_2 on the Keldysh contour [149]

$$G(1,2) = \begin{cases} G_c(1,2) & t_1, t_2 \in C_1 \\ G^>(1,2) & t_1 \in C_2,\, t_2 \in C_1 \\ G^<(1,2) & t_1 \in C_1,\, t_2 \in C_2 \\ G_{\tilde{c}}(1,2) & t_1, t_2 \in C_2 \end{cases}. \tag{B.8}$$

The four different Green's functions are the time-ordered Green's function

$$\begin{aligned} G_c(1,2) &= -\mathrm{i}\left\langle T\left[\psi_H(1)\psi_H(2)\right]\right\rangle & \text{(B.9)} \\ &= -\mathrm{i}\theta(t_1-t_2)\left\langle\psi_H(1)\psi_H(2)\right\rangle + \mathrm{i}\theta(t_2-t_1)\left\langle\psi_H(2)\psi_H(1)\right\rangle, & \text{(B.10)} \end{aligned}$$

the greater Green's function

$$G^>(1,2) = -\mathrm{i}\left\langle\psi_H(1)\psi_H(2)\right\rangle, \tag{B.11}$$

the lesser Green's function

$$G^<(1,2) = \mathrm{i}\left\langle\psi_H(2)\psi_H(1)\right\rangle \tag{B.12}$$

and the antitime-ordered Green's function

$$\begin{aligned} G_{\tilde{c}}(1,2) &= -\mathrm{i}\left\langle\tilde{T}\left[\psi_H(1)\psi_H(2)\right]\right\rangle \\ &= -\mathrm{i}\theta(t_2-t_1)\left\langle\psi_H(1)\psi_H(2)\right\rangle + \mathrm{i}\theta(t_1-t_2)\left\langle\psi_H(2)\psi_H(1)\right\rangle. & \text{(B.13)} \end{aligned}$$

The four equations can be grouped in a 2×2 matrix which defines the Keldysh space

$$\breve{\boldsymbol{G}} = \begin{pmatrix} \boldsymbol{G}_c & \boldsymbol{G}^< \\ \boldsymbol{G}^> & \boldsymbol{G}_{\tilde{c}} \end{pmatrix}, \tag{B.14}$$

we also define the self-energy matrix respectively as

$$\check{\mathbf{\Sigma}} = \begin{pmatrix} \mathbf{\Sigma}_c & \mathbf{\Sigma}^< \\ \mathbf{\Sigma}^> & \mathbf{\Sigma}_{\tilde{c}} \end{pmatrix}. \tag{B.15}$$

Due to the arguments presented in the previous section, a perturbative expansion of $G(1,2)$ is possible. The following Dyson equation holds [153, 149, 66]

$$\begin{aligned} \check{\boldsymbol{G}}(1,2) = \check{\boldsymbol{g}}(1,2) &+ \int \mathrm{d}^3x_3 \int_{C^K} \mathrm{d}t_3 \check{\boldsymbol{g}}(1,3)\boldsymbol{V}(3)\check{\boldsymbol{G}}(3,2) \\ &+ \int \mathrm{d}^3x_3 \int_{C^K} \mathrm{d}t_3 \int \mathrm{d}^3x_4 \int_{C^K} \mathrm{d}t_4 \check{\boldsymbol{g}}(1,3)\hat{\Sigma}(3,4)\check{\boldsymbol{G}}(4,2), \end{aligned} \tag{B.16}$$

where we have assumed that the non-equilibrium part in Eq. (B.1) can be represented by a single particle potential $\hat{V}(x,t) = \int \mathrm{d}x \psi(x) V(x,t) \psi^\dagger(x)$.
In addition to these four Green's functions it is convenient in a lot of cases to introduce some more Green's functions by forming appropriate linear combinations of the above functions. Thus we define the retarded Green's function

$$G^r(1,2) = -\mathrm{i}\theta(t_1 - t_2) \left\langle \left\{ \psi_H(1) \psi_H^\dagger(2) \right\} \right\rangle = \theta(t_1 - t_2) \left[G^>(1,2) - G^<(1,2) \right] \tag{B.17}$$

and the advance Green's function

$$G^a(1,2) = -\mathrm{i}\theta(t_2 - t_1) \left\langle \left\{ \psi_H(1) \psi_H^\dagger(2) \right\} \right\rangle = \theta(t_2 - t_1) \left[G^<(1,2) - G^>(1,2) \right]. \tag{B.18}$$

Since only three of the four Green's functions are linearly independent, we can introduce a new set of equations [66]

$$\tilde{\boldsymbol{G}} = \begin{pmatrix} 0 & \boldsymbol{G}^a \\ \boldsymbol{G}^r & \boldsymbol{G}^K \end{pmatrix}, \tag{B.19}$$

where in addition to the previously introduced G^r and G^a, we have defined the Keldysh function $G^K = G^< + G^> = G_c + G_{\tilde{c}}$. A similar representation exist for the self-energy matrix

$$\tilde{\mathbf{\Sigma}} = \begin{pmatrix} \mathbf{\Sigma}^K & \mathbf{\Sigma}^r \\ \mathbf{\Sigma}^a & \mathbf{0} \end{pmatrix}, \tag{B.20}$$

with $\mathbf{\Sigma}^K = \mathbf{\Sigma}_c + \mathbf{\Sigma}_{\tilde{c}} = -(\mathbf{\Sigma}^< + \mathbf{\Sigma}^>)$, $\mathbf{\Sigma}^r = \mathbf{\Sigma}_c + \mathbf{\Sigma}^< = -(\mathbf{\Sigma}_{\tilde{c}} + \mathbf{\Sigma}^>)$ and $\mathbf{\Sigma}^a = \mathbf{\Sigma}_c + \mathbf{\Sigma}^> = -(\mathbf{\Sigma}_{\tilde{c}} + \mathbf{\Sigma}^<)$.
In the following the integration over intermediate arguments is implicitly assumed. Eq. (B.16) then reads

$$\check{\boldsymbol{G}} = \check{\boldsymbol{g}} + \check{\boldsymbol{g}}\check{\mathbf{\Sigma}}\check{\mathbf{G}}. \tag{B.21}$$

By means of Eq. (B.19) and Eq. (B.20) relations between the different Green's functions can be derived. We will just state the most important relations here. For their derivation we refer for example to Refs. [66] and [149]. We have for each element of Eq. (B.19) an independent Dyson's equation

$$\boldsymbol{G}^{r,a} = \boldsymbol{g}^{r,a} + \boldsymbol{g}^{r,a}\mathbf{\Sigma}^{r,a}\boldsymbol{G}^{r,a} \tag{B.22}$$

$$\boldsymbol{G}^K = \boldsymbol{g}^K + \boldsymbol{g}^K\boldsymbol{\Sigma}^a\boldsymbol{G}^a + \boldsymbol{g}^r\boldsymbol{\Sigma}^r\boldsymbol{G}^K + \boldsymbol{g}^r\boldsymbol{\Sigma}^K\boldsymbol{G}^a. \tag{B.23}$$

As $G^<$ and $G^>$ are of special interest for the calculation of the current through molecular systems we give in addition their Dyson's equations

$$\boldsymbol{G}^< = (\mathbf{1} + \boldsymbol{G}^r\boldsymbol{\Sigma}^r)\boldsymbol{g}^<(1 + \boldsymbol{\Sigma}^a\boldsymbol{G}^a) - \boldsymbol{G}^r\boldsymbol{\Sigma}^<\boldsymbol{G}^a \tag{B.24}$$

$$\boldsymbol{G}^> = (\mathbf{1} + \boldsymbol{G}^r\boldsymbol{\Sigma}^r)\boldsymbol{g}^>(1 + \boldsymbol{\Sigma}^a\boldsymbol{G}^a) - \boldsymbol{G}^r\boldsymbol{\Sigma}^>\boldsymbol{G}^a. \tag{B.25}$$

B.3 Equation of motion for $G^<$ and G^r

To derive the equation of motion for $G^<(t,t')$ and $G^r(t,t')$ we first express the field operators in Eq. (B.12) and Eq. (B.17) in second quantization by means of Eq. (A.33)

$$G^<_{ij} = \mathrm{i}\left\langle d^\dagger_j(t')d_i(t)\right\rangle \tag{B.26}$$

$$G^r_{ij} = -\mathrm{i}\theta(t-t')\left\langle\left\{d_i(t)d_j(t')\right\}\right\rangle \tag{B.27}$$

We will need the time derivative of the creation $d_i^\dagger$ and annihilation d_i operators. However, we have to take into account the nonorthogonal basis. In the following the system is described by an effective single particle Hamiltonian of the form given in Eq. (4.1). The time evolution is determined by the Heisenberg equation of motion. Thus, one finds

$$\frac{\partial}{\partial t}d_i = [d_i, H] = \sum_{kl}(S^{-1})_{ik}H_{kl}d_l \tag{B.28}$$

and

$$\frac{\partial}{\partial t}d_i^\dagger = \left[d_i^\dagger, H\right] = -\sum_{kl} d_k^\dagger H_{kl}(S^{-1})_{li}. \tag{B.29}$$

The time derivative of $G^<(t,t')$ with respect to t is than given by

$$\mathrm{i}\hbar\frac{\partial}{\partial t}G^<_{ij}(t,t') = \mathrm{i}\left\langle d^\dagger_j(t')\frac{\partial}{\partial t}d_i(t)\right\rangle = \sum_{kl}(S^{-1})_{ik}H_{kl}\left\langle d^\dagger_j(t')d_l(t)\right\rangle \tag{B.30}$$

$$= \sum_{kl}(S^{-1})_{ik}H_{kl}G^<_{lj}(t,t') \tag{B.31}$$

and for t' by

$$-\mathrm{i}\hbar\frac{\partial}{\partial t'}G^<_{ij}(t,t') = \mathrm{i}\left\langle d^\dagger_j(t')\frac{\partial}{\partial t'}d_i(t)\right\rangle = \sum_{kl}\left\langle d^\dagger_j(t')d_l(t)\right\rangle H_{lk}(S^{-1})_{ki} \tag{B.32}$$

$$= \sum_{kl}G^<_{ik}(t,t')H_{kl}(S^{-1})_{lj} \tag{B.33}$$

respectively. Writing the above equation in matrix from and multiplying with S from the left or right yields

$$\mathrm{i}\hbar\frac{\partial}{\partial t}\boldsymbol{S}\boldsymbol{G}^{<}(t,t') = \boldsymbol{H}\boldsymbol{G}^{<}(t,t') \tag{B.34}$$

and

$$-\mathrm{i}\hbar\frac{\partial}{\partial t'}\boldsymbol{G}^{<}(t,t')\boldsymbol{S} = \boldsymbol{G}^{<}(t,t')\boldsymbol{H}. \tag{B.35}$$

As we will need the explicit matrix with respect to L,C and R later (see Sec. Section 4.1), we rewrite them in block matrix form according to L,C and R

$$\begin{aligned}
&\mathrm{i}\hbar\frac{\partial}{\partial t}\begin{pmatrix} S_{LC}G^{<}_{CL}+S_{LL}G^{<}_{LL} & S_{LC}G^{<}_{CC}+S_{LL}G^{<}_{LC} & S_{LC}G^{<}_{CR}+S_{LL}G^{<}_{LR} \\ S_{CC}G^{<}_{CL}+S_{CL}G^{<}_{LL}+S_{CR}G^{<}_{RL} & S_{CC}G^{<}_{CC}+S_{CL}G^{<}_{LC}+S_{CR}G^{<}_{RC} & S_{CC}G^{<}_{CR}+S_{CL}G^{<}_{LR}+S_{CR}G^{<}_{RR} \\ S_{RC}G^{<}_{CL}+S_{RR}G^{<}_{RL} & S_{RC}G^{<}_{CC}+S_{RR}G^{<}_{RC} & S_{RC}G^{<}_{CR}+S_{RR}G^{<}_{RR} \end{pmatrix} \\
&= \begin{pmatrix} H_{LC}G^{<}_{CL}+H_{LL}G^{<}_{LL} & H_{LC}G^{<}_{CC}+H_{LL}G^{<}_{LC} & H_{LC}G^{<}_{CR}+H_{LL}G^{<}_{LR} \\ H_{CC}G^{<}_{CL}+H_{CL}G^{<}_{LL}+H_{CR}G^{<}_{RL} & H_{CC}G^{<}_{CC}+H_{CL}G^{<}_{LC}+H_{CR}G^{<}_{RC} & H_{CC}G^{<}_{CR}+H_{CL}G^{<}_{LR}+H_{CR}G^{<}_{RR} \\ H_{RC}G^{<}_{CL}+H_{RR}G^{<}_{RL} & H_{RC}G^{<}_{CC}+H_{RR}G^{<}_{RC} & H_{RC}G^{<}_{CR}+H_{RR}G^{<}_{RR} \end{pmatrix}
\end{aligned} \tag{B.36}$$

$$\begin{aligned}
&-\mathrm{i}\hbar\frac{\partial}{\partial t'}\begin{pmatrix} G^{<}_{LC}S_{CL}+G^{<}_{LL}S_{LL} & G^{<}_{LC}S_{CC}+G^{<}_{LL}S_{LC}+G^{<}_{LR}S_{RC} & G^{<}_{LC}S_{CR}+G^{<}_{LR}S_{RR} \\ G^{<}_{CC}S_{CL}+G^{<}_{CL}S_{LL} & G^{<}_{CC}S_{CC}+G^{<}_{CL}S_{LC}+G^{<}_{CR}S_{RC} & G^{<}_{CC}S_{CR}+G^{<}_{CR}S_{RR} \\ G^{<}_{RC}S_{CL}+G^{<}_{RL}S_{LL} & G^{<}_{RC}S_{CC}+G^{<}_{RL}S_{LC}+G^{<}_{RR}S_{RC} & G^{<}_{RC}S_{CR}+G^{<}_{RR}S_{RR} \end{pmatrix} \\
&= \begin{pmatrix} G^{<}_{LC}H_{CL}+G^{<}_{LL}H_{LL} & G^{<}_{LC}H_{CC}+G^{<}_{LL}H_{LC}+G^{<}_{LR}H_{RC} & G^{<}_{LC}H_{CR}+G^{<}_{LR}H_{RR} \\ G^{<}_{CC}H_{CL}+G^{<}_{CL}H_{LL} & G^{<}_{CC}H_{CC}+G^{<}_{CL}H_{LC}+G^{<}_{CR}H_{RC} & G^{<}_{CC}H_{CR}+G^{<}_{CR}H_{RR} \\ G^{<}_{RC}H_{CL}+G^{<}_{RL}H_{LL} & G^{<}_{RC}H_{CC}+G^{<}_{RL}H_{LC}+G^{<}_{RR}H_{RC} & G^{<}_{RC}H_{CR}+G^{<}_{RR}H_{RR} \end{pmatrix}.
\end{aligned} \tag{B.37}$$

For $G^r(t,t')$ we obtain in the same way

$$\mathrm{i}\hbar\frac{\partial}{\partial t}G^r_{ij}(t,t') = \delta(t-t')[S^{-1}]_{il} + \sum_{kl}[S^{-1}]_{ik}H_{kl}G^r_{lj}(t,t'). \tag{B.38}$$

Multiplying the above equation from the left with S and writing the equation in matrix form yields

$$\left[\mathrm{i}\hbar\boldsymbol{S}\frac{\partial}{\partial t} - \boldsymbol{H}\right]\boldsymbol{G}^r(t,t) = \mathbf{1}\delta(t-t'). \tag{B.39}$$

B.4 Perturbation theory for the lead coupling

Here we derive a explicit formula for the central part of G^r, which appears in the equation for the current (Eq. (4.16)). The coupling to the leads is treated as a single particle perturbation of the central part. Assuming that we are in a steady state of the system we can Fourier transform the equation of motion for G^r (Eq. (B.39))

$$[E^+\boldsymbol{S} - \boldsymbol{H}]\boldsymbol{G}^r(E) = \mathbf{1}, \tag{B.40}$$

where $E^+ = E + \mathrm{i}\eta$ with a small broadening $\eta = 0^+$. (Implicitly we take the limit $\eta \to 0$ at appropriate situations during the calculations.) Considering the definition of $\boldsymbol{H}$ and

$\boldsymbol{S}$ (Eq. (4.2)) we can write [26]

$$\begin{pmatrix} E^+\boldsymbol{S}_{LL}-\boldsymbol{H}_{LL} & E^+\boldsymbol{S}_{LC}-\boldsymbol{H}_{LC} & 0 \\ E^+\boldsymbol{S}_{CL}-\boldsymbol{H}_{CL} & E^+\boldsymbol{S}_{CC}-\boldsymbol{H}_{CC} & E^+\boldsymbol{S}_{RC}-\boldsymbol{H}_{RC} \\ 0 & E^+\boldsymbol{S}_{CR}-\boldsymbol{H}_{CR} & E^+\boldsymbol{S}_{RR}-\boldsymbol{H}_{RR} \end{pmatrix} \begin{pmatrix} \boldsymbol{G}_{LL} & \boldsymbol{G}_{LC} & \boldsymbol{G}_{LR} \\ \boldsymbol{G}_{CL} & \boldsymbol{G}_{CC} & \boldsymbol{G}_{CR} \\ \boldsymbol{G}_{RL} & \boldsymbol{G}_{RC} & \boldsymbol{G}_{RR} \end{pmatrix} = \begin{pmatrix} 1_{LL} & \mathbf{0} & \mathbf{0} \\ \mathbf{0} & 1_{CC} & \mathbf{0} \\ \mathbf{0} & \mathbf{0} & 1_{RR} \end{pmatrix}. \tag{B.41}$$

Now we will tread the couplings of the central part C to the left and right leads ($X = L, R$) as perturbation

$$\boldsymbol{t}_{CX} = \boldsymbol{H}_{CX} - E\boldsymbol{S}_{CX} = (\boldsymbol{t}_{XC})^T. \tag{B.42}$$

The Green's function for the central system can be directly obtained from the matrix equation (Eq. (B.39))

$$\boldsymbol{G}^r_{CC}(E) = (E^+\boldsymbol{S}_{CC} - \boldsymbol{H}_{CC} - \boldsymbol{\Sigma}^r_L(E) - \boldsymbol{\Sigma}^r_R(E)) \tag{B.43}$$

$$\boldsymbol{\Sigma}^r_X(E) = \boldsymbol{t}_{CX} g^r_{XX} \boldsymbol{t}_{XC}, \tag{B.44}$$

where we have defined the self-energies Σ^r_X and the free Green's functions g^r_{XX} of the leads. The Green's functions are formally given by

$$g^r_{XX} = \left(E^+ S_{XX} - H_{XX}\right)^{-1}, \tag{B.45}$$

but one has to keep in mind that we are describing a infinite system and g^r_{XX} are semi-infinitely dimensional matrices which cannot be calculated directly. Due to the finite-range couplings t_{CX}, we model them as surface Green's functions describing the semi-infinite leads as finite effective surfaces. For details about their calculations within the cluster-based transport formalism we refer to Ref. [26].

C Wide-band limit for the inelastic current

The calculation of the inelastic current requires to evaluate (numerically) two dimensional energy integrals over the whole energy range from minus infinity to plus infinity. Hence, it is computationally a very cumbersome task and practically extremely time-consuming. Therefore we consider the so called wide-band limit (WBL). It takes advantage of the fact that in the energy window around E_F relevant for transport, is typically of the order of $eU + k_BT$, with $U = 50\,\text{meV}$and $T = 10\,\text{K}$, while the scale on which the density of states of the gold leads vary is of the order of several eV. Therefore we assume that we can evaluate all electronic Green's functions at the Fermi energy.

Furthermore, we will not consider the renormalization of the phonon density of states (DOS) and use the DOS of free phonons as an approximation

$$\rho_\alpha(\epsilon) = \frac{1}{\pi}\left(\frac{\eta/2}{(\epsilon-\epsilon_\alpha)^2+\eta^2/4} - \frac{\eta/2}{(\epsilon+\epsilon_\alpha)^2+\eta^2/4}\right) \tag{C.1}$$

In the expression we keep $\eta > 0$ finite to describe the broadening of the phonons due to their coupling to the leads. This leads then also to the approximation of the full phonon Green's function $D^r_\alpha(\epsilon)$ by the free propagators

$$D^r_\alpha(\epsilon) \approx d^r_\alpha(\epsilon) = \frac{2\epsilon_\alpha}{\epsilon^2-\epsilon_\alpha^2+\mathrm{i}\eta\epsilon-\eta^2/4}, \tag{C.2}$$

where we keep η finite again.

Before deriving the current formulas in the WBL we will give some analytical solutions to integrals over Fermi functions and present some other useful relations between Fermi and Bose functions.

C.1 Useful integrals and relations

In the following chapter we will encounter improper energy integrals over Fermi functions, which can be calculated analytically. The most important relations are summarized here. First we state some important indefinite integrals

$$\begin{aligned}\int \mathrm{d}x \frac{1}{\mathrm{e}^{x-a}+1} &= \int \mathrm{d}x \frac{\mathrm{e}^a}{\mathrm{e}^x+\mathrm{e}^a} = \int \mathrm{d}u \frac{1}{u}\cdot\frac{\mathrm{e}^a}{u+\mathrm{e}^a} \\ &= \int \mathrm{d}u \frac{1}{u} - \frac{1}{\mathrm{e}^a+u} = \ln(u) - \ln(\mathrm{e}^a+u) = x - \ln(\mathrm{e}^a+\mathrm{e}^x) + c,\end{aligned}$$

$$\int \mathrm{d}x \frac{1}{\mathrm{e}^{x-a}+1} = x - \ln(\mathrm{e}^a+\mathrm{e}^x) + c, \tag{C.3}$$

$$\begin{aligned}\int \mathrm{d}x \frac{1}{\mathrm{e}^{x-a}+1}\cdot\frac{1}{\mathrm{e}^{x-b}+1} &= \int \mathrm{d}x \frac{\mathrm{e}^a}{\mathrm{e}^x+\mathrm{e}^a}\cdot\frac{\mathrm{e}^b}{\mathrm{e}^x+\mathrm{e}^b} = \int \mathrm{d}u \frac{1}{u}\frac{\mathrm{e}^a}{u+\mathrm{e}^a}\cdot\frac{\mathrm{e}^b}{u+\mathrm{e}^b} \\ &= \int \mathrm{d}u \left(\frac{1}{u} + \frac{\mathrm{e}^b}{(\mathrm{e}^a-\mathrm{e}^b)(u+\mathrm{e}^a)} - \frac{\mathrm{e}^a}{(\mathrm{e}^a-\mathrm{e}^b)(u+\mathrm{e}^b)}\right) \\ &= x + \frac{\mathrm{e}^b}{(\mathrm{e}^a-\mathrm{e}^b)}\ln(\mathrm{e}^x+\mathrm{e}^a) - \frac{\mathrm{e}^a}{(\mathrm{e}^a-\mathrm{e}^b)}\ln(\mathrm{e}^x+\mathrm{e}^b) + c,\end{aligned}$$

and

$$\int \mathrm{d}x \frac{1}{\mathrm{e}^{x-a}+1}\cdot\frac{1}{\mathrm{e}^{x-b}+1} = x + \frac{\mathrm{e}^{b}}{(\mathrm{e}^{a}-\mathrm{e}^{b})}\ln(\mathrm{e}^{x}+\mathrm{e}^{a}) - \frac{\mathrm{e}^{a}}{(\mathrm{e}^{a}-\mathrm{e}^{b})}\ln(\mathrm{e}^{x}+\mathrm{e}^{b}) + c. \quad \text{(C.4)}$$

With the help of these indefinite integral we can obtain the following improper energy integrals over the Fermi functions

$$\int_{-\infty}^{\infty} \mathrm{d}x \frac{1}{\mathrm{e}^{x-a}+1} - \frac{1}{\mathrm{e}^{x-b}+1} = a - b, \quad \text{(C.5)}$$

$$\int_{-\infty}^{\infty} \mathrm{d}x \frac{1}{\mathrm{e}^{x-a}+1}\left(1 - \frac{1}{\mathrm{e}^{x-b}+1}\right) = \frac{a-b}{1-\mathrm{e}^{b-a}}, \quad \text{(C.6)}$$

and

$$\int_{-\infty}^{\infty} \mathrm{d}x \frac{1}{\mathrm{e}^{x-a}+1}\left(\frac{1}{\mathrm{e}^{x-b}+1} - \frac{1}{\mathrm{e}^{x-c}+1}\right) = \frac{a-c}{1-\mathrm{e}^{b-a}} - \frac{a-b}{1-\mathrm{e}^{b-a}}. \quad \text{(C.7)}$$

For Bose distribution like functions the following relation holds

$$n(-x) = \frac{1}{\mathrm{e}^{-x}-1} = -1 - \frac{1}{\mathrm{e}^{x}-1} = -1 - n(x). \quad \text{(C.8)}$$

C.2 Current formulas in the Wide-band limit

The current formulas in the lowest order expansion given by the Eq. (4.52), Eq. (4.53) and Eq. (4.54) can be brought into the following form [22]

$$I^{0}_{el} = G_0 \int \mathrm{d}\epsilon T_0(\epsilon)\left(f_L(\epsilon) - f_R(\epsilon)\right) \quad \text{(C.9)}$$

$$\begin{aligned}\delta I^{0}_{el} = G_0 \sum_{\alpha}\Big\{ \int \mathrm{d}\epsilon \sum_{\sigma=\pm 1} \sigma \int_{0}^{\infty} \mathrm{d}\omega_1 \rho_{\alpha}(\omega_1) \left[T^{ec}_{\sigma\alpha}(\epsilon,\omega_1) + T^{ecL}_{\sigma\alpha}(\epsilon,\omega_1) f_L(\epsilon_\sigma) + T^{ecR}_{\sigma\alpha}(\epsilon,\omega_1) f_R(\epsilon_\sigma)\right] \\ \times \left(f_L(\epsilon) - f_R(\epsilon)\right) + \int \mathrm{d}\epsilon \left(-J^{L}_{\alpha}(\epsilon) - J^{R}_{\alpha}(\epsilon) + T^{II}_{\alpha}(\epsilon)\left[J^{IIL}_{\alpha} + J^{IIR}_{\alpha}\right]\right)\left(f_L(\epsilon) - f_R(\epsilon)\right)\Big\}\end{aligned} \quad \text{(C.10)}$$

$$I_{inel} = G_0 \sum_{\alpha} \Big\{ \int \mathrm{d}\epsilon \sum_{\sigma=\pm 1} \sigma \int_0^{\infty} \rho_{\alpha}(\omega_1) T^{in}_{\sigma\alpha}(\epsilon,\omega_1) \Big(N_{\alpha}(\sigma\omega_1) f_L(\epsilon)\left[1 - f_R(\epsilon_{\sigma\alpha})\right] + N_{\alpha}(-\sigma\omega_1) f_R(\epsilon_{\sigma\alpha})\left[1 - f_L(\epsilon)\right] \Big) \Big\}. \tag{C.11}$$

where $\epsilon_{\sigma} = \epsilon + \sigma\omega_1$ and $\sum_{\alpha}$ runs over all (non zero) vibrational modes. The energy dependent transmission functions are defined as follows

$$T_0(\epsilon) = \mathrm{Tr}\left[G^r(\epsilon)\Gamma_R(\epsilon)G^a(\epsilon)\Gamma_L(\epsilon)\right] \tag{C.12}$$

$$T^{ec}_{\sigma\alpha}(\epsilon,\omega_1) = 2\mathrm{Re}\ \mathrm{Tr}\left[G^r(\epsilon)\Gamma_R(\epsilon)G^a(\epsilon)\Gamma_L(\epsilon)G^r(\epsilon)\lambda^{\alpha}G^r(\epsilon_{\sigma})\lambda^{\alpha}\right] \tag{C.13}$$

$$T^{ecL}_{\sigma\alpha}(\epsilon,\omega_1) = \mathrm{Im}\ \mathrm{Tr}\left[G^r(\epsilon)\Gamma_R(\epsilon)G^a(\epsilon)\Gamma_L(\epsilon)G^r(\epsilon)\lambda^{\alpha}G^r(\epsilon_{\sigma})\Gamma_L(\epsilon_{\sigma})G^a(\epsilon_{\sigma})\lambda^{\alpha}\right] \tag{C.14}$$

$$T^{ecR}_{\sigma\alpha}(\epsilon,\omega_1) = \mathrm{Im}\ \mathrm{Tr}\left[G^r(\epsilon)\Gamma_R(\epsilon)G^a(\epsilon)\Gamma_L(\epsilon)G^r(\epsilon)\lambda^{\alpha}G^r(\epsilon_{\sigma})\Gamma_R(\epsilon_{\sigma})G^a(\epsilon_{\sigma})\lambda^{\alpha}\right] \tag{C.15}$$

$$T^{in}_{\sigma\alpha}(\epsilon,\omega_1) = \mathrm{Tr}\left[G^r(\epsilon_{\sigma})\Gamma_R(\epsilon_{\sigma})G^a(\epsilon_{\sigma})\lambda^{\alpha}G^a(\epsilon)\Gamma_L(\epsilon)G^r(\epsilon_{\sigma})\lambda^{\alpha}\right] \tag{C.16}$$

$$T^{II}_{\alpha}(\epsilon,\omega_1) = 2\mathrm{Re}\ \mathrm{Tr}\left[G^r(\epsilon)\Gamma_R(\epsilon)G^a(\epsilon)\Gamma_L(\epsilon)G^r(\epsilon)\lambda^{\alpha}\right] \tag{C.17}$$

The factors $J^L_{\alpha}(\epsilon)$ and $J^R_{\alpha}(\epsilon)$ are given by the energy integrals

$$J^L_{\alpha}(\epsilon) = \frac{1}{\pi}\int \mathrm{d}\omega_1 \mathrm{Re}\left[D^r_{\alpha}(\omega_1)\right] T^{JL}_{\alpha}(\epsilon,\omega_1) f_L(\epsilon-\omega_1), \tag{C.18}$$

$$J^R_{\alpha}(\epsilon) = \frac{1}{\pi}\int \mathrm{d}\omega_1 \mathrm{Re}\left[D^r_{\alpha}(\omega_1)\right] T^{JR}_{\alpha}(\epsilon,\omega_1) f_R(\epsilon-\omega_1) \tag{C.19}$$

with

$$T^{JL}_{\alpha}(\epsilon,\omega_1) = \mathrm{ReTr}\left[\boldsymbol{G}^r(\epsilon)\Gamma_R(\epsilon)G^a(\epsilon)\Gamma_L(\epsilon)G^r(\epsilon)\lambda^{\alpha}G^r(\epsilon-\omega_1)\Gamma_L(\epsilon-\omega_1)G^a(\epsilon-\omega_1)\lambda^{\alpha}\right] \tag{C.20}$$

$$T^{JR}_{\alpha}(\epsilon,\omega_1) = \mathrm{ReTr}\left[G^r(\epsilon)\Gamma_R(\epsilon)G^a(\epsilon)\Gamma_L(\epsilon)G^r(\epsilon)\lambda^{\alpha}G^r(\epsilon-\omega_1)\Gamma_R(\epsilon-\omega_1)G^a(\epsilon-\omega_1)\lambda^{\alpha}\right] \tag{C.21}$$

and the factors $J^{IIL}_{\alpha}(\epsilon)$ and $J^{IIR}_{\alpha}(\epsilon)$ are given by

$$J^{IIL}_{\alpha} = \frac{D^r_{\alpha}(0)}{2\pi}\int \mathrm{d}\omega_1 T^{JIIL}_{\alpha}(\omega_1) f_L(\omega_1) \tag{C.22}$$

$$J_\alpha^{IIR} = \frac{D_\alpha^r(0)}{2\pi} \int \mathrm{d}\omega_1 T_\alpha^{JIIR}(\omega_1) f_R(\omega_1) \tag{C.23}$$

with

$$T_\alpha^{JIIL}(\omega_1) = \mathrm{Tr}[G^r(\omega_1)\Gamma_L(\omega_1)G^a(\omega_1)\lambda^\alpha] \tag{C.24}$$

$$T_\alpha^{JIIR}(\omega_1) = \mathrm{Tr}[G^r(\omega_1)\Gamma_R(\omega_1)G^a(\omega_1)\lambda^\alpha]. \tag{C.25}$$

The distribution function

$$N_\alpha(\epsilon) = -\frac{1}{2}\frac{\mathrm{Im}\Pi_\alpha^{+-}(\epsilon) + n(\epsilon)\eta\epsilon/\epsilon_\alpha}{\mathrm{Im}\Pi_\alpha^r(\epsilon) - \eta\epsilon/(2\epsilon_\alpha)} \tag{C.26}$$

takes the nonequilibrium occupation of the phonons into account.

Considering now the current formulas Eq. (C.9)-Eq. (C.11) in WBL gives

$$I_{el}^0 = G_0 T_0(E_F) \int \mathrm{d}\epsilon \left(f_L(\epsilon) - f_R(\epsilon)\right), \tag{C.27}$$

$$\begin{aligned}
\delta I_{el}^0 = G_0 \sum_\alpha \Big\{ \int_0^\infty \mathrm{d}\omega_1 \rho_\alpha(\omega_1) \Big(& T_\alpha^{ec}(E_F) \left[N(\omega_1) - N(-\omega_1)\right] \int \mathrm{d}\epsilon \left(f_L(\epsilon) - f_R(\epsilon)\right) + \\
& T_\alpha^{ecL}(E_F) \int \mathrm{d}\epsilon \left(f_L(\epsilon+\omega_1) - f_L(\epsilon-\omega_1)\right)\left(f_L(\epsilon) - f_R(\epsilon)\right) + \\
& T_\alpha^{ecR}(E_F) \int \mathrm{d}\epsilon \left(f_R(\epsilon+\omega_1) - f_R(\epsilon-\omega_1)\right)\left(f_L(\epsilon) - f_R(\epsilon)\right) \Big) + \\
& -\frac{1}{\pi} T_\alpha^{JL}(E_F) \int \mathrm{d}\omega_1 \mathrm{Re}\left[D_\alpha^r(\omega_1)\right] \int \mathrm{d}\epsilon f_L(\epsilon-\omega_1)\left(f_L(\epsilon) - f_R(\epsilon)\right) + \\
& -\frac{1}{\pi} T_\alpha^{JR}(E_F) \int \mathrm{d}\omega_1 \mathrm{Re}\left[D_\alpha^r(\omega_1)\right] \int \mathrm{d}\epsilon f_R(\epsilon-\omega_1)\left(f_L(\epsilon) - f_R(\epsilon)\right) + \\
& T_\alpha^{II}(E_F) \left[J_\alpha^{IIL} + J_\alpha^{IIR}\right] \int \mathrm{d}\epsilon \left(f_L(\epsilon) - f_R(\epsilon)\right)
\end{aligned} \tag{C.28}$$

$$\begin{aligned}
I_{inel}^L = G_0 \sum_\alpha \Big\{ \int_0^\infty \rho_\alpha(\omega_1) T_\alpha^{in}(E_F) \times \Big(& N_\alpha(\omega_1) \int \mathrm{d}\epsilon f_L(\epsilon)\left[1 - f_R(\epsilon+\omega_1)\right] - \\
N_\alpha(-\omega_1) \int \mathrm{d}\epsilon f_L(\epsilon)\left[1 - f_R(\epsilon-\omega_1)\right] + & N_\alpha(-\omega_1) \int \mathrm{d}\epsilon f_R(\epsilon+\omega_1)\left[1 - f_L(\epsilon)\right] - \\
& N_\alpha(\omega_1) \int \mathrm{d}\epsilon f_R(\epsilon-\omega)\left[1 - f_L(\epsilon)\right] \Big)
\end{aligned} \tag{C.29}$$

What remains to be calculated after taking the transmission functions just at E_F are integrals over different products of Fermi functions for which we can evaluate one energy integration analytical. The Fermi-functions are defined

$$f_{L,R}(\epsilon) = \frac{1}{e^{(\epsilon-\mu_{L,R})\beta}+1}$$

with $\mu_{L,R} = E_F \pm \frac{eV}{2}$ and $\beta = \frac{1}{kT}$. Explicitly we have the following integrals

$$\int d\epsilon \left(f_L(\epsilon) - f_R(\epsilon)\right) = \mu_L - \mu_R = U, \tag{C.30}$$

$$\begin{gathered}\int d\epsilon \left(f_L(\epsilon+\omega_1) - f_L(\epsilon-\omega_1)\right)\left[f_L(\epsilon) - f_R(\epsilon)\right] = \\ \frac{\mu_L-\omega_1-\mu_R}{1-e^{\beta(\mu_R-(\mu_L-\omega_1))}} - \frac{-\omega_1}{1-e^{\beta(\mu_L-(\mu_L-\omega_1))}} - \frac{\mu_L+\omega_1-\mu_R}{1-e^{\beta(\mu_R-(\mu_L+\omega_1))}} + \frac{\omega_1}{1-e^{\beta(\mu_L-(\mu_L+\omega_1))}} = \\ (\omega_1-U)n(\omega_1-U) - \omega_1 n(\omega_1) + (\omega_1+U)n(-(U+\omega_1)) - \omega_1 n(-\omega_1) = \\ (\omega_1-U)n(\omega_1-U) - \omega_1 n(\omega_1) + (U+\omega_1)(-1-n(U+\omega_1)) - \omega_1(-1-n(\omega_1)) = \\ -U + (\omega_1-U)n(\omega_1-U) - (\omega_1+U)n(\omega_1+U)\end{gathered} \tag{C.31}$$

$$\begin{gathered}\int d\epsilon \left(f_R(\epsilon+\omega_1) - f_R(\epsilon-\omega_1)\right)\left[f_L(\epsilon) - f_R(\epsilon)\right] = \\ \frac{-\omega_1}{1-e^{\beta(\mu_R-(\mu_R-\omega_1))}} - \frac{\mu_R-\omega_1-\mu_L}{1-e^{\beta(\mu_L-(\mu_R-\omega_1))}} - \frac{\omega_1}{1-e^{\beta(\mu_R-(\mu_R+\omega_1))}} + \frac{\mu_R+\omega_1-\mu_L}{1-e^{\beta(\mu_L-(\mu_R+\omega_1))}} = \\ \omega_1 n(\omega_1) - (\omega_1+U)n(\omega_1+U) + \omega_1 n(-\omega_1) - (\omega_1-U)n(-(\omega_1-U)) \\ \omega_1 n(\omega_1) - (\omega_1+U)n(\omega_1+U) + \omega_1(-1-n(\omega_1)) - (\omega_1-U)(-1-n(\omega_1-U)) \\ -U + (\omega_1-U)n(\omega_1-U) - (\omega_1+U)n(\omega_1+U)\end{gathered} \tag{C.32}$$

$$\begin{gathered}\int d\epsilon f_L(\epsilon-\omega_1)[f_L(\epsilon) - f_R(\epsilon)] = \frac{\mu_L+\omega_1-\mu_R}{1-e^{\beta(\mu_R-(\omega_1+\mu_L))}} - \frac{\omega_1}{1-e^{-\beta\omega_1}} = \\ -(\omega_1+U)n(-\omega_1-U) + \omega_1 n(-\omega_1) = \\ (\omega_1+U) + (\omega_1+U)n(\omega_1+U) - \omega_1 - \omega_1 n(\omega_1) = \\ U + (\omega_1+U)n(\omega_1+U) - \omega_1 n(\omega_1)\end{gathered} \tag{C.33}$$

$$\begin{gathered}\int d\epsilon f_R(\epsilon-\omega_1)[f_L(\epsilon) - f_R(\epsilon)] = \frac{\omega_1}{1-e^{-\beta\omega_1}} - \frac{\mu_R+\omega_1-\mu_L}{1-e^{\beta(\mu_L-(\omega_1+\mu_R))}} = \\ -\omega_1 n(-\omega_1) + (\omega_1-U)n(-\omega_1+U)\end{gathered}$$

$$\int \mathrm{d}\epsilon f_L(\epsilon)\left[1-f_R(\epsilon+\omega_1)\right] = \frac{\mu_L-(\mu_R-\omega_1)}{1-\mathrm{e}^{\beta((\mu_R-\omega_1)-\mu_L)}} = -(\omega_1+U)n(-U-\omega_1) = (\omega_1+U)+(\omega_1+U)n(\omega_1+U) \tag{C.34}$$

$$\int \mathrm{d}\epsilon f_L(\epsilon)\left[1-f_R(\epsilon-\omega_1)\right] = \frac{\mu_L-(\mu_R+\omega_1)}{1-\mathrm{e}^{\beta((\mu_R+\omega_1)-\mu_L)}} = (\omega_1-U)n(\omega_1-U) \tag{C.35}$$

$$\int \mathrm{d}\epsilon f_R(\epsilon+\omega_1)\left[1-f_L(\epsilon)\right] = \frac{(\mu_R-\omega_1)-\mu_L}{1-\mathrm{e}^{\beta(\mu_L-(\mu_R-\omega_1))}} = (\omega_1+U)n(\omega_1+U) \tag{C.36}$$

$$\int \mathrm{d}\epsilon f_R(\epsilon-\omega_1)\left[1-f_L(\epsilon)\right] = \frac{(\mu_R+\omega_1)-\mu_L}{1-\mathrm{e}^{\beta(\mu_L-(\mu_R+\omega_1))}} = -(\omega_1-U)n(-(\omega_1-U)) = (\omega_1-U)+(\omega_1-U)n(\omega_1-U) \tag{C.37}$$

Using the integrals above and the relation for the distribution function $N(-\epsilon) = -1 - N(\epsilon)$ in the expressions for the current we find

$$I_{el}^0 = G_0 T_0(E_F) U \tag{C.38}$$

$$\delta I_{el}^0 = G_0 \sum_\alpha \Big\{ \int_0^\infty \mathrm{d}\omega_1 \rho_\alpha(\omega_1) \Big(T_\alpha^{ec}(E_F)\left[2N(\omega_1)+1\right] U + \Big(T_\alpha^{ecL}(E_F)+T_\alpha^{ecR}(E_F)\Big)\left((\omega_1-U)n(\omega_1-U)-(\omega_1+U)n(\omega_1+U)-U\right)\Big)$$

$$-\frac{1}{\pi}T_\alpha^{JL}(E_F)\int \mathrm{d}\omega_1 \mathrm{Re}\left[D_\alpha^r(\omega_1)\right]\left(U+(\omega_1+U)n(\omega_1+U)-\omega_1 n(\omega_1)\right) \tag{C.39}$$

$$-\frac{1}{\pi}T_\alpha^{JR}(E_F)\int \mathrm{d}\omega_1 \mathrm{Re}\left[D_\alpha^r(\omega_1)\right]\left((\omega_1-U)n(-\omega_1+U)-\omega_1 n(-\omega_1)\right) \tag{C.40}$$

$$T_\alpha^{II}(E_F)\left[J_\alpha^{IIL}+J_\alpha^{IIR}\right]\int \mathrm{d}\epsilon\left(f_L(\epsilon)-f_R(\epsilon)\right)$$

$$I_{inel} = G_0 \sum_\alpha \Big\{ T_\alpha^{in}(E_F) \int_0^\infty \rho_\alpha(\omega_1) \Big(N_\alpha(\omega_1)\left((\omega_1+U)+(\omega_1+U)n(\omega_1+U)\right)$$
$$-(-1-N_\alpha(\omega_1))(\omega_1-U)n(\omega_1-U)+(-1-N_\alpha(\omega_1))(\omega_1+U)n(\omega_1+U)$$
$$-N_\alpha(\omega_1)\left((\omega_1-U)+(\omega_1-U)n(\omega_1-U)\right)\Big) =$$
$$G_0 \sum_\alpha \Big\{ T_\alpha^{in}(E_F) \int_0^\infty \rho_\alpha(\omega_1)\left(2N(\omega_1)U+(\omega_1-U)n(\omega_1-U)-(\omega_1+U)n(\omega_1+U)\right). \tag{C.41}$$

The integrals in Eq. (C.39) and Eq. (C.40) in δI_{el}^0 can be further simplified. In the integral Eq. (C.39) we note that the term $\int \mathrm{d}\omega_1 \mathrm{Re}\left[D_\alpha^r(\omega_1)\right] = 0$ vanishes and thus

$$\int \mathrm{d}\omega_1 \mathrm{Re}\left[D_\alpha^r(\omega_1)\right]\left(U+(\omega_1+U)n(\omega_1+U)-\omega_1 n(\omega_1)\right) =$$
$$\int \mathrm{d}\omega_1 \mathrm{Re}\left[D_\alpha^r(\omega_1)\right]\left((\omega_1+U)n(\omega_1+U)-\omega_1 n(\omega_1)\right). \tag{C.42}$$

In integral Eq. (C.40) we substitute $\tilde{\omega}_1 = -\omega_1$ and use that $\mathrm{Re}\left[D_\alpha^r(\omega_1)\right] = \mathrm{Re}\left[D_\alpha^r(-\omega_1)\right]$ is a symmetric function

$$\int_{-\infty}^{\infty} \mathrm{d}\omega_1 \mathrm{Re}\left[D_\alpha^r(\omega_1)\right]\left((\omega_1-U)n(-\omega_1+U)-\omega_1 n(-\omega_1)\right) =$$
$$-\int_{\infty}^{-\infty} \mathrm{d}\tilde{\omega}_1 \mathrm{Re}\left[D_\alpha^r(\tilde{\omega}_1)\right]\left((-\tilde{\omega}_1-U)n(\tilde{\omega}_1+U)+\tilde{\omega}_1 n(\tilde{\omega}_1)\right) =$$
$$-\int_{-\infty}^{\infty} \mathrm{d}\omega_1 \mathrm{Re}\left[D_\alpha^r(\omega_1)\right]\left((\omega_1+U)n(\omega_1+U)-\omega_1 n(\omega_1)\right). \tag{C.43}$$

Now we can combine the two integrals which gives a more compact form for δI_{el}^0. The last term given by $\left[J_\alpha^{IIL}+J_\alpha^{IIR}\right]$ turns out to be the most complicated one, because it is not well defined in the WBL. However, it can be approximated by the equilibrium density matrix ρ

$$J_\alpha^{IIL}+J_\alpha^{IIR} \approx \frac{D_\alpha^r(0)}{2\pi}\mathrm{Tr}[\rho\lambda^\alpha]. \tag{C.44}$$

Additionally we need an expression for the distribution function $N_\alpha(\epsilon)$ in the WBL. The full energy-dependent distribution function is given by [22]

$$N_\alpha(\epsilon) = -\frac{1}{2}\frac{\mathrm{Im}\Pi_\alpha^{+-}(\epsilon)+n(\epsilon)\eta\epsilon/\epsilon_\alpha}{\mathrm{Im}\Pi_\alpha^r(\epsilon)-\eta\epsilon/(2\epsilon_\alpha)} \tag{C.45}$$

with the phonon polarization functions

$$\Pi^r_\alpha(\epsilon) = \frac{-\mathrm{i}}{2\pi}\int \mathrm{d}\omega_1 \mathrm{Tr}\left[\lambda^\alpha \tilde{G}^<(\omega_1+\epsilon)\lambda^\alpha \tilde{G}^a(\omega_1) + \lambda^\alpha \tilde{G}^<(\omega_1-\epsilon)\lambda^\alpha \tilde{G}(\omega_1)\right] \tag{C.46}$$

$$\Pi^{+-}_\alpha(\epsilon) = \frac{\mathrm{i}}{2\pi}\int \mathrm{d}\omega_1 \mathrm{Tr}\left[\lambda^\alpha \tilde{G}^<(\omega_1)\lambda^\alpha \tilde{G}^>(\omega_1-\epsilon)\right]. \tag{C.47}$$

In WBL one finds the following expressions

$$\mathrm{Im}\Pi^r_\alpha(\epsilon) = -\frac{1}{\pi}\epsilon\ \mathrm{Tr}[\lambda^\alpha \mathrm{Im}\tilde{G}^r \lambda^\alpha \mathrm{Im}\tilde{G}^r]\big|_{E_F} \tag{C.48}$$

$$\begin{aligned}\mathrm{Im}\Pi^{+-}_\alpha(\epsilon) = \frac{1}{2\pi}\Bigg[&T^{\Pi LR}(E_F)\left((\epsilon+U)n(\epsilon+U) + (\epsilon-U)n(\epsilon-U)\right)\\ &\left(T^{\Pi LL}(E_F) + T^{\Pi RR}(E_F)\right)\epsilon n(\epsilon)\Bigg]\end{aligned} \tag{C.49}$$

with

$$T^{\Pi LR}(\epsilon) = \mathrm{Tr}[\lambda^\alpha \tilde{G}^r(\epsilon)\Gamma_L(\epsilon)\tilde{G}^a(\epsilon)\lambda^\alpha \tilde{G}^r(\epsilon)\Gamma_R(\epsilon)\tilde{G}^a(\epsilon)] \tag{C.50}$$

$$T^{\Pi LL}(\epsilon) = \mathrm{Tr}[\lambda^\alpha \tilde{G}^r(\epsilon)\Gamma_L(\epsilon)\tilde{G}^a(\epsilon)\lambda^\alpha \tilde{G}^r(\epsilon)\Gamma_L(\epsilon)\tilde{G}^a(\epsilon)] \tag{C.51}$$

$$T^{\Pi RR}(\epsilon) = \mathrm{Tr}[\lambda^\alpha \tilde{G}^r(\epsilon)\Gamma_R(\epsilon)\tilde{G}^a(\epsilon)\lambda^\alpha \tilde{G}^r(\epsilon)\Gamma_R(\epsilon)\tilde{G}^a(\epsilon)]. \tag{C.52}$$

The final expressions for I^0, δI^0_{el} and I_{inel} are

$$I^0_{el} = G_0 T_0(E_F) U, \tag{C.53}$$

$$\begin{aligned}\delta I^0_{el} = G_0 \sum_\alpha \Bigg\{ \int_0^\infty \rho_\alpha(\omega_1) \Bigg(&T^{ec}_\alpha(E_F)\left[2N(\omega_1)+1\right]U +\\ &\left(T^{ecL}_\alpha(E_F) + T^{ecR}_\alpha(E_F)\right)\left((\omega_1-U)n(\omega_1-U) - (\omega_1+U)n(\omega_1+U) - U\right)\Bigg) +\\ -\frac{1}{\pi}\left(T^{JR}_\alpha(E_F) - T^{JL}_\alpha(E_F)\right)&\int \mathrm{d}\omega_1 \mathrm{Re}\left[D^r_\alpha(\omega_1)\right]\left(\omega_1 n(\omega_1) - (\omega_1+U)n(\omega_1+U)\right) +\\ &T^{II}_\alpha(E_F)\frac{D^r_\alpha(0)}{2\pi}\mathrm{Tr}[\rho\lambda^\alpha]U,\end{aligned} \tag{C.54}$$

$$I_{inel} = G_0 \sum_\alpha \Big\{ T^{in}_\alpha(E_F) \int_0^\infty \rho_\alpha(\omega_1)\left(2N(\omega_1)U + (\omega_1-U)n(\omega_1-U) - (\omega_1+U)n(\omega_1+U)\right). \tag{C.55}$$

D Relation between the tight-binding and Lorentz model

The Lorentz model (LM) is frequently used to describe the transmission in the field of molecular electronics. Typically, a Lorentzian function is fitted to the resonance dominating the transmission at the Fermi energy. Here, we discuss, in which situation the LM coincides with the TBM.

We consider the non-Hermitian eigenvalue problem $(\hat{H}+\hat{\Sigma}^r)|\mu\rangle = \lambda_\mu|\mu\rangle$ with $\lambda_\mu = \epsilon_\mu + i\gamma_\mu$, the symmetric and Hermitian Hamilton operator $\hat{H}$, and the symmetric, but non-Hermitian retarded self-energy operator $\hat{\Sigma}^r = \hat{\Sigma}^r_L + \hat{\Sigma}^r_R$ composed of contributions from the L and R electrodes. By $\langle\tilde{\mu}|$ we denote the left eigenstate with the same eigenvalue λ_μ as the corresponding right eigenstate $|\mu\rangle$, i.e. $\langle\tilde{\mu}|(\hat{H}+\hat{\Sigma}^r) = \lambda_\mu\langle\tilde{\mu}|$. The C region is assumed to be identical to the molecule in the TBM (see Fig. 9.6a). Using the spectral decomposition of the Green's function in the expression for the energy-dependent transmission $\tau(E)$ (see Eq. (4.24) and Eq. (4.25)), we obtain

$$\tau(E) = \sum_{\mu,\nu} \frac{\langle\tilde{\mu}|\hat{\Gamma}_L|\nu\rangle\langle\tilde{\nu}|\hat{\Gamma}_R|\mu\rangle}{(E-\epsilon_\mu-i\gamma_\mu)(E-\epsilon_\nu+i\gamma_\nu)}, \tag{D.1}$$

where the sum is over all those eigenstates $|\mu\rangle$ of the biphenyl which obtain a finite linewidth $\gamma_\mu \neq 0$ by the coupling to the electrodes and which hence contribute to the transport.

Let us now make the wide-band approximation and consider the energy-independent expression $\hat{\Sigma}^r = -i(\hat{\Gamma}_L+\hat{\Gamma}_R)/2$ to be a small perturbation. Within lowest-order perturbation theory we obtain $\lambda_\mu = \epsilon^0_\mu + i\gamma_\mu$ with $\hat{H}|\mu^0\rangle = \epsilon^0_\mu|\mu^0\rangle$ and $\gamma_\mu = \langle\mu^0|\hat{\Sigma}^r|\mu^0\rangle$. Additionally, we assume a symmetric coupling $(\Gamma_L)_{\alpha\alpha} = (\Gamma_R)_{\omega\omega} = \Gamma$, where the indices α, ω refer to those atoms of the biphenyl backbone which are closest to the L,R electrodes (see Fig. 9.6a) and where local basis states are understood to be orthogonal in the spirit of the Hückel approximation. By exploiting the inversion symmetry of the TBM, it follows that $\gamma_\mu = \langle\mu^0|\hat{\Gamma}_X|\mu^0\rangle$ since $\hat{M}^2 = \hat{1}$, $\hat{M}\hat{H}\hat{M} = \hat{H}$, and $\hat{M}\hat{\Gamma}_L\hat{M} = \hat{\Gamma}_R$ with the operator $\hat{M} = \hat{M}^\dagger$ describing the inversion of the molecule.

The perturbation theory is valid in the regime $\Gamma \ll t$, where t determines the separation between the resonance energies ϵ_μ relevant for transport. When they are well separated, the largest contributions to the transmission in Eq. (D.1) arise when $\mu = \nu$, since cross-terms are suppressed by a large off-resonant denominator. In this case the transmission is well represented as the sum of incoherent Lorentz resonances

$$\tau(E) \approx \sum_\mu \frac{\gamma_\mu^2}{(E-\epsilon_\mu)^2+\gamma_\mu^2}, \tag{D.2}$$

and the TBM simplifies to the LM.

References

[1] H. Iwai, *Roadmap for 22 nm and beyond*, Microelectron. Eng. **86**, 1520 (2009).

[2] H. Kuhn and D. Möbius, *Systems of Monomolecular Layers Assembling and Physico-Chemical Behavior*, Angew. Chem. Int. Ed. Engl. **10**, 620 (1971).

[3] A. Aviram and M. A. Ratner, *Molecular rectifiers*, Chem. Phys. Lett. **29**, 277 (1974).

[4] R. Ballardini, V. Balzani, A. Credi, M. T. Gandolfi, and M. Venturi, *Artificial Molecular-Level Machines: Which Energy To Make Them Work?*, Acc. Chem. Res. **34**, 445 (2001).

[5] Z. L. Wang and J. Song, *Piezoelectric Nanogenerators Based on Zinc Oxide Nanowire Arrays*, Science **312**, 242 (2006).

[6] R. Venkatasubramanian, E. Siivola, T. Colpitts, and B. O'Quinn, *Thin-film thermoelectric devices with high room-temperature figures of merit*, Nature **413**, 597 (2001).

[7] B. Mann, H. Kuhn, and L. Szentpaly, *Tunnelling through fatty acid monolayers and its relevance to photographic sensitization*, Chem. Phys. Lett. **8**, 82 (1971).

[8] B. Mann and H. Kuhn, *Tunneling through Fatty Acid Salt Monolayers*, J. Appl. Phys. **42**, 4398 (1971).

[9] G. Binnig, H. Rohrer, C. Gerber, and E. Weibel, *Vacuum tunneling*, Phys. B **2075**, 109 (1982).

[10] G. Binnig, H. Rohrer, C. Gerber, and E. Weibel, *Surface Studies by Scanning Tunneling Microscopy*, Phys. Rev. Lett. **49**, 57 (1982).

[11] C. J. Muller, J. M. van Ruitenbeek, and L. J. de Jongh, *Experimental observation of the transition from weak link to tunnel junction*, Phys. C **191**, 485 (1992).

[12] J. M. van Ruitenbeek, A. Alvarez, I. Pineyro, C. Grahmann, P. Joyez, M. H. Devoret, D. Esteve, and C. Urbina, *Adjustable nanofabricated atomic size contacts*, Rev. Sci. Instrum. **67**, 108 (1996).

[13] M. A. Reed, C. Zhou, C. J. Muller, T. P. Burgin, and J. M. Tour, *Conductance of a Molecular Junction*, Science **278**, 252 (1997).

[14] L. Venkataraman, J. E. Klare, C. Nuckolls, M. S. Hybertsen, and M. L. Steigerwald, *Dependence of single-molecule junction conductance on molecular conformation*, Nature **442**, 904 (August 2006). ISSN 0028-0836. URL `http://dx.doi.org/10.1038/nature05037`.

[15] A. Mishchenko, L. A. Zotti, D. Vonlanthen, M. Bürkle, F. Pauly, J. C. Cuevas, M. Mayor, and T. Wandlowski, *Single-Molecule Junctions Based on Nitrile-Terminated*

Biphenyls: A Promising New Anchoring Group, J. Am. Chem. Soc. **133**, 184 (January 2011). ISSN 0002-7863. URL http://dx.doi.org/10.1021/ja107340t.

[16] B. Xu and N. J. Tao, *Measurement of Single-Molecule Resistance by Repeated Formation of Molecular Junctions*, Science **301**, 1221 (2003).

[17] P. Reddy, S.-Y. Jang, R. A. Segalman, and A. Majumdar, *Thermoelectricity in Molecular Junctions*, Science **315**, 1568 (2007).

[18] A. Leni, *Electroluminescent polymers*, Prog. Polym. Sci. **28**, 875 (2003). ISSN 0079-6700.

[19] C. W. Marquardt, S. Grunder, A. Blaszczyk, S. Dehm, F. Hennrich, H. v. Lohneysen, M. Mayor, and R. Krupke, *Electroluminescence from a single nanotube-molecule-nanotube junction*, Nat Nano **5**, 863 (2010). ISSN 1748-3387.

[20] *Basel Universität, Departement Physik, Nanoelectronics* (2011). URL http://www.nanoelectronics.ch/research/molecular.php.

[21] Y. Xue, S. Datta, and M. A. Ratner, *First-principles based matrix Green's function approach to molecular electronic devices: general formalism*, Chem. Phys. **281**, 151 (2002).

[22] J. K. Viljas, J. C. Cuevas, F. Pauly, and M. Häfner, *Electron-vibration interaction in transport through atomic gold wires*, Phys. Rev. B **72**, 245415 (2005).

[23] L. Hedin, *New Method for Calculating the One-Particle Green's Function with Application to the Electron-Gas Problem*, Phys. Rev. **139**, A796 (1965).

[24] K.-H. Müller, *Thermoelectrics in an array of molecular junctions*, J. Chem. Phys. **129**, 044708 (2008).

[25] J. S. Hummelshøj, D. D. Landis, J. Voss, T. Jiang, A. Tekin, N. Bork, M. Duak, J. J. Mortensen, L. Adamska, J. Andersin, J. D. Baran, G. D. Barmparis, F. Bell, A. L. Bezanilla, J. Bjork, M. E. Björketun, F. Bleken, F. Buchter, M. Bürkle, P. D. Burton, B. B. Buus, A. Calborean, F. Calle-Vallejo, S. Casolo, B. D. Chandler, D. H. Chi, I. Czekaj, S. Datta, A. Datye, A. DeLaRiva, V. Despoja, S. Dobrin, M. Engelund, L. Ferrighi, P. Frondelius, Q. Fu, A. Fuentes, J. Fürst, A. García-Fuente, J. Gavnholt, R. Goeke, S. Gudmundsdottir, K. D. Hammond, H. A. Hansen, D. Hibbitts, J. E. Hobi, J. G. Howalt, S. L. Hruby, A. Huth, L. Isaeva, J. Jelic, I. J. T. Jensen, K. A. Kacprzak, A. Kelkkanen, D. Kelsey, D. S. Kesanakurthi, J. Kleis, P. J. Klüpfel, I. Konstantinov, R. Korytar, P. Koskinen, C. Krishna, E. Kunkes, A. H. Larsen, J. M. G. Lastra, H. Lin, O. Lopez-Acevedo, M. Mantega, J. I. Martínez, I. N. Mesa, D. J. Mowbray, J. S. G. Mýrdal, Y. Natanzon, A. Nistor, T. Olsen, H. Park, L. S. Pedroza, V. Petzold, C. Plaisance, J. A. Rasmussen, H. Ren, M. Rizzi, A. S. Ronco, C. Rostgaard, S. Saadi, L. A. Salguero, E. J. G. Santos, A. L. Schoenhalz, J. Shen, M. Smedemand, O. J. Stausholm-Møller, M. Stibius, M. Strange, H. B. Su, B. Temel, A. Toftelund, V. Tripkovic, M. Vanin, V. Viswanathan, A. Vojvodic,

S. Wang, J. Wellendorff, K. S. Thygesen, J. Rossmeisl, T. Bligaard, K. W. Jacobsen, J. K. Nørskov, and T. Vegge, *Density functional theory based screening of ternary alkali-transition metal borohydrides: A computational material design project*, J. Chem. Phys. **131**, 014101 (2009).

[26] F. Pauly, J. K. Viljas, U. Huniar, M. Häfner, S. Wohlthat, M. Bürkle, J. C. Cuevas, and G. Schön, *Cluster-based density-functional approach to quantum transport through molecular and atomic contacts*, New Journal of Physics **10**, 125019 (2008).

[27] R. Ahlrichs, M. Bär, M. Häser, H. Horn, and C. Kölmel, *Electronic structure calculations on workstation computers: The program system turbomole*, Chem. Phys. Lett. **162**, 165 (1989).

[28] M. Born and K. Huang. *Dynamical Theory of Crystal Lattices* (Oxford Univ. Pr., 1998).

[29] G. V. Chester and A. Houghton, *Electron-Phonon Interaction in Metals I: The Harmonic Approximation*, Proc. Phys. Soc. **73**, 609 (1959).

[30] G. Chester, *The theory of the interaction of electrons with lattice vibrations in metals*, Adv. Phys. **10**, 357 (1961).

[31] K. Capelle. *A bird's-eye view of density-functional theory* (2002).

[32] G. Czycholl. *Theoretische Festkörperphysik* (Springer Berlin Heidelberg; Auflage: 3., 2007).

[33] G. Grimvall. *The electron-phonon interaction in metals* (North-Holland Pub. Co, 1981).

[34] C. Møller and M. S. Plesset, *Note on an Approximation Treatment for Many-Electron Systems*, Phys. Rev. **46**, 618 (1934).

[35] A. Szabo and N. Ostlund. *Modern Quantum Chemistry: Introduction to Advanced Electronic Structure Theory* (McGraw-Hill, New York, 1989).

[36] P. Hohenberg and W. Kohn, *Inhomogeneous Electron Gas*, Phys. Rev. **136**, B864 (1964).

[37] R. Parr and W. Yang. *Density-Functional Theory of Atoms and Molecules* (Oxford Univ. Pr., 1989).

[38] R. Dreizler and E. Gross. *Density Functional Theory* (Springer-Verlag Berlin Heidelberg, 1990).

[39] C. Fiolhais, F. Nogueira, and M. Marques. *A Primer in Density Functional Theory* (Springer-Verlag Berlin Heidelberg, 2003).

[40] S. Kurth, M. A. L. Marques, and E. K. U. Gross. *Electronic Strucure: Density-Functional Theory* (Elsevier, Oxford, 2005). ISBN 978-0-12-369401-0.

[41] W. Kohn and L. J. Sham, *Self-Consistent Equations Including Exchange and Correlation Effects*, Phys. Rev. **140**, A1133 (1965).

[42] P. A. M. Dirac, *Quantum Mechanics of Many-Electron Systems*, Proc. R. Soc. Lond. A **123**, 714 (1929).

[43] J. C. Slater, *A Simplification of the Hartree-Fock Method*, Phys. Rev. **81**, 385 (1951).

[44] S. H. Vosko, L. Wilk, and M. Nusair, *Accurate spin-dependent electron liquid correlation energies for local spin density calculations: a critical analysis*, Can. J. Phys. **58**, 1200 (1980).

[45] J. P. Perdew and Y. Wang, *Accurate and simple analytic representation of the electron-gas correlation energy*, Phys. Rev. B **45**, 13244 (1992).

[46] A. D. Becke, *Density-functional exchange-energy approximation with correct asymptotic behavior*, Phys. Rev. A **38**, 3098 (1988).

[47] C. Lee, W. Yang, and R. G. Parr, *Development of the Colle-Salvetti correlation-energy formula into a functional of the electron density*, Phys. Rev. B **37**, 785 (1988).

[48] J. P. Perdew, *Density-functional approximation for the correlation energy of the inhomogeneous electron gas*, Phys. Rev. B **33**, 8822 (1986).

[49] J. P. Perdew, K. Burke, and M. Ernzerhof, *Generalized Gradient Approximation Made Simple*, Phys. Rev. Lett. **77**, 3865 (1996).

[50] T. Kato, *On the eigenfunctions of many-particle systems in quantum mechanics*, Commun. on Pure Appl. Math. **10**, 151 (1957).

[51] S. F. Boys, *Electronic Wave Functions. I. A General Method of Calculation for the Stationary States of Any Molecular System*, Proc. R. Soc. Lond. A **200**, 542 (1950).

[52] L. E. McMurchie and E. R. Davidson, *One- and two-electron integrals over cartesian gaussian functions*, J. Comput. Phys. **26**, 218 (1978).

[53] J. A. Pople and W. J. Hehre, *Computation of electron repulsion integrals involving contracted Gaussian basis functions*, J. Comput. Phys. **27**, 161 (1978).

[54] S. Obara and A. Saika, *Efficient recursive computation of molecular integrals over Cartesian Gaussian functions*, J. Chem. Phys. **84**, 3963 (1986).

[55] J. A. Pople, R. Krishnan, H. B. Schlegel, and J. S. Binkley, *Derivative studies in hartree-fock and moller-plesset theories*, Int. J. Quantum Chem. **16**, 225 (1979).

[56] P. Deglmann, F. Furche, and R. Ahlrichs, *An efficient implementation of second analytical derivatives for density functional methods*, Chem. Phys. Lett. **362**, 511 (2002).

[57] V. Heine. *The Pseudopotential Concept*, volume Volume 24 (Academic Press, 1970).

[58] W. E. Pickett, *Pseudopotential methods in condensed matter applications*, Comput. Phys. Rep. **9**, 115 (1989).

[59] A. Komornicki, K. Ishida, K. Morokuma, R. Ditchfield, and M. Conrad, *Efficient determination and characterization of transition states using ab-initio methods*, Chem. Phys. Lett. **45**, 595 (1977).

[60] B. Jürgen, T. Walter, and K. Andrew, *Analytical second derivatives for effective core potentials*, Chem. Phys. Lett. **153**, 76 (1988).

[61] J. P. Perdew and W. Yue, *Accurate and simple density functional for the electronic exchange energy: Generalized gradient approximation*, Phys. Rev. B **33**, 8800 (1986).

[62] Y. Meir and N. S. Wingreen, *Landauer formula for the current through an interacting electron region*, Phys. Rev. Lett. **68**, 2512 (1992).

[63] K. S. Thygesen, *Electron transport through an interacting region: The case of a nonorthogonal basis set*, Phys. Rev. B **73**, 035309 (2006).

[64] R. S. Mulliken, *Electronic Population Analysis on LCAO?MO Molecular Wave Functions. I*, J. Chem. Phys. **23**, 1833 (1955).

[65] C. Caroli, R. Combescot, P. Nozieres, and D. Saint-James, *Direct calculation of the tunneling current*, J. Phys. C Solid State Phys. **4**, 916 (1971).

[66] J. Cuevas and E. Scheer. *MOLECULAR ELECTRONICS: An Introduction to Theory and Experiment* (World Scientific Publishing Company, 2010).

[67] R. Landauer, *Electrical resistance of disordered one-dimensional lattices*, Philos. Mag. **21**, 863 (1970).

[68] M. Büttiker, Y. Imry, R. Landauer, and S. Pinhas, *Generalized many-channel conductance formula with application to small rings*, Phys. Rev. B **31**, 6207 (1985).

[69] J. K. Viljas. *On the calculation of Greens functions in nonequilibrium Fermi systems* (2008). URL `http://ltl.tkk.fi/~jviljas/keldysh.pdf`.

[70] Y. M. Blanter and M. Büttiker, *Shot noise in mesoscopic conductors*, Phys. Rep. **336**, 1 (2000).

[71] M. Paulsson and M. Brandbyge, *Transmission eigenchannels from nonequilibrium Green's functions*, Phys. Rev. B **76**, 115117 (2007).

[72] U. Sivan and Y. Imry, *Multichannel Landauer formula for thermoelectric transport with application to thermopower near the mobility edge*, Phys. Rev. B **33**, 551 (1986).

[73] K. Esfarjani, M. Zebarjadi, and Y. Kawazoe, *Thermoelectric properties of a nanocontact made of two-capped single-wall carbon nanotubes calculated within the tight-binding approximation*, Phys. Rev. B **73**, 085406 (2006).

[74] N. Ashcroft and D. Mermin. *Festkörperphysik* (Oldenbourg Wissenschaftsverlag; Auflage: 1, 2001).

[75] D. Segal, *Thermoelectric effect in molecular junctions: A tool for revealing transport mechanisms*, Phys. Rev. B **72**, 165426 (2005).

[76] M. J. Mehl. *Tight-Binding parameters for the Elements* (2011). URL `http://cst-www.nrl.navy.mil/bind/`.

[77] J. Mozos, O. Pablo, B. Mads, T. Jeremy, and S. Kurt, *Simulations of quantum transport in nanoscale systems: application to atomic gold and silver wires*, Nanotechnology **13**, 346 (2002).

[78] M. Brandbyge, J.-L. Mozos, P. Ordejón, J. Taylor, and K. Stokbro, *Density-functional method for nonequilibrium electron transport*, Phys. Rev. B **65**, 165401 (2002).

[79] Y. J. Lee, M. Brandbyge, M. J. Puska, J. Taylor, K. Stokbro, and R. M. Nieminen, *Electron transport through monovalent atomic wires*, Phys. Rev. B **69**, 125409 (2004).

[80] T. Frederiksen, N. Lorente, M. Paulsson, and M. Brandbyge, *From tunneling to contact: Inelastic signals in an atomic gold junction from first principles*, Phys. Rev. B **75**, 235441 (2007).

[81] T. Frederiksen, M. Paulsson, M. Brandbyge, and A.-P. Jauho, *First-principles Theory of Inelastic Transport and Local Heating in Atomic Gold Wires*, AIP Conf. Proc. **893**, 727 (2007).

[82] I. K. Yanson, O. I. Shklyarevskii, S. Csonka, H. van Kempen, S. Speller, A. I. Yanson, and J. M. van Ruitenbeek, *Atomic-Size Oscillations in Conductance Histograms for Gold Nanowires and the Influence of Work Hardening*, Phys. Rev. Lett. **95**, 256806 (2005).

[83] W. H. A. Thijssen, D. Marjenburgh, R. H. Bremmer, and J. M. van Ruitenbeek, *Oxygen-Enhanced Atomic Chain Formation*, Phys. Rev. Lett. **96**, 026806 (2006).

[84] M. Paulsson, T. Frederiksen, and M. Brandbyge, *Modeling inelastic phonon scattering in atomic- and molecular-wire junctions*, Phys. Rev. B **72**, 201101 (2005).

[85] M. Paulsson, T. Frederiksen, H. Ueba, N. Lorente, and M. Brandbyge, *Unified Description of Inelastic Propensity Rules for Electron Transport through Nanoscale Junctions*, Phys. Rev. Lett. **100**, 226604 (2008).

[86] J. C. Cuevas, A. L. Yeyati, and A. Martian-Rodero, *Microscopic Origin of Conducting Channels in Metallic Atomic-Size Contacts*, Phys. Rev. Lett. **80**, 1066 (1998).

[87] J. C. Cuevas, J. Heurich, F. Pauly, W. Wenzel, and G. Schön, *Theoretical description of the electrical conduction in atomic and molecular junctions*, Nanotechnology **14**, R29 (2003).

[88] E. Scheer, N. Agraït, J. C. Cuevas, A. L. Yeyati, B. Ludoph, A. Martin-Rodero, G. R. Bollinger, J. M. van Ruitenbeek, and C. Urbina, *The signature of chemical valence in the electrical conduction through a single-atom contact*, Nature **394**, 154 (1998).

[89] T. Böhler, A. Edtbauer, and E. Scheer, *Point-contact spectroscopy on aluminium atomic-size contacts: longitudinal and transverse vibronic excitations*, New Journal of Physics **11**, 013036 (2009).

[90] E. Scheer, P. Joyez, D. Esteve, C. Urbina, and M. H. Devoret, *Conduction Channel Transmissions of Atomic-Size Aluminum Contacts*, Phys. Rev. Lett. **78**, 3535 (May 1997).

[91] R. Egger and A. O. Gogolin, *Vibration-induced correction to the current through a single molecule*, Phys. Rev. B **77**, 113405 (2008).

[92] O. Entin-Wohlman, Y. Imry, and A. Aharony, *Voltage-induced singularities in transport through molecular junctions*, Phys. Rev. B **80**, 035417 (2009).

[93] G. Fagas and J. C. Greer, *Tunnelling in alkanes anchored to gold electrodes via amine end groups*, Nanotechnology **18**, 424010 (2007).

[94] C. A. Martin, D. Ding, H. S. J. van der Zant, and J. M. van Ruitenbeek, *Lithographic mechanical break junctions for single-molecule measurements in vacuum: possibilities and limitations*, New J. Phys. **10**, 065008 (2008).

[95] J. Klein, A. Léger, M. Belin, D. Défourneau, and M. J. L. Sangster, *Inelastic-Electron-Tunneling Spectroscopy of Metal-Insulator-Metal Junctions*, Phys. Rev. B **7**, 2336 (1973).

[96] P. K. Hansma, *Inelastic electron tunneling*, Phys. Rep. **30**, 145 (1977). ISSN 0370-1573.

[97] W. Wang, T. Lee, I. Kretzschmar, and M. A. Reed, *Inelastic Electron Tunneling Spectroscopy of an Alkanedithiol Self-Assembled Monolayer*, Nano Lett. **4**, 643 (2004). ISSN 1530-6984.

[98] L. H. Yu, C. D. Zangmeister, and J. G. Kushmerick, *Origin of Discrepancies in Inelastic Electron Tunneling Spectra of Molecular Junctions*, Phys. Rev. Lett. **98**, 206803 (2007).

[99] H. Song, Y. Kim, Y. H. Jang, H. Jeong, M. A. Reed, and T. Lee, *Observation of molecular orbital gating*, Nature **462**, 1039 (2009). ISSN 0028-0836.

[100] M. Paulsson, C. Krag, T. Frederiksen, and M. Brandbyge, *Conductance of Alkanedithiol Single-Molecule Junctions: A Molecular Dynamics Study*, Nano Letters **9**, 117 (2009). ISSN 1530-6984.

[101] J. G. Kushmerick, J. Lazorcik, C. H. Patterson, R. Shashidhar, D. S. Seferos, and G. C. Bazan, *Vibronic Contributions to Charge Transport Across Molecular Junctions*, Nano Lett. **4**, 639 (2004). ISSN 1530-6984.

[102] C. R. Arroyo, T. Frederiksen, G. Rubio-Bollinger, M. Vélez, A. Arnau, D. Sánchez-Portal, and N. Agraït, *Characterization of single-molecule pentanedithiol junctions by inelastic electron tunneling spectroscopy and first-principles calculations*, Phys. Rev. B **81**, 075405 (Feb 2010).

[103] A. Pecchia, A. Di Carlo, A. Gagliardi, S. Sanna, T. Frauenheim, and R. Gutierrez, *Incoherent Electron-Phonon Scattering in Octanethiols*, Nano Letters **4**, 2109 (2004). ISSN 1530-6984.

[104] G. C. Solomon, A. Gagliardi, A. Pecchia, T. Frauenheim, A. D. Carlo, J. R. Reimers, and N. S. Hush, *Understanding the inelastic electron-tunneling spectra of alkanedithiols on gold*, J. Chem. Phys. **124**, 094704 (2006).

[105] L. Venkataraman, J. E. Klare, I. W. Tam, C. Nuckolls, M. S. Hybertsen, and M. L. Steigerwald, *Single-Molecule Circuits with Well-Defined Molecular Conductance*, Nano Lett. **6**, 458 (March 2006).

[106] Z. Li and D. S. Kosov, *Nature of well-defined conductance of amine-anchored molecular junctions: Density functional calculations*, Phys. Rev. B **76**, 035415 (2007).

[107] J. Hihath, C. R. Arroyo, G. Rubio-Bollinger, N. Tao, and N. Agrait, *Study of Electron-Phonon Interactions in a Single Molecule Covalently Connected to Two Electrodes*, Nano Letters **8**, 1673 (2008). ISSN 1530-6984.

[108] Y. Kim, T. J. Hellmuth, M. Bürkle, F. Pauly, and E. Scheer, *Characteristics of Amine-Ended and Thiol-Ended Alkane Single-Molecule Junctions Revealed by Inelastic Electron Tunneling Spectroscopy*, ACS Nano **5**, 4104 (May 2011).

[109] G. Rubio-Bollinger, S. R. Bahn, N. Agrait, K. W. Jacobsen, and S. Vieira, *Mechanical Properties and Formation Mechanisms of a Wire of Single Gold Atoms*, Phys. Rev. Lett. **87**, 026101 (2001).

[110] A. Mishchenko, D. Vonlanthen, V. Meded, M. Bürkle, C. Li, I. V. Pobelov, A. Bagrets, J. K. Viljas, F. Pauly, F. Evers, M. Mayor, and T. Wandlowski, *Influence of Conformation on Conductance of Biphenyl-Dithiol Single-Molecule Contacts*, Nano Lett. **10**, 156 (January 2010).

[111] E. Leary, S. J. Higgins, H. van Zalinge, W. Haiss, and R. J. Nichols, *Chemical control of double barrier tunnelling in α,ω-dithiaalkane molecular wires*, Chem. Commun. p. 3939 (2007).

[112] L. Venkataraman, Y. S. Park, A. C. Whalley, C. Nuckolls, M. S. Hybertsen, and M. L. Steigerwald, *Electronics and Chemistry: Varying Single-Molecule Junction Conductance Using Chemical Substituents*, Nano Lett. **7**, 502 (2007).

[113] F. Hüser, M. Bürkle, T. Kirchner, G. Schön, and F. Pauly. *Density functional study of the transport properties of substituted benzene derivatives*.

[114] A. Shaporenko, M. Elbing, A. Błaszczyk, C. von Hänisch, M. Mayor, and M. Zharnikov, *Self-Assembled Monolayers from Biphenyldithiol Derivatives: Optimization of the Deprotection Procedure and Effect of the Molecular Conformation*, J. Phys. Chem. B **110**, 4307 (March 2006).

[115] D. Vonlanthen, A. Mishchenko, M. Elbing, M. Neuburger, T. Wandlowski, and M. Mayor, *Chemically Controlled Conductivity: Torsion-Angle Dependence in a Single-Molecule Biphenyldithiol Junction13*, Angew. Chem., Int. Ed. **48**, 8886 (2009).

[116] D. Vonlanthen, J. Rotzler, M. Neuburger, and M. Mayor, *Synthesis of Rotationally Restricted and Modular Biphenyl Building Blocks*, Eur. J. Org. Chem. **2010**, 120 (2010).

[117] F. Pauly, J. K. Viljas, J. C. Cuevas, and G. Schön, *Density-functional study of tilt-angle and temperature-dependent conductance in biphenyl dithiol single-molecule junctions*, Phys. Rev. B **77**, 155312 (2008).

[118] Y. Xue and M. A. Ratner, *Microscopic study of electrical transport through individual molecules with metallic contacts. II. Effect of the interface structure*, Phys. Rev. B **68**, 115407 (2003).

[119] J. Tomfohr and O. F. Sankey, *Theoretical analysis of electron transport through organic molecules*, J. Chem. Phys. **120**, 1542 (2004).

[120] C. Li, I. Pobelov, T. Wandlowski, A. Bagrets, A. Arnold, and F. Evers, *Charge Transport in Single Au | Alkanedithiol | Au Junctions: Coordination Geometries and Conformational Degrees of Freedom*, J. Am. Chem. Soc. **130**, 318 (2008).

[121] W. Haiss, C. Wang, R. Jitchati, I. Grace, S. Martín, A. S. Batsanov, S. J. Higgins, M. R. Bryce, C. J. Lambert, P. S. Jensen, and R. J. Nichols, *Variable contact gap single-molecule conductance determination for a series of conjugated molecular bridges*, J. Phys.: Condens. Matter **20**, 374119 (2008).

[122] S. Y. Quek, M. Kamenetska, M. L. Steigerwald, H. J. Choi, S. G. Louie, M. S. Hybertsen, J. B. Neaton, and L. Venkataraman, *Mechanically controlled binary conductance switching of a single-molecule junction*, Nat. Nanotechnol. **4**, 230 (April 2009).

[123] I. Diez-Perez, J. Hihath, T. Hines, Z.-S. Wang, G. Zhou, K. Mullen, and N. Tao, *Controlling single-molecule conductance through lateral coupling of [pi] orbitals*, Nat. Nanotechnol. **6**, 226 (April 2011).

[124] S. Y. Quek, L. Venkataraman, H. J. Choi, S. G. Louie, M. S. Hybertsen, and J. B. Neaton, *Amine-Gold Linked Single-Molecule Circuits: Experiment and Theory*, Nano Lett. **7**, 3477 (2007).

[125] M. Strange, C. Rostgaard, H. Häkkinen, and K. S. Thygesen, *Self-consistent GW calculations of electronic transport in thiol- and amine-linked molecular junctions*, Phys. Rev. B **83**, 115108 (Mar 2011).

[126] J. K. Viljas, F. Pauly, and J. C. Cuevas, *Modeling elastic and photoassisted transport in organic molecular wires: Length dependence and current-voltage characteristics*, Phys. Rev. B **77**, 155119 (April 2008).

[127] F. Pauly, J. K. Viljas, and J. C. Cuevas, *Length-dependent conductance and thermopower in single-molecule junctions of dithiolated oligophenylene derivatives: A density functional study*, Phys. Rev. B **78**, 035315 (2008).

[128] G. C. Solomon, A. Gagliardi, A. Pecchia, T. Frauenheim, A. D. Carlo, J. R. Reimers, and N. S. Hush, *The symmetry of single-molecule conduction*, J. Chem. Phys. **125**, 184702 (2006).

[129] M. Kiguchi, O. Tal, S. Wohlthat, F. Pauly, M. Krieger, D. Djukic, J. C. Cuevas, and J. M. van Ruitenbeek, *Highly Conductive Molecular Junctions Based on Direct Binding of Benzene to Platinum Electrodes*, Phys. Rev. Lett. **101**, 046801 (Jul 2008).

[130] N. Agraït, A. L. Yeyati, and J. M. van Ruitenbeek, *Quantum properties of atomic-sized conductors*, Phys. Rep. **377**, 81 (April 2003).

[131] Y. Xue and M. A. Ratner, *End group effect on electrical transport through individual molecules: A microscopic study*, Phys. Rev. B **69**, 085403 (2004).

[132] L. A. Zotti, T. Kirchner, J.-C. Cuevas, F. Pauly, T. Huhn, E. Scheer, and A. Erbe, *Revealing the Role of Anchoring Groups in the Electrical Conduction Through Single-Molecule Junctions*, Small **6**, 1529 (2010).

[133] K. Baheti, J. A. Malen, P. Doak, P. Reddy, S.-Y. Jang, T. D. Tilley, A. Majumdar, and R. A. Segalman, *Probing the Chemistry of Molecular Heterojunctions Using Thermoelectricity*, Nano Lett. **8**, 715 (2008).

[134] S. M. Lindsay and M. A. Ratner, *Molecular Transport Junctions: Clearing Mists*, Adv. Mater. **19**, 23 (2007).

[135] J. Reichert, R. Ochs, D. Beckmann, H. B. Weber, M. Mayor, and H. v. Löhneysen, *Driving Current through Single Organic Molecules*, Phys. Rev. Lett. **88**, 176804 (April 2002).

[136] W. F. Reynolds, P. Dais, D. W. MacIntyre, R. D. Topsom, S. Marriott, E. Von Nagy-Felsobuki, and R. W. Taft, *Nature of π-electron-transfer effects in organic systems with varying π-electron demand*, J. Am. Chem. Soc. **105**, 378 (1983).

[137] M. Paulsson and S. Datta, *Thermoelectric effect in molecular electronics*, Phys. Rev. B **67**, 241403 (2003).

[138] A. Tan, S. Sadat, and P. Reddy, *Measurement of thermopower and current-voltage characteristics of molecular junctions to identify orbital alignment*, Appl. Phys. Lett. **96**, 013110 (2010).

[139] J. A. Malen, P. Doak, K. Baheti, T. D. Tilley, R. A. Segalman, and A. Majumdar, *Identifying the Length Dependence of Orbital Alignment and Contact Coupling in Molecular Heterojunctions*, Nano Lett. **9**, 1164 (2009).

[140] Y.-S. Liu, Y.-R. Chen, and Y.-C. Chen, *Thermoelectric Efficiency in Nanojunctions: A Comparison between Atomic Junctions and Molecular Junctions*, ACS Nano **3**, 3497 (2009).

[141] S.-H. Ke, W. Yang, S. Curtarolo, and H. U. Baranger, *Thermopower of Molecular Junctions: An ab Initio Study*, Nano Lett. **9**, 1011 (2009).

[142] K.-H. Müller, *Effect of the atomic configuration of gold electrodes on the electrical conduction of alkanedithiol molecules*, Phys. Rev. B **73**, 045403 (2006).

[143] M. H. Lee, G. Speyer, and O. F. Sankey, *Electron transport through single alkane molecules with different contact geometries on gold*, Phys. Status Solidi B **243**, 2021 (2006).

[144] M. Dell'Angela, G. Kladnik, A. Cossaro, A. Verdini, M. Kamenetska, I. Tamblyn, S. Y. Quek, J. B. Neaton, D. Cvetko, A. Morgante, and L. Venkataraman, *Relating Energy Level Alignment and Amine-Linked Single Molecule Junction Conductance*, Nano Lett. **10**, 2470 (2010).

[145] S. Y. Quek, H. J. Choi, S. G. Louie, and J. B. Neaton, *Thermopower of Amine-Gold-Linked Aromatic Molecular Junctions from First Principles*, ACS Nano **5**, 551 (2011).

[146] C. H. Suresh and S. R. Gadre, *A Novel Electrostatic Approach to Substituent Constants: Doubly Substituted Benzenes*, J. Am. Chem. Soc. **120**, 7049 (1998).

[147] E. Artacho and L. Miláns del Bosch, *Nonorthogonal basis sets in quantum mechanics: Representations and second quantization*, Phys. Rev. A **43**, 5770 (1991).

[148] R. Van Leeuwen and N. Dahlen. *An Introduction to Nonequilibrium Green Functions* (2005). URL `http://theochem.chem.rug.nl/research/vanleeuwen/literature/NGF.pdf`.

[149] A. P. Jauho. *Introduction to Keldysh non-equilibrium Green function technique*. URL `http://nanohub.org/resources/1878/download/jauho_negf.pdf`.

[150] A. L. Fetter and J. D. Walecka. *Quantum Many-Particle Systems* (McGraw-Hill, New York, 1971).

[151] J. Wu. *Keldysh Formalism: Non-equilibrium Green's Function* (2005). URL `http://www.physics.ubc.ca/~berciu/TEACHING/PHYS503/PROJECTS/05_jinshan.pdf`.

[152] J. Rammer and H. Smith, *Quantum field-theoretical methods in transport theory of metals*, Rev. Mod. Phys. **58**, 323 (1986).

[153] G. Mahan. *Many-Particle Physics* (Springer US; Auflage: 3rd ed. (31. Oktober 2000), 2000).

[154] R. Mills. *Propagators for Many Particl-e Systems* (Gordon and Breach, New York, 1969).

[155] L. V. Keldysh, *Diagram technique for nonequilibrium processes*, Zh. Eksp. Teor. Fiz. **47**, 1515 (1964).

Abbreviations

BPDT	biphenyl-dithiol
CPKS	coupled perturbed Kohn-Sham theory
DFT	density functional theory
DOS	density of states
GGA	generalized gradient approximation
HOMO	highest occupied orbital
IETS	inelastic electron tunneling spectroscopy
KS	Kohn-Sham
KSF	Kohn-Sham-Fock
LCAO	linear combination of atomic orbitals
LDA	local density approximation
LM	Lorentz model
LUMO	lowest unoccupied orbital
MCBJ	mechanical controlled break junction
NEGF	nonequilibrium Green's functions
ODA	octance-diamine
ODT	octance-dithiol
TBM	tight binding model
WBL	wide-band limit

List of publications

Regular articles:

1. *Cluster-based density-functional approach to quantum transport through molecular and atomic contacts,* F. Pauly, J. K. Viljas, U. Huniar, M. Häfner, S. Wohlthat, M. Bürkle, J. C. Cuevas, and G. Schön, New J. Phys. **10**, 125019 (2008)
2. I*nfluence of conformation on conductance of biphenyl-dithiol single-molecule contacts,* A. Mishchenko, D. Vonlanthen, V. Meded, M. Bürkle, C. Li, I. V. Pobelov, D. A. Bagrets, J. K. Viljas, F. Pauly, F. Evers, M. Mayor, and T. Wandlowski, Nano Lett. **100**, 156 (2010)
3. *Characteristics of amine-ended and thiol-ended alkane single-molecule junctions revealed by inelastic electron tunneling spectroscopy,* Y. Kim, T. J. Hellmuth, M. Bürkle, F. Pauly, and E. Scheer ACS, Nano **5**, 4104 (2011)
4. *Single-Molecule Junctions Based on Nitrile-Terminated Biphenyls: A Promising New Anchoring Group,* A. Mishchenko, L. A. Zotti, D. Vonlanthen, M. Bürkle, F. Pauly, J. C. Cuevas, M. Mayor, and T. Wandlowski, J. Am. Chem. Soc. **133**, 184 (2011)

Preprint:

1. *Molecular dynamics study of the thermopower of Ag, Au, and Pt nanocontacts,* F. Pauly, J. K. Viljas, M. Bürkle, M. Dreher, P. Nielaba, and J. C. Cuevas, submitted to Phys. Rev. B
2. *Conduction mechanisms in biphenyl-dithiol single-molecule junctions* M. Bürkle, J. K. Viljas, A. Mishchenko, D. Vonlanthen, G. Schön, M. Mayor, T. Wandlowski, and F. Pauly, submitted to Phys. Rev. B
3. *Electronic transport through single noble gas atoms,* L. A. Zotti, M. Bürkle, Y. Dappe, F. Pauly, and J. C. Cuevas, submitted to Phys. Rev. Lett.

Joint Project at 2008 CAMD Summer School in Electronic Structure Theory and Materials Design

1. *Density functional theory based screening of ternary alkali-transition metal borohydrides: A computational material design project* J. S. Hummelshøj, D. D. Landis, J. Voss, T. Jiang, A. Tekin, N. Bork, M. Dułak, J. J. Mortensen, L. Adamska, J. Andersin, J. D. Baran, G. D. Barmparis, F. Bell, A. L. Bezanilla, J. Bjork, M. E. Björketun, F. Bleken, F. Buchter, M. Bürkle, P. D. Burton, B. B. Buus, A. Calborean, F. Calle-Vallejo, S.

Casolo, B. D. Chandler, D. H. Chi, I Czekaj, S. Datta, A. Datye, A. DeLaRiva, V Despoja, S. Dobrin, M. Engelund, L. Ferrighi, P. Frondelius, Q. Fu, A. Fuentes, J. Fürst, A. García-Fuente, J. Gavnholt, R. Goeke, S. Gudmundsdottir, K. D. Hammond, H. A. Hansen, D. Hibbitts, E. Hobi, Jr., J. G. Howalt, S. L. Hruby, A. Huth, L. Isaeva, J. Jelic, I. J. T. Jensen, K. A. Kacprzak, A. Kelkkanen, D. Kelsey, D. S. Kesanakurthi, J. Kleis, P. J. Klüpfel, I Konstantinov, R. Korytar, P. Koskinen, C. Krishna, E. Kunkes, A. H. Larsen, J. M. G. Lastra, H. Lin, O. Lopez-Acevedo, M. Mantega, J. I. Martínez, I. N. Mesa, D. J. Mowbray, J. S. G. Mýrdal, Y. Natanzon, A. Nistor, T. Olsen, H. Park, L. S. Pedroza, V Petzold, C. Plaisance, J. A. Rasmussen, H. Ren, M. Rizzi, A. S. Ronco, C. Rostgaard, S. Saadi, L. A. Salguero, E. J. G. Santos, A. L. Schoenhalz, J. Shen, M. Smedemand, O. J. Stausholm-Møller, M. Stibius, M. Strange, H. B. Su, B. Temel, A. Toftelund, V Tripkovic, M. Vanin, V Viswanathan, A. Vojvodic, S. Wang, J. Wellendorff, K. S. Thygesen, J. Rossmeisl, T. Bligaard, K. W. Jacobsen, J. K. Nørskov, and T. Vegge, J. Chem. Phys. **131**, 014101 (2009)

Acknowledgment

First of all I would like to thank Prof. Dr. Gerd Schön for giving me the possibility to write my PhD thesis in his group, at such a nice place as the Institut für Theoretische Festkörperphysik. Then I would like to thank Prof. Dr. Juan Carlos Cuevas, for being the second referee of this thesis and coming all the way from Spain to my defense. Especially I would like to express my gratitude to Fabian Pauly for supervising my thesis, teaching me physics and being my roommate and friend for almost 5 years now. Janne Viljas I would like to thank for the various times he helped me out when I was stuck in some physical problem and I hope i can visit you in Finland again some time. I am deeply indebted to Florian Weigend, without his priceless insights into the depths of TURBOMOLE, this thesis would not have been possible the way it is. I would like to thank Linda Zotti for the good collaborations in various projects. A special thanks goes also to my roommate, coffee and boulder buddy Thomas Hellmut. For proof reading (despite of any problems), i would like to thank Richard Korytar. Regine Frank i would like to thank for the last minute proof reading of this thesis and for being a charming partner in afternoon coffee parties. Also best regards to my first semester physics buddy Tobias König. Of course I would like not to not thank Ferhat and Ralf my very good friends. Certainly I would like also whole-hearted thank Janine von Hodenberg. The most important person I have to thank is of course my mother, for supporting me all the time in the last 30 years, God bless you !!